27696

NATIONAL LIBRARY
OTTAWA

CANADA

BIBLIOTHÈQUE NATIONALE
OTTAWA

NAME OF AUTHOR Donald C.D. McKen

TITLE OF THESIS A Parametric Study of Ultra-Violet Photoionization for CO_2-Lasers

UNIVERSITY U. of Alberta

DEGREE FOR WHICH THESIS WAS PRESENTED Ph.D.

YEAR THIS DEGREE GRANTED 1976

Permission is hereby granted to THE NATIONAL LIBRARY OF CANADA to microfilm this thesis and to lend or sell copies of the film.

The author reserves other publication rights, and neither the thesis nor extensive extracts from it may be printed or otherwise reproduced without the author's written permission.

(Signed) Don C.D. McKen

PERMANENT ADDRESS:

DATED April 26, 1976

NL-91 (10-68)

INFORMATION TO USERS

THIS DISSERTATION HAS BEEN MICROFILMED EXACTLY AS RECEIVED

This copy was produced from a microfiche copy of the original document. The quality of the copy is heavily dependent upon the quality of the original thesis submitted for microfilming. Every effort has been made to ensure the highest quality of reproduction possible.

PLEASE NOTE: Some pages may have indistinct print. Filmed as received.

Canadian Theses Division
Cataloguing Branch
National Library of Canada
Ottawa, Canada K1A 0N4

AVIS AUX USAGERS

LA THESE A ETE MICROFILMEE TELLE QUE NOUS L'AVONS RECUE

Cette copie a été faite à partir d'une microfiche du document original. La qualité de la copie dépend grandement de la qualité de la thèse soumise pour le microfimage. Nous avons tout fait pour assurer une qualité supérieure de reproduction.

NOTA BENE: La qualité d'impression de certaines pages peut laisser à désirer. Microfilmée telle que nous l'avons reçue.

Division des thèses canadiennes
Direction du catalogage
Bibliothèque nationale du Canada
Ottawa, Canada K1A 0N4

The University of Alberta

A PARAMETRIC STUDY OF ULTRA-VIOLET PHOTOIONIZATION FOR CO_2 LASERS

by

Donald Charles David McKen ©

A Thesis

Submitted to the Faculty of Graduate Studies and Research in Partial Fulfilment of the Requirements for the Degree of Doctor of Philosophy.

Department of Electrical Engineering

Edmonton, Alberta

Spring, 1976.

The University of Alberta

Faculty of Graduate Studies and Research

The undersigned certify that they have read, and recommend to the Faculty of Graduate Studies and Research, for acceptance, a thesis entitled A PARAMETRIC STUDY OF ULTRA-VIOLET PHOTOIONIZATION FOR CO_2 LASERS submitted by Donald Charles David McKen in partial fulfilment of the requirements for the degree of Doctor of Philosophy in Electrical Engineering.

A Segre
Supervisor

G. W. Robinson

John

F. E. Vermeulen

J. A. Kernahan

M. E. Vedimoff
External Examiner

Date April 26, 1976

DEDICATION

To my wife and son for providing purpose for this work;

To my Father, Mother, and Sister for instilling the importance of education and for encouraging the pursuit of an academic life;

To my Uncle Jack and Aunt Ellen for providing unfailing inspiration and for motivating intellectual achievement;

I sincerely dedicate this thesis.

ABSTRACT

A detailed study of the parameters involved in CO_2 Laser photoionization has been undertaken. Various overvoltaged condensed spark discharge geometries were investigated. An inexpensive automotive type spark plug was found to provide a practical source element. A fast high peak current discharge was found to be the most efficient means of delivering a given amount of energy.

Average density measurements on photoplasma generated by a single spark source operating at 1Hz have been performed using an X-band microwave interferometer constructed for this project. This test facility provided adequate temporal resolution to follow the decay of the photoplasma. Spatial resolution was limited but average photoplasma density as a function of distance from the spark source has been obtained. The interferometer was sensitive to a plasma density of approximately $10^7 cm^{-3}$ and the plasma cutoff frequency was reached at a plasma density of $10^{12} cm^{-3}$. Measurements have been obtained in various gases and mixtures of gases applicable to a CO_2 laser device, over a wide pressure range. The effects of numerous seedant vapors have also been observed. A bare spark was employed primarily because window materials were vulnerable to the disruptive environment which resulted from the high voltage, condensed spark discharge.

A vacuum ultra-violet monochromator provided the necessary wavelength resolution to allow identification of those portions of the spectrum most useful for uniform volume photoionization in a CO_2 environment. Photographic recordings of the emission spectra of the spark sources employed have revealed that they are closely spaced line spectra largely independent of the gas dominating the environment. Identification of the useful part of the spectrum indicated that a LiF window could be used to isolate the spark source. This window was placed at the exit slit of the monochromator and it was sufficiently removed from the spark so as to avoid being damaged.

To obtain the photoionization spectrum of a given gas or vapor or some mixture of these, the monochromator was equipped with electronic recording apparatus. This apparatus effectively counted the total number of photons passing through a test cell and the total number of photogenerated electrons in the test cell for a single spark discharge. The photon counter was sensitive to approximately 2×10^5 photons and the charge collector to about 6.6×10^3 elementary charges. As the source was scanned by the monochromator, bar graph displays were generated with the use of twin x-y recorders. This display was characteristic of the photoabsorption and photoionization spectra of the gas or vapor in the test cell. The uncalibrated test facility has provided an abundance of relative data and its calibration has resulted in obtaining absolute values for the photoabsorption and photoionization cross-sections of tri-n-propyl amine.

Analyses of the data provided by these two test facilities have resulted in establishing criteria on which to base the design of the photoionization structure of CO_2 lasers. Less efficient two-step photoionization has been observed and this may be successfully exploited by high pressure CO_2 lasers.

Some substances in addition to those tested here have been suggested as being feasible to employ and which may warrant investigation.

ACKNOWLEDGEMENTS

The author wishes to acknowledge his supervisor, Dr. H.J.J. Seguin, for allowing the flexibility necessary for the development of this project and for providing specific guidance in experiments which subsequently resulted in publications.

The unfailing cooperation received by the author from both the academic and non-academic staff is gratefully acknowledged. Special thanks is conveyed to Mr. J. Radzion who exhibited electronic expertise and who devoted a great deal of time to the design and construction of the photon counter-charge collector assembly. Appreciation is extended to Mr. K. Doerrbecker and his staff for the excellent service provided in the machine shop.

The author wishes to thank the National Research Council of Canada for the postgraduate scholarships provided.

TABLE OF CONTENTS

		Page
Chapter 1	Introduction	1
1-1	Problems Encountered in CO_2 Laser Design	4
1-2	Review of Excitation Concepts and Techniques	6
1-3	Project Definition	14
Chapter 2	The Ultra-Violet Photoionization Technique	16
2-1	Basic Principles of Ultra-Violet Photoionization	18
2-2	Review of Ultra-Violet Sustained CO_2 Lasers	22
Chapter 3	Investigation of the Ultra-Violet Photoionization Process	27
3-1	Basic Apparatus and Experimental Method	29
3-2	Theoretical Considerations	35
3-2-1	The Ultra-Violet Light Source	36
3-2-2	Microwave Interferometer Design and Operation	43
3-2-2(a)	Propagation Through Unbounded Plasma	47
3-2-2(b)	Application to Photogenerated Plasma	54
3-2-3	Monochromator Test Facility	65
3-2-3(a)	Camera-Photomicrodensitometer Assembly	68
3-2-3(b)	Photoelectric Recording with Photon Counter	68

Page

3-2-3(c) Photoionization Detection by Charge Collection 70

3-2-3(d) Application to Cross-Sections 73

Chapter 4 Detailed Description of Photon Counter and Charge Collector Electronics 78

4-1 Photon Counter 87

4-2 Charge Collector 92

Chapter 5 Microwave Interferometer Phase Shift Measurements 105

5-1 The Ionization Chamber 106

5-2 The Source 110

5-3 The Signal 113

5-4 Theory Relevant to the Analysis of Plasma Decay Data 115

5-4-1 Diffusion 116

5-4-2 Attachment 120

5-4-3 Recombination 122

5-5 Plasma Decay Results 124

5-5-1 Helium and Nitrogen 126

5-5-2 Carbon Dioxide and Carbon Monoxide 143

5-5-3 Gas Mixtures 152

5-5-4 Oxygen and Air 161

5-5-5 Additives 173

5-5-6 Effect of a Leak 190

5-6 Photoelectron Density Dependence on Pressure and Distance 205

5-7 Investigation of Source Parameters 229

Page

5-8 Validity of Method 237
5-9 Role of Metastables 245
5-10 Discussion and Conclusion 249
Chapter 6 Results of Photoionization Parameter Investigation with a Vacuum Monochromator 254
6-1 Photographic Recording of Emission Spectra 255
6-2 Electronic Recording of Emission Spectra, Absorption Spectra and Photoplasma 266
6-2-1 Photoelectric Record of Emission Spectra 268
6-2-2 Charge Collection Mechanism 278
6-2-3 Photoionization Dependence on Wavelength 283
6-2-4 Photon Production and Photoionization Mechanism 291
6-2-5 Charge Collection Characteristics 304
6-2-6 Calibration of the Electronic Recording Devices 329
6-2-7 Photoionization and Photoabsorption Spectra of Selected Additives 346
6-2-8 Determination of Photoabsroption and Photoionization Cross-Section 371
6-3 Discussion and Conclusion 387
Chapter 7 Concluding Remarks 396
References 404
Vita 419

List of Tables

Table	Description	Page
4-1	Key to Components in Figures 4-2, 4-3, and 4-4	100
5-1	Experimental Time Constants	131
5-2	Attachment Cross-Sections	146
5-3	Experimental CO_2 Attachment Cross-Sections for Two Laser Mixtures	153
5-4	Experimental Values of the Two Body (β) and Three Body (K_a) Rate Coefficients for Attachment ot Oxygen	163
5-5	List of Additives Tested and Some Observations	175
5-6	Three Body Attachment Rate Coefficient in CO_2	202
5-7	Three Body Attachment Rate Coefficient in Laser Mixtures	203
5-8	Three Body Attachment Coefficient in CO	204
5-9	Photoabsorption Cross-Section in CO_2	212
5-10	Ionization Thresholds of Some Gases and Vapors	215
5-11	Short and Long Range Photoabsorption Coefficient	220

Page

5-12 Worst Case Error Involved in Neglecting the Electron Collision Frequency 241

6-1 Electron Diffusion Coefficients 314
6-2 Electron Diffusion Losses 317
6-3 Electron Avalanche Data 325
6-4 Photomultiplier Current Gains 338
6-5 Calibration of the "Quantum Efficiency" 343
6-6 CO_2 Photoabsorption Cross-Sections 373
6-7 Photoabsorption and Photoionization Cross-Sections for Tri-n-propyl Amine 377
6-8 Photoabsorption and Photoionization Cross-Sections for Tri-n-propyl Amine in a Laser Mixture 382
6-9 Two-Step Photoionization Coefficients for Tri-n-propyl Amine 385

List of Figures

Figure		Page
1-1	Vibrational Energy Level Diagram of CO_2 and N_2	2
3-1	Microwave Interferometer and Test Facility	30
3-2	Monochromator Test Facility	32
3-3	Spark Source Geometries	37
3-4	Spark Source Driving Circuit	40
4-1	Block Diagram of the Photon Detector	80
4-2	Photon Counter Circuit	81
4-3	Block Diagram of the Charge Collector	82
4-4	Charge Collector and Transmitter Circuit	83
4-5	Charge Collector Receiver Circuit	84
4-6	Monostable Flip-Flops	85
4-7	Analog Switches	86
5-1	Ionization Chamber and Gas Handling Plant	107
5-2	Discharge Current Waveforms	111
5-3	Typical Microwave Interferometer Signals	114
5-4	Plasma Decay in He	133
5-5	Reciprocal Electron Density Versus Time for He at High Pressures	134

Page

5-6 Reciprocal Electron Density Versus Time for He at Low Pressures 135

5-7 Electron Density Versus Time for He at Low Pressures 136

5-8 Plasma Decay in N_2 137

5-9 Reciprocal Electron Density Versus Time for N_2 at High Pressures 138

5-10 Reciprocal Electron Density Versus Time for N_2 at Low Pressures 139

5-11 Electron Density Versus Time for N_2 at Low Pressures 140

5-12 Reduced Mobility in He, Ne, and Ar 141

5-13 Reduced Mobility in N_2 142

5-14 Plasma Decay in CO_2 147

5-15 Electron Density Versus Time for CO_2 at High Pressures 148

5-16 Electron Density Versus Time for CO_2 at Low Pressures 149

5-17 Plasma Decay in CO 150

5-18 Electron Density Versus Time for CO 151

5-19 Plasma Decay in a CO_2:N_2:He = 1:1:8 Laser Mixture 155

5-20 Electron Density Versus Time for a CO_2:N_2:He = 1:1:8 Laser Mixture 156

5-21 Reciprocal Electron Density Versus Time for a CO_2:N_2:He = 1:1:8 Laser Mixture 157

		Page
5-22	Plasma Decay in a CO_2:N_2:He = 1:1:3 Laser Mixture	158
5-23	Electron Density Versus Time for a CO_2:N_2:He = 1:1:3 Laser Mixture	159
5-24	Reciprocal Electron Density Versus Time for a CO_2:N_2:He = 1:1:3 Laser Mixture	160
5-25	Plasma Decay in O_2	166
5-26	Electron Density Versus Time for O_2	167
5-27	Plasma Decay in Air	168
5-28	Electron Density Versus Time for Air	169
5-29	Two Body Electron Attachment Coefficient for O_2	170
5-30	Three Body Electron Attachment Coefficient for O_2	171
5-31	Secondary Signal	172
5-32	Electron Decay in Acetone	179
5-33	Reciprocal Electron Density Versus Time for Acetone	180
5-34	Electron Decay in Benzene	181
5-35	Reciprocal Electron Density Versus Time for Benzene	182
5-36	Electron Decay in Methyl Ethyl Ketone	183
5-37	Reciprocal Electron Density Versus Time for Methyl Ethyl Ketone	184
5-38	Electron Decay in Tri-ethyl Amine	185

Page

5-39 Reciprocal Electron Density Versus Time for Tri-ethyl Amine 186

5-40 Electron Decay in Tri-n-propyl Amine 187

5-41 Reciprocal Electron Density Versus Time for Tri-n-propyl Amine 188

5-42 Plasma Decay Time Versus Gas Pressure 189

5-43 Photoabsorption Characteristics of O_2 192

5-44 Electron Decay in H_2 at Low Pressures 199

5-45 Photoabsorption Characteristics of CO_2 223

5-46 Photoelectron Density Versus Gas Pressure for Various Gases 224

5-47 Photoelectron Density Versus Total Pressure for Various Laser Mixtures 225

5-48 Photoelectron Density Versus Total Pressure for a $CO_2:N_2:He = 1:1:1$ Laser Mixture with Selected Additives 226

5-49 Photoelectron Density Versus CO_2 Partial Pressure for Laser Mixtures 227

5-50 Variation in Photoelectron Density with Distance from a Single Ultra-Violet Source in Laser Mixtures Plus Tri-n-propyl Amine 228

5-51 Electron Density Versus Charging Voltage for Various Capacitors 234

5-52 Electron Density Versus Energy Stored in the Capacitor 235

Page

5-53 Semi-Log Plot of Electron Density Versus Charging Voltage 236
5-54 Schematic Diagram of a Test Discharge and Preionization Laser System 251

6-1 Emission Spectra from an Automotive Surface Gap Spark Plug 260
6-2 Emission Spectra from Colinear Tungsten Pins 261
6-2A Tungsten Pin Emission Spectrum and Microdensitometer Scan 262
6-3 Key to Spectra Photographs 263
6-4 Spectra of a Hg-Vapor Lamp 264
6-5 Emission and Absorption Spectra from an Automotive Surface Gap Spark Plug 265
6-6 Spark Source Emission Spectrum from Individual Laser Gases 273
6-7 Spark Source Emission Spectrum for a Laser Mixture 274
6-7A Broadband Spark Source Emission Spectrum for N_2 275
6-8 Effect of a LiF window on the Spark Source Emission Spectrum 276
6-9 Spark Source Emission Spectra for Hy-Purity N_2 and for Contaminated N_2 277

		Page
6-10	Hypothetical Charge Collector Characteristics	279
6-11	Photon Intensity and Photoionization Density in a Laser Mixture	288
6-12	Photon Intensity and Photoionization Density in a Laser Mixture plus tri-n-propyl Amine	289
6-13	Photoionization Spectra of the Individual Laser Gases	290
6-14	Logarithm of Photon Intensity Versus Logarithm of Circuit Inductance	294
6-15	Spark Discharge Current and Photon Waveforms	296
6-16	Relative Electron Density Versus Relative Photon Intensity	303
6-17	Charge Collector Characteristics in He	305
6-18	Charge Collector Characteristics in CO_2	306
6-19	Charge Collector Characteristics in N_2	307
6-20	Charge Collector Geometry	321
6-21	Effect of Tri-n-propyl Amine on the Spark Source Emission Spectrum	347
6-22	Photoabsorption and Photoionization in 40 torr of Laser Mixture Plus 0.05 torr of Tri-n-propyl Amine	350

Page

6-23 Photoabsorption and Photoionization in 40 torr of Laser Mixture Plus 0.3 torr of Tri-n-propyl Amine 351

6-24 Photoabsorption and Photoionization in 40 torr of Laser Mixture Plus 2 torr of Tri-n-propyl Amine 352

6-25 Photoionization in 40 torr of Laser Mixture Plus Tri-n-propyl Amine 353

6-26 Photoabsorption and Photoionization in 60 torr of Laser Mixture Plus 0.05 torr of Tri-n-propyl Amine 354

6-27 Photoabsorption and Photoionization in 60 torr of Laser Mixture Plus 0.25 torr of Tri-n-propyl Amine 355

6-28 Photoabsorption and Photoionization in 60 torr of Laser Mixture Plus 2 torr of Tri-n-propyl Amine 356

6-29 Photoionization in 60 torr of Laser Mixture Plus Tri-n-propyl Amine 357

6-30 Photoionization in 20 torr of Laser Mixture Plus Tri-n-propyl Amine 358

6-31 Photoabsorption and Photoionization in 4 torr of NO 363

6-32 Photoabsorption and Photoionization in 20 torr of Laser Mixture Plus 0.1 torr of Benzene 364

Page

6-33 Photoabsorption Spectra of CO_2 365

6-34 Photoabsorption and Photoionization in 0.1 torr of Tri-n-propyl Amine 370

6-35 Photoabsorption in 20 torr of Laser Mixture Plus Tri-n-propyl Amine 380

Chapter 1

Introduction

Pulsed and continuous-wave CO_2 laser operation was first announced by Patel in 1964 [26,27,28]. However, the laser achieved only low power output and, except for its characteristic wavelength at 10.6 microns, it was not appreciably different from the many laser systems that had been operated to that date. Shortly thereafter the addition of N_2 and He to the CO_2 was shown to significantly increase the output power and efficiency of the laser [29,30,31,32]. Since that time the CO_2 laser has remained of great interest [36] and in only a decade the output has been increased from millijoules per pulse and watts peak power to hundreds of joules per pulse and gigawatts peak power with efficiency as high as 25% [1]. These improvements came about largely due to operating at ever increasing pressures [1] and volumes and also by developing techniques to increase the pumping energy to a device. This has been discussed in more detail in Section 1-2.

The active medium of the conventional CO_2 laser is an electrically excited mixture of CO_2, N_2 and He. A typical volume ratio is $CO_2 : N_2 : He = 1 : 1 : 3$, however, devices can be operated at ratios far from this.

The relevant energy levels involved in a carbon dioxide gain media are shown in Figure 1-1. Laser action occurs on a vibrational-rotational transition of the ground

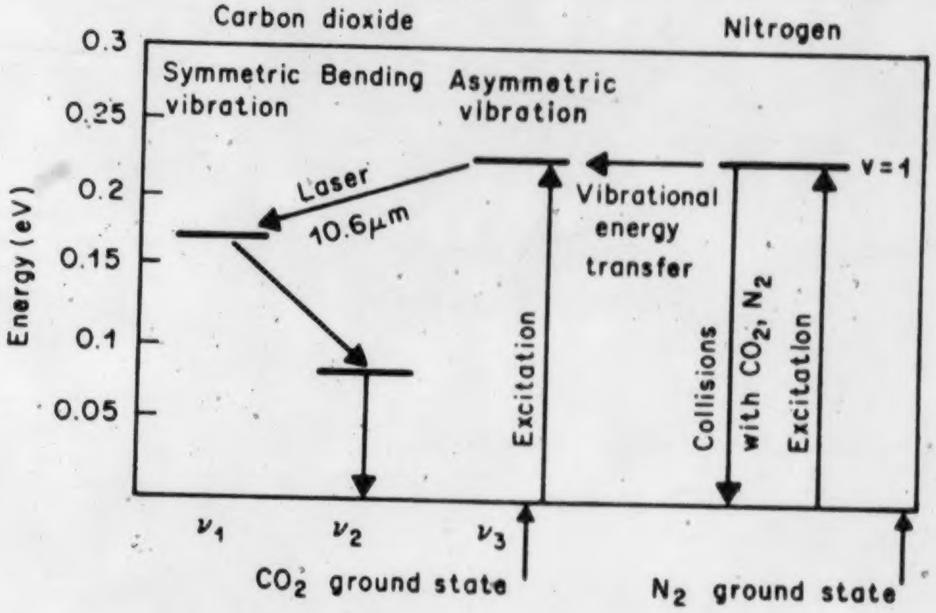
Carbon dioxide
Nitrogen
0.3
0.25
0.2
0.15
0.1
0.05
Energy (eV)
Symmetric vibration
Bending
Asymmetric vibration
Laser
10.6μm
Vibrational energy transfer
v = 1
Excitation
Collisions with CO₂, N₂
Excitation
ν₁
ν₂
ν₃
CO₂ ground state
N₂ ground state

FIGURE 1-1 ENERGY LEVEL DIAGRAM Vibrational energy level diagram of CO_2 and N_2 (simplified) illustrating the mechanism resulting in gain at 10.6 μm [33].

electronic state of CO_2. The $\nu = 1$ level of N_2 is in close energy coincidence with the upper laser level, (0, 0°, 1), of CO_2 and rapid collisional energy exchange between the two takes place. The N_2 level, which is readily excited by electron collisions, is metastable and this provides a reservoir of stored energy for selective and efficient excitation of the (0, 0°, 1) level of CO_2. In addition, direct excitation of CO_2 by electron bombardment takes place. Some relaxation of the upper laser level to the ground state occurs through non-radiative collisions with neighboring molecules. However, the time constant for this to occur is larger than the time constant for stimulated radiative decay to the lower laser level (1, 0°, 0). The lower laser level decays to the ground state by way of (0, 2°, 0) and the rate of depopulation of this level can be the rate-limiting process in the laser. Because of the proximity of the (0, 2°, 0) level to the ground state, the gas temperature must be kept low, (room temperature or a little higher) to prevent this level from becoming thermally populated. He, because of its high thermal conductivity, helps to cool the gas and also increases the relaxation rate of the lower laser level by rapid collision with CO_2 molecules in the (0, 2°, 0) state [33]. In addition He has a low dielectric constant and tends to stabilize the electric excitation pulse across the laser gas.

1-1 Problems Encountered in CO_2 Laser Design

A number of difficulties are encountered in the operation of a high power CO_2 laser. Some of these are associated with the optics. High power pulses have a tendency to damage lenses and windows as well as the reflective coatings on mirrors. Good quality, large aperture lenses and windows are not readily available in the infrared portion of the spectrum. Operation of devices at near optical breakdown of the laser gas has indicated the need for large aperture devices [13]. High power continuous-wave operation and rapid pulsed operation results in heating the laser gas and thermally populating the (0, 2°, 0) level and even the lower laser level, (1, 0°, 0). Unless complex heat exchangers are built into the system the laser operation is severly retarded. Prolonged operation of the laser can result in an impurity build-up due to dissociation of molecules during the excitation discharge. Actually, one of the attractive features of the CO_2 laser is that it can operate well with various impurities in the laser gas, and in fact, operates more efficiently under these conditions. Nevertheless, the laser will not tolerate excessive impurity concentrations since the upper laser level can be rapidly reduced by collisions with many types of impurities. However, these problems have not been the limiting factor in high power CO_2 laser development and consequently are of minor concern here.

Uniform electric excitation of the laser gas has always been the limiting factor. Laser output can be increased by increasing the operating pressure, excitation energy, or active volume of the device. However, all of these are inconsistent with establishing a uniform and high current density glow discharge necessary for effective pumping of the laser gas. Inevitably, as one or more of these parameters are increased, the discharge will occur in the form of an intense and constricted arc. This is highly detrimental since the arc short-circuits the supply and reduces the energy available for excitation. The arc reflects and refracts the laser beam and gives rise to various dissociation impurities that may affect the operation of the laser. In addition the electrodes are often pitted by the intense heat [34].

1-2 Review of Excitation Concepts and Techniques

Patel increased the cw output power of the CO_2 laser by five orders of magnitude to 100 watts by adding N_2 and He to the CO_2 and also by flowing the gas through the structure to promote cooling [29,30,31,32,35]. These devices operated at pressures less than 50 torr and were excited by a longitudinal glow discharge. Excessive pressure would result in a glow-to-arc transition.

Hill was the first to operate a pulsed CO_2 laser successfully [2]. The excitation was longitudinal to the laser axis and required an electric field to pressure ratio (E/P) of above breakdown for effective pumping. He obtained 5 J - 200 kW CO_2 laser pulses from a device eight feet long by three inches in diameter. This was an increase in peak power of about three orders of magnitude over the previous cw lasers. The operating pressure was 60 torr. However, the necessary excitation voltage was in the range 200 kV to 1 MV depending on the diameter of the device. Consequently direct scaling of these lasers to large volumes and high pressures would require an impractically high voltage to maintain an above breakdown E/P.

Beaulieu, using a row of closely spaced resistors for a cathode and a flat or cylindrical anode, was able to transversely excite an atmospheric pressure mixture of CO_2, N_2 and He [3]. The acronym TEA was used to describe this type of laser. He was able to obtain pulses of 150 mJ at peak powers of 0.5 MW from a device employing 150 cathode resistors (1000 ohms each). The device was 1.25 m long and the cathode anode spacing was 2.5 cm. It was repeatedly excited by a discharge from a 0.02 μf capacitor charged to 25 kV. The gas mixture was in the ratio $CO_2 : N_2 : He = 1.2 : 1 : 10$. This was a significant step in the development of high power lasers, since the average power available per unit volume is proportional to the square of the operating pressure [4]. The square law power dependence on pressure results since an increased pressure means more molecules are available to contribute to the laser field build up; and the collisionally excited upper laser level is more rapidly populated at high pressures. Also the lower state of the laser transition must decay to ground via collisions before the gas can be re-excited. This implies a maximum repetition rate at which the laser can be operated. Another advantage is that narrower pulse widths can be obtained as a result of the collision broadening of the laser transition at high pressures [4,5]. Finally, transverse excitation results in a decreased electrode spacing and large electric fields can be obtained with relatively low voltage.

In order to obtain a more uniform excited density distribution, Beaulieu attempted to initiate a distributed discharge between two long parallel electrodes. An increase in the gas pressure above 20 torr forced the discharge into an arc [1].

A distributed discharge can be obtained with extended electrodes even at atmospheric pressure provided that the discharge time is shorter than the arc formation time [6,7,34,93]. To delay the arc formation for some time the electrodes must be uniformly spaced and well polished to eliminate burrs [7]. A fast discharge time also applies to driving a number of pin electrodes in parallel from a single capacitive source. However, at the volumes, electrode areas, and input energies of interest the discharge time becomes too long with conventional curcuitry and arcs have time to form. In addition a fast discharge time does not correspond to the most efficient pumping rate of CO_2 lasers [8]. Consequently, a fast discharge rate is not a good method of arc suppression even if it could be obtained at high energies.

An alternate solution to the problem is to prevent the current density from reaching a large enough value to initiate an arc.

One such device employing this technique is the so called "double discharge device" or D^3 [6,7]. This system makes use of a mesh or grid cathode with a third electrode placed close to it on the side opposite the anode. A fast low energy discharge is triggered between the cathode and third electrode producing a cloud of electrons around the cathode. These electrons facilitate the main discharge to the anode by effectively increasing the discharge area and thereby reducing the current density enough to prevent the formation of a constricted arc. Laflamme obtained 9 J per pulse with a peak power of 12 MW from a 3.8 m long laser. The output energy density was 5.5 J/ℓ.

Nichols and Brandenberg used a similar electrode structure but produced a cloud of electrons with an 11 MHz RF generator connected between the grid and cathode. This device operated very well at 160 torr total pressure and the volume flow ratio of $CO_2 : N_2 : He = 1 : 1 : 8$. With gas flow transverse to the optical axis at Mach 3, 17 kHz pulsed laser output was obtained [9]. The flow was necessary to promote cooling of the gas.

Thirdly, it has been suggested that a discharge could be stabilized if the volume electron-ion production mechanism in the plasma was made independent of the applied electric field through the use of an external ionization source such as high energy electron beam injection or photoionization [10]. In such externally controlled plasmas, the applied electric field can be much lower than that required for self-sustaining discharges and the Townsend multiplication process in the volume can be effectively zero eliminating this breakdown mechanism.

Electron beam controlled lasers have been constructed and operated [10,11,12] producing plasma densities of 10^{12} - 10^{13} electrons per cm^3 [10,11] and resulting peak output powers of hundreds of MW at up to 2000 J/pulse [13].

Also this technique does not depend to such a great extent on the concentration of He. Consequently, the concentration of active CO_2 and N_2 can be increased. This technique also lends itself to stabilizing discharges at pressures of many atmospheres where very short pulses can be generated. However, the electron gun can be very complicated and expensive requiring high voltage supplies to generate electrons in the hundreds of kev to Mev energy range [14]. In addition, a thin window material is required to isolate the high vacuum gun from the high pressure laser. Usually titanium, a few mils thick, is used. Often it must be supported by some type of mesh structure.

Another mechanism that has been used is to shape the electrodes to Rogowski or Bruce profiles and to establish preionization by an additional discharge to a trigger electrode in the form of one or more wires parallel to, but laterally displaced from the discharge axis. This has resulted in input energies greater than 400 J/ℓ.

Pearson and Lamberton[15] used this technique and subsequently showed that it was superior to the previously employed D^3 technique. They suggested that the discharge from the wire to the anode provided ultra-violet light from the 584 Å resonance line in He. Streak photography revealed that the discharge started from the cathode and so it was indicated that photoemission and not volume photoionization was the initiating mechanism. However, there may not have been sufficient volume ionization from the particular arrangement to be effective. Apparently, the arcs are suppressed by providing a large current cross-section and low current density.

Output energy increases with increased charging voltage and increased N_2 concentration, and since this device can tolerate larger increases in these parameters than the double discharge laser, its output energy per pulse is about three times higher (18 J/ℓ).

It was the suggestion that the trigger wire produces ultra-violet light that motivated the current interest in arc suppression by ultra-violet photoionization. Recently, a physical model has been proposed which has elucidated the basic physics of the conditioning mechanism apparently inherent in the devices discussed here and in the ultra-violet sustained devices reviewed in the following chapter [92]. Palmer asserted that for sufficiently high values of Pd common to CO_2 TEA lasers, that a breakdown mechanism termed streamer breakdown occurs without an initial glow phase. For sufficiently high Pd, the space-charge E-field developed at the head of a single avalanche (upon application of the above breakdown E/P excitation voltage) becomes comparable to the applied E-field. The local field gradients resulting from the summation of primary avalanches causes the ionization to become filamentary prior to breakdown. To develop his model, Palmer considered only a single primary avalanche. As this avalanche propagates across the gap photons emitted from the head of the avalanche promote secondary avalanches by photoionization. These secondary avalanches tend to converge upon the primary avalanche as a consequence of the initiating photoionization spatial parameters and the local space charge field. This rapidly leads to the development of a highly conducting filamentary channel resulting in electrical breakdown. Assuming that the radius of the head of the primary avalanche is controlled by diffusion (electrostatic repulsion may play a part) and by applying the streamer breakdown condition of equality between the applied field and the resulting space charge field Palmer obtained Raether's breakdown criterion.

$$\left(\frac{\alpha_t}{P}\right)Pd = 20 + \ln d \qquad 1\text{-}1$$

in MKS units

α_t = Townsend's first ionization coefficient $[m^{-1}]$

P = gas pressure [torr]

d = gap spacing [m]

Palmer argued that if a sufficient number of primary avalanches were initiated, then the secondary effects of each primary avalanche would overlap to such an extent so as not to favour convergence on any particular primary avalanche. Subsequently, he calculated that a uniform volume density greater than 10^4 electron cm^{-3} would be sufficient to suppress streamer breakdown and to initiate a glow discharge. He emphasized the importance of uniform volume preionization and pointed out that the streamer breakdown could develop ahead of a layer of electrons produced in the vicinity of the cathode. Therefore, the strength of the D^3 devices discussed may have been in producing volume photopreionization in addition to the cloud of electrons at the cathode.

In addition to the brief description of the physical processes described above, detailed Russian work on the subject of electric discharges in gases has recently come to the attention of the author. Detailed information can be obtained from the publication [118].

1-3 Project Definition

The mounting evidence supporting ultra-violet photopreionization control of the CO_2 laser excitation discharge, promoted a relative abundance of literature on the subject. A review has been included in the following chapter.

Although some theoretical considerations have been published, the majority of the work has been essentially trial and error experimentation. Typically, the photopreionization concept has been incorporated into a laser device and the resulting change of laser input/output characteristics monitored. The resulting changes have been related to such parameters as energy dissipation in the ultra-violet source, seedant concentration if any, and the ultra-violet filling factor. The filling factor describes how uniformly the active laser volume is irradiated and depends entirely on the source geometry. Attempts to determine the relative importance of cathode photoemission and volume photoionization were made with the results largely favoring the latter.

In general the employment of photopreionization devices resulted in marked improvement in laser operation. Unfortunately, information relative to the photopreionization process was meagre and optimum exploitation of the concept was inhibited.

The primary objective of this project has been to provide test facilities and to utilize these facilities to provide detailed parametric information regarding the CO_2 laser photopreionization mechanism. Test facilities have been designed and constructed in such a manner as to yield information regarding the functional relationship among the pertinent parameters. Primary targets for investigation have been average photoplasma density measurements in a CO_2 photopreionization simulated device, source emission spectra, laser gas photoabsorption and photoionization spectra both with and without additives, and the determination of absolute photoabsorption and photoionization cross-sections. The results provide criteria on which to base the selection of ultra-violet sources and laser mixtures to obtain maximum photopreionization densities. The test facilities provide a convenient means of determining the optimum operating point for ultra-violet sources and laser mixtures that may warrant investigation in the future.

Chapter 2

The Ultra-Violet Photoionization Technique

Not only can the CO_2 laser be controlled by an electron beam, but it also can be effectively controlled by ultra-violet photoionization.

Since the ultraviolet source can operate within the laser gas environment, there is no need for high vacuum construction. Ultra-violet control does not require a thin delicate foil window and so scaling to pressures of many atmospheres should be much easier. High voltage sources needed to accelerate electrons in electron guns are not required for ultra-violet control. Ultra-violet sources can be readily constructed in large arrays giving rise to uniform illumination over a large aperture while it is relatively difficult and expensive to construct large area electron guns.

Ultra-violet control of a CO_2 TEA laser discharge can be divided into two regimes. The first is really a partial control mechanism or a discharge stabilization technique. The glow discharge phase for an above break-down E/P excitation pulse can be initiated by uniform volume photopreionization. The required density is low being any density greater than 10^4 electrons cm^{-3}. The second regime of ultra-violet control is indeed total control. Here, photoionization densities exceeding 10^{12} to 10^{13}

electrons cm^{-3} must be maintained during the pumping of the laser. Here the laser can be efficiently pumped by heating the electrons with a below breakdown value of E/P. This total control mechanism would completely eliminate electrical breakdown problems. The regime of operation will be determined by the development of practical photoionization methods.

2-1 Basic Principles of Ultra-Violet Photoionization

Single-step, two-step, and multi-step ionization mechanisms have been proposed as being feasible to exploit [16]. The species to be photoionized could be any one of, or combination of, the following:

Laser gases - CO_2, N_2, He

Impurities - Industrial grade gases are known to have a relatively high concentration of impurities, particularly hydrocarbons.

- Background impurities in typical laser devices may also be sufficiently high.

Additives - Usually low ionization threshold molecules such as alkaline metals or hydrocarbons.

Assuming that sufficient ultra-violet radiation in a given bandwidth can be produced, two basic problems are encountered in obtaining volume photoionization.

(1) The first is related to the high ionization potential of the laser gases. Ultra-violet light of wavelength less than 900 Å is required for one-step photoionization of even the most easily ionized constituent - CO_2 at 14.4 ev. This renders the use of transparent windows practically impossible. In addition, absorp-

tion bands in N_2 at these wavelengths reduce the ionization efficiency. Also, one-step ionization of He and N_2 is precluded by the fact that CO_2 is heavily absorbing for $\lambda < 1700 - 1800$ Å except for a narrow window at $\lambda = 1200$ Å and the ionization wavelength of both N_2 and He are considerably below this.

(2) The second problem involves the high photoionization cross-section of most gases. A typical photoionization cross-sections, σ_i, may be about 1×10^{-18} cm^2 for any one of the laser gases. At a total pressure of 760 torr the molecular concentration, n_o of any one of the gases will be about 2.7×10^{19} cm^{-3}. This results in a penetration depth of:

$$L \simeq 1/n_o \sigma_i \simeq 0.37 \text{ mm}$$

Consequently, a one-step process seems unlikely and if indeed one of the laser gases is responsible for the ionization then a two- or multi-step process must be the mechanism. However, it is quite feasible that an impurity in the laser with a low ionization threshold is the agent responsible for volume photoionization and that it follows the one-step mechanism. The necessary density is difficult to estimate because of the lack of knowledge of the impurities' photoionization cross-section. However, if one assumes a value of $\sigma_i \simeq 10^{-18}$ cm^2 then, for a desired penetration depth of $L \simeq 100$ cm then $N \simeq 1/\sigma_i L \simeq 10^{16}$ cm^{-3}.

This is about three orders of magnitude less than the concentration of the laser gases and could be present in the industrial grade gases or as a product of dissociation.

In fact the first problem can be overcome by seeding the laser gas with a small amount of some type of low ionization threshold substance. Cesium, rubidium, tripentylamine, tri-n-propyl amine and tributylamine have been proposed [16]. Such additives must meet stringent requirements and not too many substances meet all of the following specifications:

(1) High vapor pressure

(2) Large photoionization cross-section

(3) Transparency at the laser wavelength

(4) Low ionization threshold

(5) Small cross-section for collisional depopulation of the upper laser level (00°1).

A narrow window in CO_2 around 1200 Å somewhat reduces the requirement for low ionization threshold but it increases the necessity for large photoionization efficiency. Also the source would have to be intense across the window bandwidth.

It should be pointed out here that Nygaard [17] has proposed using Cs or Cs_2 vapor as a seed material and to photoionize it by a two-step process. The required wavelength would be around 5000 Å where very high power sources are available. This would in turn reduce the necessity of high concentrations requiring high temperatures.

However, Cs is very reactive and toxic and may not be practical from a safety point of view. Also it has a tendency to relax the upper laser level [16]. In addition Russian work has shown that Cs reacts with CO_2 in the laser mixture, producing compounds that are not easily ionized [119]. This was consistent with tests performed on Na and Cd vapors for this thesis. No measurable photoionization of these vapors occurred at room temperature. Heating the elements to 200 or 300°C did not result in any improvement. Although the experiment was performed at low pressure (< 0.1 torr) the metal vapor probably reacted with background gases producing compounds that were not easily ionized. Further attempts to produce large photoelectron densities with metal vapors were not made.

The second problem can be solved by taking advantage of the high photoionization cross-section of most gases and proposing a two- or multi-step process. Here, (for a two-step process) the ionizing species becomes excited by absorption of a photon approximately 1/2 the energy required for ionization. If the photon flux is high enough it will absorb another photon and become ionized before it has time to decay to the ground state. Of course, this mechanism could apply to seed materials as well as impurities.

2-2 Review of Ultra-Violet Sustained CO_2 Lasers

Since this project began a number of papers have appeared in the literature reporting the successful operation of CO_2 TEA lasers depending on arc suppression by ultra-violet photoionization.

A laser depending on the ultra-violet radiation from a high voltage spark to stabilize the discharge was reported to yield output energies of 50 J/ℓ at 15% efficiency [18]. In this device the solid cathode could see the spark sources through a grid anode and it is likely that both surface photoemission at the cathode and volume photoionization played a part in stabilizing the discharge. When the spark sources were shielded with a CaF_2 window arcing occurred indicating that the useful ultra-violet was below the window cutoff wavelength of about 1250 Å. $CO_2 : N_2 : He = 1 : 1 : 8$ flow ratios were used with an E-field of 10 kV/cm. It was significant that the maximum capacitance to be discharged without arc formation increased with electrode separation indicating that the technique would be useful for large aperture lasers. In a similar device it was reported that the ultra-violet responsible for ionization was below 1000 Å but no details of how this was determined were given [19]. In this case the output was 40 J/ℓ at 24% efficiency.

Operation by ionizing tri-n-propyl amine by a two-step process was successfully demonstrated [20] with output energies of 15 J/ℓ. In this case the output energy exhibited a sharp peak as a function of E/P and it could be readily tuned. The amount of additive was estimated to be about 0.25 torr and it was added by bubbling a portion of the incoming N_2 through it. Xenon flashlamps employing quartz envelopes were used, effectively forcing any photoionization to occur in a two-step process.

It has also been demonstrated that a laser depending on ultra-violet volume photoionization can be scaled up to active volumes of almost 19 ℓ with resulting output energy of 300 J/pulse and peak powers greater than 3 GW [13]. This laser was similar in construction to the double discharge type except that the preionization discharge occurred near the anode. The ultra-violet source took the form of a two dimensional array of copper discs separated from a ground plane by a thin dielectric. Rows of these discs were connected to charged capacitors and sparks between the discs developed. Time resolved photography indicated that the stability of the discharge depended on the ultra-violet volume photoionization from the primary discharge. In this case large E-fields were found to be the most effective. No additive was used. It was determined that the energy density of the beam was 40% of that which would result in optical breakdown of the laser gas indicating the need for larger aperture devices. In a later publication the authors reported having successfully obtained a stable discharge across a gap 30 cm wide and 600 cm^2 in cross-sectional area [21]. As before the same ultra-violet source was placed behind one of the perforated electrodes. Since the polarity of the main discharge made no difference to the stability it was concluded that volume photoionization was responsible for arc suppression. The total gas pressure was atmospheric and in the ratio $CO_2 : N_2 : He = 1 : 1 : 3$.

No attempt was made to optimize any parameters and it was felt that with such an attempt beam cross-section in excess of 10^3 cm^2 and total output energy capabilities of about 10^4 J could be reached.

In a recent publication Judd points out the necessity for good spatial uniformity of volume photoionization for proper plasma conditioning. This implies that the source must have a geometry conducive to yielding constant intensity over the entire volume. Also he pointed out that energy transfer to the plasma is dependent on circuit parameters and that increasing the capacitance voltage may or may not increase the energy delivered to the plasma [22]. Finally, he employed a preionizer with a current that could last from 2 μs to 10 μs, and was able to pump the gas from 0.5 μs to 10 μs and consequently extended the length of the output laser pulse accordingly.

He also pointed out that, at least in his system, the energy to the ultra-violet source must exceed a critical value for proper plasma conditioning and that the peak power is not as critical. No additive was used and with the use of a filter (LiF) he concluded that the useful ultra-violet occurred at wavelengths less than 1200 Å. He also determined that 60% of the photon flux from the source occurred in a spectral range less than 1200 Å. This spectral information does not agree with experimental results obtained for this thesis.

Further work by Levine and Javan [23] resulted in establishing an average cross-section for excitation of tri-n-propyl amine into an intermediate state to be 7.3 Mb. Again, they made use of a Xenon flashlamp and the cross-section was the average over the flashlamp spectrum. The absorption coefficient for the first step photon is actually wavelength dependent and peaks at 2150 Å, at 25 Mb. They used an ion collector that could see the source which may have resulted in surface photoemission. Finally, they arrived at a formula for electron density based on a two-step process for either an attachment or recombination controlled plasma.

In one of the most recent publications Clark and Lind [24] constructed a device which employed a total of 1000 arcs in 25 parallel arrays similar to Richardson's [13]. This was placed 2.1 cm behind a mesh electrode and the volume between the main electrodes was illuminated. The mixture was 0.3 torr of tri-n-propyl amine and a 2.8% : 47.2% : 50%=CO_2 : N_2 : He ratio at 700 torr total pressure. The ultra-violet source circuit had a ring period of 10 μs and a decay time of about 45 μs. Fast oscilloscope traces of the small signal gain revealed that it followed the ringing variation of the ultra-violet source current. Also they discovered that the gain was only flat between the electrodes if the mesh electrode was connected as the cathode. In a later publication they reported to have obtained laser pulse lengths up to 37 μs at 47 J/ℓ. For a 23 μs long pulse they obtained 60 J/ℓ [25]. They also established that the ultra-violet responsible for ionizing the tri-n-propyl amine was in the range 1200 - 1700 Å which indicated a one-step process. The concentration of CO_2 had to be kept low, 2 - 3%, so as to prevent ultra-violet absorption by CO_2.

The emphasis has been on demonstrating that ultra-violet sustained lasers can be operated on a competitive basis with electron beam sustained lasers. Relatively little effort has been expended on determining the precise mechanism of photoionization in the laser gas or in determining the relationship among the parameters involved in the process.

Chapter 3

Investigation of the Ultra-Violet Photoionization Process

Ultra-violet photoionization involves a large number of parameters and they must be well understood before this method of arc suppression can be fully exploited. The task is made particularly difficult since most parameters are intimately linked to each other and it is very difficult to vary one parameter and simultaneously hold the others constant. An observed system response to a parameter variation may in fact be due to a combination of factors. Consequently, a very thorough investigation of the mechanism is required in order to reveal the parametric relationship. In turn this requires that the following studies be made:

(1) Determine the total average electron density in the following gases as a function of time, distance from the source, and gas pressure.

CO_2, N_2, He

Mixture of $CO_2 : N_2 : He = 1 : 1 : 1$

$= 1 : 1 : 3$

$= 1 : 1 : 8$

(2) Photograph the spectrum of sources of different geometry and gaseous environment for comparison.

(3) Using the most intense source observe the dependence of the intensity as a function of wavelength on the discharge circuit parameters. These include inductance, capacitance, energy, voltage, ringing frequency, rate of change of current, and peak current.

(4) Observe the time response of the light at various wavelengths while the source parameters are varied.

(5) Observe photoabsorption and photoionization spectra for various gas mixtures of interest.

(6) Determine photoabsorption and photoionization cross-sections for promising additives.

These measurements will reveal the following:

(1) The optimum spectral distribution of light for most efficient photoionization of a particular laser mixture.

(2) The dependence of the spectral distribution of a source on its geometry and discharge circuit parameters.

(3) The efficiency of a source over a desired bandwidth.

(4) The effectiveness of a source in producing electrons.

(5) The number of steps involved in the ionization process.

(6) The lifetime of the photoionization plasma.

(7) Photoabsorption and photoionization cross-sections of additives as a function of wavelength.

3-1 Basic Apparatus and Experimental Method

The apparatus required for the experiment takes the form of two separate units. A great deal of auxillary equipment was required but will not be listed separately.

Interferometer

The first basic experimental unit consists of an x-band microwave interferometer used to measure plasma density in a cylindrical vacuum ionization chamber. This device is illustrated in Figure 3-1. The ionization chamber is a 40 cm section of 15 cm diameter pyrex with aluminum end plates. A pump-out port is placed in one end plate and the gas inlets are placed in the other. Flow meters and a pressure gauge are used to monitor the gas flow (if a gas flow is used) and pressure inside the ionization chamber. Provision is made to seed the gas with various types of additives at will. A spark source is symmetrically mounted in the gas inlet end plate and can be isolated from the ionization chamber by a vacuum window if desired.

A superheterodyne receiver is used on the interferometer for increased sensitivity. When plasma is produced in the ionization chamber the bridge becomes unbalanced and a signal appears on the oscilloscope. The amount of phase shift and attenuation required to null

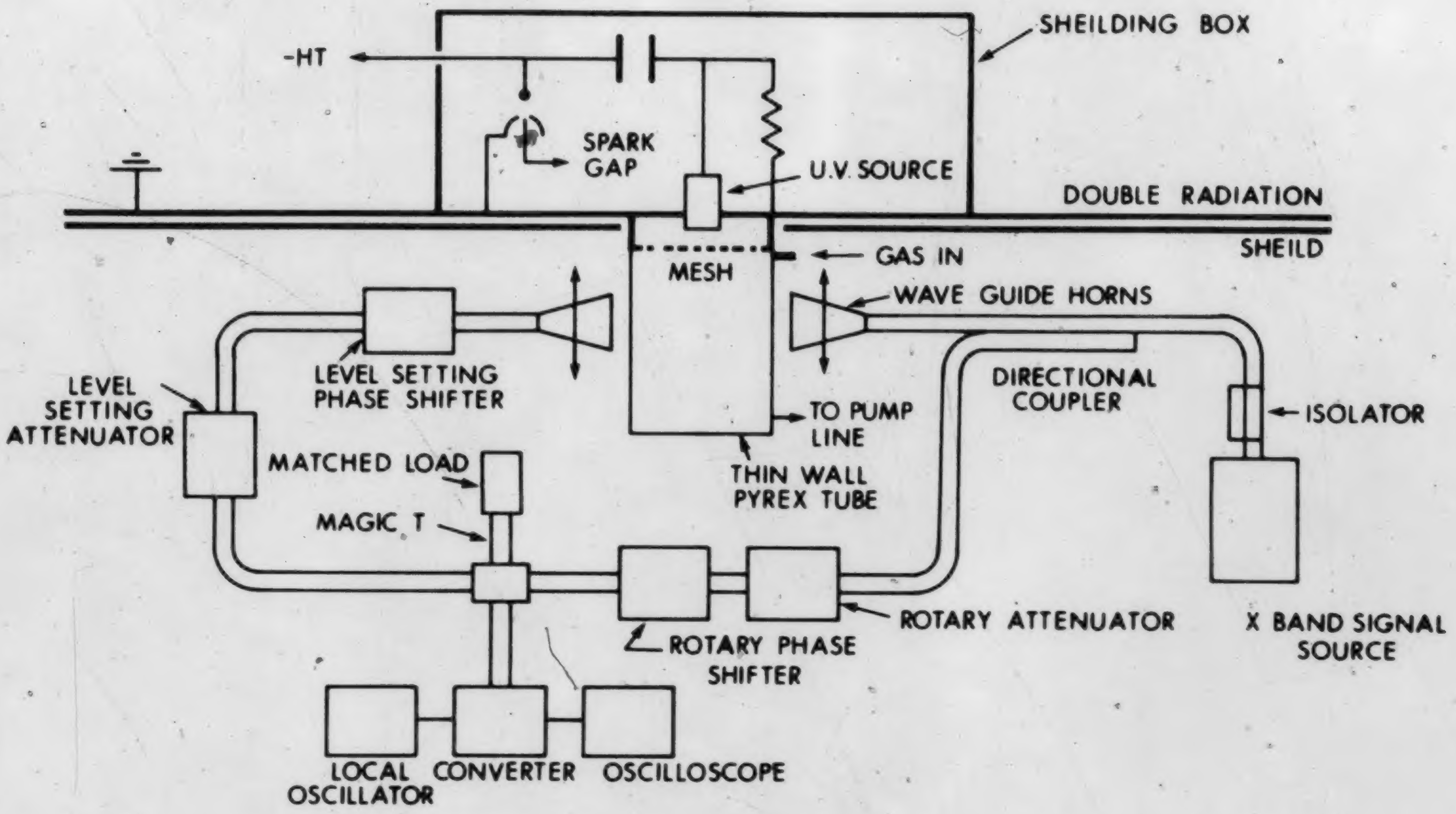
SHEILDING BOX
-HT
SPARK GAP
U.V. SOURCE
DOUBLE RADIATION SHEILD
GAS IN
MESH
WAVE GUIDE HORNS
LEVEL SETTING ATTENUATOR
LEVEL SETTING PHASE SHIFTER
DIRECTIONAL COUPLER
ISOLATOR
TO PUMP LINE
THIN WALL PYREX TUBE
MATCHED LOAD
MAGIC T
ROTARY ATTENUATOR
X BAND SIGNAL SOURCE
ROTARY PHASE SHIFTER
LOCAL OSCILLATOR
CONVERTER
OSCILLOSCOPE

X BAND WAVEGUIDE INTERFEROMETER

FIGURE 3-1 MICROWAVE INTERFEROMETER TEST FACILITY. In addition to the microwave interferometer the spark driving circuitry and ionization chamber are illustrated.

the signal at a particular time (rebalance the bridge) can be related to the electron density at that time. The response of the bridge is about one microsecond and since the decay time of the plasma is typically greater than this the interferometer can follow the decay time easily. In addition the interferometer is mounted on a track and can be moved to yield plasma density as a function of distance from the source.

Monochromator

The second unit consists of a vacuum ultra-violet monochromator which can be used in conjunction with a camera or a charge collector and photon counter illustrated in Figure 3-2. The output signals are recorded either by x-y recorders or displayed on an oscilloscope screen.

The monochromator must be connected to the vacuum facility and evacuated. Vacuum ultra-violet windows could be used at the entrance and exit slits if desired. The source is placed a few centimeters in front of the entrance slit and care must be taken to insure proper source alignment so that the grating can be fully illuminated. When the exit slit is replaced by the vacuum tight camera the spectrum over the bandwidth of interest can be photographed. When the photomultiplier tube is mounted behind the exit slit the generation of light as a function of time can be obtained for any desired bandwidth and center

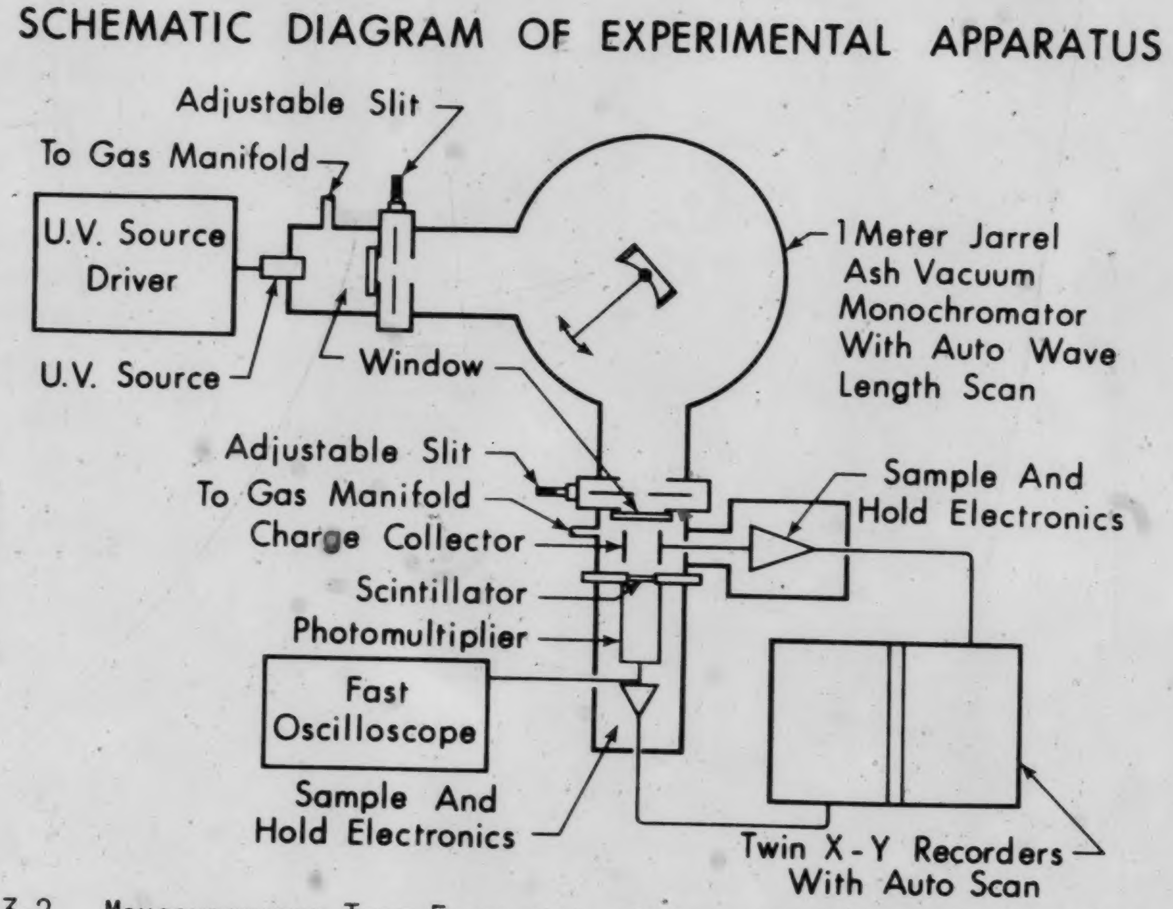
SCHEMATIC DIAGRAM OF EXPERIMENTAL APPARATUS
Adjustable Slit
To Gas Manifold
U.V. Source Driver
U.V. Source
Window
1 Meter Jarrel Ash Vacuum Monochromator With Auto Wave Length Scan
Adjustable Slit
To Gas Manifold
Charge Collector
Scintillator
Photomultiplier
Sample And Hold Electronics
Fast Oscilloscope
Sample And Hold Electronics
Twin X-Y Recorders With Auto Scan

FIGURE 3-2 MONOCHROMATOR TEST FACILITY The monochromator has been illustrated with the electronic recording apparatus attached. This can be removed along with the adjustable slit and a camera can be fitted to the monochromator.

frequency. Furthermore, when the signal is integrated a signal proportional to the total number of photons is generated. This can be calibrated to yield the absolute number of photons. A sodium salicylate scintillator is used to sensitize the photomultiplier tube surface to the ultra-violet light. The addition of a charge collector with the collecting plates placed parallel to the optical axis and between the photomultiplier tube and exit slit will yield total charge produced as a result of photoionization. The exit slit must be sealed with a window so that the cell containing the charge collector electrodes and photomultiplier tube can be "filled" with any desired gas at any pressure without increasing attenuation in the monochromator.

Noise Shielding

The high voltage spark source generates strong radio frequency noise and affects the operation of both the interferometer and the photon counter - charge collector combination. The following techniques have been successfully employed to increase the signal to noise ratio to an acceptable figure:

(1) Floating all electrical equipment.

(2) Replacing d.c. supplies with batteries where ever possible.

(3) One point grounding with wide metal strips.

(4) Double ferromagnetic shielding between the source circuitry and monitoring devices.

(5) Double ferromagnetic shielding around the discharge circuitry.

(6) Double ferromagnetic shielding enclosing the electronics for the photoncounter and charge collector combination.

(7) Double ferromagnetic shielding around the spark source when used on the monochromator. Only narrow slits in the shields can be tolerated to allow the transmission of light to the grating.

3-2 Theoretical Considerations

In the following sections each piece of apparatus has been discussed thoroughly and the theory pertaining to its design presented where ever necessary. In addition, the theory required for the interpretation of data has been included.

3-2-1 The Ultra-Violet Light Source

Spark sources of different geometrical shapes have been constructed as shown in Figure 3-3. The sparks produced by these are termed "condensed spark discharges" because of the nature of the discharge circuitry [37,38]. In addition, the sparks from the first two structures take the form of "sliding spark discharges". The name arose because the spark tends to slide over the surface of the ceramic dielectric. These structures are similar to the Garton flash-source [39] except that they are operated at a higher gas pressure than the Garton flash-source. Unless vacuum ultra-violet windows are used the sources must operate at the laser gas pressure. These sources appear to produce a closely spaced line spectrum from about 3000 Å down to about 1000 Å. A very weak continuum may be superimposed. The spectrum is affected by such things as electrode spacing, electrode material, presence of ceramic, gas type, gas pressure and discharge circuit parameters. The plasma jet tends to foul the source gas by ejecting vaporized ceramic and electrode material. It also tends to damage any window employed by pitting and clouding the surface. The pin spark plug is by far the cleanest of the three, however it appears to give rise to a lesser plasma density than the plasma jet.

The spark sources are designed for screw-in mounting and O-ring sealing. An adapter has been used to

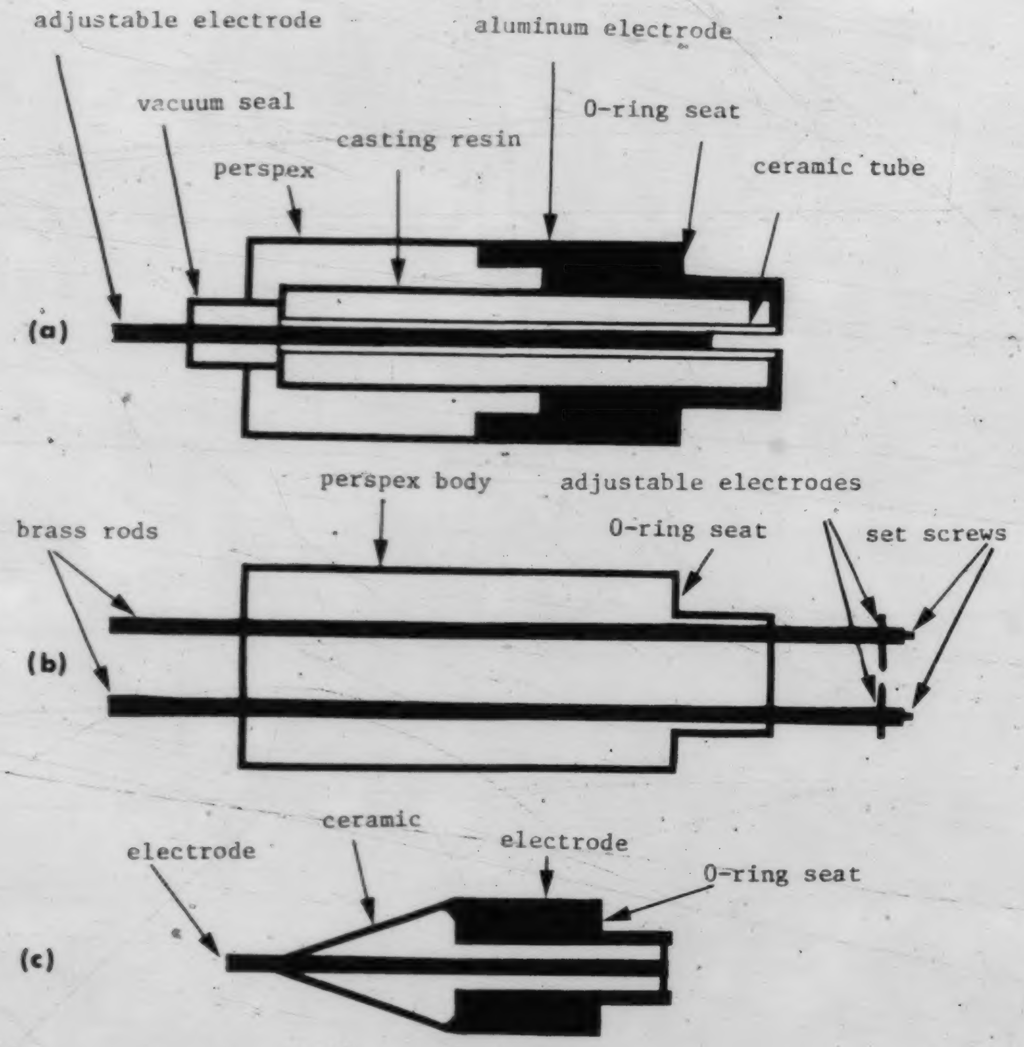
adjustable electrode
aluminum electrode
vacuum seal
O-ring seat
casting resin
perspex
ceramic tube
(a)
perspex body
adjustable electrodes
brass rods
O-ring seat
set screws
(b)
ceramic
electrode
electrode
O-ring seat
(c)

FIGURE 3-3 SPARK SOURCE GEOMETRYS Cross-sectional views of some of the condensed spark discharge sources employed have been illustrated (a) plasma jet spark plug; (b) pin spark plug; (c) conventional surface gap spark plug. These devices have been designed for "screw-in" mounting (not illustrated).

mount the commercially available surface-gap spark plug. Electrical connections are securely made with hose clamps. This design facilitates changing from one source to another for comparative testing.

The plasma jet spark plugs are filled with casting resin to support the ceramic tube and to afford better isolation between electrodes. The center electrodes fit tightly and are adjustable over approximately 8 cm. The structure illustrated in Figure 3-3(a) has a 1/8 inch diameter ceramic tube and electrode; another similar structure employs a 1/16 inch diameter ceramic tube and electrode. The outside case is made of aluminum and the center electrode of tungsten, however, the center electrode can be replaced with any desired material. The surface-gap spark plug employs a 1/8 inch center electrode separated from the outside case by a ceramic filled body. Typically, the case is made from a nickel alloy and the center pin of the same material. Alternatively, the center electrode may be tungsten. The pin spark plug is constructed from a solid piece of perspex with brass rod feedthroughs to the electrodes. The electrodes are 1/16 inch in diameter and the gap spacing is adjustable over about 2 cm. Tungsten electrodes have been used but can be readily changed. These sources have been tested and operate satisfactorily at 50 kV and 125 joules per spark. The discharges last a few microseconds and are repeated once every second. This low spark rate corresponds to an average power dissipation of only 125 watts. The sources handle this without the necessity of built-in heat exchangers.

The circuitry used to drive the spark sources is illustrated in Figure 3-4. Typical parameter values are $V = 40$ kV and $C = 0.1$ μf. The equivalent series inductance may be dependent on the type of capacitor used. It is necessary to submerge all the circuitry in transformer oil so as to prevent corona discharge and breakdown to ground points.

The spark gap is pressurized with N_2 so that it can stand off the charging voltage. The spark gap is triggered by a pulse from a coil to a spark plug in the spark gap. The rate of triggering is controlled by a separate device. The spark gap is necessary for the operation of the plasma jet and the surface gap plug because the ceramic becomes coated with a layer of metal sputtered from the electrodes. This causes a free running discharge to behave erratically. On the contrary, the pin spark plug is well suited for free running operation and the spark gap may be shorted with a metal strip. This would be desirable from the point of view of reducing the circuit inductance. However, over-voltage operation is desired in order to increase the discharge current.

The following equations describe the discharge

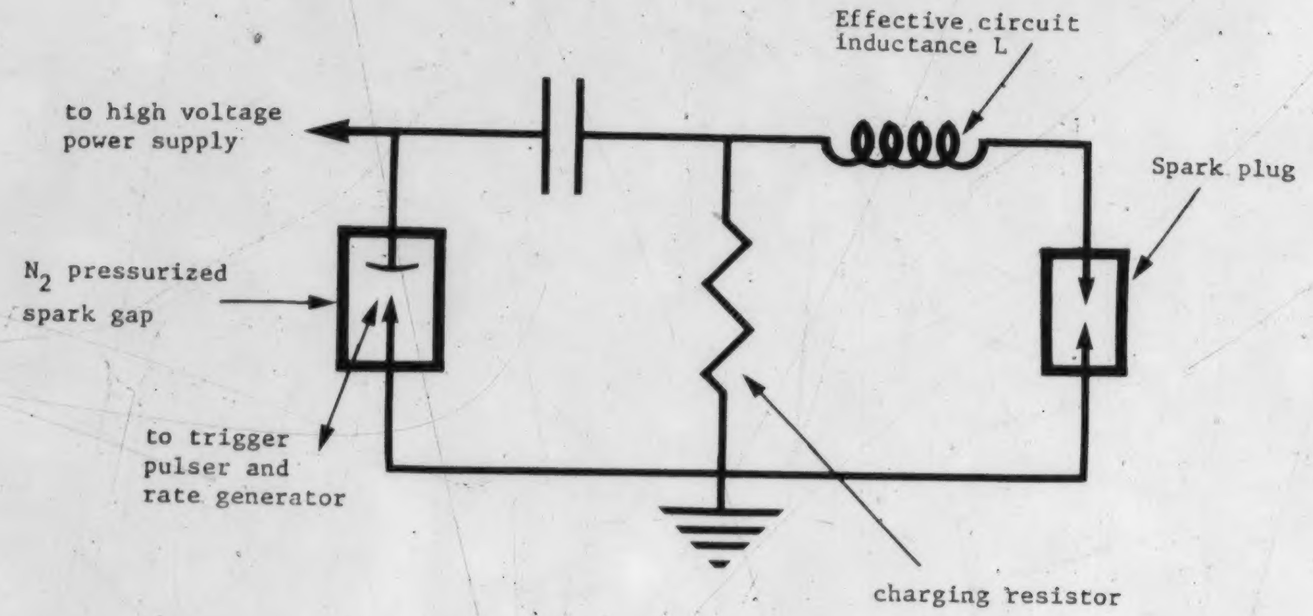
to high voltage power supply
Effective circuit inductance L
Spark plug
N_2 pressurized spark gap
to trigger pulser and rate generator
charging resistor

FIGURE 3-4 SPARK SOURCE DRIVING CIRCUIT

characteristics [37]:

$$i_{max} = V_o \omega C e^{-\gamma\tau} \quad 1 + \frac{\log dec^2}{\pi^2} \qquad 3\text{-}1$$

$$\gamma = 2 f \log dec \qquad 3\text{-}2$$

$$\log dec = \ln(i_1/i_2) \qquad 3\text{-}3$$

$$L = 1/\omega^2 C(1 + \log dec^2/\pi^2) \qquad 3\text{-}4$$

$$\omega = 1/(LC)^{1/2} \qquad 3\text{-}5$$

$$E_o = \frac{C V_o^2}{2} \qquad 3\text{-}6$$

$$Q_o = C V_o \qquad 3\text{-}7$$

$$i_{max} \alpha 1/\sqrt{L} \qquad 3\text{-}8$$

where i = current [A]

V_o = initial capacitor voltage [volts]

C = capacitance [F]

L = total inductance [h]

f = cyclic ringing frequency [$\sec^{-1}$]

ω = radian ringing frequency [rad $\sec^{-1}$]

τ = time to the first current maximum [sec]

i_1/i_2 represents the ratio of any two consecutive current peaks

E_o = energy [joules]

Q_o = initial charge [coul]

3-2-2 Microwave Interferometer Design and Operation

Microwaves were chosen as the primary plasma density diagnostic tool for a number of reasons [44,45]. For the low microwave power densities required, the electron velocities imposed by the electromagnetic field are negligible compared to the random thermal motions. Consequently, microwaves do not perturb the plasma. Furthermore, microwave techniques exhibit good sensitivity and temporal resolution. The method does not possess effective spatial resolution, however this has not been a prime requirement. Microwave techniques are not affected by photoemission as for example electric probes are. The most sensitive microwave technique is a microwave cavity perturbation method. However, this does not lend itself physically to the application required. Furthermore, portability of the test facility was required in order to allow plasma density measurements on a variety of laser cavity structures. Microwave interferometry possesses almost as much sensitivity and lends itself physically to the requirements of the project. The resulting test facility is illustrated in Figure 3-1.

The klystron source in Figure 3-1 can be continuously adjusted from 7 to 10 GHz (TE_{10} mode) [94,95,96]. When a measurement is to be performed it is set to some value in this range and then left unchanged throughout the measurement. The directional coupler splits the signal approximately in half. The signal in one arm traverses the plasma and is reunited with the original signal at the magic tee for comparison. The magic tee is connected so that a signal proportional to the sum of the two incoming signals is transmitted to a matched load and the phasor difference between the signals is transmitted to the balanced mixer. In the absence of plasma the level setting phase shifter and attenuator are adjusted so that the signals are equal in phase and magnitude at the magic tee. Hence the difference signal is zero and no power is coupled to the mixer. When the ultra-violet source is triggered and plasma created, the signals are unbalanced due to phase shift and attenuation suffered by the signal traversing the plasma. Consequently, a difference signal is transmitted to the mixer. The amplitude of this difference signal is dependent upon the phase shift and attenuation suffered in the plasma. The local oscillator is set so that the IF frequency out of the mixer is 200 MHz. This low frequency signal can be amplified in the conventional manner. The 200 MHz signal is fed into a narrow band (2 MHz) amplifier [97]. The narrow band provides noise suppression. Also this unit drops the signal to 20 MHz by mixing it with a 180 MHz internal local oscillator signal. This undemodulated signal can then be displayed on a CRT. The phase shift and attenuation caused by the plasma can be determined at any desired time by nulling the signal at that time. This is accomplished by adjusting the phase shifter and attenuator in the plasma arm until a null is produced at the desired location (time) on the CRT. Taking the difference between the "before" adjustment and "after" adjustment on the phase shifter and attenuator, yields the phase shift and attenuation. In principle the entire procedure can be repeated at a different test frequency and then the average plasma density and collision frequency may be determined.

One of the most difficult problems encountered was the phase shift, $\Delta\phi_r$, due to a random drift in frequency, Δf_r, of the source klystron [44]. In general for a waveguide of length L the phase shift due to a frequency excursion, Δf_r, is given by

$$\Delta\phi_r \simeq \frac{2\pi L}{\lambda_g}\left(\frac{\lambda_g}{\lambda}\right)^2 \frac{\Delta f_r}{f} \qquad 3\text{-}9$$

where λ_g is the guide wavelength and λ is the wavelength in space. The phase change seen by the bridge is then due to the path difference of the two arms ΔL:

or

$$\Delta\phi_r \simeq \frac{2\pi\Delta L}{\lambda_g}\left(\frac{\lambda_g}{\lambda}\right)^2 \frac{\Delta f_r}{f} \qquad 3\text{-}10$$

In order to stabilize the system ΔL was made as small as practically possible and Δf was reduced by immersing the klystrons in an oil bath. The oil was cooled by circulating it through a water jacket. Prior to this it had been determined that the frequency fluctuated rapidly due to temperature differences and air currents in the laboratory. Here "rapidly" means relative to the length of time to take a measurement ($\approx$ 30 sec). The local oscillator klystron had to be temperature compensated as well, to prevent the difference frequency of 200 MHz from drifting out of the amplifier bandwidth of 2 MHz.

The interference from the ultra-violet source high voltage discharge was reduced by providing a double ferromagnetic shield between it and the bridge and associated equipment. A copper mesh continued the shield over the source. Ground loops had to be avoided as well.

Finally, it should be pointed out that the response of the circuit was limited by the 2 MHz bandwidth of the narrow band amplifier to about 0.5 μs to 1 μs. Also a phase shift of about 1/100 of a degree could be measured. This implies that the interferometer was sensitive to plasma densities as low as 10^7 electron cm^{-3}. The upper limit is determined by the plasma cut off frequency and is about 10^{12} electron cm^{-3}.

The microwave bridge was mounted on a roller bearing track so that it could be moved along the pyrex cylinder. This allows one to make plasma density measurements as a function of the distance from the source.

3-2-2 (a) Propagation Through Unbounded Plasma

It will be assumed that the electromagnetic waves are traversing an infinite, uniform Lorentz plasma. A Lorentz plasma is one in which the electrons interact with each other only through collective spacecharge forces and that the heavier neutrals and ions are at rest. The ions and neutrals are regarded as a stationary fluid through which the electrons move with viscous friction. This plasma is "cold" and effects that depend explicitly on temperature can be neglected. Also in this particular case no static magnetic field has been used to contain or orient the plasma. Consequently, the medium is isotropic and exhibits no dispersion, and a one-dimensional analysis is justified. Since the plasma is "cold" relativistic effects can be ignored and classical mechanics applies to the analysis [44,45]. Newton's relation F = ma gives rise to:

$$m\ddot{x} = -eE - \nu m\dot{x} \qquad 3\text{-}11$$

for an electron in the plasma:

where m is the electronic mass [g]

x is the displacement [cm]

e is the electronic charge [coul]

E is the electric field [volts cm^{-1}]

ν is a viscous damping term [rad sec^{-1}]

The time and space varying magnetic field associated with the electromagnetic wave can be ignored since its effect is proportional to v/c where v is the thermal velocity of the electrons and c is the velocity of light. In this cold,nonrelativistic plasma $v << c$ and so $v/c << 1$.

E is actually the sum of the internal electric field due to electron space charge and the externally applied electric field. In this case the external electric field is the electric field component of an electromagnetic wave which varies as exp $j\omega t$ in time.

ν is a factor that accounts for all remaining interactions of the electrons with its neighbors. It is the collision frequency for momentum transfer of an electron with its neighbors and thus manifests itself as a damping term. The collision frequency for momentum transfer for a particular collision process - say electron neutral collisions is given by:

$$\nu = n_t q_m v \qquad 3\text{-}12$$

where n_t is the density of target particles [cm^{-3}] - in this case neutrals of a certain species [41]. q_m is the collision cross-section for momentum transfer or probability of collision for this process or event [cm^{-2}]. As before v is the thermal velocity of the electrons.

Of course the electrons can suffer other elastic collisions with other particles such as ions, impurity particles,and with other electrons. In many experimental situations inelastic collisions such as excitation, ionization and dissociation can also be involved. Each of these processes whether elastic or inelastic can be assigned a collision cross-section for momentum transfer. This cross-section multiplied by the effective number of target particles in each case and by the electron thermal velocity yield the collision frequency for momentum transfer for each collision process. The effective collision frequency or damping coefficient to be used in Equation 3-11 is then the sum of all of these.

i.e.

$$\nu = \sum_{i=1}^{k} n_{ti}\, q_{mi}\, v \qquad 3\text{-}13$$

for k different types of collision processes.

It has been stressed that ν is the collision frequency for momentum transfer and not necessarily the total collision frequency, (or more correctly not the total cross-section). Recall that the fractional energy transfer upon an elastic collision of two bodies depends on their relative masses and impact parameter [45]. The fractional energy lost by a particle of mass m upon striking a "stationary" particle of mass M is given by:

$$\Delta E_f = \frac{2m}{M}(1 - \cos\phi) \qquad 3\text{-}14$$

provided that $m \ll M$ as in the case of an electron-ion or electron-neutral elastic collision. ϕ is the scattering angle and is related to the impact parameter. In terms of fractional forward momentum, P_f, lost by the electron one may write $\Delta P_f = 1 - \cos\phi$. This is treating each collision separately and to get the collision cross-section for momentum transfer one must multiply the total collision cross-section q_t, by the average value of ΔP_f.

i.e. $q_m = \langle 1 - \cos\phi \rangle q_t$ for a particular collision process.

However, for most atoms or molecules of energy around 1 ev scattering is approximately isotropic and $\langle 1 - \cos\phi \rangle = 1$ so $q_m = q_t$.

This discussion was included only to show why the viscous damping term may be important and how it originates. No attempt will be made to calculate possible collision cross-sections.

To obtain the steady-state solution to Equation 3-11 one may replace the operator d/dt with $j\omega$, since the time variation of the E-field is exp $(j\omega t)$.

$$m(j\omega)^2 x = -eE - \nu m\, j\omega x \qquad 3\text{-}15$$

or

$$x = eE/m\omega(\omega - j\nu) \qquad 3\text{-}16$$

The current density is given by:

$$J = - n_e \dot{x} e \tag{3-17}$$

J = current density [A cm^{-2}]

n_e = electron density [cm^{-3}]

The raised dot denotes the time derivative with $d/dt \rightarrow j\omega$

$$J = - n_e j\omega x e \tag{3-18}$$

substituting Equation 3-16 one arrives at:

$$J = - n_e e^2 E j / m(\omega - j\nu) \tag{3-19}$$

comparing this to Ohm's law

$$J = \sigma E \tag{3-20}$$

σ = conductivity [cm ohm^{-1}]

we see that a conductivity can be defined such that:

$$\hat{\sigma} = \frac{n_e e^2 (\nu - j\omega)}{m(\nu^2 + \omega^2)} \tag{3-21}$$

where "^" indicates that the conductivity is complex. This is known as the Lorentz conductivity. It can be absorbed in the dielectric constant by defining an equivalent complex "Lorentz dielectric constant" (dimensionless) as follows:

$$\hat{k} = k_r - jk_i = 1 - \frac{j\hat{\sigma}}{\varepsilon_o \omega} \tag{3-22}$$

so

$$\hat{k} = \left(1 - \frac{\omega_p^2}{\omega^2 + \nu^2}\right) - j\left[\left(\frac{\omega_p^2}{\omega^2 + \nu^2}\right)\frac{\nu}{\omega}\right] \qquad 3\text{-}23$$

$$\omega_p = \left(\frac{n_e e}{\varepsilon_o m}\right)^{1/2} \qquad \text{plasma frequency [rad sec}^{-1}] \qquad 3\text{-}24$$

For plane travelling waves having the form $\exp(j\omega t - \gamma z)$ the propagation in a uniform medium may be expressed in terms of the complex "Lorentz dielectric constant".

i.e. $$\hat{\gamma} = \alpha + j\beta = j\,\hat{k}^{1/2}\,k_m^{1/2}\,\frac{\omega}{c} \qquad 3\text{-}25$$

k_m is the relative permeability and is equal to 1 for most practical plasmas. α and β are the attenuation and phase constants respectively.

$\hat{\gamma}$ = Lorentz dielectric constant [cm^{-1}]

c = velocity of light [3×10^{10} cm sec^{-1}]

The quantity that will be of most use is the complex refractive index (dimensionless) which is defined as:

$$\hat{\mu} = \mu - j\chi = -j\,\hat{\gamma}\,\frac{c}{\omega} \qquad 3\text{-}26$$

substituting Equation 3-25 one obtains:

$$\mu = (k\ k_m)^{1/2} \qquad 3\text{-}27$$

μ and χ are the real refractive index and the real attenuation index respectively.

With $k_m = 1$ Equations 3-23 and 3-27 can be solved to yield

$$\mu = \left[\frac{k_r + \left(k_r^2 + k_i^2\right)^{1/2}}{2}\right]^{1/2} \qquad 3\text{-}28$$

$$\chi = \left[\frac{-k_r + \left(k_r^2 + k_i^2\right)^{1/2}}{2}\right]^{1/2} \qquad 3\text{-}29$$

where

$$k_r = 1 - \frac{\omega_p^2}{\omega^2 + \nu^2} \qquad 3\text{-}30$$

and

$$k_i = \left(\frac{\omega_p^2}{\omega^2 + \nu^2}\right) \frac{\nu}{\omega} \qquad 3\text{-}31$$

Now

$$\beta = \mu \frac{\omega}{C} \qquad 3\text{-}32$$

$$\alpha = \chi \frac{\omega}{C} \qquad 3\text{-}33$$

These last two equations will be used to extract the desired information from the microwave propagation measurements in the plasma. β is the amount of phase

shift suffered per unit length of plasma [rad cm^{-1}].
α is the attenuation suffered per unit length of plasma [nepers cm^{-1}].

3-2-2 (b) Application to Photogenerated Plasma

The actual laboratory plasma has boundaries of a particular shape and can, only under special circumstances be, treated as an infinite plasma so that the preceeding analysis applies without correction [44,45].

Typical parameters will be:

$\omega \simeq 2\pi \times 9 \times 10^9$ rad sec^{-1}	test frequency
$D \simeq 15$ cm	dimension of plasma
$\omega_p \simeq 56417 (n_e[\text{cm}^{-3}])^{1/2}$ rad sec^{-1}	plasma frequency

Then for this plasma $\omega^2/\omega_p^2 > 10/1$ even for the largest expected electron density of $n_e = 10^{11}$ cm^{-3}. Then $\omega^2 >> \omega_p^2$ and the particularly complex propagation theory close to the plasma resonance can be avoided.

For these same conditions it can be shown that $\omega^2/(C/D)^2 \approx 800$ and that $\omega^2 >> (C/D)^2$. This means that the plasma dimension is very much greater than a free space wavelength at the test frequency and therefore permits one to ignore the effects of diffraction. This allows one to reduce the problem of propagation of the finite beam of electromagnetic waves through a finite plasma to a one-dimensional plane wave problem as a first approximation. Now the theory developed earlier in this paper may be employed.

To further simplify the problem it will be assumed that the plasma has planar boundaries ($\omega^2 >> (C/D)^2$) so that a one-dimensional analysis can be employed. It will also be assumed that the adiabatic approximation applies. This ignores the effect of reflection at the boundaries and resulting interference.

The following analysis shows how the average plasma density and collision frequency damping coefficient can be determined from the measured phase shift.

In the adiabatic approximation

$$\Delta\phi = \int (\beta_o - \beta_p)\, dx \qquad 3\text{-}34$$

where $\Delta\phi$ is the measured phase shift [radians] and β_o and β_p are the phase constants for no plasma (approximately free space) and plasma respectively.

$\beta_o = \omega/C$ $\quad$ $\beta_p = \mu\, \omega/C$ From Equation 3-32

From Equation 3-28

$$\mu = \left[\frac{k_r + \left(k_r^2 + k_i^2\right)^{1/2}}{2}\right]^{1/2} \qquad 3\text{-}35$$

In the case of $\omega > \omega_p$ the plasma appears as a low loss dielectric [45] where $k_r^2 >> k_i^2$ and $k_r > 0$. Now μ can be simplified.

Rewriting

$$\mu = \left[\frac{k_r}{2} + \frac{k_r}{2}\left(1 + \frac{k_i^2}{k_r^2}\right)^{1/2}\right]^{1/2} \qquad 3\text{-}36$$

but for $k_i^2/k_r^2 << 1$ then

$$\left(1 + \frac{k_i^2}{k_r^2}\right)^{1/2} \simeq 1 + \frac{k_i^2}{2k_r^2} \qquad 3\text{-}37$$

(first two terms of a Taylor series expansion about zero).

Now

$$\mu = \frac{k_r^{1/2}}{2}\left(1 + \frac{k_i^2}{4k_r^2}\right)^{1/2} \qquad 3\text{-}38$$

as before

$$\left(1 + \frac{k_i^2}{4k_r^2}\right)^{1/2} \simeq 1 + \frac{k_i^2}{8k_r^2} \qquad 3\text{-}39$$

so

$$\mu \simeq k_r^{1/2}\left(1 + \frac{k_i^2}{8k_r^2}\right) \qquad 3\text{-}40$$

Upon substituting Equations 3-30 and 3-31 into 3-40 one obtains for μ:

$$\mu = \left(1 - \frac{\omega_p^2}{\omega^2 + \nu^2}\right)^{1/2} \left[1 + \frac{\left[\left(\frac{\omega_p^2}{\omega^2 + \nu^2}\right)\frac{\nu}{\omega}\right]^2}{8\left(1 - \frac{\omega_p^2}{\omega^2 + \nu^2}\right)^2}\right] \qquad 3\text{-}41$$

for

$$\frac{\omega_p^2}{\omega^2 + \nu^2} << 1 \qquad (\omega^2 >> \omega_p^2) \qquad 3\text{-}42$$

then

$$\left(1 - \frac{\omega_p^2}{\omega^2 + \nu^2}\right)^{1/2} \approx 1 - \frac{\omega_p^2}{2(\omega^2 + \nu^2)} \qquad 3\text{-}43$$

For approximation by the first two terms of a Taylor series expansion about zero.

Now

$$\mu = \left(1 - \frac{\omega_p^2}{2(\omega^2 + \nu^2)}\right)\left(1 + \frac{1}{8}\left[\frac{\omega_p^2 \nu}{(\omega^2 + \nu^2 \underset{\text{neglect}}{\underbrace{- \omega_p^2}})\omega}\right]^2\right) \qquad 3\text{-}44$$

since $\omega^2 >> \omega_p^2$

Using Equation 3-34 where

$$\beta_o - \beta_p = (1 - \mu)\ \omega/C \qquad 3\text{-}45$$

one obtains:

$$\Delta\phi = \frac{\omega}{C}\int\left\{\frac{\omega_p^{\,2}}{2(\omega^2+\nu^2)} - \left(1 - \frac{\omega_p^{\,2}}{2(\omega^2+\nu^2)}\right)\left[\frac{1}{8}\left(\frac{\omega_p^{\,2}\nu}{\omega(\omega^2+\nu^2)}\right)^2\right]\right\}dx \qquad 3\text{-}46$$

but

$$\omega_p^{\,2} = A\, n_e(x) \qquad \text{where } A = \frac{e^2}{\varepsilon_o\, m} \qquad 3\text{-}47$$

$$\Delta\phi = \frac{\omega}{2C(\omega^2+\nu^2)}\int\left\{A\, n_e(x) - \frac{(2\omega^2 + 2\nu^2 - \underbrace{\omega_p^{\,2}}_{\text{negligible since } 2\omega^2 \gg \omega_p^{\,2}})}{8}\left(\frac{\omega_p^{\,2}\nu}{\omega(\omega^2+\nu^2)}\right)^2\right\}dx \qquad 3\text{-}48$$

$$\Delta\phi = \frac{\omega}{2C(\omega^2+\nu^2)}\int\left\{A\, n_e(x) - \frac{A^2\, n_e(x)^2\nu^2}{4\omega^2(\omega^2+\nu^2)}\right\}dx \qquad 3\text{-}49$$

In order to perform the integration one must know the density distribution shape function along x, that is $n_e(x)$. However, in this application, it is reasonable to assume that the density will be approximately constant with x.

i.e. n_e (for any x) $\approx \bar{n}_e$

Upon performing the integration on Equation 3-49 between x = 0 and x = L one obtains:

$$\Delta\phi = \frac{\omega}{2C(\omega^2 + \nu^2)} \left\{ A \cdot \bar{n}_e L - \frac{A^2 \bar{n}_e^2 \nu^2 L}{4\omega^2(\omega^2 + \nu^2)} \right\} \quad 3\text{-}50$$

It is satisfying to note that in the absence of collisions ($\nu = 0$) that Equation 3-50 reduces to

$$\Delta\phi = \frac{\omega A \bar{n}_e L}{2C \omega^2} \quad 3\text{-}51$$

or

$$\bar{n}_e = \frac{2\varepsilon_o m \omega C \Delta\phi}{e^2 L} \quad 3\text{-}52$$

However, if ν becomes significant Equation 3-50 may be solved for $\bar{n}_e$ by use of the quadratic formula. Rewriting Equation 3-50

$$\frac{A \nu^2}{4\omega^2(\omega^2 + \nu^2)} \bar{n}_e^2 - \bar{n}_e + \frac{2C(\omega^2 + \nu^2) \Delta\phi}{\omega AL} = 0$$

3-53

$$\bar{n}_e = \frac{1 \pm \left(1 - \frac{2\nu^2 \; \Delta\phi}{\omega^3 L} C\right)^{1/2}}{\frac{A \; \nu^2}{2\omega^2(\omega^2 + \nu^2)}} \qquad 3\text{-}54$$

Although Equation 3-54 contains two unknowns namely $\bar{n}_e$ and ν these parameters can be determined for a particular plasma by measuring $\Delta\phi$ at two different frequencies ω_1 and ω_2 (say ω_1 = 7 GHz, ω_2 = 10 GHz).

Then

$$\bar{n}_e = \frac{1 - \left(1 - \frac{2\nu^2 \; \Delta\phi_1 \; C}{\omega_1^{\;3} L}\right)^{1/2}}{\frac{A \; \nu^2}{2\omega_1^{\;2}(\omega_1^{\;2} + \nu^2)}} \qquad 3\text{-}55$$

$$\bar{n}_e = \frac{1 - \left(1 - \frac{2\nu^2 \; \Delta\phi_2 \; C}{\omega_2^{\;3} \; L}\right)^{1/2}}{\frac{A \; \nu^2}{2\omega_2^{\;2}(\omega_2^{\;2} + \nu^2)}} \qquad 3\text{-}56$$

where

$$A = \frac{e^2}{\varepsilon_o m}$$

The negative sign was chosen since Equation 3-54 must reduce to

$$\bar{n}_e = \frac{2\varepsilon_o m \omega C \Delta\phi}{e^2 L} \quad \text{in the limit } \nu \to 0$$

This can be shown from Equation 3-54

$$\bar{n}_e = \lim_{\nu \to 0} \left\{ \frac{1 \pm \left(1 - \frac{2\nu^2 \Delta\phi C}{\omega^3 L}\right)^{1/2}}{\frac{A \nu^2}{2\omega^2(\omega^2 + \nu^2)}} \right\} \qquad 3\text{-}57$$

as ν → 0

then

$$\frac{2\nu^2 \Delta\phi C}{\omega^3 L} << 1 \qquad 3\text{-}58$$

and

$$\left(1 - \frac{2\nu^2 \Delta\phi C}{\omega^3 L}\right)^{1/2} \simeq 1 - \frac{2\nu^2 \Delta\phi C}{2\omega^3 L} \qquad 3\text{-}59$$

By approximation by the first two terms of a Taylor series expansion about zero.

Then

$$\bar{n}_e = \lim_{\nu \to 0}\left[\frac{2\omega^2(\omega^2+\nu^2)}{A\nu^2}(1 \pm 1) \mp \frac{2\omega^2(\omega^2+\underbrace{\nu^2}_{\text{negligible}})}{A\nu^2}\,\frac{\nu^2\,\Delta\phi\, C}{\omega^3\, L}\right] \tag{3-60}$$

If and only if the negative sign is chosen does the equation reduce as required

$$\bar{n}_e = \lim_{\nu \to 0}\left[\frac{2\omega^2(\omega^2+\nu^2)}{A\nu^2}(1-1) + \frac{2\omega\,\Delta\phi\, C}{AL}\right] \tag{3-61}$$

or

$$\bar{n}_e = \frac{2\varepsilon_o\, m\, \omega C\, \Delta\phi}{e^2\, L} \tag{3-62}$$

with

$$A = \frac{e^2}{\varepsilon_o m}$$

Equations 3-55 and 3-56 are not linear and so it would be difficult to solve for each variable analytically. However, they lend themselves to a graphical solution. i.e., for a given set of ω_1, $\Delta\phi_1$, ω_2 and $\Delta\phi_2$ all possible solutions to each equation can be plotted. Their intersection will yield the values of $\bar{n}_e$ and ν which simultaneously solve the equations.

Upon examining Equation 3-50 one sees that for constant ω and $\bar{n}_e$, $\Delta\phi$ decreases with increasing ν. This, along with some typical numbers, may be used to simplify

Equations 3-54, 3-55 and 3-56. A typical phase shift recorded at high pressure with an additive might be $\Delta\phi = 0.5°$ at $\omega = 6 \times 10^{10}$ rad sec^{-1}.

With $\nu \approx \omega$,

$$\frac{2\nu^2 \, \Delta\phi \, C}{\omega^3 \, L} = 6 \times 10^{-4} \qquad 3\text{-}63$$

$\Delta\phi$ must be in radians.

So by a Taylor series approximation

$$\left(1 - \frac{2\nu^2 \, \Delta\phi \, C}{\omega^3 \, L}\right)^{1/2} \simeq 1 - \frac{\nu^2 \, \Delta\phi \, C}{\omega^3 \, L} \qquad 3\text{-}64$$

Equations 3-55 and 3-56 become:

$$\bar{n}_e = \frac{\Delta\phi_1 \; 2C(\omega_1^{\,2} + \nu^2) \; \varepsilon_o m}{\omega_1 \, L \, e^2} \qquad 3\text{-}65$$

$$\bar{n}_e = \frac{\Delta\phi_2 \; 2C(\omega_2^{\,2} + \nu^2) \; \varepsilon_o m}{\omega_2 \, L \, e^2} \qquad 3\text{-}66$$

Equating these two yields

$$\nu = \left(\frac{\Delta\phi_2 \, \omega_2 - \Delta\phi_1 \, \omega_1}{\dfrac{\Delta\phi_1}{\omega_1} \quad \dfrac{\Delta\phi_2}{\omega_2}} \right)^{1/2} \qquad 3\text{-}67$$

The positive sign has been chosen since only positive frequencies have physical meaning.

So for collision frequencies such that $\nu = \omega$ then the equation can be solved analytically and the method is much easier to make use of.

It should be pointed out that an alternate method of determining the collision frequency and average electron density would be to relate the attenuation measurement to the attenuation index χ. Then a determination of $\Delta\phi$ and the attenuation at only one test frequency would be sufficient to determine $\bar{n}_e$ and ν even for large ν. However, due to reflections from the surface of the pyrex cylinder the attenuation measurement is not at all dependable - in fact it is not even true attenuation. The accuracy could be improved by placing a second directional coupler in the transmitting arm of the bridge and using the transmitting horn as a receiver of the reflected signal. A portion of the signal is still scattered but the reflected signal could conceivably be monitored and used to correct the attenuation measurement. However, unless tremendous care is taken this method would probably be less accurate than the one discussed in the paper.

3-2-3 Monochromator Test Facility

The monochromator assembly has been illustrated in Figure 3-2. A diffraction grating ruled to 30,000 lines per inch has been employed [99].

The unique focusing properties of the concave diffraction grating were first analysed by Rowland [37,38]. Basically, the spectrum of a point source lying on a circle of diameter equal to the radius of curvature of the grating and tangent to the grating will be focused on the circle (called the Rowland circle). The equation relating the angular dispersion to the wavelength is:

$$\pm m\lambda = d(\sin\alpha + \sin\beta) \qquad 3\text{-}68$$

where m is the order of the spectrum

$+$ corresponds to an inside order

$-$ corresponds to an outside order

λ is the wavelength [cm]

d is the line separation [cm]

α is the angle of incidence to the grating normal

β is the angle of diffraction to the grating normal

An infinite number of spectra are produced and the light is shared among these. In this project the first outside order has been employed and the grating is blazed to reflect most of the light into this order. Care must be taken to see that spectra of different orders do not overlap and give rise to erroneous results. For this project a quartz window (short wavelength cutoff of λ = 1800 to 2000 Å) has been satisfactorily employed to isolate the first order.

The angular dispersion is given by:

$$\frac{d\beta}{d\lambda} = \frac{m}{d \cos \beta} \qquad 3\text{-}69$$

The linear dispersion:

$$\frac{d\ell}{d\lambda} = \frac{m R}{d \cos \beta} \qquad 3\text{-}70$$

R = radius of curvature of the grating [0.5 m]

when R is in meters and (1/d) is the number of lines per mm

$$\frac{d\ell}{d\lambda} = \frac{\cos \beta}{m R (1/d)} \times 10^4 \text{ Å/mm} \qquad 3\text{-}71$$

where ℓ is the length along the Rowland circle where the spectrum is focused. The plate factor is the reciprocal of the linear dispersion and for the case under consideration is about 12 Å/mm. The resolving power is given by mN (N is the number of grating lines illuminated) and is about 20,000 for the first order spectrum. Also with the particular grating used the monochromator can see wavelengths extending essentially from zero angstroms to the visible at about 4500 Å. The shorter wavelengths can only propagate in a vacuum. An oil diffusion pump is built into the monochromator and only a rotary backing pump is required.

The Seya Namioka mounting technique is used in the monochromator. This mounting is mechanically very simple and facilitates scanning of the source. Built-in synchronous motors and gear reduction chains rotate the grating in either direction and the source can be scanned at a number of calibrated rates. However, this type of mounting yields perfect horizontal focus of the entrance slit at the exit slit only when the slits subtend an angle at the grating of 70.13°. In addition, this mounting results in a great deal of astigmatism. Astigmatism is the tendency for a point on the entrance slit to be imaged into a vertical line at the exit. The length of astigmatic image is given by:

$$Z = \left[\ell \frac{\cos\beta}{\cos\alpha}\right] + L[\sin^2\beta + \sin\alpha \tan\alpha \cos\beta] \tag{3-72}$$

where ℓ = length of entrance slit [cm]

L = length of ruled lines [cm]

In this particular case the only serious effect will be the loss of intensity.

3-2-3 (a) Camera - Photomicrodensitometer Assembly

If a camera is mounted on the exit arm of the monochromator so that the photographic plate lies on the Rowland circle the spectrum can be photographed. However, perfect focus is only obtained at one point on the circle because of the mounting technique employed. To obtain good focus over the entire photographic plate the orientation of the plate must be adjusted each time the grating angle is changed. This is extremely tedious since only a trial and error technique can be used. However, comparative data can be obtained even without perfect focus. In order to obtain intensity as a function of wavelength from the plate a microdensitometer must be used. However, for anything other than perfect focus on the plate, decreased intensity and apparent line broadening will result. In addition, the film is very non-linear and the entire system would be very difficult to calibrate. Also, gelatin cannot be used on ultra-violet sensitive film and so it can be easily marked by handling.

3-2-3 (b) Photoelectric Recording with Photon Counter

If the camera is replaced by an adjustable slit at the point of perfect focus on the Rowland circle then a narrow bandwidth of light at any desired center frequency can be filtered out and the intensity monitored photoelectrically as illustrated in Figure 3-2. This results in a loss of wavelength resolution but is of little concern in this application. The gear drive assembly is calibrated and a counter indicates the wavelength at the center of the slit.

Most photomultiplier tubes are equipped with quartz vacuum windows. The quartz is not transparent at wavelengths much lower than 2000 Å. Consequently, sodium salicylate has been used to sensitize the cathode surface to ultra-violet light. This particular phosphor has high quantum efficiency and has a linearly flat response over the wavelength range of interest [37,38,46,40]. Sodium salicylate fluoresces in the blue around 4200 Å [40]. This matches the peak sensitivity of the cathode surface used (S-11). The photomultiplier tube must be mounted so that all the light from the exit slit falls on the scintillator surface for maximum sensitivity.

When the slit width was decreased to obtain a narrow bandwidth and good wavelength resolution, the photomultiplier gain was not sufficient. Consequently, two additional stages of voltage gain of x14.2 and x9.2 have been constructed. The final stage can be switched in or out at will. The overall rise time of the circuit is less than 50 ns. This is sufficiently fast to follow the generation of light as a function of time at a given frequency. To obtain the total number of photons per spark over a narrow bandwidth the signal must be integrated. An integrator has been built with a rise time less than 30 ns. The integrated signal is then sampled and recorded as a function of wavelength with an x-y recorder. The integrater is automatically reset in time to integrate the next signal. The x-y recorder horizontal drive has been synchronized with the monochromator wavelength drive. As the source is scanned the x-y recorder generates a bar graph type of display characteristic of the source total photon output per spark.

In order for the data to be useful in determining such parameters as photoionization and photoabsorption cross-sections the device must be calibrated. This can be done by considering the cathode sensitivity, the photomultiplier tube gain, the electronic amplifier and integrator gain, and the quantum efficiency of the scintillator. All of these values were either available on the manufacturer's specification sheets or could be calculated. The only exception was the scintillator, quantum efficiency, and this has been determined experimentally. The entire calibration procedure has been described in Section 6-26.

3-2-3 (c) Photoionization Detection by Charge Collection

The geometric relationship of the charge collector is illustrated in Figure 3-2. The collector plates are 6 cm by 12 cm in area and separated by 2.54 cm. This was sufficient separation to ensure that light expanding from the exit did not strike the electrode surface and so risk causing photoemission. The length of 12 cm was chosen so that the beam of light would expand to a cross-sectional area almost as large as the scintillator surface. The collector plate bias voltage has been made adjustable from 10 volts to 1170 volts.

For low photoionization density no space charge E-fields will develop that would shield the ensemble of photogenerated charges from the applied E-field [41]. Under such conditions, each charged particle whether positive or negative responds to the applied E-field independent of all other charges. The electron motion will give rise to a current flow as will the positive ion motion. (It has been assumed that the positive ion will be singly charged). The total current, i_c, will be given by the sum of these.

The total amount of charge that will have moved is given by:

$$\int_{0}^{t_c} i_c(t)dt = |Q| \text{ [coul]} \qquad 3\text{-}73$$

where t_c[sec] is the time required for all of the individual charges to reach their respective collector electrodes. This time will depend on the value of E/P where E is the applied electric field [volts cm^{-1}] and P is the gas pressure in the test cell. Since time resolution of the current has not been required, integration of the current has been done by simply placing a series capacitor in the external circuit. The voltage appearing on the capacitor will be directly proportional to the total amount of photogenerated charge. This is, assuming that all photogenerated charge reaches the collector plates. The sensitivity of such a device is inversely proportional to the capacitor value. The resulting signal can be amplified and displayed with an x-y recorder. The "integrator" is then reset and ready to process the next signal. The horizontal drive of the x-y recorder has been linked to that of the first x-y recorder and photoabsorption and photoionization spectra can be generated simultaneously.

Considering that the higher electron densities observed on the bridge were typically around 10^{10} to 10^{11} cm^{-3}, one can estimate the expected electron density in the test cell to be about 10^5 cm^{-3}. Such parameters as entrance and exit slit width, window transparency, and diffraction grating efficiency have been taken into account in estimating the value. Since this charge will expand to fill a larger volume the density will decrease somewhat and a consideration of the Debye length [41] reveals that no significant space charge E-field should develop. This has been treated more thoroughly in Section 6-3 In any case, the photoionization density can be reduced to a level precluding space charge E-field development by reducing the source intensity. The only remaining condition to satisfy, is whether the resulting input signal is sufficiently high to overcome amplifier noise (assuming that the device has been adequately shielded from all external noise sources). Typically, parasitic front end capacitance may be a few pico farads. For an electron density of 10^5 cm^{-3} over 6 cm^3 the total charge that may be collected is $1.2 \times 10^6 \times 1.6 \times 10^{-19}$ coulombs where both electron and ion charge have been assumed to have been collected. The resulting front end voltage signal will be a few millivolts. This is 2 or 3 orders of magnitude above the noise level of many solid state devices. Schematics of the resulting electronic network are shown in Chapter 4 where a brief discussion of the photon counter and charge collector electronic design has been given. The calibration procedure of the device has been included in Section 6-2-6.

3-2-3 (d) Application to Cross-Sections

Data obtained from the calibrated photon counter-charge collector assembly can be used to determine absorption coefficients, total absorption cross-sections, and photoionization cross-sections.

Lambert's law states that "if the diminution of a parallel beam of monochromatic radiation through a homogeneous absorbing medium is considered, it is found that the intensity is reduced by the same fractional amount in equal succeeding portions of its path" [42].

$$-\Delta I = I\mu\Delta\chi \qquad 3\text{-}74$$

I = intensity [ergs $\sec^{-1}$ cm^{-2}]

μ = absorption coefficient [cm^{-1}]

χ = distance [cm]

The solution to Equation 3-74 is:

$$I = I_o \exp(-\mu\chi) \qquad 3\text{-}75$$

I_o = initial intensity [ergs $\sec^{-1}$ cm^{-2}]

It is conventional to reduce χ to standard conditions of pressure and temperature (STP)

$$\chi = \frac{LP273}{760T} \qquad 3\text{-}76$$

L = test cell length [cm]

P = test cell gas pressure [torr]

T = test cell gas temperature [K°]

This implies that measurements at different temperatures, pressures, and lengths should yield the same value of μ. This is a statement of Beer's Law [42].

Absorption coefficients are often expressed in terms of an absorption cross-section.

$$\mu \doteq \sigma_t n_o \qquad 3\text{-}77$$

σ_t = total absorption cross-section [cm^2]

n_o = Loschmidt's number [$2.7 \times 10^{19}\ cm^{-3}$]

Since the photon counter output is proportional to the integrated intensity, then Equation 3-75 must be integrated with respect to time and since only I and I_o are functions of time, the results can be written as:

$$N_p = N_{po} \exp(-\mu\chi) \qquad 3\text{-}78$$

$$N_p = \int_0^{t_d} I(t)dt \qquad 3\text{-}79$$

$$N_{po} = \int_0^{t_d} I_o(t)dt \qquad 3\text{-}80$$

t_d = spark duration time [sec] (usually a few μs)

N_{po} is the total number of photons, at wavelength λ, incident on the scintillator surface with the test cell evacuated. Alternatively, N_{po} can be thought of as the total number of photons incident on the test cell.

N_p is the total number of photons, at wavelength λ, incident on the scintillator surface after suffering absorption in the test cell gas.

Equations 3-76, 3-77 and 3-78 can be combined to yield:

$$\sigma_t = \frac{760T}{LP273\, n_o} \ln\left(\frac{N_{po}}{N_p}\right) \qquad 3\text{-}81$$

It only remains to determine a relationship for the photoionization cross-section. In order to determine this, one must measure the photoionization efficiency, or the number of electron ion pairs created per photon absorbed. This number multiplied by the total absorption cross-section yields the photoionization cross-section [42].

$$\sigma_i = \varepsilon_f \sigma_t \qquad 3\text{-}82$$

ε_f = photoionization efficiency (dimensionless)

σ_i = photoionization cross-section [cm^2]

The number of electron-ion pairs can be easily determined from the charge collector signal. This can be represented by n_{eo}. The total number of photons is simply the difference, $N_{po} - N_p$. Consequently one may write the photoionization efficiency as:

$$\varepsilon_f = \frac{n_{eo}}{N_{po} - N_p} \qquad 3\text{-}83$$

Equations 3-81, 3-82, and 3-83 combine to yield a relationship for the photoionization cross-section.

$$\sigma_i = \frac{760T}{LP273\, n_o} \frac{n_{eo}}{N_{po} - N_p} \ln \frac{N_{po}}{N_p} \qquad 3\text{-}84$$

Determination of photoabsorption and photoionization cross-sections with Equations 3-81 and 3-84 requires an intense and stable source over the wavelengths of interest. A high voltage condensed spark discharge in atmospheric pressure N_2 was found to be suitable. An intense line spectrum from about 3000 Å down to at least 1000 Å was observed. The "pin spark plug" in Figure 3-3(b) results in a spark that can be accurately aligned with the entrance slit. This results in a constant intensity from spark to spark.

Furthermore photoabsorption by CO_2 limited the useful part of the spectrum to wavelengths above $\lambda \simeq 1150$ Å. LiF with a short wavelength cut-off of $\lambda \simeq 1050$ Å could be conveniently used to isolate the test cell from the monochromator and spark source [37,38,43].

Chapter 4

Detailed Description of Photon Counter and Charge Collector Electronics

Working circuit diagrams as well as block diagrams of the specialized electronics, developed for the photon counter and charge collector assembly illustrated in Figure 3-2, have been included in this chapter. These appear in Figures 4-1 throughout to Figure 4-7. All component values and solid-state device numbers have been included in Table 4-1 so that duplication, if desired, may be facilitated.

As a starting point the photon intensity and resulting charge density were estimated as discussed in Chapter 3. However, these estimates ranged over as much as 2 orders of magnitude. Consequently, preliminary circuits were constructed to sample the signals and to provide more detailed information regarding their nature. Although the basic requirements imposed on the electronics and illustrated in the block diagrams remained unchanged throughout the design and construction of the circuits, the necessary sophistication developed as the basic physical processes giving rise to the input signal were elucidated. This experimental technique helped provide criteria from which the necessary amplifier gains, rise times, sampling intervals, and integrating intervals could be established. Furthermore, difficulty was encountered by the high voltage and high current spark discharge, which generated high frequency electrical noise. Subtle features have been incorporated into the design in order to suppress the effect of external noise. Eventually the circuits illustrated in Figures 4-2, 4-4, and 4-5 were developed. These proved to be reliable and to possess the required features to provide data over a broad dynamic range (Chapter 7). The more important features have been discussed in the following sections [100, 101, 102, 103, 104, 105, 106, 107, 108, 109, 110, 111, 112, 113, 114, 115, 116, 117].

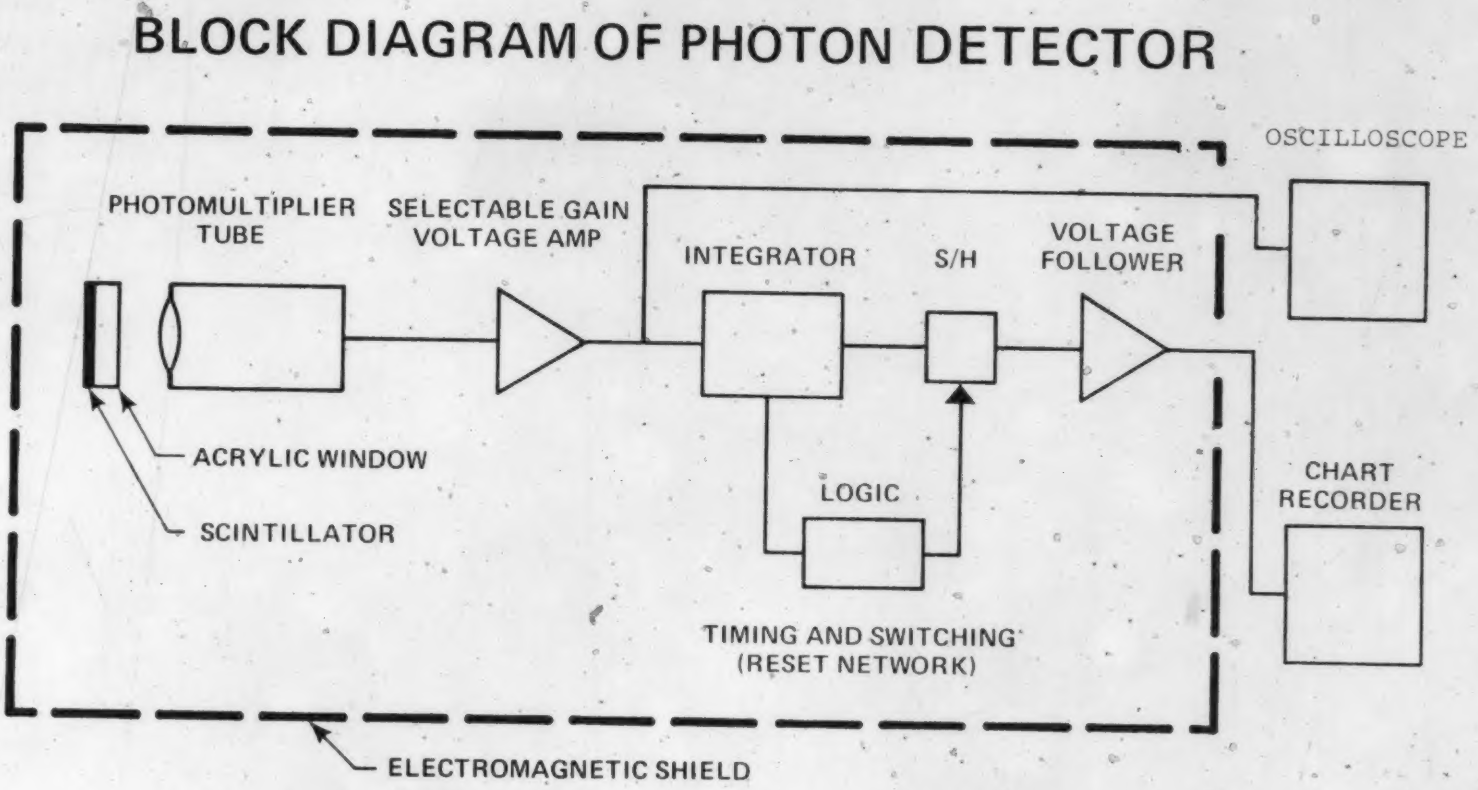
BLOCK DIAGRAM OF PHOTON DETECTOR

PHOTOMULTIPLIER TUBE
SELECTABLE GAIN VOLTAGE AMP
INTEGRATOR
S/H
VOLTAGE FOLLOWER
OSCILLOSCOPE
ACRYLIC WINDOW
SCINTILLATOR
LOGIC
TIMING AND SWITCHING (RESET NETWORK)
CHART RECORDER
ELECTROMAGNETIC SHIELD

Figure 4-1 Block Diagram of the Photon Detector

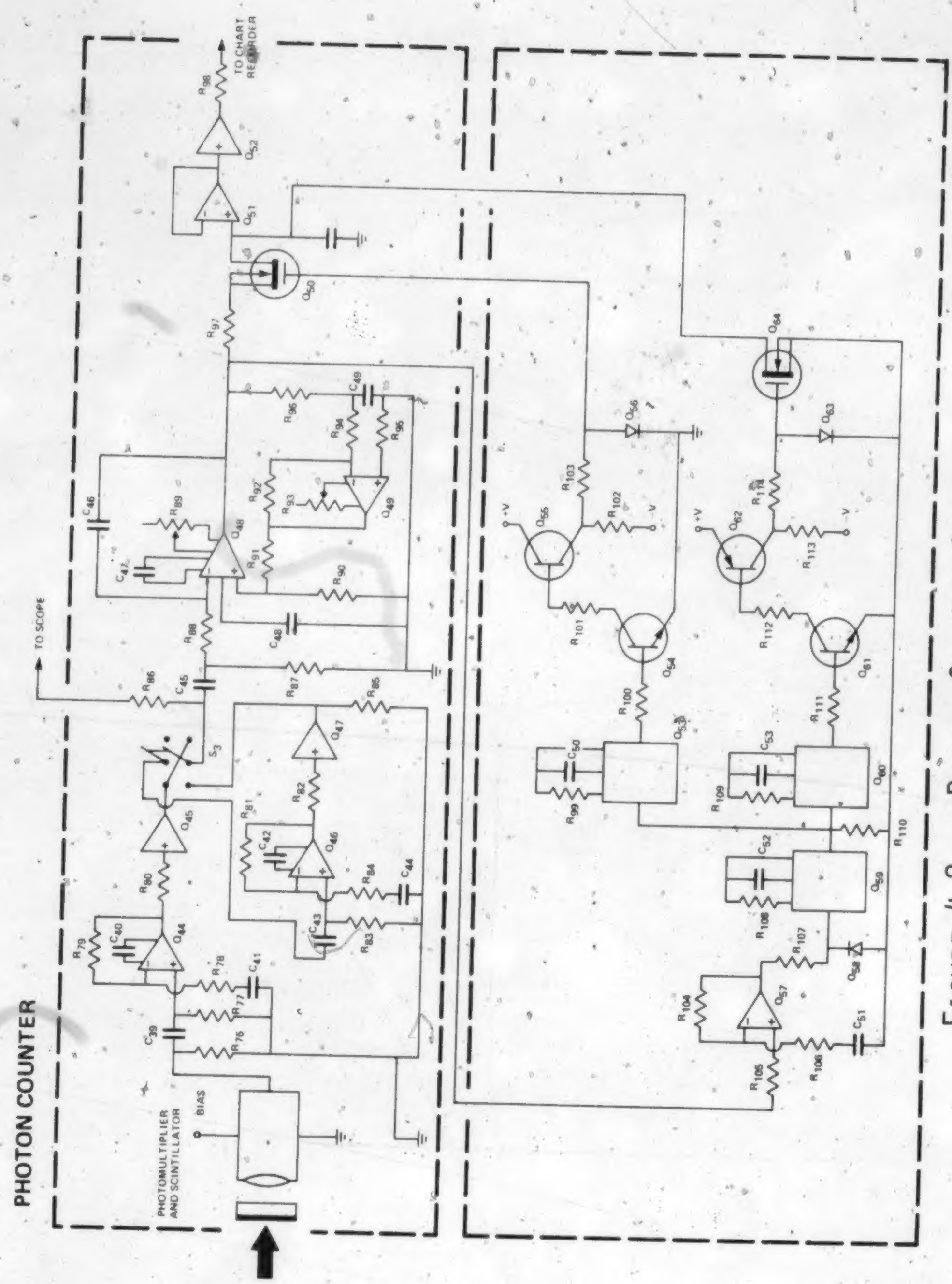
PHOTON COUNTER
PHOTOMULTIPLIER AND SCINTILLATOR
BIAS
TO SCOPE
TO CHART RECORDER
S3
Q44
Q45
Q46
Q47
Q48
Q49
Q50
Q51
Q52
Q53
Q54
Q55
Q56
Q57
Q58
Q59
Q60
Q61
Q62
Q63
Q64
+V
-V

FIGURE 4-2 PHOTON COUNTER CIRCUIT

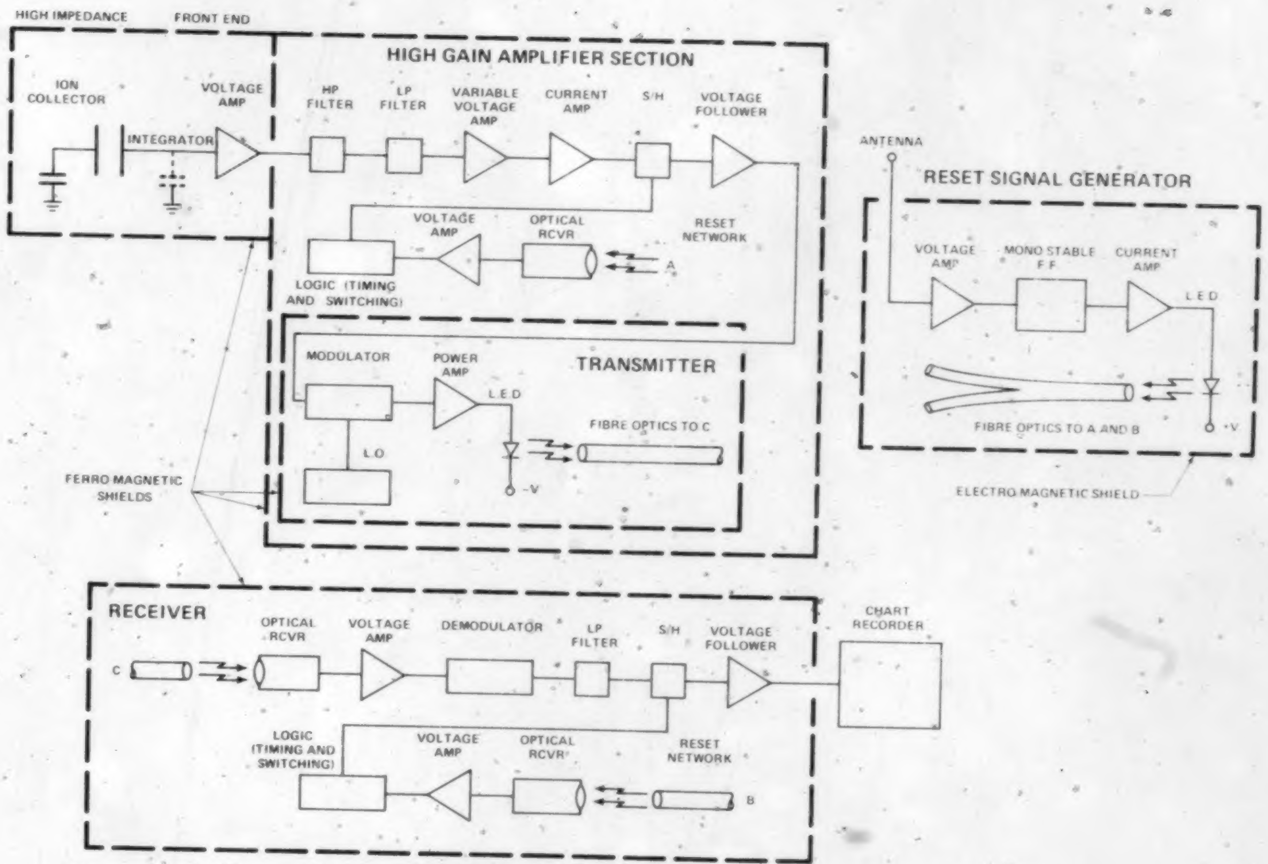
HIGH IMPEDANCE
FRONT END
HIGH GAIN AMPLIFIER SECTION
ION COLLECTOR
INTEGRATOR
VOLTAGE AMP
HP FILTER
LP FILTER
VARIABLE VOLTAGE AMP
CURRENT AMP
S/H
VOLTAGE FOLLOWER
VOLTAGE AMP
OPTICAL RCVR
RESET NETWORK
A
LOGIC (TIMING AND SWITCHING)
MODULATOR
POWER AMP
TRANSMITTER
L.E.D
FIBRE OPTICS TO C
L.O
-V
FERRO MAGNETIC SHIELDS
ANTENNA
RESET SIGNAL GENERATOR
VOLTAGE AMP
MONO STABLE F.F
CURRENT AMP
L.E.D
FIBRE OPTICS TO A AND B
+V
ELECTRO MAGNETIC SHIELD
RECEIVER
C
OPTICAL RCVR
VOLTAGE AMP
DEMODULATOR
LP FILTER
S/H
VOLTAGE FOLLOWER
CHART RECORDER
LOGIC (TIMING AND SWITCHING)
VOLTAGE AMP
OPTICAL RCVR
RESET NETWORK
B

FIGURE 4-3 BLOCK DIAGRAM OF THE CHARGE COLLECTOR

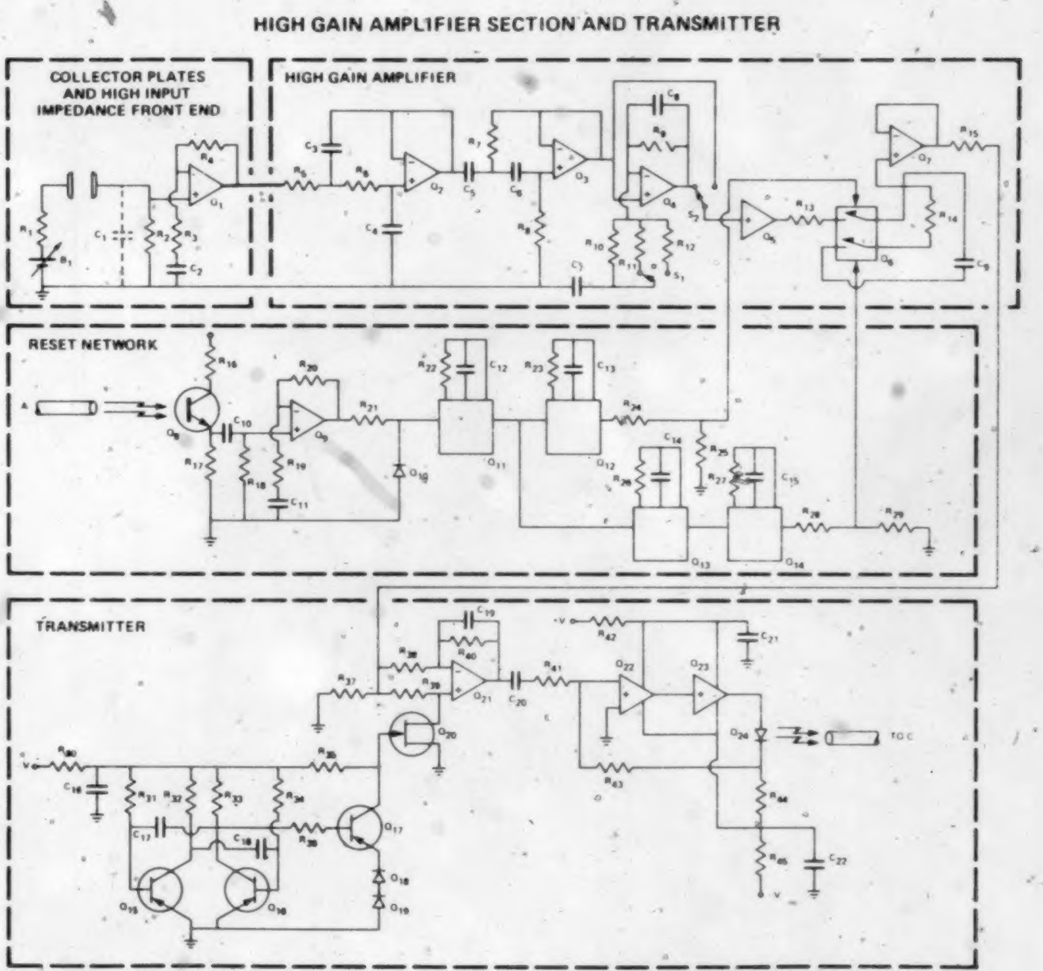
HIGH GAIN AMPLIFIER SECTION AND TRANSMITTER
COLLECTOR PLATES AND HIGH INPUT IMPEDANCE FRONT END
HIGH GAIN AMPLIFIER
RESET NETWORK
TRANSMITTER
TO C

FIGURE 4-4 CHARGE COLLECTOR AND TRANSMITTER CIRCUIT

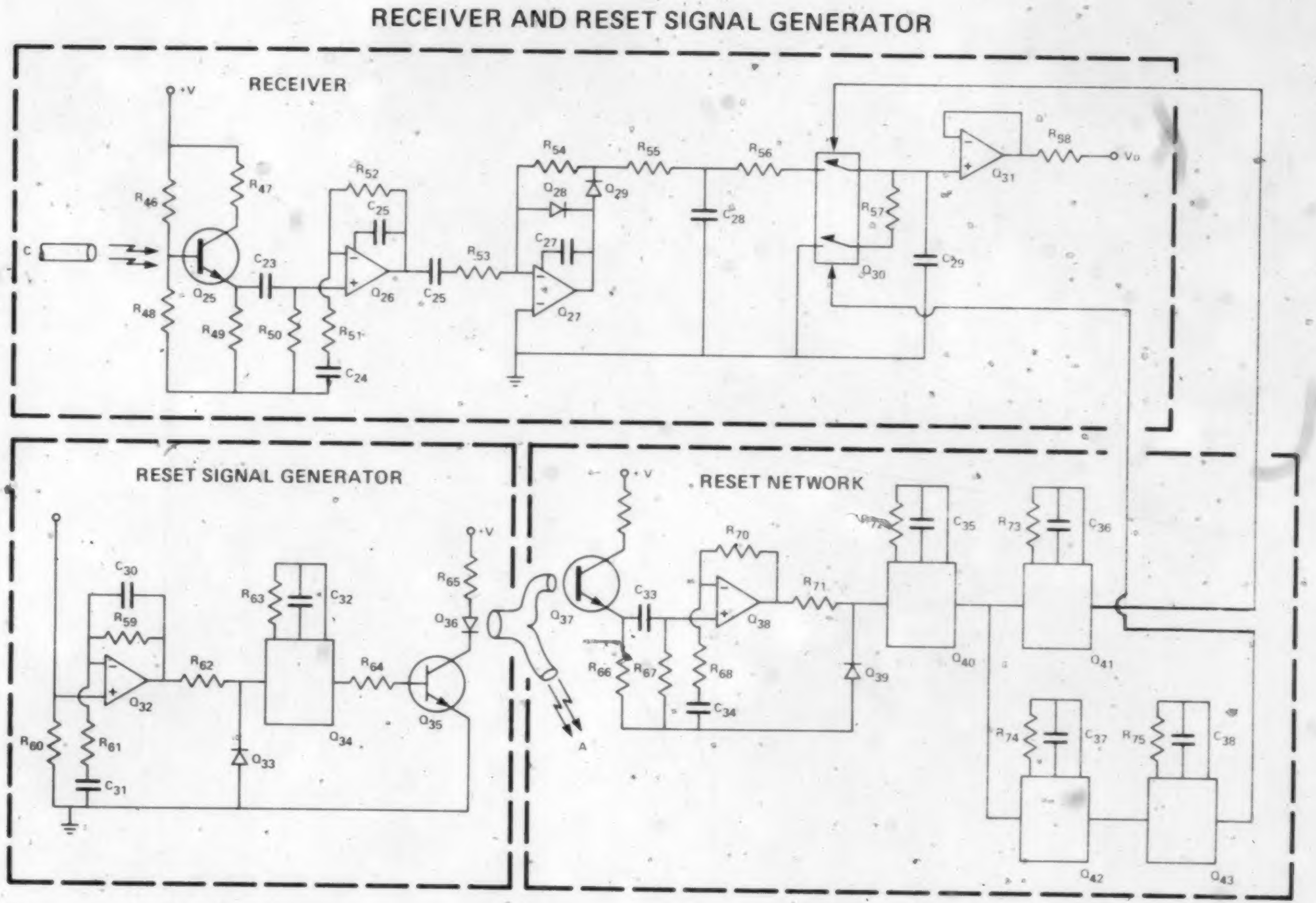
RECEIVER AND RESET SIGNAL GENERATOR
RECEIVER
RESET SIGNAL GENERATOR
RESET NETWORK
+V
C
A
Vo
R46
R47
R48
R49
R50
R51
R52
R53
R54
R55
R56
R57
R58
R59
R60
R61
R62
R63
R64
R65
R66
R67
R68
R70
R71
R72
R73
R74
R75
C23
C24
C25
C27
C28
C29
C30
C31
C32
C33
C34
C35
C36
C37
C38
Q25
Q26
Q27
Q28
Q29
Q30
Q31
Q32
Q33
Q34
Q35
Q36
Q37
Q38
Q39
Q40
Q41
Q42
Q43

FIGURE 4-5 CHARGE COLLECTOR RECEIVER CIRCUIT

PIN CONNECTIONS FOR MONO STABLE FLIP-FLOPS (VIEWING FROM THE TOP)

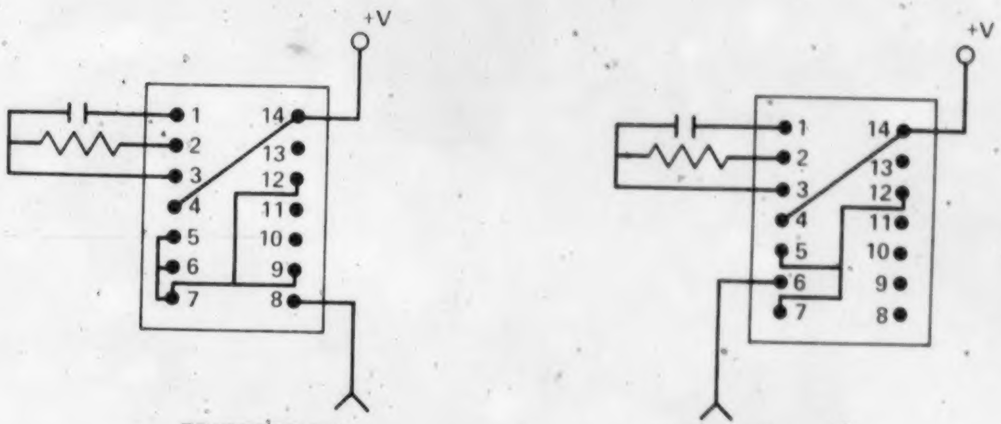
+V
1
2
3
4
5
6
7
14
13
12
11
10
9
8
+V
1
2
3
4
5
6
7
14
13
12
11
10
9
8

TRIGGERS ON LEADING EDGE OF A POSITIVE PULSE

TRIGGERS ON TRAILING EDGE OF A POSITIVE PULSE

FIGURE 4-6 MONOSTABLE FLIP-FLOPS

PIN CONNECTIONS FOR ANALOG SWITCHES (VIEWING FROM THE TOP)

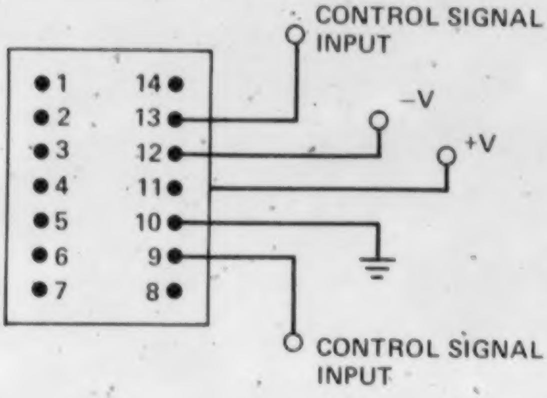
CONTROL SIGNAL INPUT
1
2
3
4
5
6
7
14
13
12
11
10
9
8
−V
+V
CONTROL SIGNAL INPUT

FIGURE 4-7 ANALOG SWITCHES

4-1. Photon Counter

The processes giving rise to current at the output of the photomultiplier tube in Figure 4-2 has been discussed in Section 6-2-6. The output current is transformed to a voltage signal and amplified by the device employing Q_{44}. C_{39} is a large capacitor which blocks the photomultiplier dark current, but which provides a low impedance path for the transient signal. The signal duration may be a few microseconds. The first stage amplifier is a FET input device providing a high input impedance so as not to load the integrating capacitor. This device, also employed in Q_{45}, Q_{46}, Q_{47}, and Q_{48} had a rise time specification of less than 20 ns. The voltage gain of the first stage is 23 db (x 14.2). Q_{45} is a voltage follower which prevents loading of the preceeding stage. Additional gain of 19 db (x 9.2) is provided by Q_{46} and can be switched into the circuit by toggle switch S_3. From this point the time resolved photon signal can be displayed on a CRT. The overall rise time was measured to be 30 ns. This was sufficiently fast to accurately follow the photon signal. Examples appear in Figures 6-15.

The signal was then integrated by the circuitry employing Q_{48}. C_{45} is a large blocking capacitor preventing d.c. drift from the preceeding stages from being integrated.

Low frequency amplifier noise was suppressed by placing a resistor (R_{88a}) in parallel with C_{46} to decrease the low frequency gain (not illustrated in Figure 4-2). A large value was used so as to maintain the integrator output long enough to be sampled (100 μs). The device was tested by supplying a square pulse at the input of the integrator. The output value was monitored for input pulses of various durations. The input/output relationship was observed to be linear for input pulses ranging from 50 ns to 100 μs in width. This adequately covered the required range as illustrated by the signals in Figure 6-15.

The network involving Q_{49} is insensitive to fast signals (large C_{49}) but is sensitive to integrator drift and provides negative feedback to limit it.

The appearance of a signal at the output of the integrator synchronizes the sampling network by activating Q_{57}. C_{51} reduces the low frequency gain of the device so that false triggering on low frequency noise does not occur. The time sequencing is subsequently controlled by the monostable flip-flops Q_{53}, Q_{59}, and Q_{60}. The pin connections for these are shown in Figure 4-6. The transistor circuitry inverts the signals. This is required by the n-channel MOSFETs. At 30 μs after the leading edge of the integrated signal appears the gate controlled by Q_{50} is opened and it remains open for 70 μs, at which time it is closed. During this time the gate controlled by Q_{64} has remained closed and the sampling capacitor C_{50} has charged to the integrator voltage.The capacitor remains charged for 0.5 seconds during which time the x-y recorder fully responds, generating a bar. Q_{51} is a high input impedance, unity gain, FET operational amplifier used to prevent loading of C_{50}. Q_{52} is a unity gain operational amplifier with low output impedance to drive the x-y recorder (input impedance $\approx 10^4$ ohms). R_{98} has been provided for short circuit protection.

At 0.5 seconds the gate controlled by Q_{64} is opened momentarily and the sampling capacitor C_{50} is discharged. A resistor (R_{115}) has been placed in the discharge path to prevent current surges. Also during this time the integrator voltage has returned to zero. Leakage contributes to the discharge but the resistor in parallel with C_{46} is primarily responsible. The discharge resulted in less than 10% signal loss at the end of the sampling time (100 μs). The timing allowed signals to be processed at spark discharge rates of 1 Hz.

The circuit was very reliable except for the MOSFET gating devices which failed periodically. These were subsequently replaced by analog switches. Devices of this type had proved to be very reliable when employed in the charge collector gating network. Pin connections have been shown in Figure 4-7.

Relative to the charge collector circuitry this device was not so susceptible to external electrical noise generated by the spark discharge. The spark current discharge was fast and generated primarily high frequency noise. This was effectively averaged to approximately zero by the integrator during the 100 μs before sampling was completed. Print circuit board fabrication of all electronic circuitry using one side of the board as a common ground plane and placing the entire assembly inside a ferromagnetic module resulted in a good signal to noise ratio. In addition it was found necessary to power the electronics by a rechargable battery pack, also placed inside the module. The bias voltage for the photomultiplier tube was derived from an external power supply, however, The supply was placed in a ferromagnetic box and a double coaxially shielded lead was used to deliver the bias voltage to the photomultiplier tube. High frequency isolation from the 60 Hz - 110 volt service was provided by an isolation transformer. These techniques resulted in essentially eliminating the effect of external noise. The sensitivity of the device was subsequently traced to optical noise but amplifier noise has been measured and observed to be only a factor of 2 or 3 less than the optical noise.

In the event that there is not a sufficiently large signal to activate Q_{57} the circuitry will not be reset on every spark and the output will drift until such time that a signal is sufficiently strong to activate the timing network. This drift is evident in Figure 6-22 for example. The sensitivity of Q_{57} was adjusted so that amplifier noise output for maximum gain settings was not quite sufficient to generate a time sequencing signal.

4-2 Charge Collector

The charge collector is illustrated in Figures 4-3, 4-4 and 4-5. The collector plate bias voltage, B_1, shown in Figure 4-4 is composed of a number of batteries of different sizes. The voltage can be applied to the collector plates in approximately 10 volt steps by the use of rotary switches (not shown). R_1 is used only to reduce short circuit current (in the event of gaseous breakdown) and has been kept small enough so as to provide a time constant less than a few microseconds so that the charge collection process will not be affected.

A simplified integrating technique has been employed with the sacrifice of temporal resolution. The charge is swept out of the volume between the collector plates and effectively stored in C_1. C_1 is the parasitic capacitance of the front end of the device (includes coaxial cable lead). Since this parameter had to be kept small for good sensitivity the front end had to be located within the test cell. Bias voltage, power supply voltage, a common ground lead, and the output signal were delivered through a vacuum tight covar to glass seal with covar leads sealed in the glass.

The voltage appearing on C_1 is then amplified by 40 db (x 100) with a FET-input operational amplifier (Q_1). R_2 is provided to bias Q_1 and to discharge C_1 in time to process the next signal (one second later). A large (10^9 ohms), low noise resistor was obtained for this application. However, amplifier noise was still the limiting factor for this device, being equivalent to about 20 μV at the input (includes filtering discussed later). The noise could be reduced by 20 db (x 10) by replacing R_2 with a J-FET (MPF102) connected with the gate to ground, the source open, and the drain to the noninverting input of Q_1. However, this only worked well for small signals since the effective resistance of the device diminishes with applied voltage. At a few millivolts the current drain is increased to such an extent that it markedly reduces the voltage of C_1 before it can be sampled.

In addition to the amplifier noise problem the circuit was found to be extremely sensitive to low frequency mechanical vibration such as building vibration or the human voice. This was attributed to vibration of the collector plates. Such vibration would change the collector plate spacing and hence the collector plate capacitance. The ensuing redistribution of charge, to maintain constant bias voltage would result in charging C_1 to some voltage. This would appear as noise. Any signal due to photoionization would be added to the slowly varying noise.

The low frequency gain of Q_1 was reduced by C_2 and this resulted in limited reduction of low frequency noise. The problem was further reduced by providing a high pass unity gain active filter (Ω_3). The 3-db point was at about 600 Hz with a low frequency roll-off of 40 db per decade.

In addition to filtering, the effects of low frequency noise were futher reduced by mounting the entire monochromator assembly on vibration absorbing rubber pads. Furthermore, the ferromagnetic modules and cases housing the electronics had to be mounted to the exit slit with nylon stud bolts. The vacuum seal was made with an over-sized o-ring. The thick o-ring reduced the transfer of vibration from the monochromator to the test cell. Also, this served the dual purpose of electrically isolating the electronic recording device from all other components.

A unity gain low-pass active filter was also employed to suppress high frequency noise (Ω_2). The filter has a 3-db point at about 25 kHz with a high frequency roll-off of 40 db per decade.

The high and low-pass filters comprized a Butterworth band-pass filter. A Butterworth filter produces a maximally flat response. The measured response time to a step input was about 25 μs (90%). The response remained approximately flat (well within 10%) for an additional 75 μs after which time it degenerated into a ring exhibiting many higher order effects.

Electric field to gas pressure ratios could be adjusted so that all charge (electrons at least) could be collected well within the 100 μs limit imposed by the filterresponse. The resulting signal was sampled in the flat filter response region. For large signals filtering was unnecessary and the filter was connected so that it could be by-passed with a toggle switch (not shown). This provided somewhat better time resolution.

Additional amplification could be provided by the circuit employing Q_4. For S_2 in the position shown three different voltage gains could be selected by switch S_1. These were 21 db (x 11), 30 db (x 32), and 40 db (x 100). Q_5 is a voltage follower used to provide sufficient current to charge the sampling capacitor C_9.

The time sequencing is provided by the reset network. The upper "switch" of Q_6 is closed at about 7 μs after the spark discharge begins. The time synchronizing signal is derived from high frequency noise generated by the spark discharge. This has been discussed later. The sampling time (the time that the upper switch remains closed) has been made adjustable from 7 μs to about 1 ms by replacing R_{23} with a potentiometer. 7 μs is the minimum toggle time of the monostable flip-flops employed (Q_{12} etc.). During this time the lower "switch" of Q_6 has remained open. However, at 0.5 seconds this switch is momentarily closed and C_9 is discharged to ground through R_{14}. At this stage the device is ready to process another signal. The front end capacitance will have discharged through R_2 by this time.

Consequently, a 0.5 second pulse appears at the output of the voltage follower, Q_7. The height of this pulse is directly proportional to the amount of charge collected.

Unfortunately, the output signal cannot be used to drive the x-y recorder directly. Any external leads connected to the output, pick up external electrical noise and this is fed back to the inputs of the various operational amplifiers. Consequently, an optical transmitter-receiver system was constructed to deliver the signal to the x-y recorder. The transmitter is illustrated in Figure 4-4 and the receiver appears in Figure 4-5. Fiber optics has been used to deliver the optical signal. In order to obtain good linearity over a number of decades the output pulse had to be amplitude modulated.

The transmitter consists of a square wave local oscillator operating at about 30 kHz, an operational amplifier modulator, and a power amplifier section. These are illustrated in Figure 4-4. The operational amplifier modulator is switched between the inverting and non-inverting modes by the 30 kHz L.O. This results in amplitude modulation of any low frequency applied signal (suppressed carrier modulation). The output section consists of a fast operational amplifier with 20 db (x 10) of gain followed by a power stage. The output section drives a LED (light emitting diode) placed in the feedback path of the power output stage to provide linearity.

This modulated signal is delivered to the reciever by fiber optics. The receiver and demodulator appear in Figure 4-5.

The optical signal is transformed to an electrical signal by a phototransistor (Q_{25}). A fast, high-gain amplifier (40 db) provides sufficient amplification so that the signal may be conveniently demodulated. The demodulator consists of a perfect rectifier circuit (Q_{27}). "Perfect" is used to describe this type of circuit because the gain of the operational amplifier is used to reduce the nonlinearity of the rectifying diodes. The resulting 1/2 wave rectification of the signal is filtered by the low pass filter circuit composed of C_{28} and R_{55}. The demodulated signal is then sampled by the analog switch (Q_{30}) and the sampling capacitor C_{29}. The upper "switch" is closed at about 0.2 seconds and remains closed for a sampling time of about 100 μs. The lower "switch" remains open for about 0.8 seconds during which time the x-y recorder fully responds. After this time the lower "switch" is momentarily closed to discharge the sampling capacitor and reset the receiver. The circuit operates at a maximum repetition rate of 1 Hz. In response to this, the x-y recorder generated a bar graph type of display.

A time sychronizing signal is produced by the reset signal generator in Figure 4-5. Q_{32} generates a large output voltage in response to noise picked up by the antenna. C_{31} limits the low frequency gain and C_{30}

limits the very high frequency gain. This results in sensitizing the device only to the bandwidth of noise generated by the spark discharge. The monostable flip-flop (Q_{34}) generates a clean pulse when the output of Q_{32} reaches sufficient amplitude to toggle Q_{34}. All subsequent time sequencing is derived from the leading edge of this pulse.

The pulse switches transistor Q_{35} on, and the LED is driven for the duration of the pulse. The LED feeds split fiber optics. Branch "A" activates the reset network controlling the integrator, high gain amplifier section, and the sampling gate in Figure 4-4. The second branch simultaneously activates the reset network controlling the receiver in Figure 4-5. The monostable flip-flops provide proper signal polarity and timing intervals. Pin connections for the monostable flip-flops and for the analog switches are illustrated in Figures 4-6 and 4-7 respectively. Bias resistors to the bases of the phototransistors Q_8 in Figure 4-4 and Q_{37} in Figure 4-5 have not been shown. These are R_{16b} and R_{69b} in Table 4-1 respectively.

Good linearity of the transmitter-receiver combination was experimentally verified. A gain of -12 db (x 0.25) was also determined experimentally.

As with the photon counter, the device was still susceptible to noise generated by the spark discharge.

However, adequate suppression was obtained by the shielding techniques employed. All circuits were fabricated on print circuit boards and one side was used as a common ground plane. In addition,each board was grounded to a common point. Ferromagnetic shielding cases were used to house all electronics. Furthermore a double ferromagnetic shield was placed around the spark source with only narrow slits used to allow illumination of the grating. Double ferromagnetic shielding was also provided for the discharge circuitry. Wide strips were used to ground all of these components to a common point. In addition to shielding,all power was derived from rechargeable batteries also placed within the shielding cases. The only exception was the reset signal generator. These techniques resulted in reducing noise pick-up to below the level of the amplifier noise. It has been previously pointed out that this was the limiting factor.

The sensitivity and dynamic range of the device has been discussed in Chapters 6 and 7 where a calibration procedure has also been dealt with. This device was found to be more sensitive than the photon counter. Photoionization could be detected even when the photon intensity was too weak to register on the photon counter.

Table 4-1

Key to Components in Figures 4-2, 4-3, and 4-4

Component Subscript(i)	Value of R_i (ohms)	Value of C_i	Part Identification Number Q_1
1	33k-470k	13pf	LH0052CH
2	1000M	10μf tantalum	LM741
3	100	400pf	LM741
4	10k	200pf	LM318CN
5	22k	2000pf	LH0002CN
6	22k	2000pf	AH0134CD
7	75k	100μf tantalum	LH0042CH
8	150k	220pf	FPT100
9	10k	4700pf	LM318CN
10	1k	0.01μf	1N914
11	500	100μf	CD4047
12	110	47pf	CD4047
13	330	500pf	CD4047
14	10k	0.22μf	CD4047
15	1k	0.22μf	2N3906
16	1k	80μf	2N3906
16_b	220k		
17	100k	1000pf	2N3906
18	220k	1000pf	1N914
19	100	68pf	1N914
20	10k	0.1μf	MPF102
21	10k	250μf	LH0042CH

22	18k	250µf	MC1741SCP1
23	15k	0.01µf	LH0002CN
24	10k	0.68µf	narrow beam LED
25	10k	2pf	FPT100
26	2.2M	0.68µf	NE531
27	2.2M	20pf	NE531
28	10k	4.7µf tantalum	Hot Carrier Diode
29	10k	0.02µf	Hot Carrier Diode
30	100	10pf	AH0134CD
31	47k	0.047µf	LH0042CH
32	4.7k	0.01µf	MC1741SCP1
33	4.7k	0.01µf	1N914
34	47k	10µf	CD4047
35	4.7k	0.047µf	2N3904
36	47k	300pf	narrow beam LED
37	33k	0.22µf	FPT100
38	15k	0.02µf	LM318CN
39	15k	100µf tantalum	1N914
40	15k	5pf	CD4047
41	10k	0.1µf	CD4047
42	22	5pf	CD4047
43	10k	400µf	CD4047
44	150	400µf	LH0032CG
45	22	100µf tantalum	LH0002CN
46	2.2M	1000pf 2%	LH0032CG
47	1k	38pf	LH0002CN

48	2.2M	33µf	LH0032CG
49	100k	1000µf	MC1741SCP1
50	220k	0.001µf	3N153
51	1k	0.22µf	LH0042CH
52	100k	0.15µf	LH0002CN
53	10k	220pf	CD4047
54	10k		2N3904
55	15k		2N3906
56	1k		1N914
57	10k		LM318CN
58	1k		1N914
59	100k		CD4047
60	220k		CD4047
61	100		2N3904
62	10k		2N3906
63	2.2k		1N914
64	1k		3N153
65	680	Photomultiplier Tube RCA 8645	
66	100k		
67	220k		
68	100k		
69	1k		
69_b	220k		
70	10k		
71	10k		
72	2.2M		

73	150k
74	2.2M
75	2.2M
76	910
77	470k
78	910
79	12k
80	1k
81	8.2k
82	1k
83	10k
84	1k
85	10k
86	39
87	1k
88	2.2k
88_a	1M
89	1k trim pot.
90	3.3k
91	33k
92	100k
93	10k trim pot
94	10k
95	10k
96	100k

97	1k
98	1k
99	22k
100	10k
101	10k
102	10k
103	10k
104	100k
105	10k
106	470k
107	10k
108	1.8M
109	1.8M
110	22k
111	10k
112	10k
113	10k
114	10k
115	

CHAPTER 5

Microwave Interferometer Phase Shift Measurements

Various plasma diagnostic results obtained with the microwave interferometer are presented and analysed in this chapter. These include, electron density as a function of time, gas type, additive type, gas pressure and distance from the ultra-violet spark source. Data on some of the more salient parameters of the ultra-violet spark source is included.

It has been assumed that the electron collision frequency and the plasma frequency are much less than the test frequency, to facilitate extraction of the electron density from the original phase shift measurements. The validity of this assumption will be discussed.

5-1. The Ionization Chamber

Figure 5-1 shows the salient features of the ionization chamber and the gas handling plant. The ionization chamber consisted of a pyrex cylinder 15 cm in diameter and 40 cm long. Fitted to this were aluminium end plates. Buna N O-rings were used to make the vacuum seals. The ultra-violet spark source was mounted in the center of one end plate. A 1/4 inch brass bellows valve was secured in the same end plate to be used as a filling port. In addition, a separate valve and line were installed to purge the spark source. This is discussed more fully in 5-2. A 3/4 inch brass bellows valve was mounted in the remaining end plate to be used as a pumping port.

To prevent oil vapor from migrating back into the ionization chamber, a cold trap was placed between the pumping port and the mechanical rotary pump. The cold trap was made simply by forming the pumping line in the shape of a U and submerging it in a container filled with liquid nitrogen. The test gas was delivered from three high pressure cylinders equipped with flow meters, so that the flow of CO_2, He, and N_2 could be independently controlled. The gas was then passed through a sealed canister filled with copper "pot scrapers" to assure uniform mixing. This was later found to be unnecessary, and was removed in the interest of simplifying the apparatus. From this point, the gas could be channelled to the ionization chamber by one of the following three alternative routes:

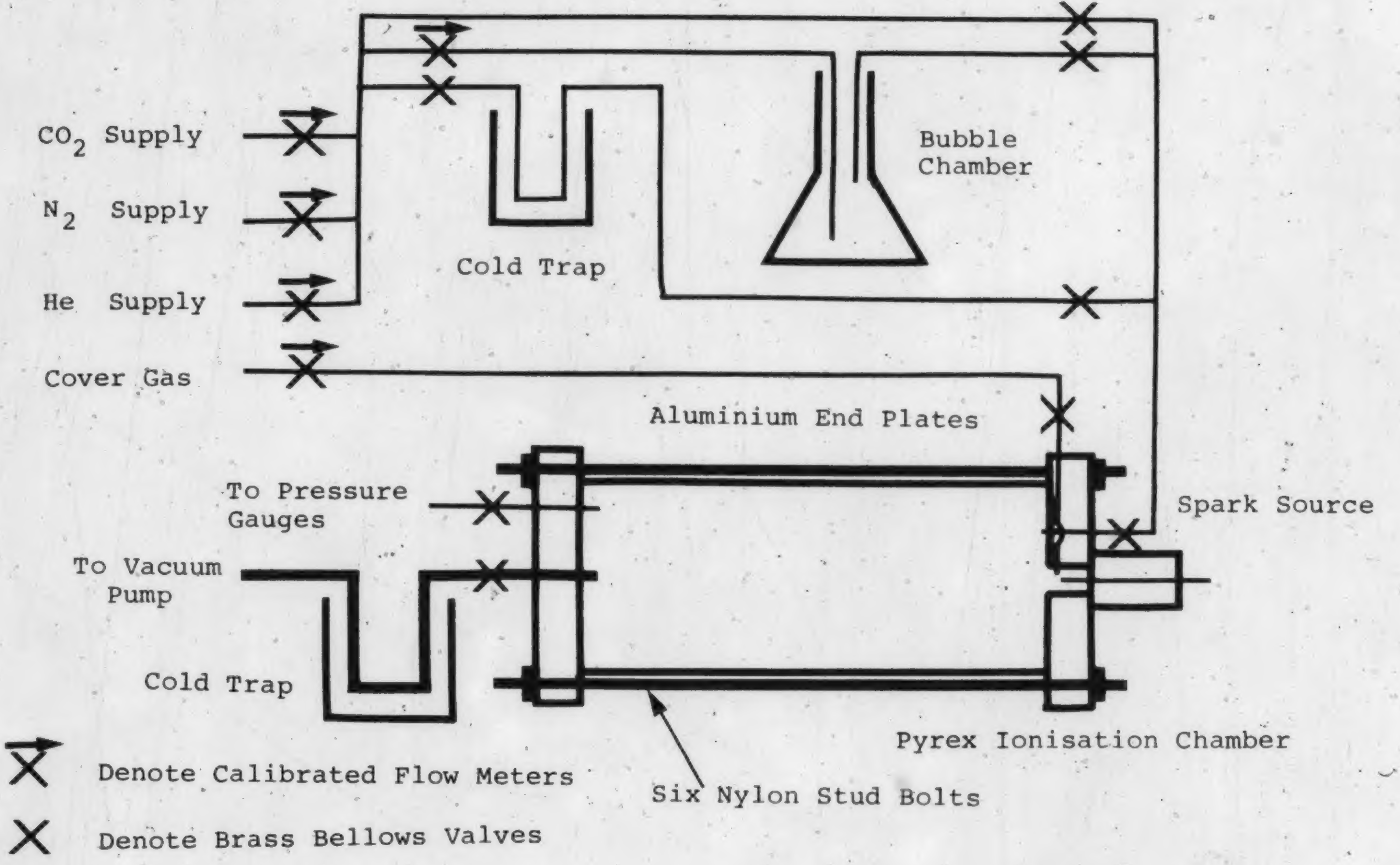
CO_2 Supply
N_2 Supply
He Supply
Cover Gas
Cold Trap
Bubble Chamber
Aluminium End Plates
To Pressure Gauges
To Vacuum Pump
Cold Trap
Spark Source
Pyrex Ionisation Chamber
Six Nylon Stud Bolts
Denote Calibrated Flow Meters
Denote Brass Bellows Valves

FIGURE 5-1 IONIZATION CHAMBER AND GAS HANDLING PLANT

(1) The gas could flow directly to the ionization chamber.

(2) The gas could pass through a cold trap consisting of 50 feet of 1/4 inch O.D. copper tubing, coiled and submerged in a coolant such as liquid nitrogen (77°K) or dry ice in acetone (195°K) [81].

(3) Any portion of the total gas could be metered through a bubble chamber. This device was used to seed the gas with vapor from substances that assumed the liquid state at S.T.P.

The pressure inside the ionization chamber was monitored at the pump-out end plate, by supplying an additional 1/4 inch brass bellows valve. Any type of gauge could be connected. However, except for leak testing, two absolute pressure gauges were used. These covered the ranges 0.1 torr to 800 torr and 0.1 torr to 20 torr.

To achieve good vacuum integrity, it was necessary to use copper tubing and good quality valves. All connections were made with buna N O-rings, swadge-lok fittings, or, by solder.

Upon completing the fabrication of the apparatus, and making the necessary adjustments to correct leaks, the total leak rate could not be detected with a He leak detector.

However, an ionization gauge calibrated for air, indicated that the chamber pressure increased at approximately 5 to 10 microns per hour, after being evacuated and isolated with appropriate values. The chamber and associated apparatus were not baked, so this may have been largely a virtual leak due to degassing.

5-2. The Source

A condensed spark discharge has been used as the source of ultra-violet light throughout the entire project. Unless otherwise stated a 0.1 μf capacitor was charged to 40 kV. The discharge was triggered by a pressurized spark gap at approximately 1 Hz. The energy was delivered to a single spark plug of coaxial geometry. The circuit was designed to keep the inductance to a minimum. However, the discharge current exhibited a ring which lasted about 8 μs with a period of approximately 1.5 μs as shown in Figure 5-2. This translates to a total circuit inductance of 0.6 μh. It is likely that most of the inductance was associated with the spark gap since short, wide leads were used, and the series equivalent inductance of the capacitor was less than 20 nh.

The source housing was designed to accommodate a 2 inch diameter vacuum window, thus providing a means of isolating the source from the chamber. Different window materials provided limited photon wavelength resolution. Unfortunately, the window would become clouded after only a few pulses. In addition, minature projectiles from the spark source pitted the surface of the window. This had the effect of seriously degrading the transmission characteristics of the window. Consequently, only limited information could be obtained with the use of windows, and they were not used for the majority of the tests performed. Lack of source isolation meant that a constant

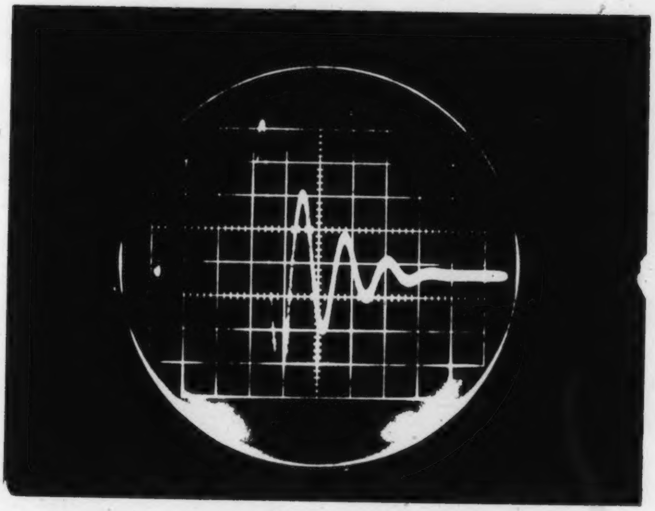

He environment at 400 torr
C = 0.1 µf
V = 40 kV
Scale 1 µs/ div
20 v/ div

FIGURE 5-2 DISCHARGE CURRENT WAVEFORM

source emission spectrum could not be depended upon, as gas type and pressure were varied in the ionization chamber. Therefore, to reduce this effect, the source housing was designed so that the source could be purged (or covered) with any desired gas, thus maintaining a more or less constant environment in the vicinity of the spark.

5-3. The Signal

The technique employed to extract the phase shift information from a given signal has been previously discussed and will not be repeated here.

Figure 5-3(a) shows a typical signal revealing the temporal imbalance of the bridge as displayed on the CRT. The signals obtained from all gas mixtures assumed the same general shape; the only differences occurring in the magnitude and rate of decay.

Figure 5-3(a) shows the inability of the receiver to follow the rate of generation of the photoionization. However, the response time was more than sufficient to follow the decay of the plasma.

Figure 5-3(b) shows the bridge having been balanced at a particular point in time. The amount of phase shift and attenuation suffered by the radio signal in traversing the plasma is that amount required to null the bridge. In addition, the bridge can be nulled at any point in time, thus yielding information regarding the time decay of the plasma.

TYPICAL INTERFEROMETER MEASUREMENT

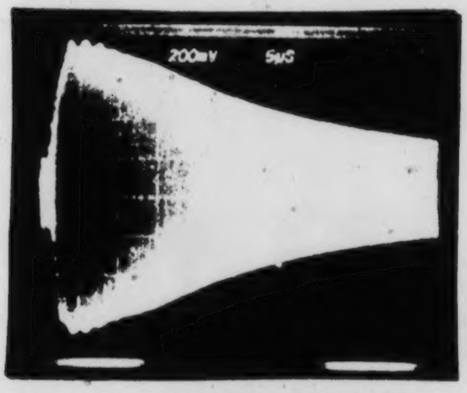

(a)

BRIDGE IONIZATION SIGNAL
HELIUM 20 TORR

SWEEP SPEED - 5μ sec./cm.

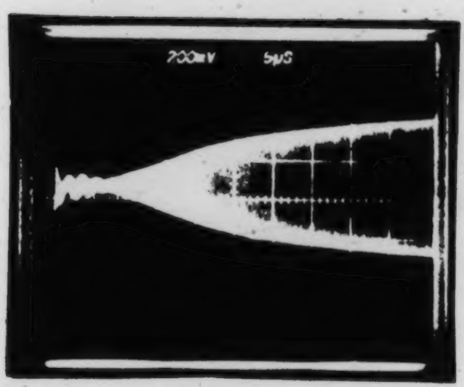

(b)

CANCELLATION MEASUREMENT $\phi = 91°$
$\bar{n} = 4.16\times10^{11}$ cm^{-3} A = 1db

SWEEP SPEED - 5μ sec./cm.

FIGURE 5-3 TYPICAL MICROWAVE INTERFEROMETER SIGNALS

5-4. Theory Relevant to the Analysis of Plasma Decay Data

Plasma decay proceeds by way of three mechanisms [47].

(1) Diffusion
(2) Attachment
(3) Recombination

If more than one of these mechanisms are operating simultaneously, the kinetic equation modeling the decay can be very complicated. In most cases, the equations are sufficiently complex, that no analytic solution can be obtained. In these cases a numerical solution may be found [41] or, appropriate simplifying assumptions made so as to obtain an analytic solution. The latter approach has been taken in this work and has been presented where it has been required for analysis of data. However, to extablish a basis on which to work, a brief mathematical formulation of each independent process has been included. A more rigorous treatment is available in the literature [41,47,48,49,50,51,52].

5-4-1. Diffusion

The time dependent diffusion equation is given by the equation

$$\frac{dN}{dt} = \nabla\cdot(D\nabla N) \qquad 5\text{-}1$$

N = electron density distribution function.

D = coefficient of diffusion [cm^2 sec^{-1}].

Equation 5-1 is a general relationship and describes the diffusion of particles of any type 1 through particles of any type 2.

If one assumes that the number density at any point will decrease exponentially with time, then the time independent diffusion equation is obtained:

$$\nabla^2 N_o + \frac{N_o}{D\tau_{ij}} = 0 \qquad 5\text{-}2$$

where $N(r,\theta,z,t) = N_o(r,\theta,z)\exp(-t/\tau_{ij})$ in cylindrical co-ordinates.

τ_{ij} = time constant (the notation will be defined later) [sec]

There is no dependence on the azimuth angle, θ, and further simplification by separation of variables leads to:

$$\frac{1}{R}\left(\frac{d^2R}{dr^2} + \frac{1}{r}\frac{dR}{dr}\right) + \frac{1}{Z}\frac{d^2Z}{dz^2} + \frac{1}{D\tau_{ij}} = 0 \qquad 5\text{-}3$$

where $N(r,t) = R(r)Z(z)$.

Since the first two terms in Equation 5-3 are related only by a constant, then each of them must equal a constant.

$$\frac{1}{R}\left(\frac{d^2R}{dr^2} + \frac{1}{r}\,\frac{dR}{dr}\right) = -\gamma^2 \qquad 5\text{-}4$$

$$\frac{1}{Z}\,\frac{d^2Z}{dz^2} = -\delta^2 \qquad 5\text{-}5$$

$$\gamma^2 + \delta^2 = \frac{1}{D\tau_{ij}} \qquad 5\text{-}6$$

The solution to Equation 5-4 is the Bessel function of the first kind, of order zero.

$$R(r) = \sum_{i=1}^{\infty} A_i J_o\left(\frac{S_i r}{r_o}\right) \qquad 5\text{-}7$$

$$\gamma = \frac{S_i}{r_o} \qquad i = 1,2,3,4... \qquad 5\text{-}8$$

A_i = constant

r_o = 7.5 cm (radius of the ionization chamber)

S_i = successive zeros of the Bessel function

s_1 = 2.4

s_2 = 5.5

s_3 = 8.7

s_4 = 11.8

s_5 = 15.0

s_6 = 18.1

s_7 = 21.2

Note that Equation 5-7 goes to zero at the wall ($r = r_o$) as required.

The solution to Equation 5-5 is the cosine function.

$$Z(z) = \sum_{j=1}^{\infty} C_j \cos \frac{(2j-1)}{H} \pi z \qquad 5\text{-}9$$

$$\delta = \frac{(2j-1)\pi}{H} \qquad j = 1,2,3,4 \ldots \qquad 5\text{-}10$$

H = 40 cm (length of the ionization chamber).

Note that Equation 5-9 also goes to zero at the wall ($z = \pm H/2$) as required. Since $N(r,z,t) = R(r)Z(z) \exp(-t/\tau_{ij})$ then Equation 5-7 and 5-9 yield the total solution.

$$N(r,z,t) = \sum_{i=1}^{\infty} \sum_{j=1}^{\infty} G_{ij} J_o\left(\frac{S_i r}{r_o}\right) \cos\frac{(2j-1)\pi z}{H} \exp(-t/\tau_{ij}) \qquad 5\text{-}11$$

G_{ij} = constant for each mode

τ_{ij} = time constants for each mode

In this particular application z is constant, and the electron density is averaged over r. Consequently, an average coefficient, B_{ij}, can be defined for each mode of diffusion. Also, since the diffusing particles under consideration are electrons then, $N(r,z,t) \rightarrow \bar{n}_e(t)$ where $\bar{n}_e(t)$ is the average electron density dependent only on time.

One may write:

$$\bar{n}_e(t) = \sum_{i=1}^{\infty} \sum_{j=1}^{\infty} B_{ij} \exp(-t/\tau_{ij}) \qquad 5\text{-}12$$

From quations 5-6, 5-8, and 5-10 one obtains the relationship:

$$\frac{1}{D\tau_{ij}} = \left(\frac{S_i}{r_o}\right)^2 + \left[\frac{(2j-1)\pi}{H}\right]^2 \qquad 5\text{-}13$$

$i = 1,2,3,4...$

$j = 1,2,3,4...$

For constant D Equation 5-13 shows that τ_{ij} decreases, for ever increasing mode numbers, ij. Eventually, (if diffusion is the decay controlling process) all higher order modes will decay out leaving only the fundamental mode. At this stage a semilog plot of electron density against time will yield a straight line. τ_{11} can then be derived from the plot.

5-4-2. Attachment

Electronegative gases may capture electrons to form ions by a number of processes. The prime requirement of any one process is that it must be able to account for the difference in total energy after the capture of an electron. Some of the possible processes are:

(1) Radiative attachment - excess energy is radiatively dissipated in the form of a photon.

(2) Excitation attachment - excess energy is absorbed by an electronic or molecular transition, to be de-excited by a collision process later.

(3) Dissociative attachment - the excess energy is used to dissociate the molecule. Additional energy will go into kinetic energy of the fragments. Any number of the fragments may be in an excited state.

(4) Three-body attachment - the excess energy is carried away by a third body.

Regardless of the particular process involved, an attachment controlled plasma decay (no ionizing sources) can be described by the following relationship:

$$\frac{dn_e}{dt} = -\nu_a n_e \qquad 5\text{-}14$$

n_e = electron density [cm^{-3}]

ν_a = attachment frequency [sec^{-1}]

The attachment frequency depends on the nature of the attachment process. This is taken into account when the data is analysed.

The solution is straight forward and is given by:

$$n_e(t) = n_{eo} \exp(-\nu_a t) \qquad 5\text{-}15$$

If the plasma decay is attachment controlled then a semilog plot of electron density against time will yield a straight line.

5-4-3. Recombination

Electron-ion recombination is a very complex subject with many possible mechanisms [41,47]. As in the case of electron attachment, the prime requirement of any recombination mechanism, is that it must be able to accommodate a change of total energy upon recombination. Such mechanisms include:

(1) Radiative recombination - excess energy is lost in the form of a photon.

(2) Dielectronic recombination - the electron may be captured into an excited state with a second electron jumping to another excited state to absorb the excess energy. The particle is energetically unstable, and is subject to autoionization (liberation of one electron and relaxation of the other). However, if the doubly excited particle stabilizes by making a radiative transition to some lower energy state, then dielectronic recombination has taken place.

(3) Dissociative recombination - the positive ion is dissociated into fragments upon collision with the electron and excess energy is carried away in the form of kinetic energy. One or both of the fragments may be in an excited state.

(4) Three-body recombination - excess energy is carried away in the form of kinetic energy of the third body.

Regardless of the exact nature of the recombination, a recombination coefficient for a two component, singly ionized, system can be defined as follows:

A recombination coefficient is defined as the number of recombination events per unit volume and unit time, R, divided by the product of the number densities of the charge carriers [41].

$$R = n^+n^- \qquad 5\text{-}16$$

α = recombination coefficient (positive) $[\mathrm{cm}^3\mathrm{sec}^{-1}]$

n^+ = number density of the positive species $[\mathrm{cm}^{-3}]$

n^- = number density of the negative species $[\mathrm{cm}^{-3}]$

Provided diffusion and attachment can be neglected, and the ionization source is passive, the recombination rate equals the loss rate of each of the carriers.

$$\frac{dn^+}{dt} = \frac{dn^-}{dt} = -\alpha n^+ n^- \qquad 5\text{-}17$$

For the simple case where $n^+ = n^- = n_e$ the solution is:

$$\frac{1}{n_e} = \frac{1}{n_{eo}} + \alpha t \qquad 5\text{-}18$$

n_{eo} = initial electron density $[\mathrm{cm}^{-3}]$

For the cases where the plasma decay is recombination controlled, then a plot of reciprocal electron density against time will yield a straight line with slope α, and y intercept $1/n_{eo}$.

5-5. Plasma Decay Results

Temporal characteristics of the plasma decay for the independent laser gases, and for laser mixtures have been plotted. Some gases likely to be present as an impurity in a typical laser device are also included.

Many of the following figures clearly indicate that the decay processes are nonsimple. It is apparent that in all cases, the decay is a strong function of such things as gas species, gas mixture, additive, and total pressure. More subtle features also have a profound effect on the observed decay rate and they tend to obscure the true nature of the decay mechanism. Such features include the initial electron spatial distribution, the initial electron energy distribution, the nature of the resulting ions, and the geometry of the ionization chamber. An extended investigation would be required to determine these factors precisely, and to facilitate identification of the decay mechanism. This was beyond the scope of the project, however.

It should be emphasized that the ionization chamber and the source were designed so as to simulate photoionization conditions in a typical laser device. No effort was made to ensure isolation of a particular decay process. Consequently, any combination of diffusion, attachment and recombination could be operating simultaneously. Nevertheless, some insight can be gained by considering each process individually and by considering combination processes under special conditions. Reasonable explanations can be given to account for the observed decay in most cases.

5-5-1. Helium and Nitrogen

Figure 5-4 and Figure 5-5 show the electron decay in He at high pressures (≈ above 10 torr).

It was found that the best straight line fit to the data was obtained when reciprocal electron density was plotted against time. The values of α range from 10^{-5} to 10^{-7} cm^3 sec^{-1} and are consistent with those expected for a dissociative recombination process [41].

Figure 5-8 and Figure 5-9 indicate that a similar condition develops in N_2. Unfortunately, the recombination coefficient is a function of many parameters, including pressure, electron energy, ion species, electron-ion density and initial electron-ion distribution [41].

At the test pressures, the electrons were likely to have reached ambient temperature at times short compared to the time of measurement - particularly since no E-field was applied. However, all the other parameters would have had an effect - the extent of which is unknown. This could very easily account for departure from linearity in the early decay. To obtain a better understanding of the exact nature of the recombination, a detailed investigation of the parameters would have to be carried out.

At lower pressures (≈ below 10 torr) a different mechanism seems to be responsible for electron decay in He and N_2.Up to 1 ms, the signal in the reference arm of the bridge had to be strongly attenuated to bring about a null reading, indicating a plasma density above cut-off (10^{12} cm^{-3}). However, the plasma was long lived and the decay was followed for a number of milliseconds.

Figure 5-6 and Figure 5-10 are plots of reciprocal density against time for He and N_2 respectively. Initially, the decay can be assigned a recombination coefficient of about 10^{-8} cm^3sec^{-1}, but the linearity ceases for the later decay. However, the data plot as straight lines on a semilog scale as shown in Figure 5-7 and Figure 5-11. This is particularly true for the lowest pressures. The straight line relationship indicates that recombination in the early decay has given way to a process involving diffusion and/or attachment in the later decay. However, attachment is unlikely to play a significant role in He or N_2, since no electronegative gas is present in sufficient quantities to account for the rapid decay. This leaves diffusion as the only candidate.

Examination of the debye length appropriate to the plasma densities under consideration, reveals that ambipolar diffusion would dominate. For even the smallest densities obtained, the debye length is much less than any linear dimension of the ionization chamber. Consequently, as the electrons tend to diffuse, a space charge will develop and the electron diffusion will be limited by the mobility of the positive ion and the electron temperature [41,47].

Assuming that the ion is a heavy molecular ion, Figure 5-12 shows that a reasonable figure for the reduced mobility is 21 $\text{cm}^2\ \text{volt}^{-1}\ \text{sec}^{-1}$ in He. The reduced mobility is the mobility reduced to standard conditions of 273°K and 760 torr. The following relationship applies:

$$K = \frac{K_o\ 760\ T}{273\ P} \qquad 5\text{-}19$$

K_o = reduced mobility $[\text{cm}^3\ \text{volt}^{-1}\text{sec}^{-1}]$

K = mobility under experimental conditions $[\text{cm}^2\ \text{volt}^{-1}\text{sec}^{-1}]$

T = gas temperature [°K]

P = gas pressure [torr]

The diffusion coefficient of the ion can be found by evoking the Einstein relationship:

$$D^+ = \frac{KT}{1.16 \times 10^4} \qquad 5\text{-}20$$

D^+ = positive ion diffusion coefficient under experimental conditions $[\text{cm}^2\text{sec}^{-1}]$

In addition, for ambient temperature electrons, the coefficient of ambipolar diffusion is twice the coefficient of diffusion for the positive ion.

$$Da = \frac{2KT}{1.16 \times 10^4} \qquad 5\text{-}21$$

Da = coefficient of ambipolar diffusion under experimental conditions [$cm^2 sec^{-1}$]

Substitution of Equation 5-19 into Equation 5-21 results in:

$$Da = \frac{2 \times 760\ Ko\ T^2}{273 \times 1.16 \times 10^4\ P} \qquad 5\text{-}22$$

For He with $Ko = 21\ cm^2\ volt^{-1} sec^{-1}$ and T = 300°K the coefficient of ambipolar diffusion becomes:

$$Da = \frac{907}{P}\ cm^2\ torr\ sec^{-1} \qquad 5\text{-}23$$

For a similar ion in N_2 the reduced mobility is about 2.8 $cm^2\ volt^{-1} sec^{-1}$ from Figure 5-13. Equation 5-22 yields the following relationship for the coefficient of ambipolar diffusion in N_2:

$$Da = \frac{121}{P}\ cm^2\ torr^{-1} sec^{-1} \qquad 5\text{-}24$$

The experimental time constants characteristic of the decay are tabulated in Table 5-1. These are determined from any two points (n_{e1}, t_1) and (n_{e2}, t_2) on the straight line characteristic and the formula:

$$\tau = \frac{t_2 - t_1}{\ln n_{e1}/n_{e_2}} \qquad 5\text{-}25$$

τ = experimental time constant [sec].

Equation 5-13 together with Equation 5-22 and 5-23 yield all theoretical time constants for He and N_2 respectively. The fundamental time constants have been calculated and tabulated in Table 5-1 for comparative purposes.

The rate of decay increases with decreasing pressure as expected for a diffusion process. However, it is apparent from comparison of the time constant in Table 5-1 that fundamental mode diffusion has not developed for the higher pressure cases. The fundamental mode was approached in both He and N_2 for the lowest pressure in each gas. Presumably, the decay is being increasingly affected by faster, higher mode diffusion with increasing pressure.

The large time constants are a direct consequence of the size of the vessel employed. Diffusion parameters can be studied much more easily in small vessels.

High order diffusion modes are expected to be excited because the initial electron spatial distribution cannot be expected to be a fundamental mode distribution. At best, it will be a recombination distribution, since the early decay was recombination controlled. As a general rule, higher modes are unlikely to be excited without simultaneously exciting the lower modes as well. This would be expected to show up as a deviation from the straight line characteristic. In fact the best straight line characteristics are obtained at the lowest pressures

Table 5-1

Experimental Time Constants

(a)

P[torr]	τ[ms]	τ_{11}[ms]
6.1	3.3	61
1.6	1.7	16
0.5	1.3	5

(b)

P[torr]	τ[ms]	τ_{11}[ms]
1.0	4.1	80
0.5	2.6	40
0.08	2.0	6.4

These are obtained for He (a) and Ne_2 (b) from Figure 5-7 and Figure 5-11 respectively. τ_{11} denotes the corresponding theoretical time constant for fundamental mode diffusion.

in both He and N_2 where most high order modes would have decayed out leaving primarily, the fundamental mode. If one were to follow the decay for a sufficiently long time, one would find that the fundamental mode of diffusion would eventually be obtained for all pressures.

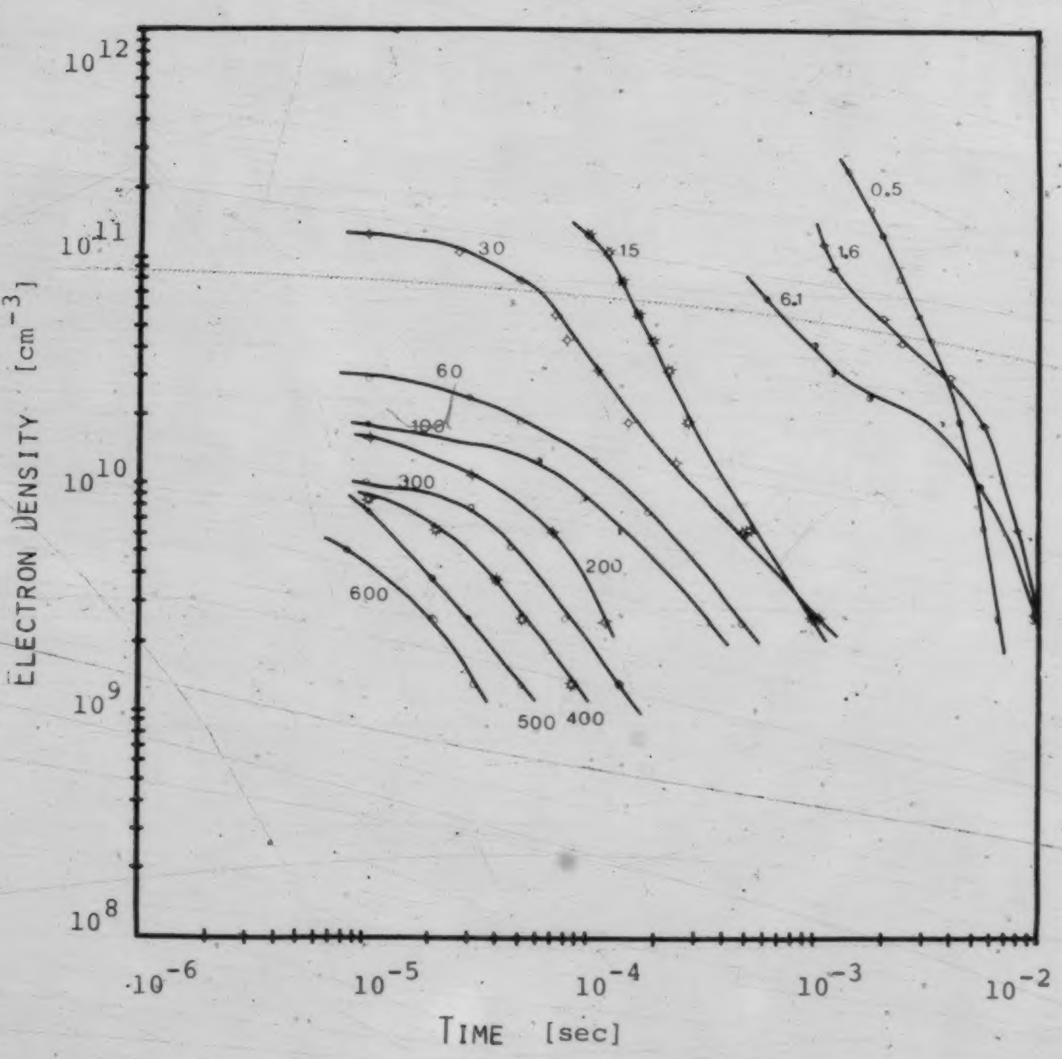

FIGURE 5-4 PLASMA DECAY IN HE The numbers represent the pressure of He in torr.

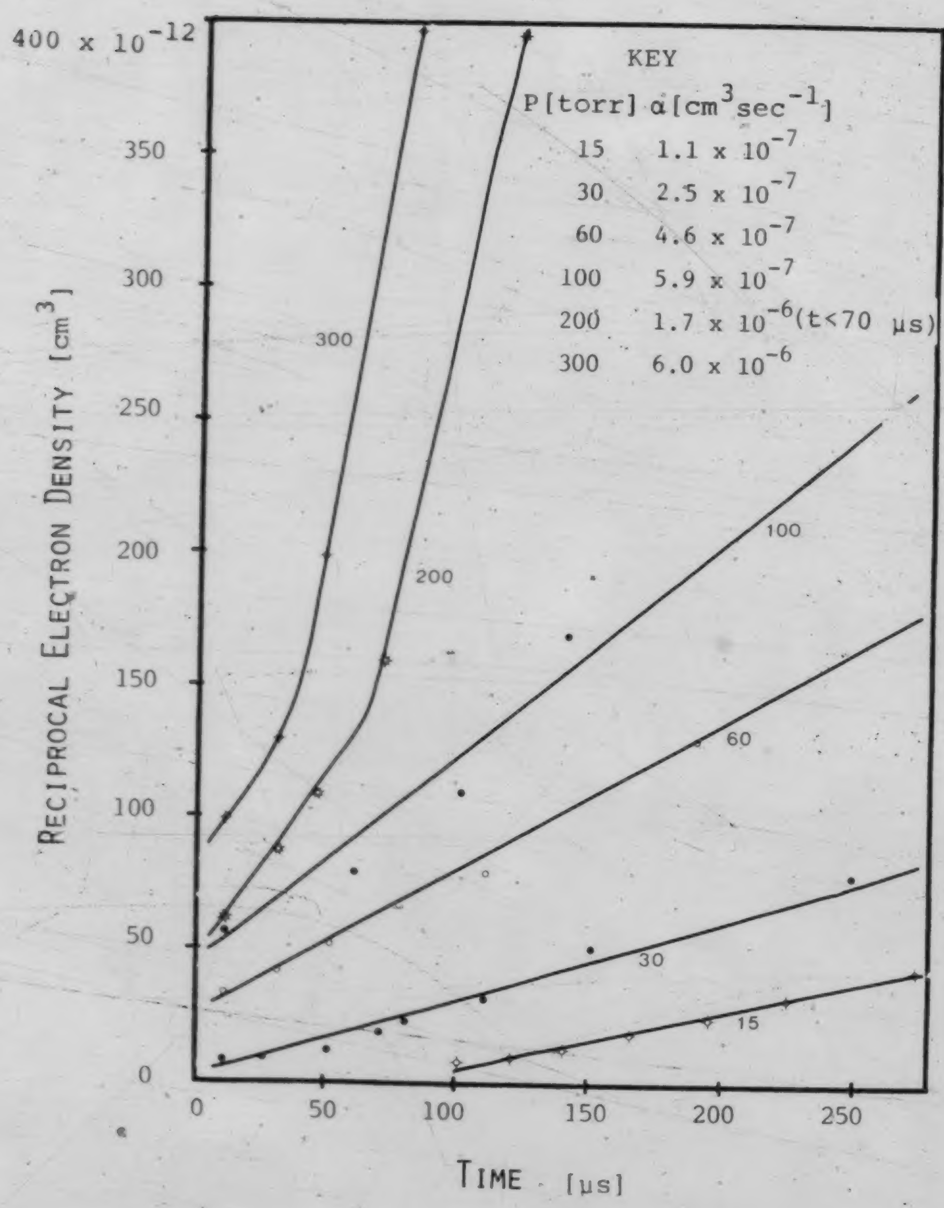

FIGURE 5-5 RECIPROCAL ELECTRON DENSITY VERSUS TIME FOR HE AT HIGH PRESSURES The number for each curve corresponds to the pressure in torr. Appropriate recombination coefficients have been assigned and appear in the key.

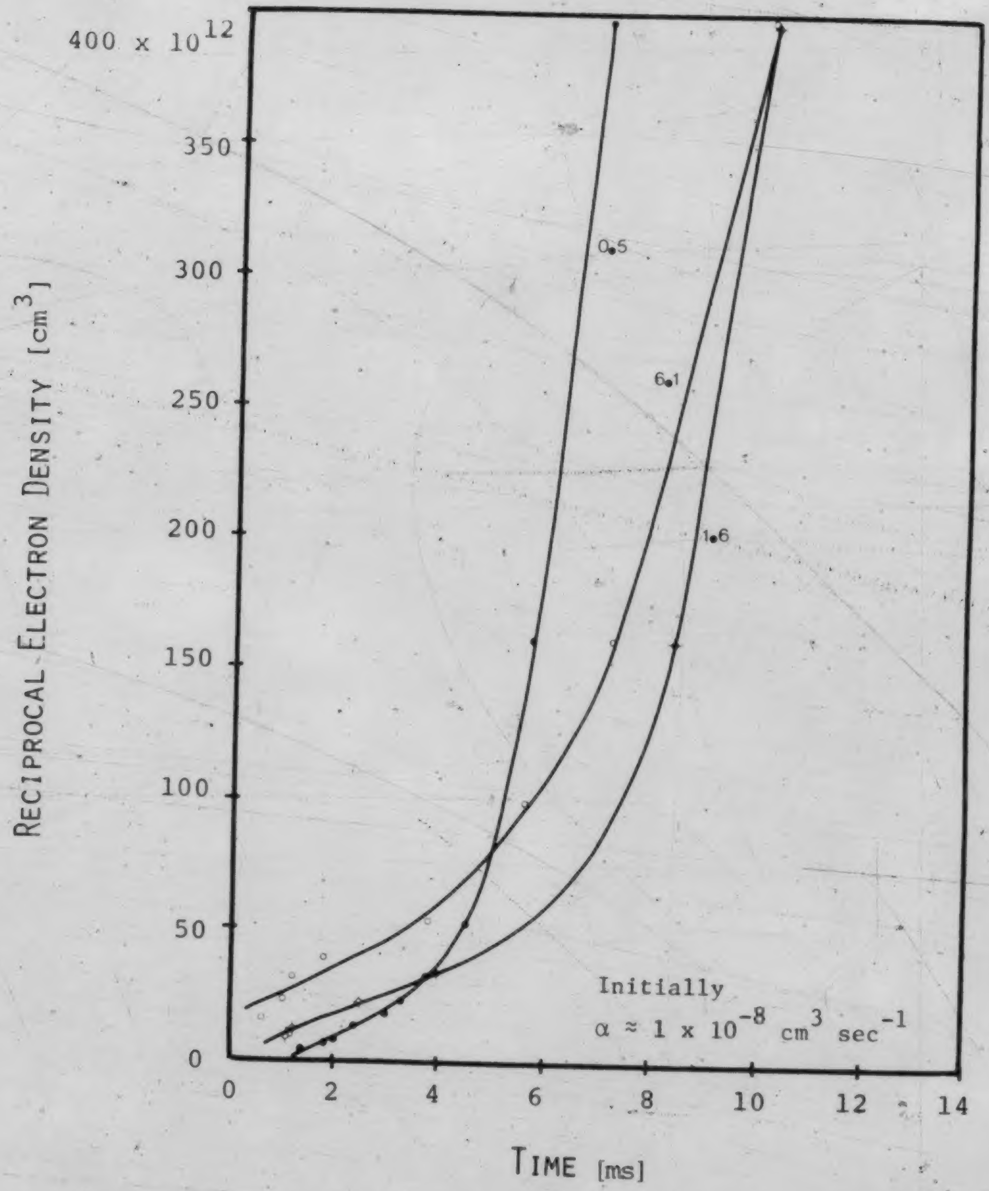

FIGURE 5-6 RECIPROCAL ELECTION DENSITY VERSUS TIME FOR HE AT LOW PRESSURES The number for each curve corresponds to the pressure in torr. A recombination coefficient has been assigned to explain the initial decay. This data is the same as that for Figure 5-7.

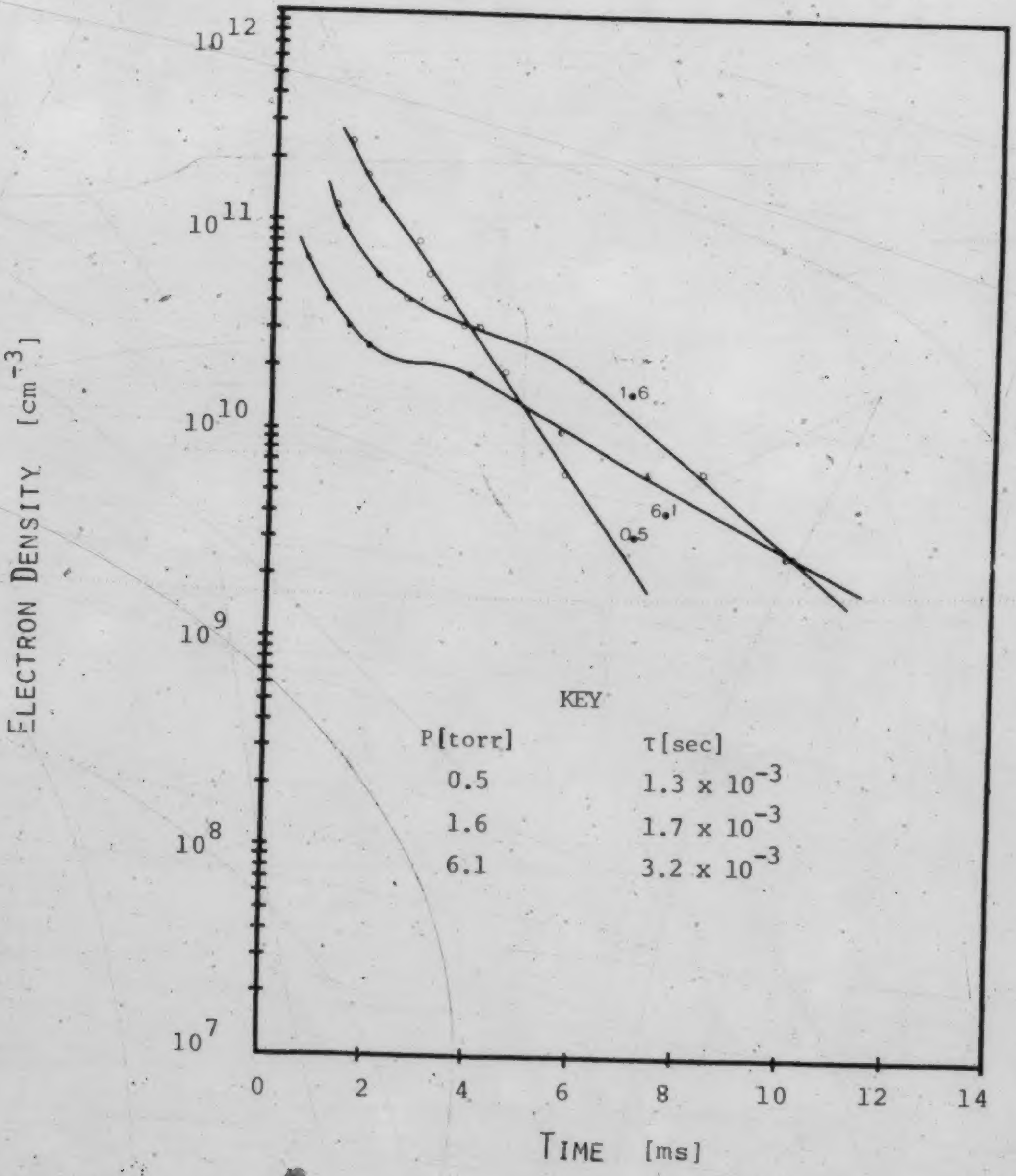

FIGURE 5-7 ELECTRON DENSITY VERSUS TIME FOR HE AT LOW PRESSURES The numbers indicate pressure in torr. Time constants for the straight line portion of the curve appear in the key. The data is the same as that for Figure 5-6.

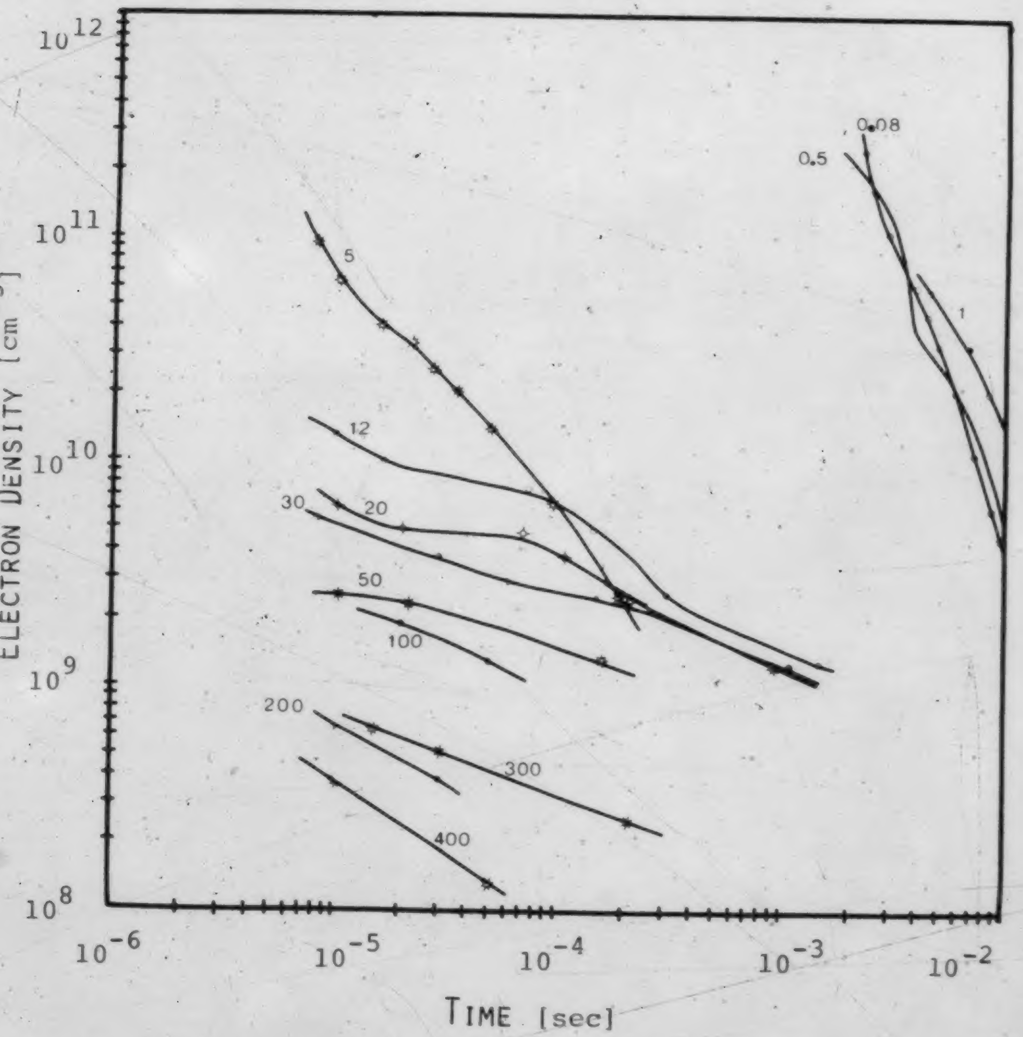

FIGURE 5-8 PLASMA DECAY IN N_2 The numbers indicate pressure in torr.

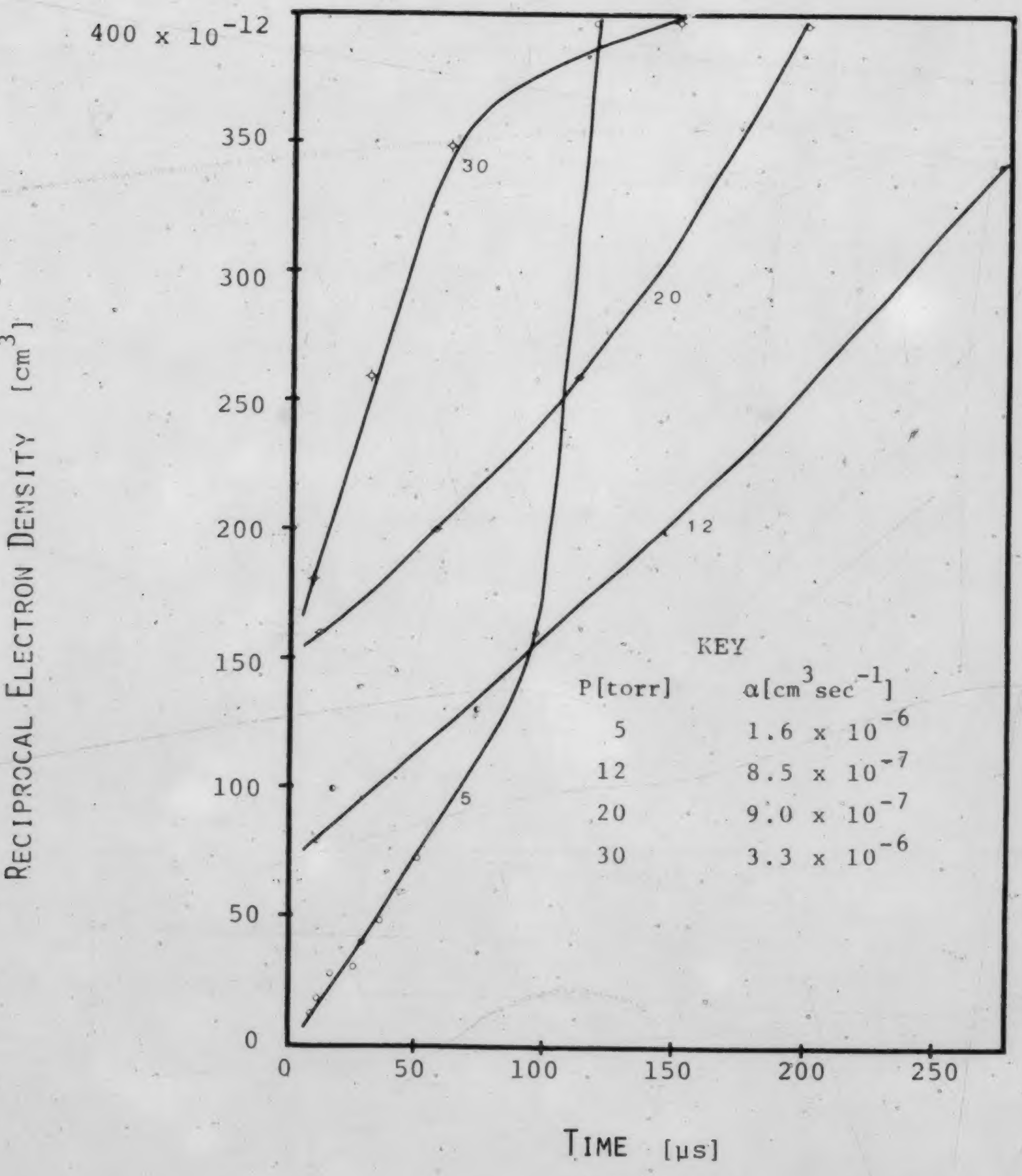

FIGURE 5-9 RECIPROCAL ELECTRON. DENSITY VERSUS TIME FOR N_2 AT HIGH PRESSURES The number for each curve corresponds to the pressure in torr. Appropriate recombination coefficients have been assigned to account for the early decay. These appear in the key.

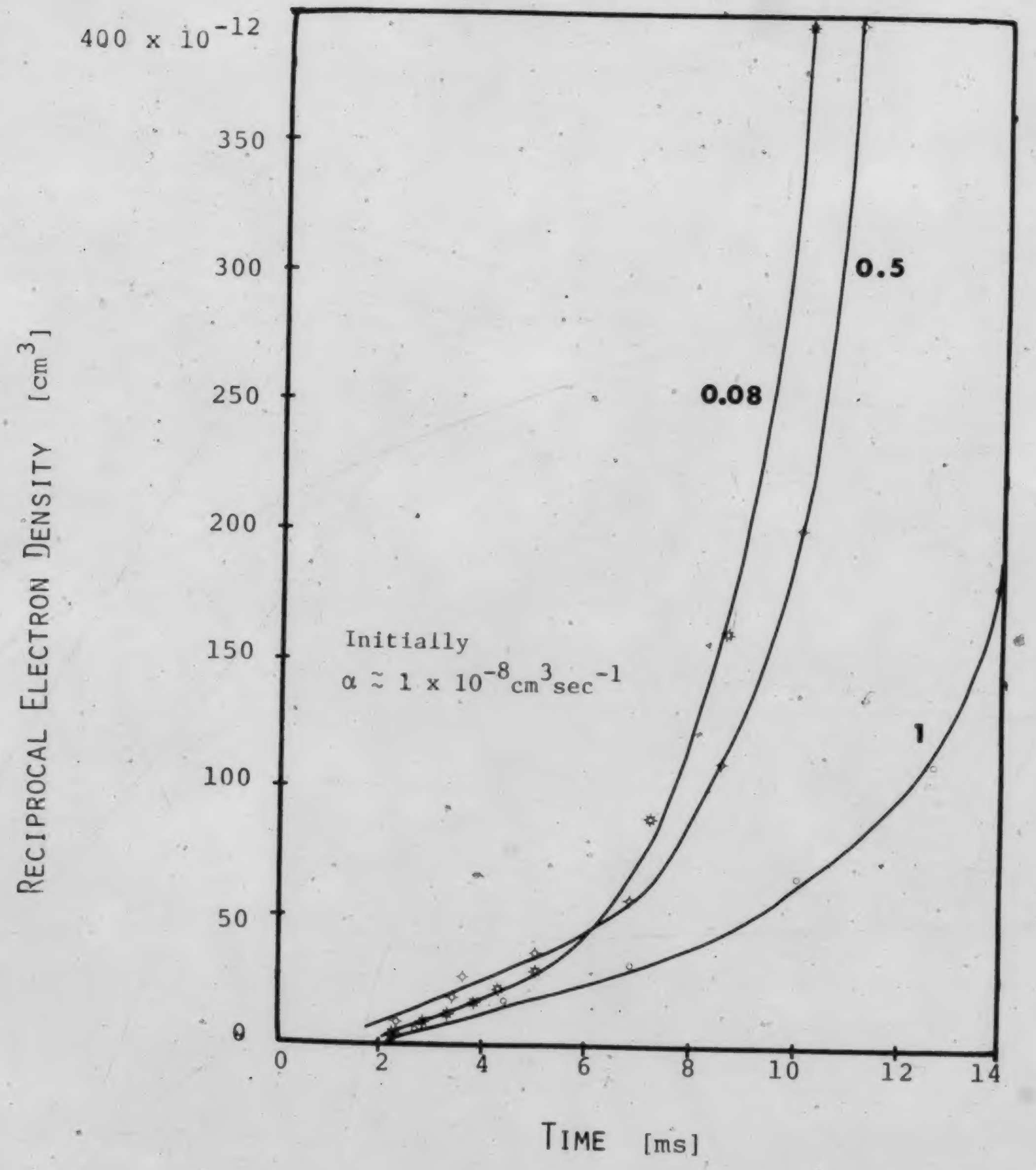

Figure 5-10 Reciprocal Electron Density Versus Time for N_2 at Low Pressures The number on each curve corresponds to the pressure in torr. A recombination coefficient has been assigned to explain the initial decay. This data is the same as that for Figure 5-11.

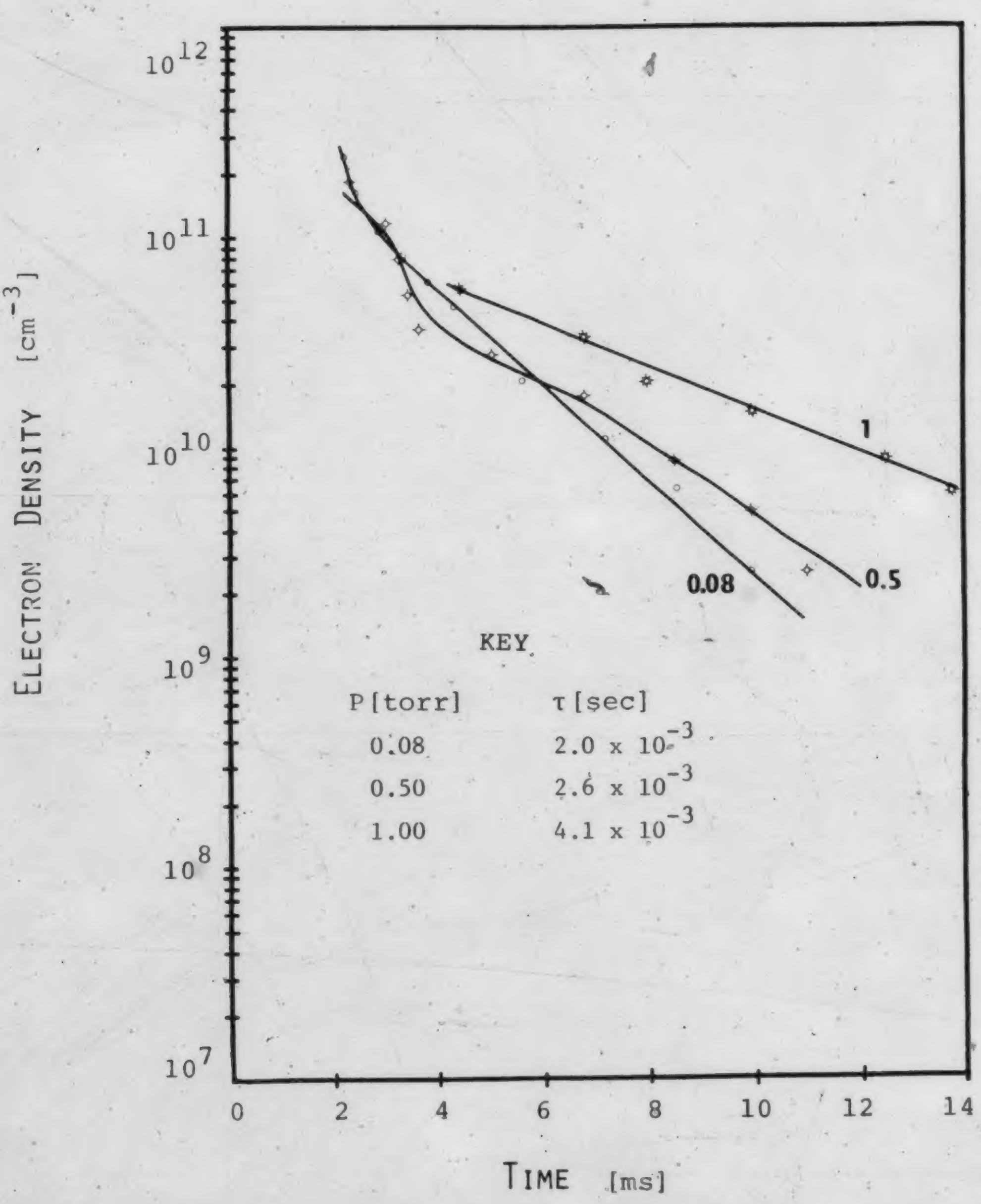

FIGURE 5-11 ELECTRON DENSITY VERSUS TIME FOR N_2 AT LOW PRESSURES The numbers on the curves indicate the pressure in torr. Time constants appropriate for the straight line portion of each curve appear in the key. The data is the same as that for Figure 5-10.

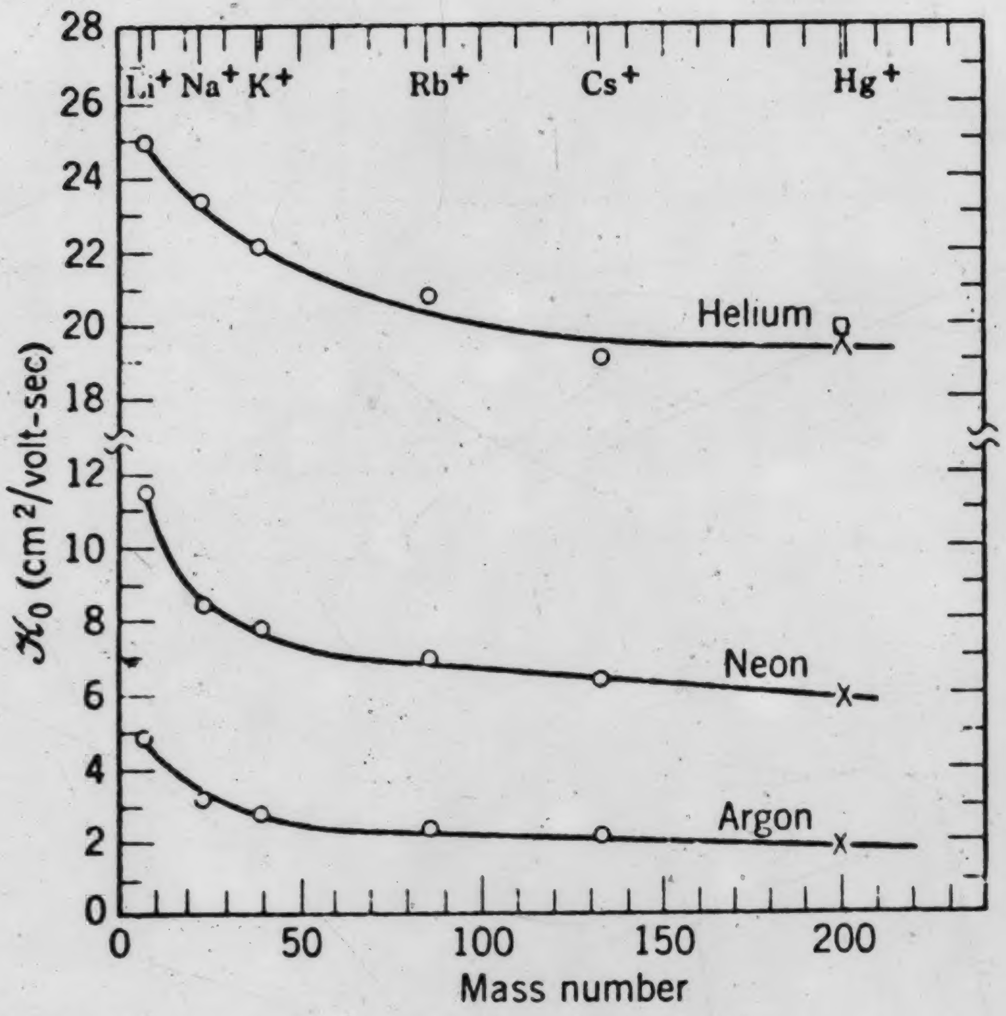

FIGURE 5-12 REDUCED MOBILITY IN HE, NE, AND AR
The reduced mobility has been plotted as a function of the mass of the positive ions. [41].

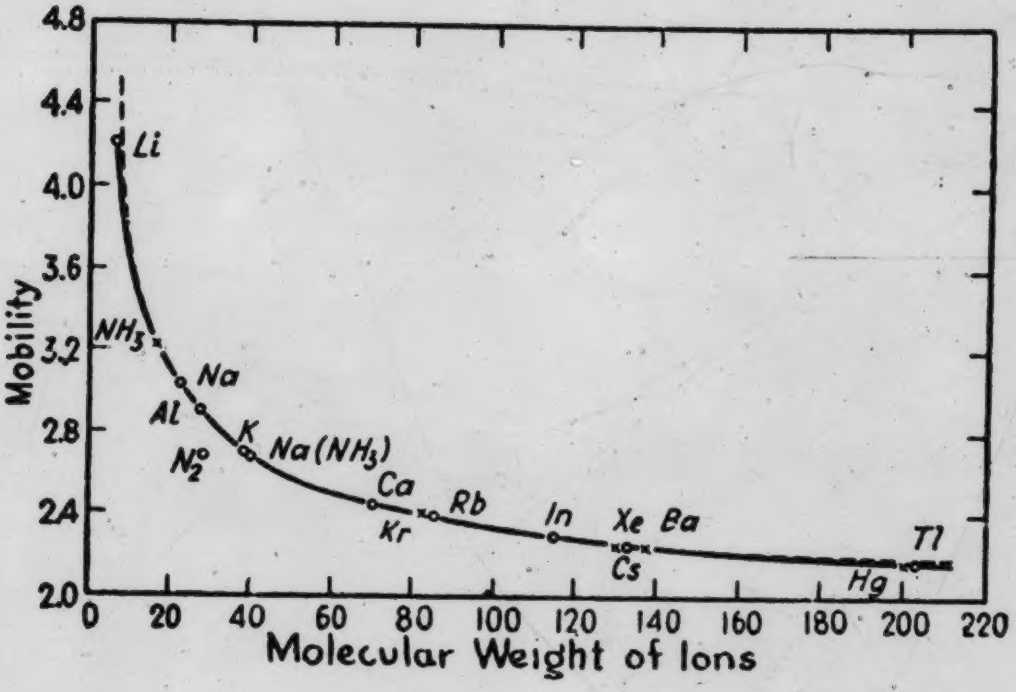

FIGURE 5-13 REDUCED MOBILITY IN N_2 The reduced mobility (K_o) has been plotted as a function of positive ion mass [52]. K_o has units cm^2 volt^{-1} sec^{-1}.

5-5-2. Carbon Dioxide and Carbon Monoxide

The plasma decay processes operating in these gases are remarkably complicated as evidenced by Figure 5-14 and Figure 5-17. It appears that all three decay processes are operating simultaneously. In addition, a growth in electron density succeeding an initial decay was observed for these gases.

A similar effect was observed in air, in O_2, and in H_2. Although no concerted effort was made to obtain detailed information about the phenomena, the following are possible explanations:

(1) An ionization shock wave excited by the source and travelling down the bore of the tube.

(2) Diffusion of high density plasma in the vicinity of the source to the test region.

(3) Collisional detachment from negative ions formed during the discharge and shortly thereafter when the electrons were sufficiently warm.

The decay data for the gases plot approximately as straight lines on a semilog graph for regions removed from increasing ionization. These appear in Figure 5-15 Figure 5-16 and Figure 5-18, and since the decay rate increases with pressure, attachment is more likely to be occurring than diffusion. (An exception is the curve for 3.8 torr of CO in Figure 5-18 where diffusion may be operating as in the cases of He and N_2.) But, it is generally accepted that CO_2 and CO can form negative ions only by a dissociative process [41,53,54,55,56]. This requires that electron energies be a few electron volts. However, in this case consistent attachment cross sections can be assigned for CO_2 and CO even though ambient temperature electrons are involved. For this analysis, Equation 5-14 must be adjusted to read:

$$\frac{dn_e}{dt} = -q_a \bar{v}_e N n_e \qquad 5\text{-}26$$

where

$$\nu_a = q_a \bar{v}_e N \qquad 5\text{-}27$$

q_a = attachment cross-section [cm^2]

$\bar{v}_e$ = 1.2×10^7 average electron velocity [$cm\ sec^{-1}$]

$N = \frac{2.7 \times 10^{19}}{760} P$ particle number density [cm^{-3}]

P = gas pressure [torr]

The solution to equation 5-27 is:

$$n_e = n_{eo} \exp(-q_a \bar{v}_e Nt) \qquad 5\text{-}28$$

n_{eo} = electron density at t = 0 assuming that the attachment process dominated at that time. [cm^{-3}]

Values of q_a can be derived from Figures 5-15, 5-16 and 5-18 by considering any two points (n_{e1}, t_1) and (n_{e2},t_2)

and the relationship:

$$q_a = \frac{\ln n_{e1}/n_{e2}}{(t_2-t_1)\bar{V}_e N} \qquad 5\text{-}29$$

The values of q_a thus obtained appear in Table 5-2.

Table 5-2 shows that an attachment cross-section of approximately 2 x 10^{-21} cm^2 to 4 x 10^{-21} cm^2 can be consistently assigned to account for the decay in CO_2. Slightly higher values at 2.3 torr and the early decay at 4.9 torr, may be due to increased electron energy expected in the early decay at low pressures.

The range of values for attachment in CO is even narrower lying between 2.2 x 10^{-21} cm^2 and 3.8 x 10^{-21} cm^2. The reaction responsible for the attachment, may be a two body reaction, with the excess energy going into an excited state of the molecule [41,54,55] to be collisionally dissipated later.

A three body process is found to yield three-body rate coefficients of the order 10^{-28} cm^6 sec^{-1} to 10^{-29} cm^6 sec^{-1} but the coefficient shows more variation with pressure than does q_a.

Table 5-2

Attachment Cross-Sections

(a)	P[torr]	$q_a[\times 10^{-21} cm^2]$	(b)	P[torr]	$q_a[\times 10^{-21} cm^2]$
	20	1.8		100	3.7
	15.5	1.9		75	3.8
	12	2.2		50	3.3
	8.1	1.8		30	2.7
	4.9	3.5 (t > 60 μs)		15	2.2
	4.9	16 (t < 60 μs)			
	2.3	8.0			
	1.2	~~4.0~~			
	0.3	4.0			

(a) CO_2, (b) CO. These are obtained from Figures 5-15, 5-16, and 5-18 for various values of pressure.

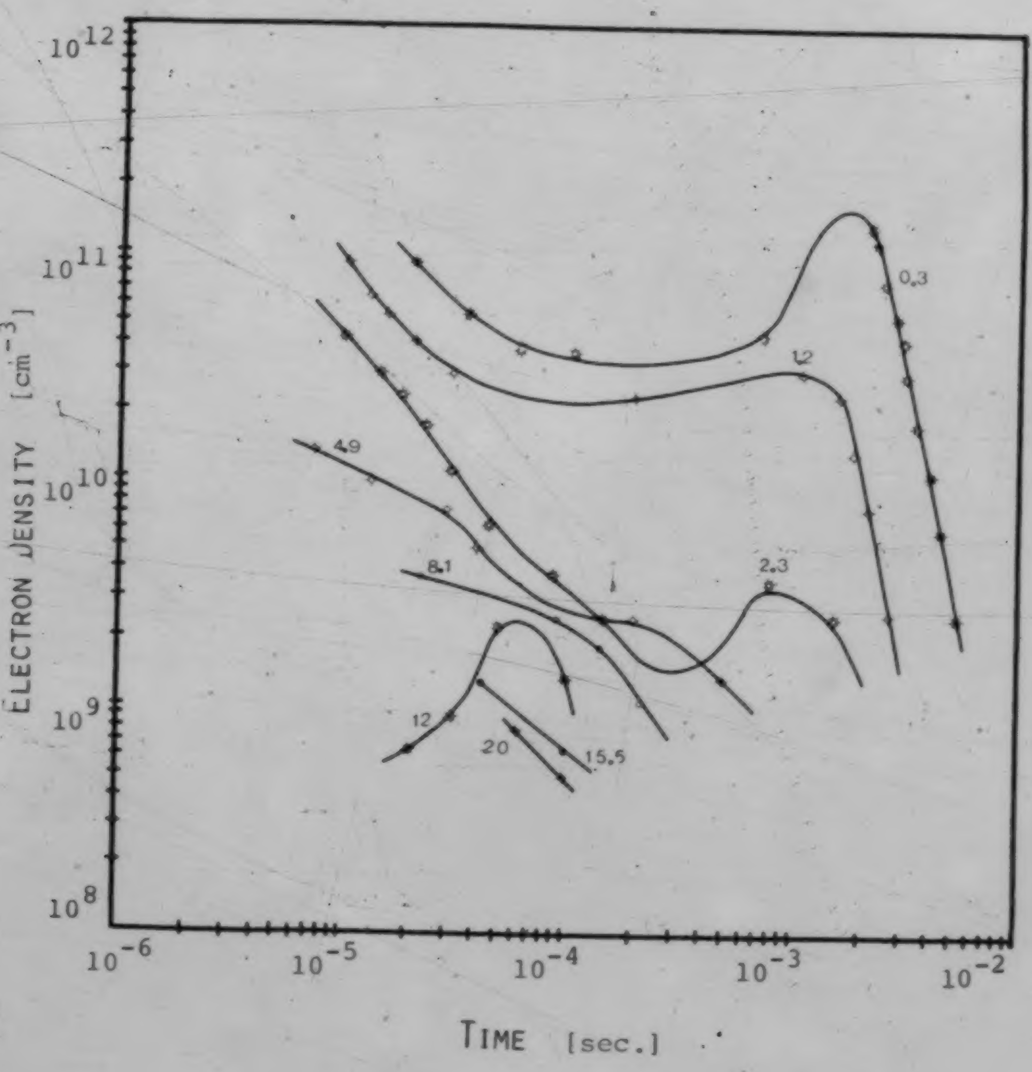

FIGURE 5-14 PLASMA DECAY IN CO_2 The numbers on the curves indicate the pressure in torr.

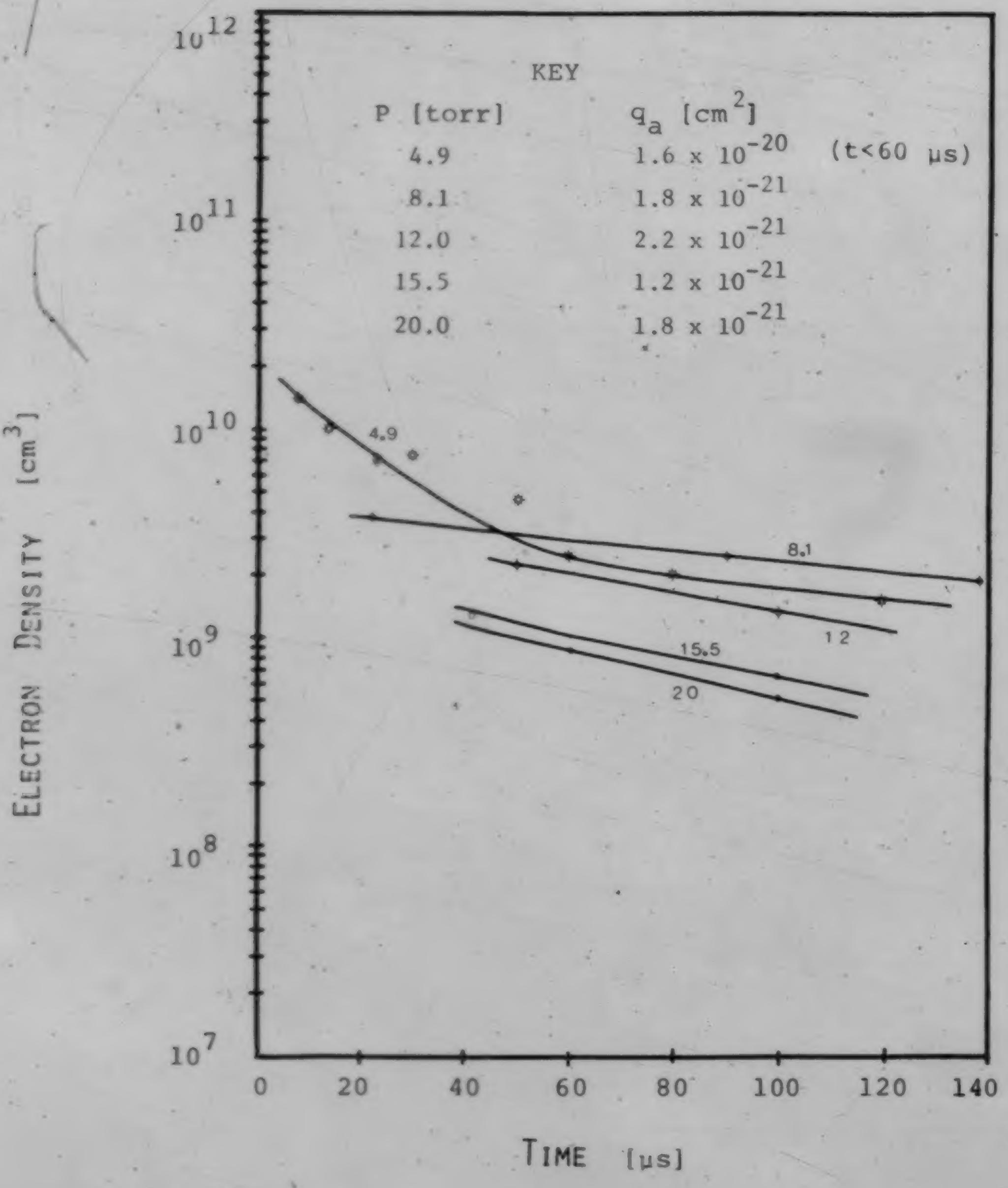

FIGURE 5-15 ELECTRON DENSITY VERSUS TIME FOR CO_2 AT HIGH PRESSURES The numbers on the curves indicate pressure in torr. Electron attachment cross-sections, appropriate for the straight line portion of each curve, appear in the key.

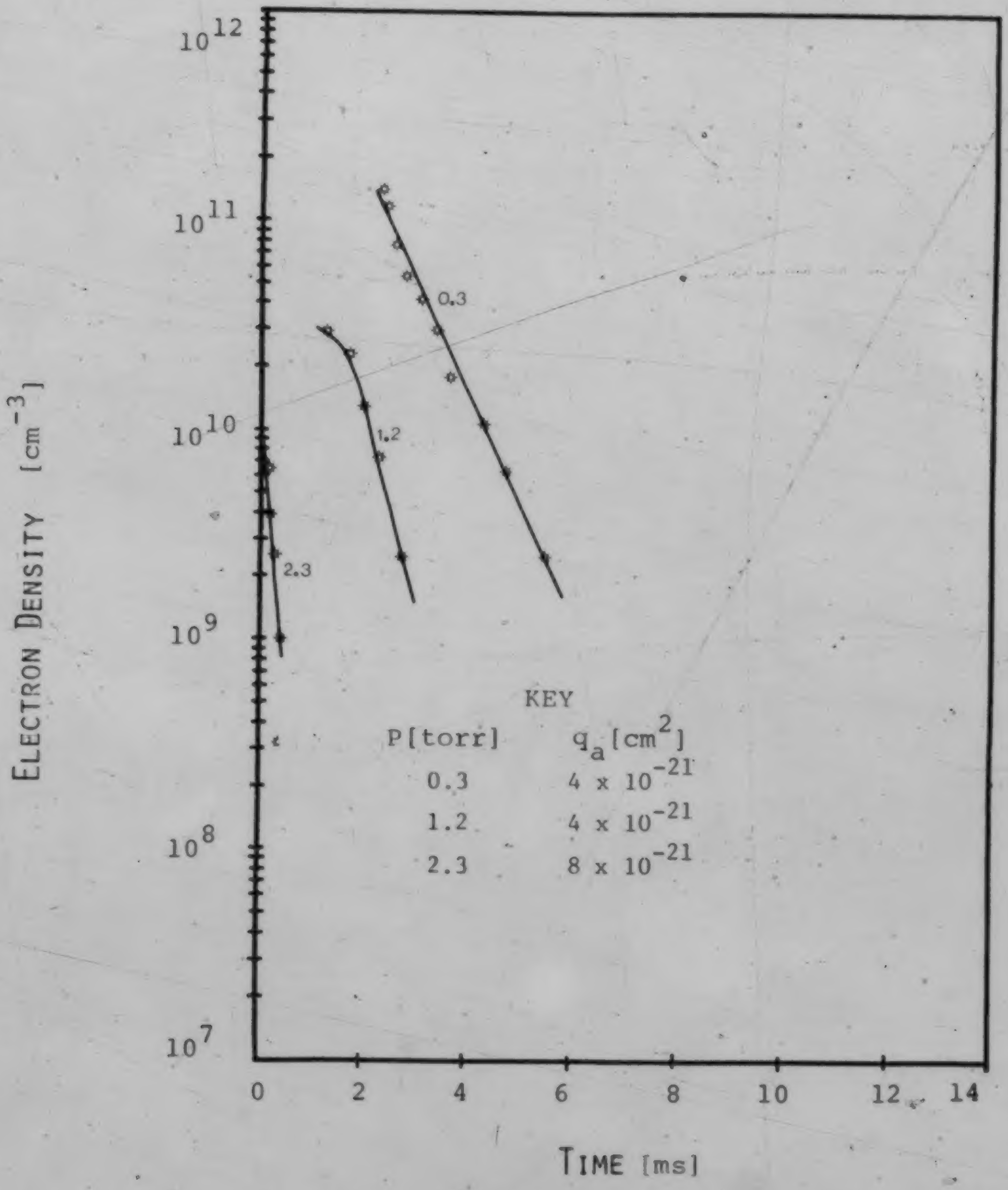

FIGURE 5-16 ELECTRON DENSITY VERSUS TIME FOR CO_2 AT LOW PRESSURES The numbers on the curves indicate the pressure in torr. Electron attachment cross-sections, appropriate for the straight line portion of each curve, appear in the key.

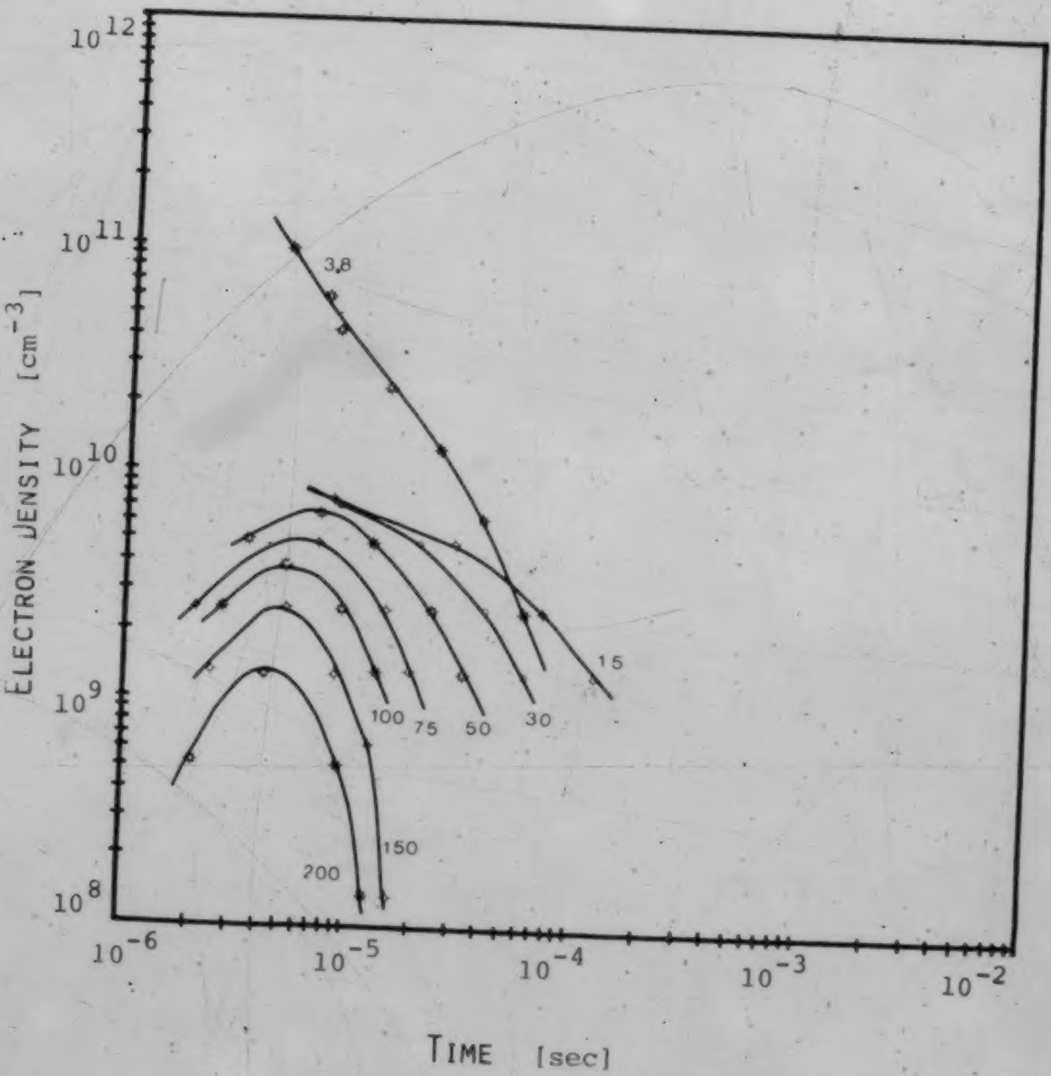

FIGURE 5-17 PLASMA DECAY IN CO The numbers on the curves indicate the pressure in torr.

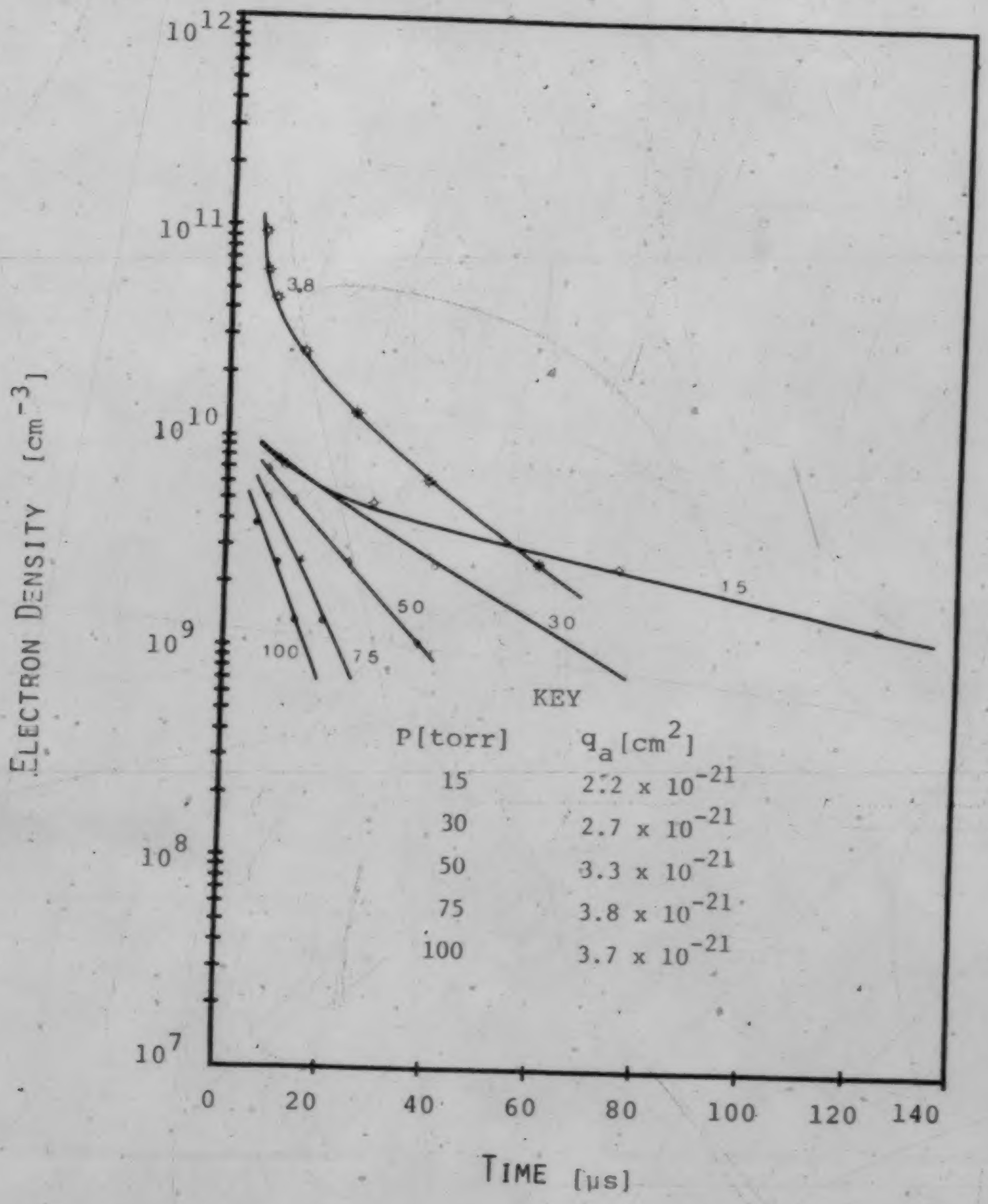

FIGURE 5-18 ELECTRON DENSITY VERSUS TIME FOR CO The numbers on the curves indicate the pressure in torr. Electron attachment cross-sections, appropriate for the straight line portion of each curve, appear in the key.

5-5-3. Gas Mixtures

Electron decay data for gas mixtures appear in Figures 5-19 through 5-24. The later decay appears to behave in a manner similar to that observed in CO_2.

Values of the two body attachment cross-section to CO_2 can be determined from the straight line characteristics in Figures 5-20 and 5-23. Equation 5-29 can be employed where N is the density of the CO_2 molecules. The resulting cross-sections appear in Table 5-3. Comparison of these with the values obtained for pure CO_2 in Table 5-2 (a), indicate that the attachment process is more effective in the laser mixture by about one order of magnitude. This indicates that the N_2 and He must play a role in the attachment.

He and N_2 can be incorporated into the attachment mechanism proposed in section 5-5-2 for CO_2 and CO It is reasonable to expect that He and/or N_2 may be more effective than CO_2 in relaxing the excited molecular state of the negative ion [47]. Otherwise, if the molecular ion were unstable, it may revert to a stable state by ejecting the electron before suffering a stabilizing collision. If this proposal is to be correct, one would expect a larger cross-section where the proportion of He and N_2 to CO_2 is the highest. In fact, a calculation of the average value for the cross-section shows that it is about 50% higher in the 90% He-N_2 mixture than in the 80% He-N_2 mixture.

Plots of reciprocal density against time for the

Table 5-3

Experimental CO_2 Attachment Cross Sections for Two Laser Mixtures

(a)

P[torr]	P_{CO_2}[torr]	q_a[cm^2]
7.4	0.74	1.5×10^{-20}
16	1.6	1.7
19	1.9	1.0
32	3.2	1.3

$$\bar{q}_a = 1.4 \times 10^{-20} \text{ cm}^2$$

(b)

P[torr]	P_{CO_2}[torr]	q_a[cm^2]
7.1	1.4	0.62×10^{-20}
13	2.6	1.2
19	3.8	0.88

$$\bar{q}_a = 0.94 \times 10^{-20} \text{ cm}^2$$

(a) $CO_2 : N_2 : He = 1 : 1 : 8$

(b) $CO_2 : N_2 : He = 1 : 1 : 3$

P denotes the total gas pressure and P_{CO_2} denotes the partial pressure of CO_2

early decay in Figures 5-21 and 5-24 do not result in good linearity. However, approximate recombination coefficients can be assigned as indicated. These compare to those obtained for He and N_2.

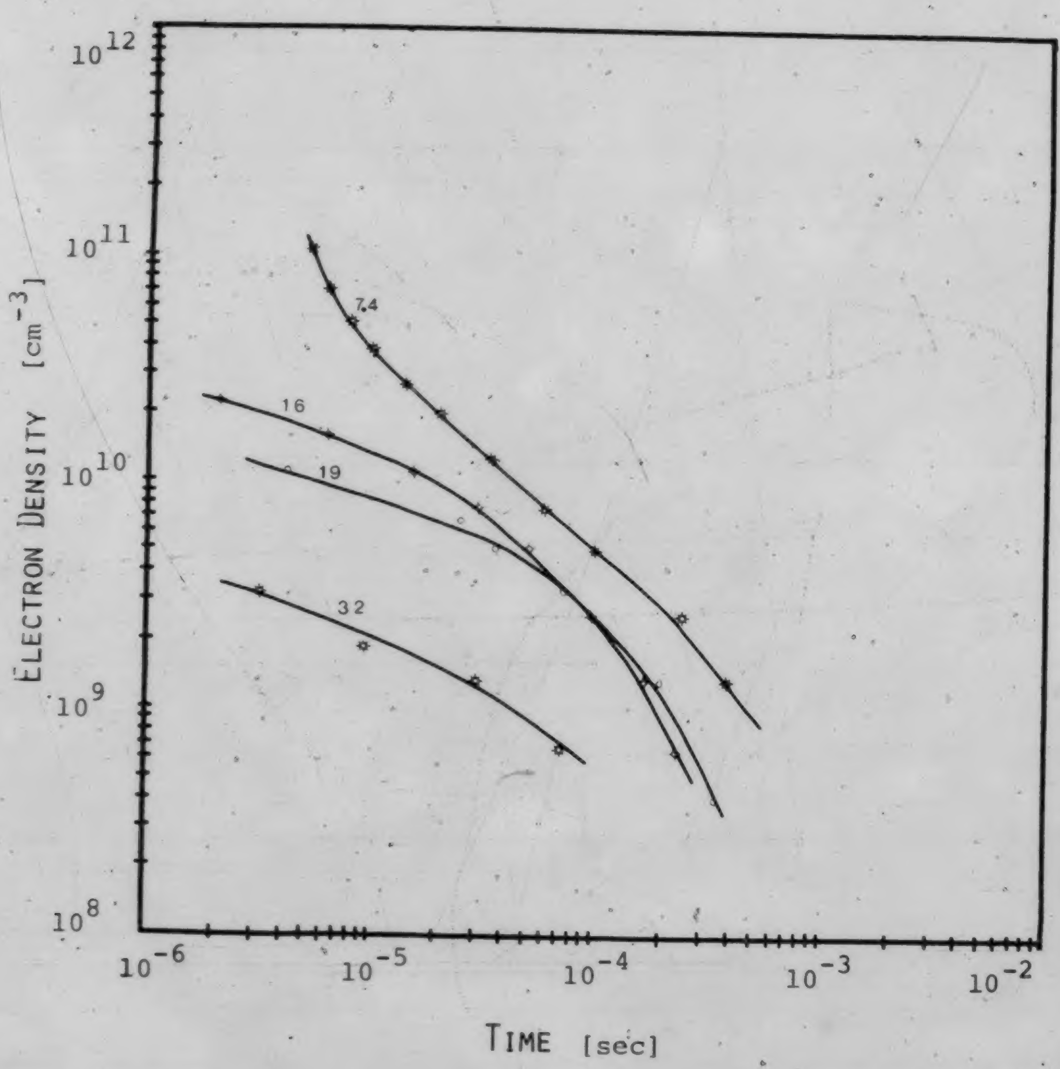

FIGURE 5-19 PLASMA DECAY IN A $CO_2:N_2:He = 1:1:8$ LASER MIXTURE The numbers on the curves indicate the total pressure in torr.

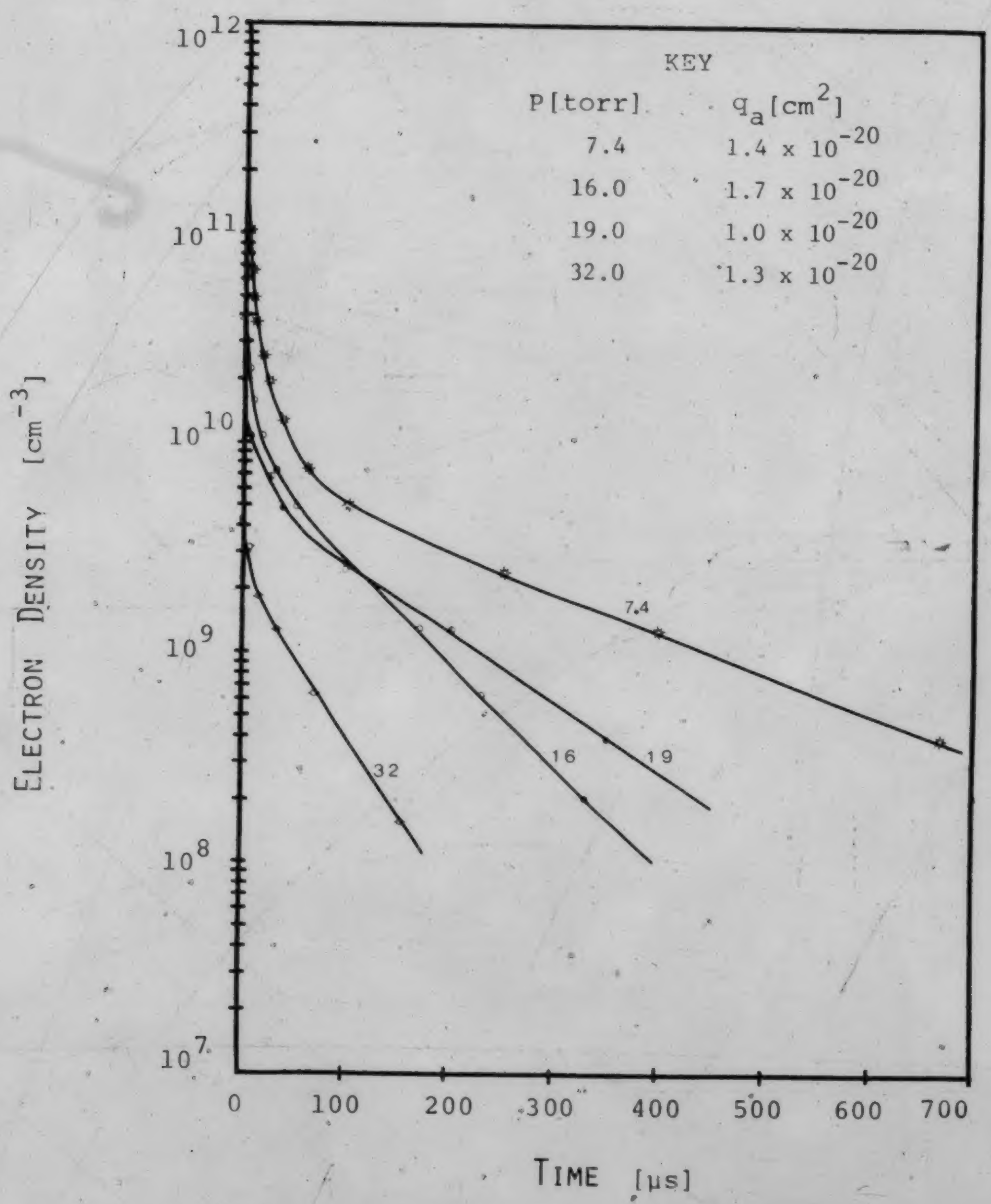

FIGURE 5-20 ELECTRON DENSITY VERSUS TIME FOR A $CO_2 : N_2 : He = 1:1:8$ LASER MIXTURE The numbers on the curves indicate the total pressure in torr. Electron attachment cross-sections, appropriate for the straight line portion of each curve, appear in the key. The data is the same as for Figure 5-21.

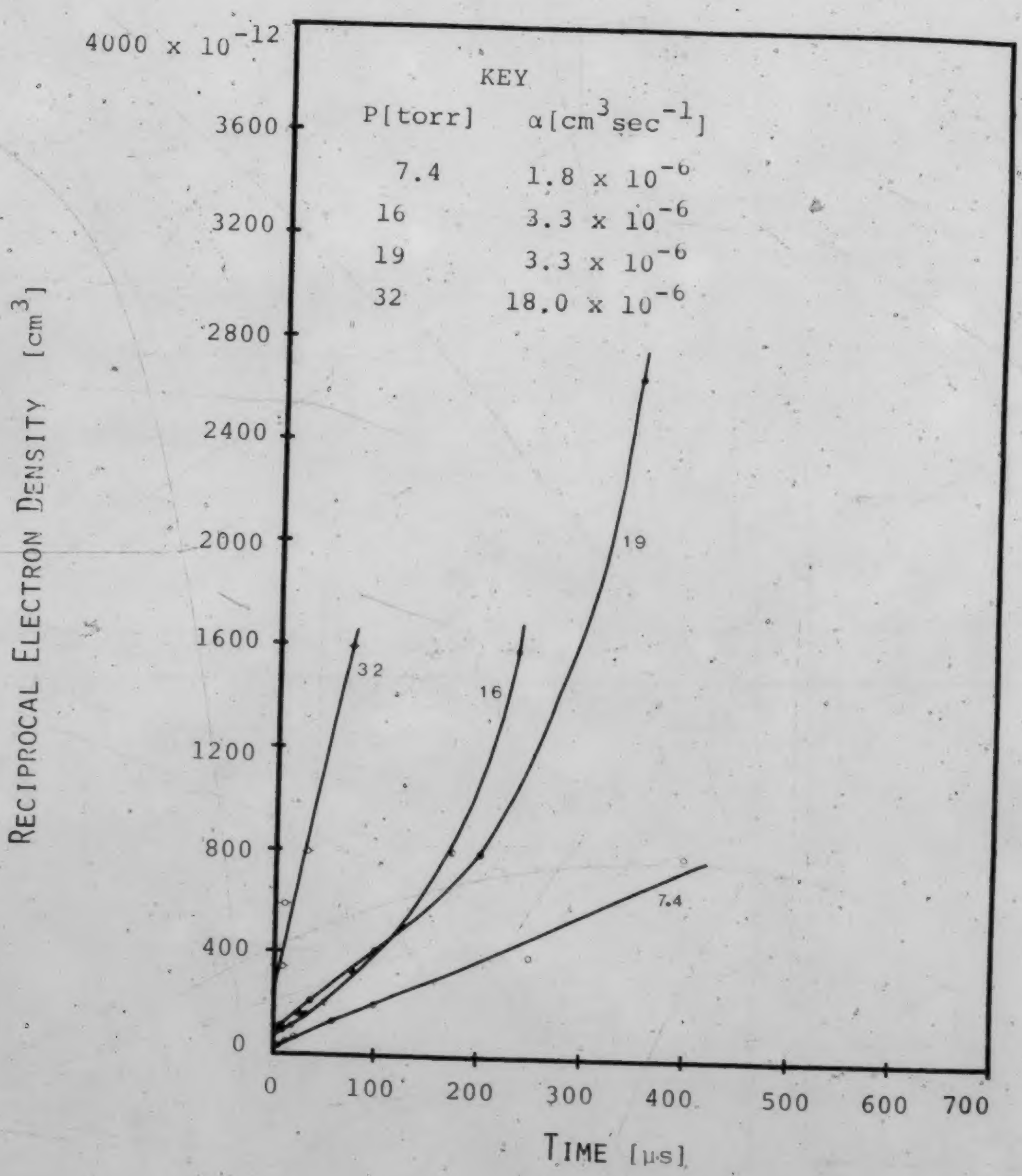

FIGURE 5-21 RECIPROCAL ELECTRON DENSITY VERSUS TIME FOR A $CO_2:N_2:He$ = 1:1:8 LASER MIXTURE The numbers on the curves indicate the total pressure in torr. Recombination coefficients have been assigned to account for the initial decay. These appear in the key. The data is the same as for Figure 5-20.

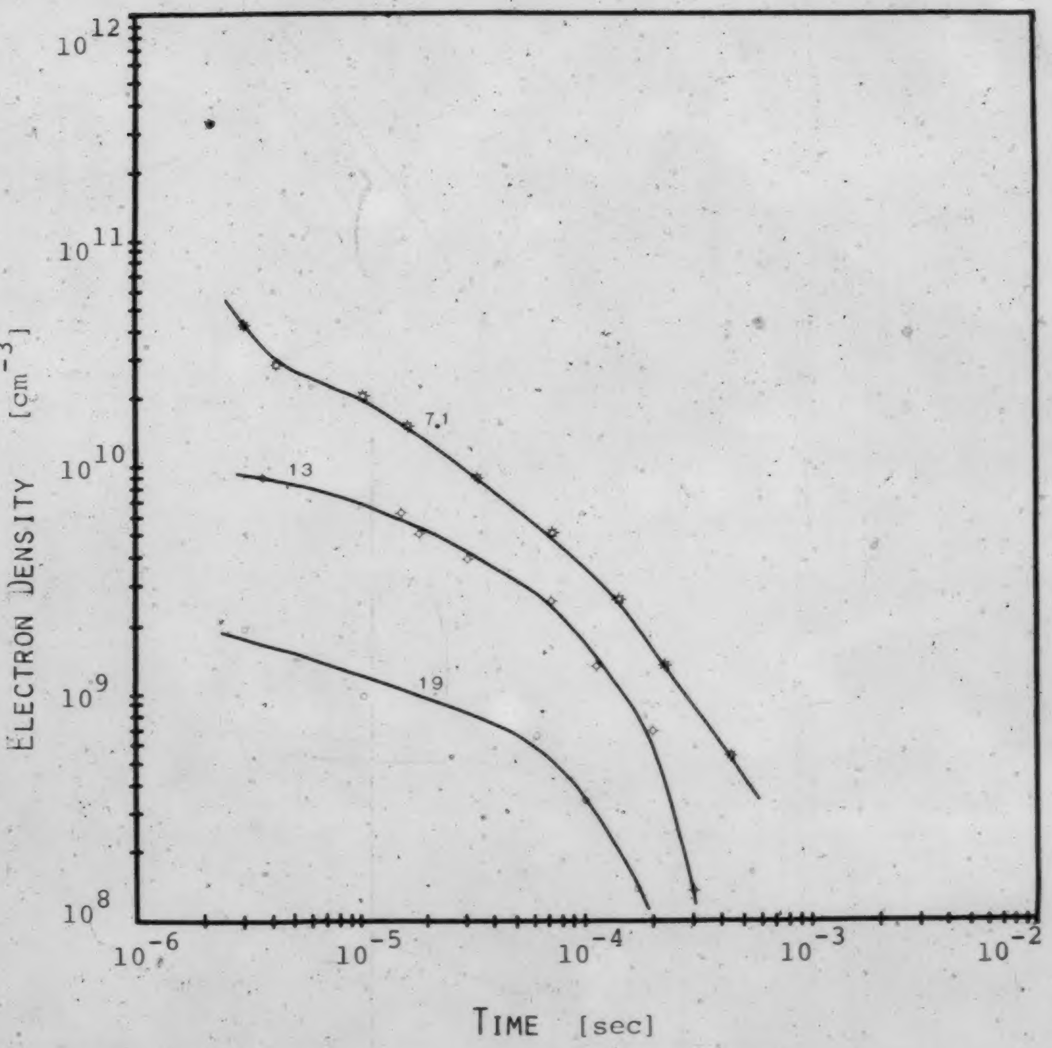

FIGURE 5-22 PLASMA DECAY IN A $CO_2:N_2:He = 1:1:3$ LASER MIXTURE The numbers on the curves indicate total pressure in torr.

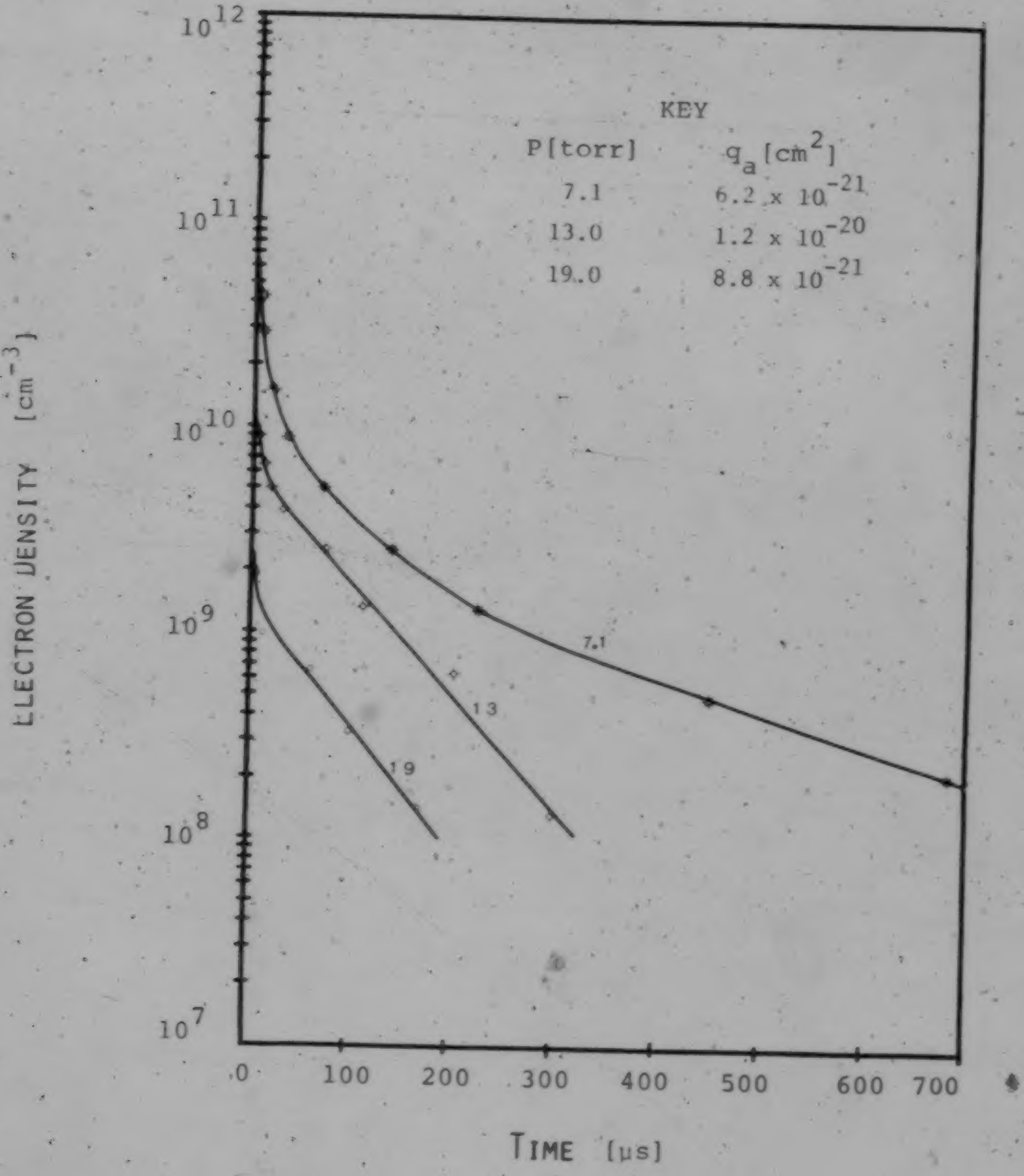

FIGURE 5-23 ELECTRON DENSITY VERSUS TIME FOR A CO :N :H
$CO_2:N_2:He$ = 1:1:3 LASER MIXTURE The numbers on the curves indicate the total pressure in torr. Electron attachment cross-sections, appropriate for the straight line segment of each curve, appear in the key. The data is the same as for Figure 5-24.

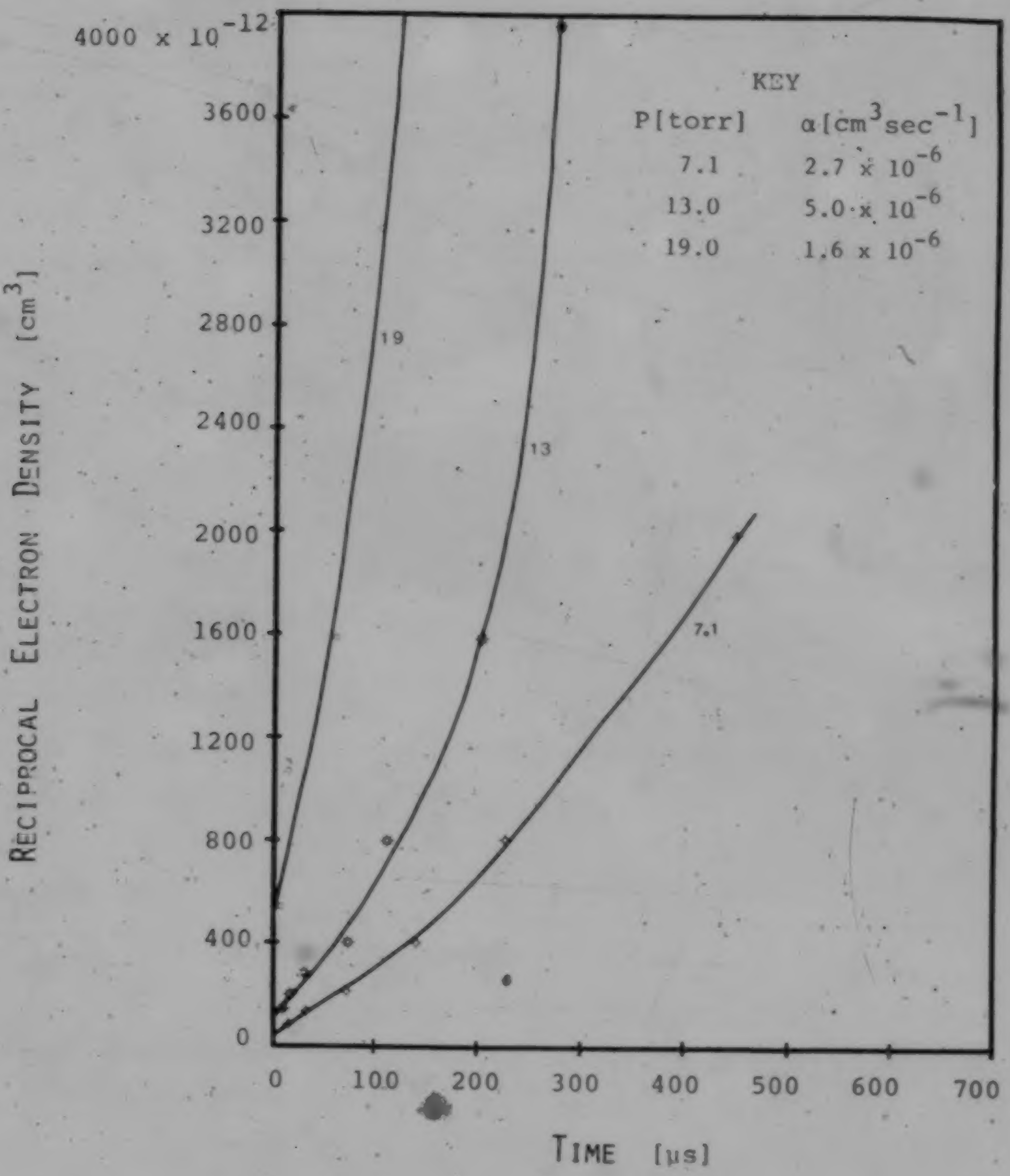

FIGURE 5-24 RECIPROCAL ELECTRON DENSITY VERSUS TIME FOR A $CO_2:N_2:He$ = 1:1:3 LASER MIXTURE The numbers on the curves indicate the total pressure in torr. Recombination coefficients have been assigned to account for the initial decay. These appear in the key. The data is the same as for Figure 5-23.

5-5-4. Oxygen and Air

Decay characteristics are shown in Figures 5-25 through 5-28. Oxygen is more electronegative than any of the gases considered thus far. At low electron energies it can form a negative molecular ion by a three body process while at higher electron energies it forms a negative atomic ion by a dissociative process [41].

The straight line features of Figure 5-26 and Figure 5-28 support this. Also, the decay rate increase with pressure supports an attachment, rather than diffusion controlled process.

Equation 5-14 must be altered to include both the two and the three body processes.

$$\frac{dn_e}{dt} = -\beta N(O_2)n_e - K_a N(O_2)N(th)n_e \qquad 5\text{-}29$$

β = the two body rate coefficient [$cm^3 sec^{-1}$]
K_a = the three body rate coefficient [$cm^6 sec^{-1}$]
$N(O_2)$ = O_2 number density [cm^{-3}]
$N(th)$ = third body number density [cm^{-3}]

The rate coefficients are given in Figure 5-29 and Figure 5-30 for a two body process and a three body process respectively [41].

The solution to Equation 5-29 is:

$$n_e = n_{eo} \exp[-\beta - K_a N(th)]N(O_2)t \qquad 5\text{-}30$$

n_{eo} = electron density at the intersection of t = 0 and the projection of the attachment curve [cm^{-3}]

For any two sets of points (n_{e1},t_1) and (n_{e2},t_2) one can determine $\beta + K_a N(th)$ by the following relationship:

$$\beta + K_a N(th) = \frac{\ln(n_{e1}/n_{e2})}{(t_2 - t_1) N(O_2)} \qquad 5\text{-}31$$

Without a knowledge of the electron energy one cannot obtain β and K_a independently. However, assuming that the other were zero, determination of each coefficient reveals information about the electron decay.

In the case of air, the third body particles are considered to be O_2 rather than N_2. O_2 is more than an order of magnitude more effective than is N_2, and so the contribution due to the N_2 component is negligible.

The coefficients of interest appear in Table 5-4. The curve for 3 torr of O_2 in Figure 5-26 has been approximated by three straight line segments. Comparison of the values in Table 5-4 with those values of β and K_a in Figure 5-29 and Figure 5-30 respectively, reveals the following:

(1) Oxygen at 3 torr, progresses from two body attachment in the early decay for warm electrons, to three body attachment in the later decay beyond 60 μs, indicating that the electrons have reached ambient temperatures by this time.

Table 5-4

Experimental Values of the Two Body (β) and Three-body (K_a) Rate Coefficients for Attachment to Oxygen

(a)

P[torr]	β[cm^{3}sec^{-1}]$K_a = 0$	K_a[cm^{6}sec^{-1}]$\beta = 0$	T_e[°K]
3[10 μs→20 μs]	13×10^{-13}	12×10^{-30}	warm
3[20 μs→60 μs]	7.0	6.5	
3[60 μs→]	2.7	2.5	
3[60 μs]	2.7	2.5	
9	6.0	1.9	
13	6.0	1.3	ambient

(b)

P[torr]	β[cm^{3}sec^{-1}]$K_a = 0$	K_a[cm^{6}sec^{-1}]$\beta = 0$	T_e[°K]
0.7	150×10^{-13}	310×10^{-30}	warm
4.2	17	57	
11	7.9	10	
20	8.7	6.1	
30	7.1	3.3	
48	9.6	2.8	ambient

... Table continued

Table 5-4 continued

(a) O_2

(b) air

T_e gives an indication of the electron temperature.

(2) At 9 torr and 13 torr of O_2, the electrons have cooled to ambient temperature, before any measurements were taken as indicated by the value of the three body attachment coefficient.

(3) In the case of air, the attachment progresses from two body attachment for the lower pressures where the electronsmay be warm, to three body attachment for the higher pressure cases, where the electron will have reached ambient temperature, before the measurement was performed.

O_2 and air exhibited an increase in electron density after an initial decay,similar to CO_2 and CO. The effect was very large in 0.7 torr of air, but was barely noticable in O_2 at the same pressure. It diminished with pressure and became too small to measure accurately. However, it remained visible on the CRT trace for even higher pressures. An example appears in Figure 5-31.This effect was also observed in H_2.

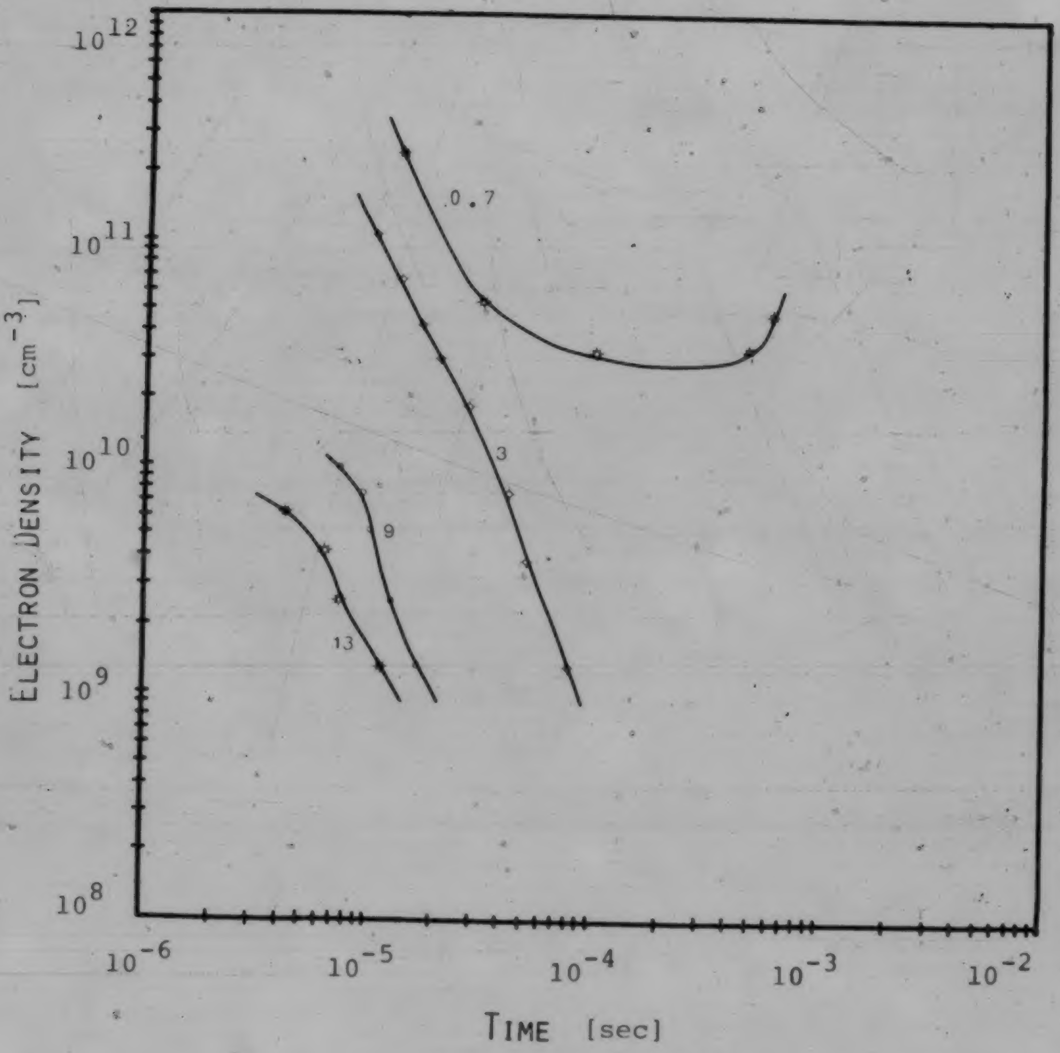

FIGURE 5-25 PLASMA DECAY IN O_2 The numbers on the curves indicate the pressure.

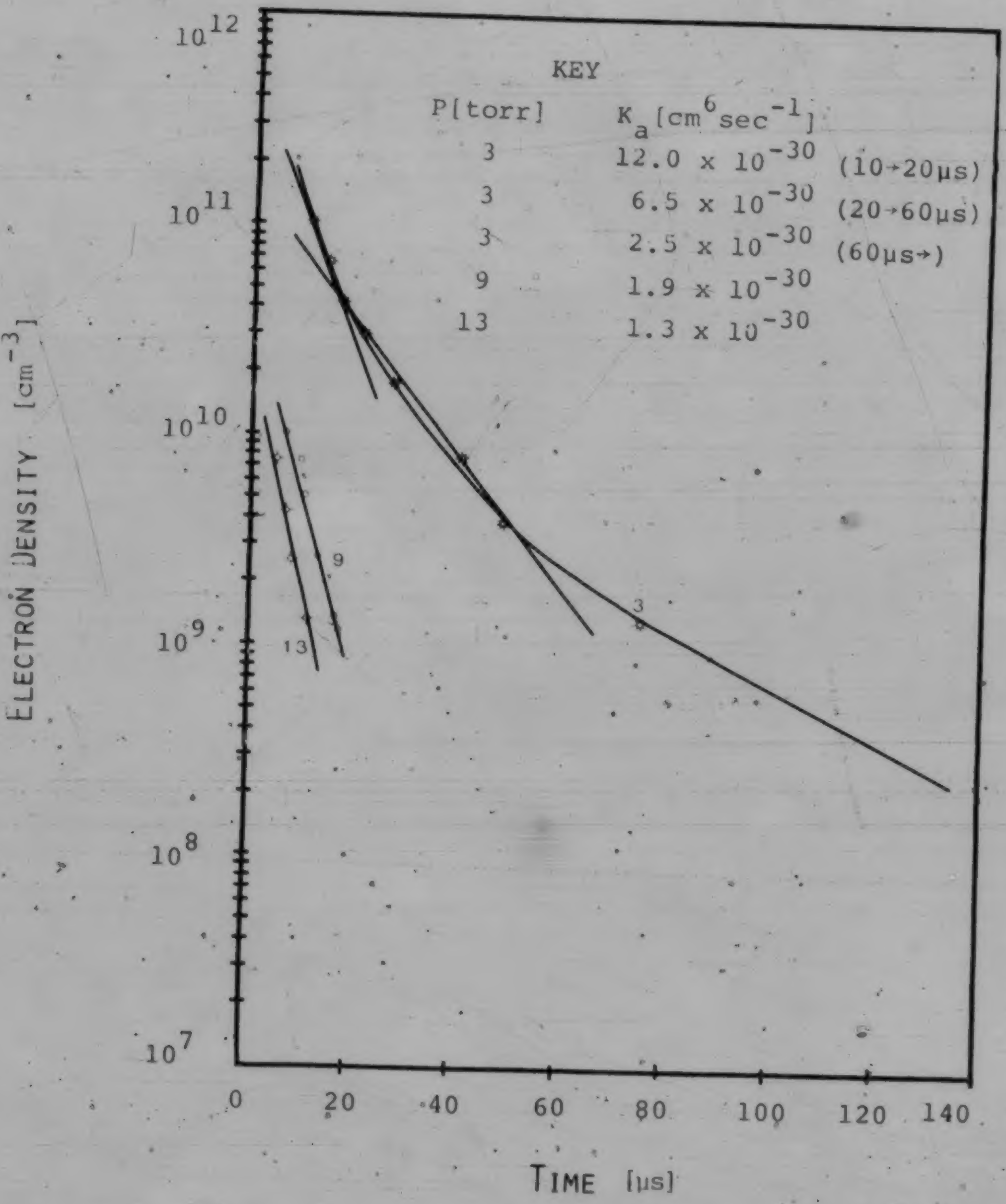

FIGURE 5-26 ELECTRON DENSITY VERSUS TIME FOR O_2 The numbers on the curves indicate the pressure in torr. Three-body attachment rate coefficients appear in the key.

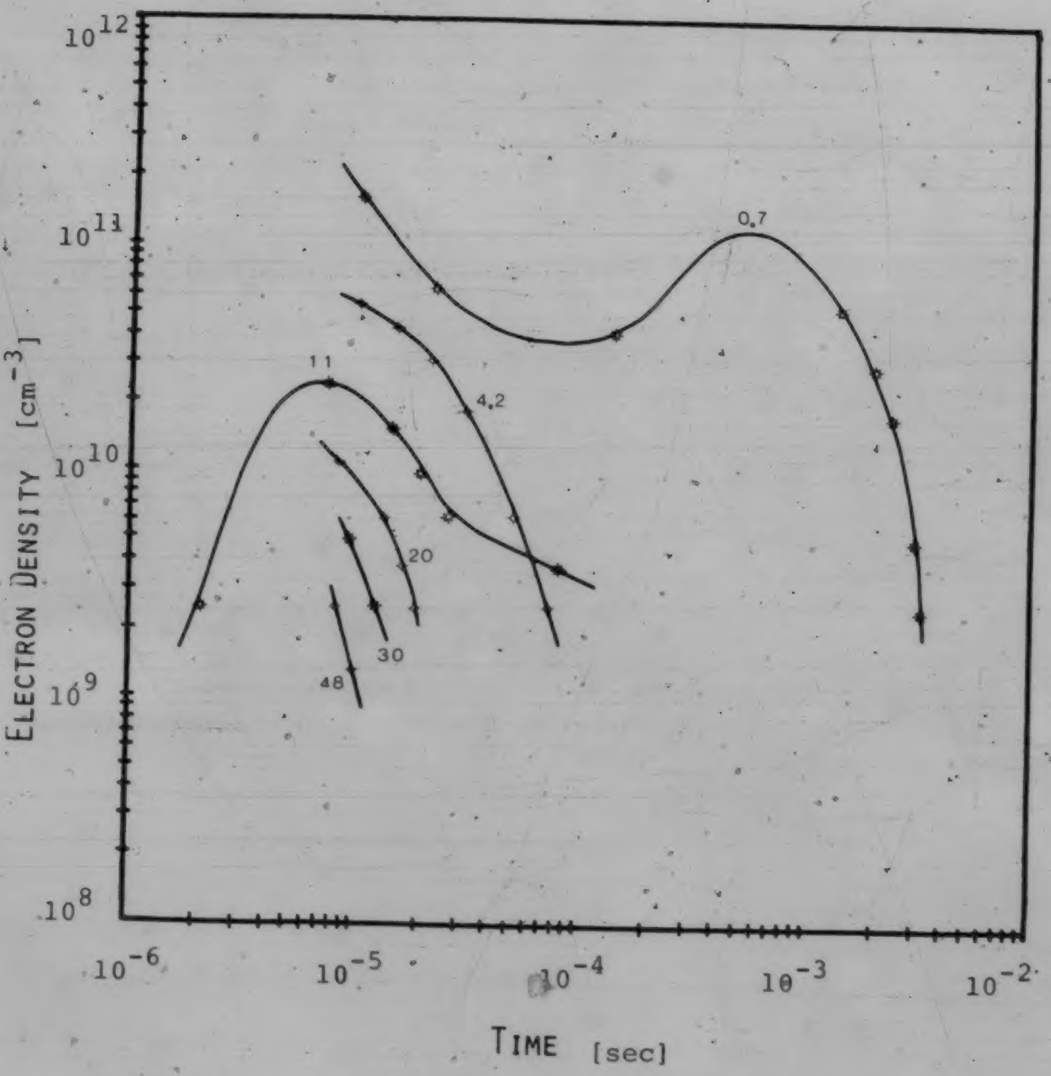

FIGURE 5-27 PLASMA DECAY IN AIR . The numbers on the curves indicate the pressure in torr.

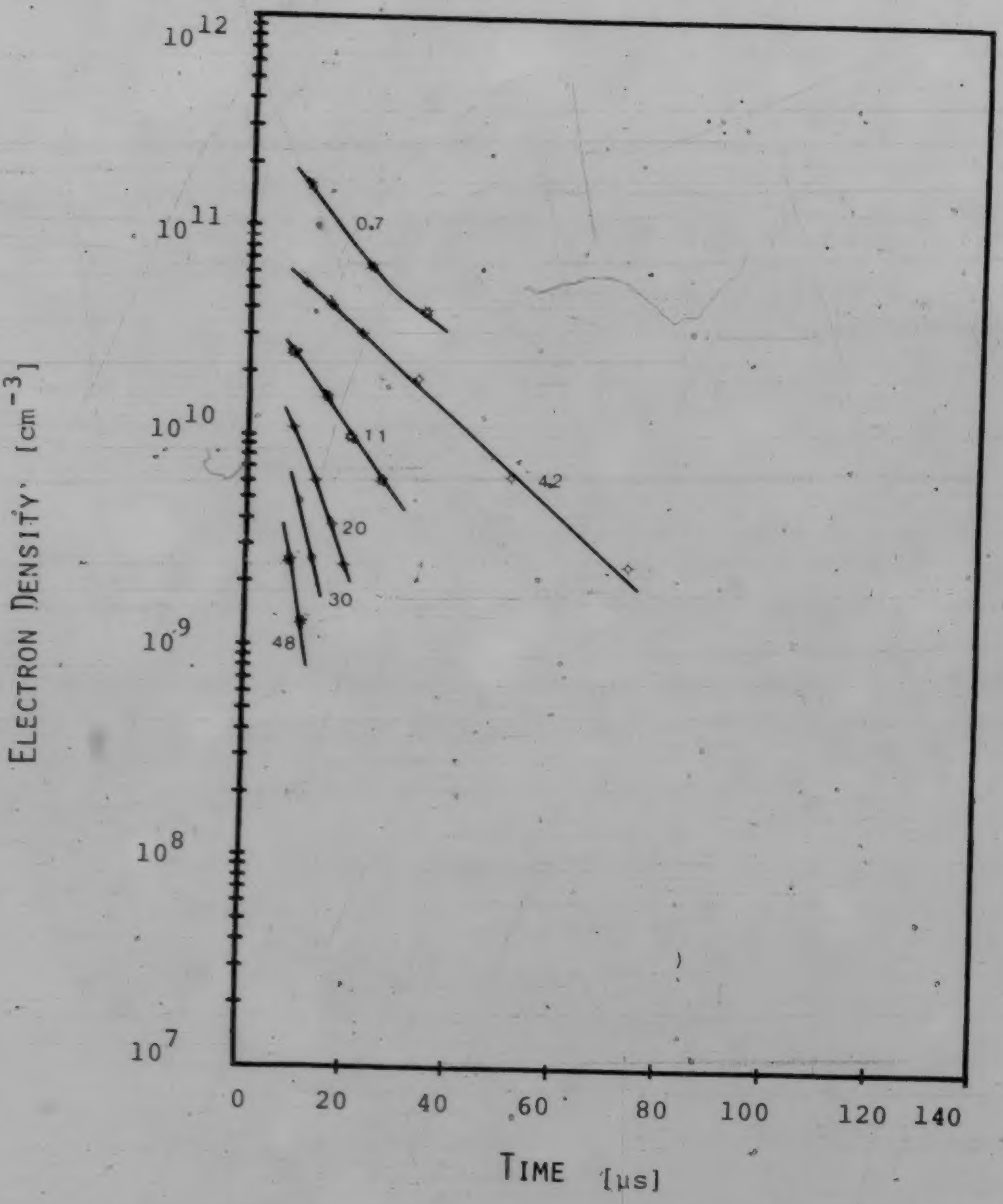

FIGURE 5-28 ELECTRON DENSITY VERSUS TIME FOR AIR The numbers on the curves indicate pressure in torr.

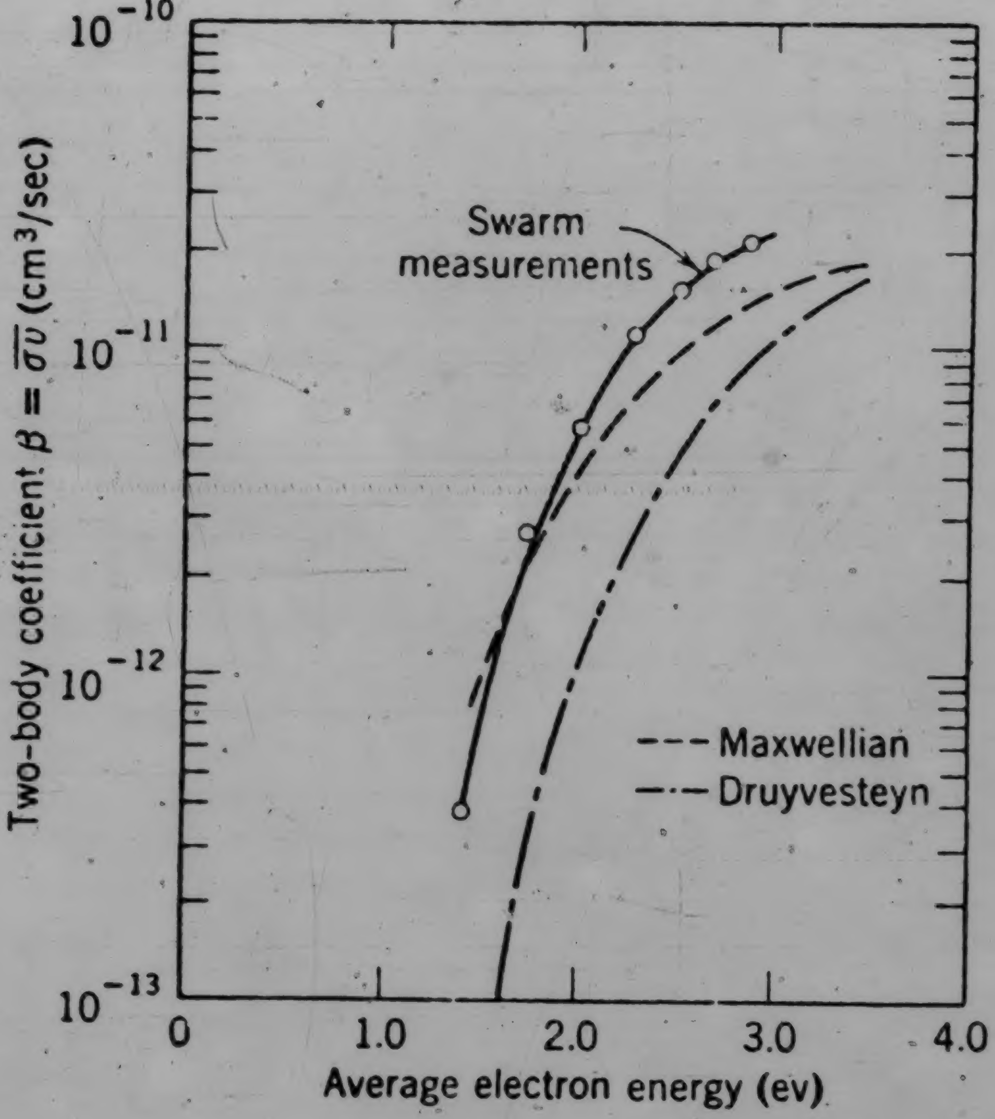

FIGURE 5-29 TWO BODY ELECTRON ATTACHMENT COEFFICIENT FOR O_2 [41]

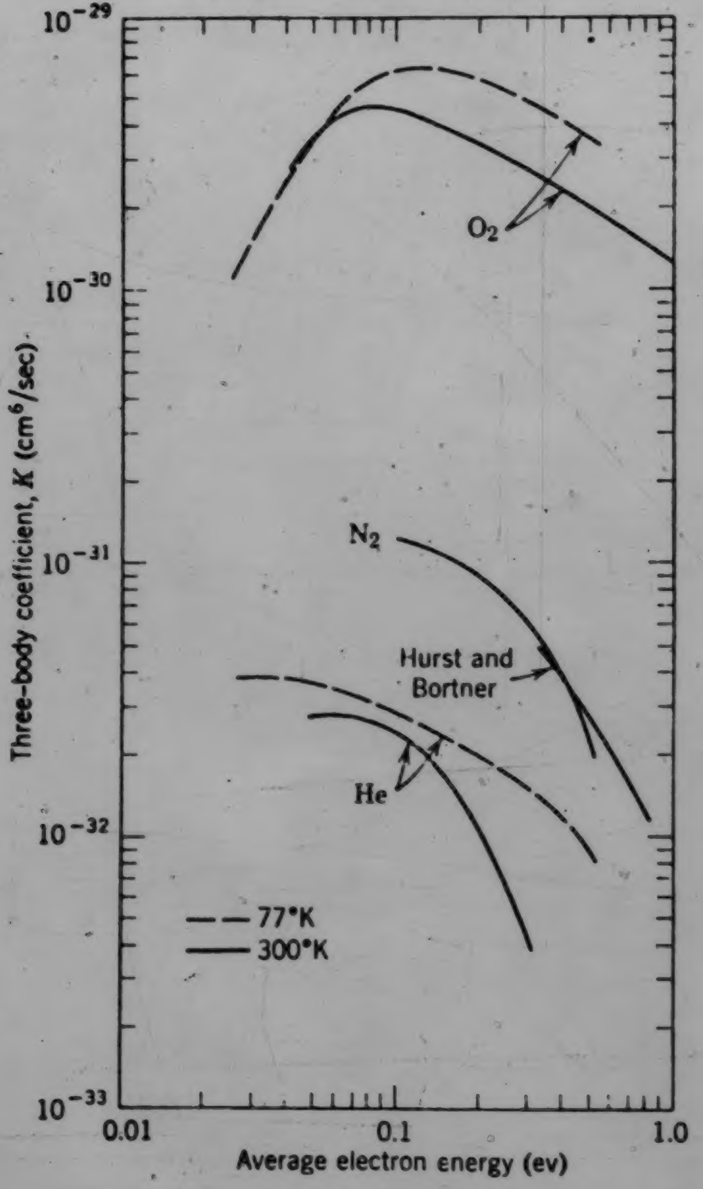

FIGURE 5-30 THREE BODY ELECTRON ATTACHMENT COEFFICIENT FOR O_2 [41]

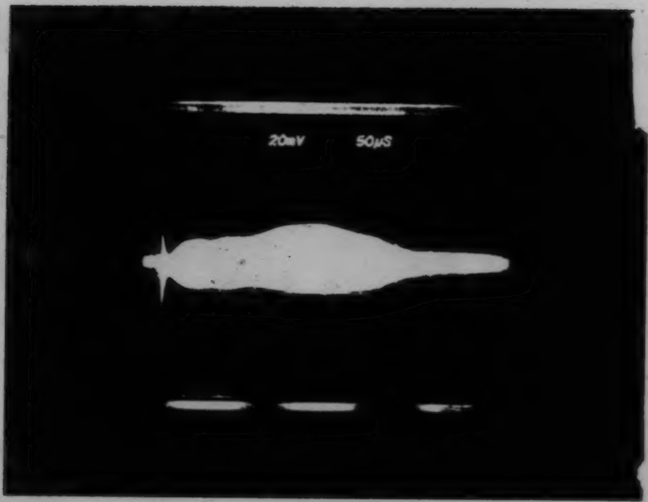

0.7 torr of air

$C = 0.1\ \mu f$
$V = 40\ kV$

20 mV/div

50 μs/div

FIGURE 5-31 SECONDARY SIGNAL The secondary part of the bridge imbalance signal is shown. The phase shift component of a signal of this magnitude could not be measured with accuracy. The first part of the signal was much more intense but shorter lived 20 μs in this example).

5-5-5. Additives

Further density measurements were made to determine the effect of traces of hydrocarbon impurities on the photogenerated plasma. The electron density was found to be influenced by the gas mixture so a reference mixture (CO_2 : N_2 : He = 1 : 1 : 3 by volumetric flow) was used. The additives were conveniently added to the gas mixture by bubbling about 10% of the gas makeup through the additive liquid as described earlier.

Upon increasing the gas pressure the percentage of gas bubbled through the admixture had to be decreased in order to maintain an optimum signal. In these instances the gas pressure was controlled either by adjusting the individual flow meter or by throttling the output valve. In all cases the percentage of gas bubbled through the additive, was adjusted to optimize the signal. This procedure was very tedious because of the length of time required for the dynamic system to reach an equilibrium after an adjustment was made.

Bubbling gas through additives with high vapor pressures such as benzene and acetone proved to be too coarse. In these cases, a small amount of gas was passed over the top of the additive in the bubble chamber picking up some of the vapors.

Many additives that were tested increased the electron peak density and decay time. The observed temporal characteristics of these are plotted in Figures 5-32 throughout Figure 5-41.

Electron density reciprocal and semilog plots have been presented for each different additive. In all cases, the number density of the additive molecules was unknown and so analysis of the decay was difficult. Also in most cases, the decay appeared to be due to attachment and recombination operating simultaneously.

Attachment serves to reduce the electron density with no effect on the positive ion population. Consequently, the density of the two charge carriers cannot be considered equal, and the simple recombination theory would not apply. A thorough analysis would involve the formation and destruction of negative ions as well as ion-ion recombination. Unfortunately, the quality and the quantity of the data on additives does not warrant such an analysis. However, Table 5-5 has been prepared, listing whatever conclusion can be derived from the decay data. Numerous other observations that were made are included in Table 5-5. Additives that had a detrimental effect are also included.

Further tests were done with various additives using a $CO_2 : N_2 : He = 1 : 1 : 1$ mixture as a standard. In these tests, only the signal duration and the phase shift corresponding to the maximum electron density were recorded. This was relatively easy since the measurement could be performed quickly, and the optimum signal did not have to be maintained for so long.

Table 5-5

List of Additives Tested and Some Observations

Additive	Electron Decay	Time Range (μs)	Pressure (torr)	Comment
Acetone	recombination $\alpha = 6 \times 10^{-6}\ \mathrm{cm}^2\mathrm{sec}^{-1}$	5→100	40	No gas passed through the bubble chamber. Vapor pressure supplies enough
	attachment	5→30	78→138	Flow does not allow vapor pressure to be reached in the chamber.
Benzene	?	5→70	19→243	Probably attachment and recombination operating simultaneously. Improved electron density more than any additive.
Carbontetrachloride				Detrimental and difficult to remove from the chamber.
Trichloroethylene				Detrimental.
Methyl Ethyl Ketone	Maybe recombination $\alpha = 8 \times 10^{-6}\ \mathrm{cm}^2\mathrm{sec}^{-1}$	5→110	19→49	Concentration appears critical.

Continued on next page

Table 5-5 continued

Additive	Electron Decay	Time Range (μs)	Pressure (torr)	Comment
Triethylamine	Maybe recombination $= 1 \times 10^{-5}\ \mathrm{cm}^2 \mathrm{sec}^{-1}$	5→70	19→50	Coarse adjustment to optimise the signal perhaps because of a low vapor pressure
Tri-n-propyl amine	Attachment and Recombination	3→100	19 and 30	Similar to Triethylamine
	attachment	3→40	49 and 93	
Methane				Inhibited ionization may have had some H_2O vapor
Ethanol				Inhibited ionization
Carbon Disulfide				Inhibited ionization

The minimum phase shift resulting in an imbalance observable on the CRT was about 0.01 degrees. Consequently, it was concluded that the time at which the signal diminished to a similar reading corresponded to 0.01 degrees. This translates to a minimum observable density of about 10^7 electrons cm^{-3}. This measurement was believed to be quite accurate, since the attenuation consistently approached zero with decreasing electron density. Also, all signals involving additives decayed smoothly, never rising after an initial decay as for the case of CO_2, CO, O_2, air and H_2. The addition of seed material to the laser mixture not only increased the electron density, but had a profound influence on the decay time. This phenomenon is illustrated in Figure 5-42, showing the time required to decay to 10^7 electrons cm^{-3} as a function of pressure. Substantial ionization can be seen to exist for relatively long periods even at atmospheric pressures.

Many more materials than those mentioned have been tested and found to enhance photoelectron density. The largest increases in electron density did not consistently correlate with the lower ionization threshold additive, possibly because of a better match between the ionization continuum and the source emission spectrum. To date the greatest ionization enhancement has been obtained with benzene.

It was interesting to observe the negative effect of an additive such as carbontetrachloride on the photoelectron density. A trace of CCl_4 not only killed all ionization, but no detectable photoplasma returned even after 36 hours of continuous pumping. The system did not return to normal until after it had been completely dismantled and washed with alcohol. The detrimental effect of CCl_4 is believed to be a direct consequence of its electronegative nature.

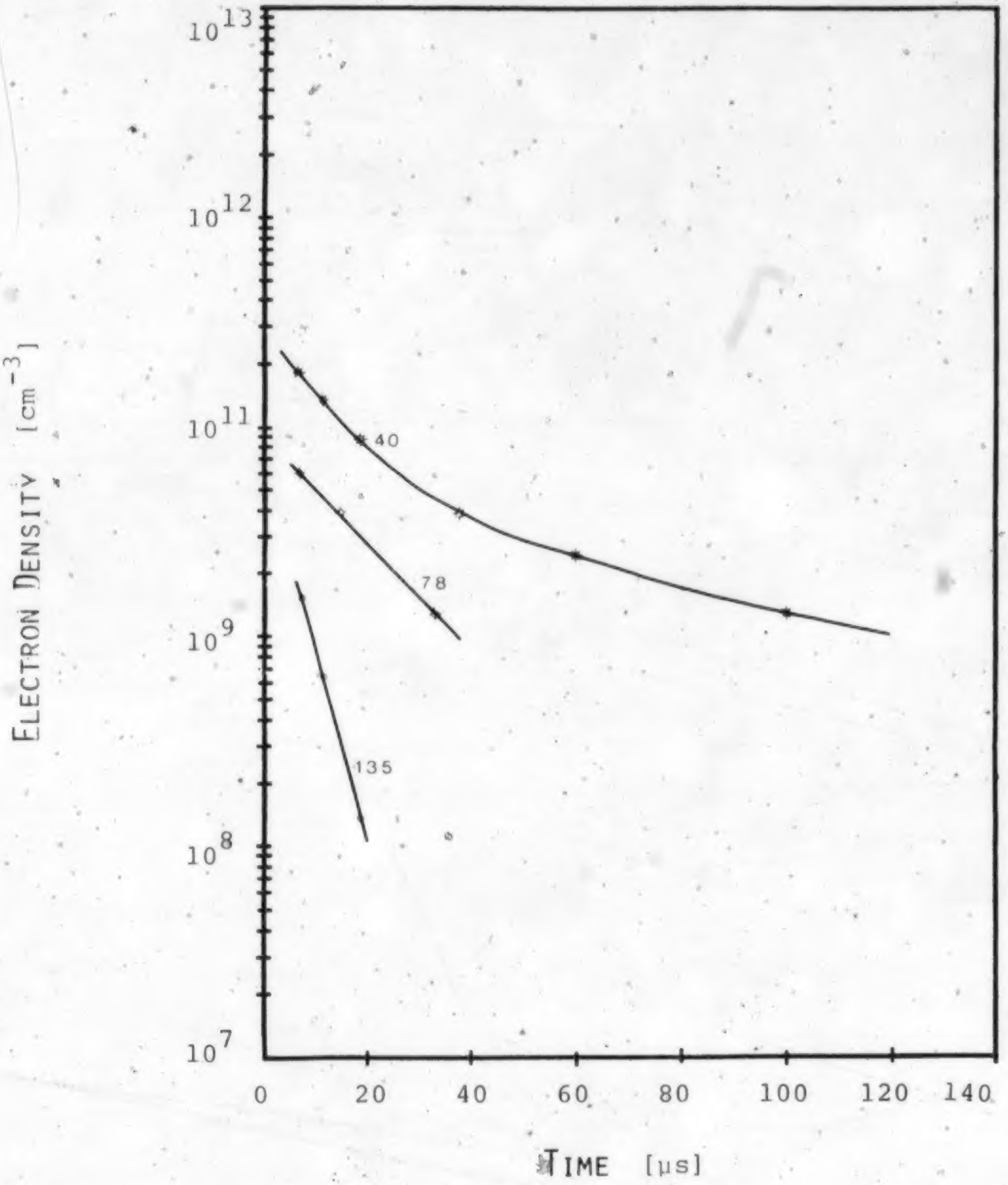

Figure 5-32 Electron Decay in Acetone. Acetone vapor was added to a $CO_2:N_2:He = 1:1:3$ flow ratio by passing a portion of the flow through a bubble chamber. The numbers on the curves indicate total pressure in torr.

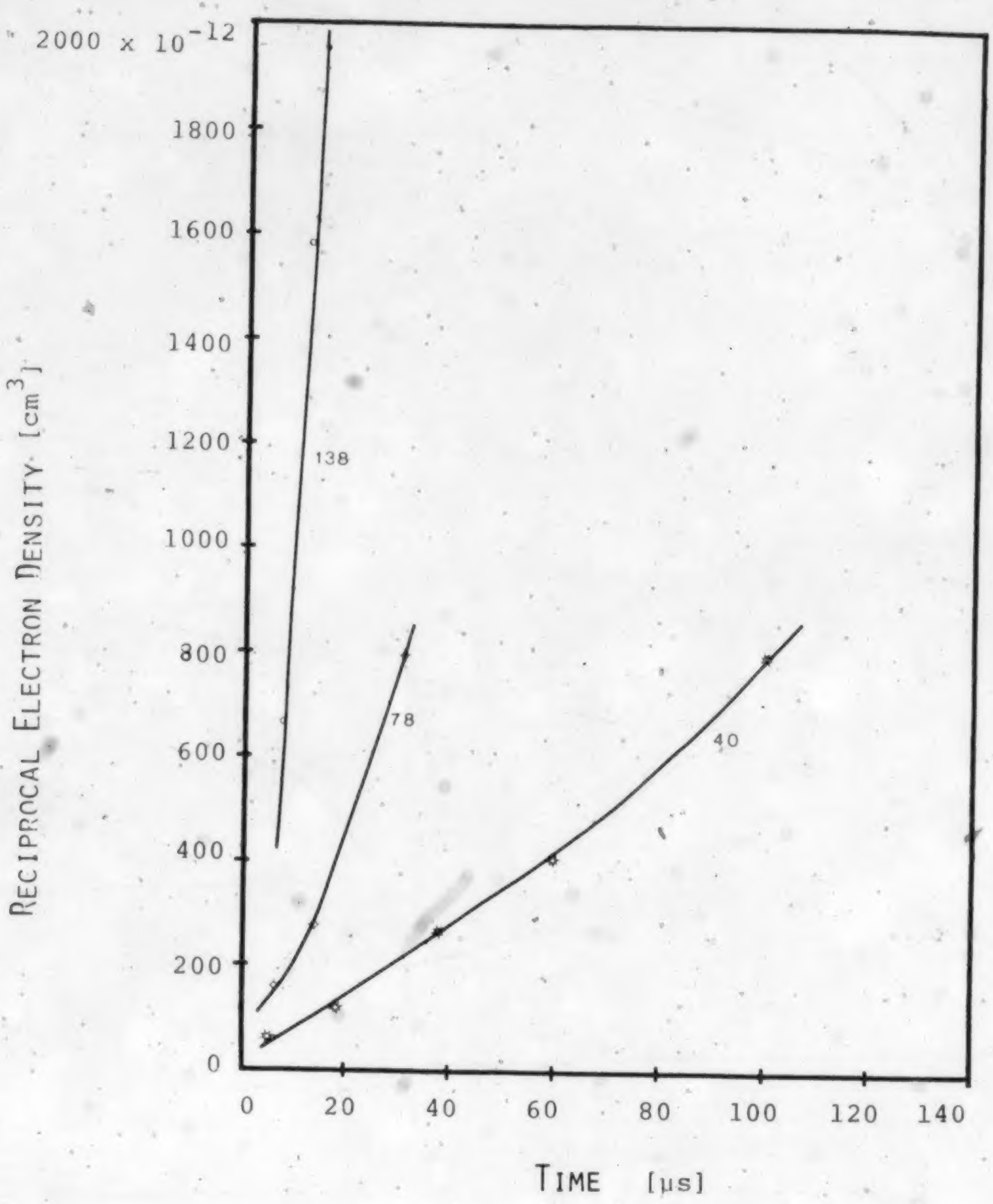

FIGURE 5-33 RECIPROCAL ELECTRON DENSITY VERSUS TIME FOR ACETONE Acetone vapor was added to a CO_2:N_2:He = 1:1:8 flow ratio by passing a portion of the flow through a bubble chamber. The number on each curve denotes the total pressure in torr.

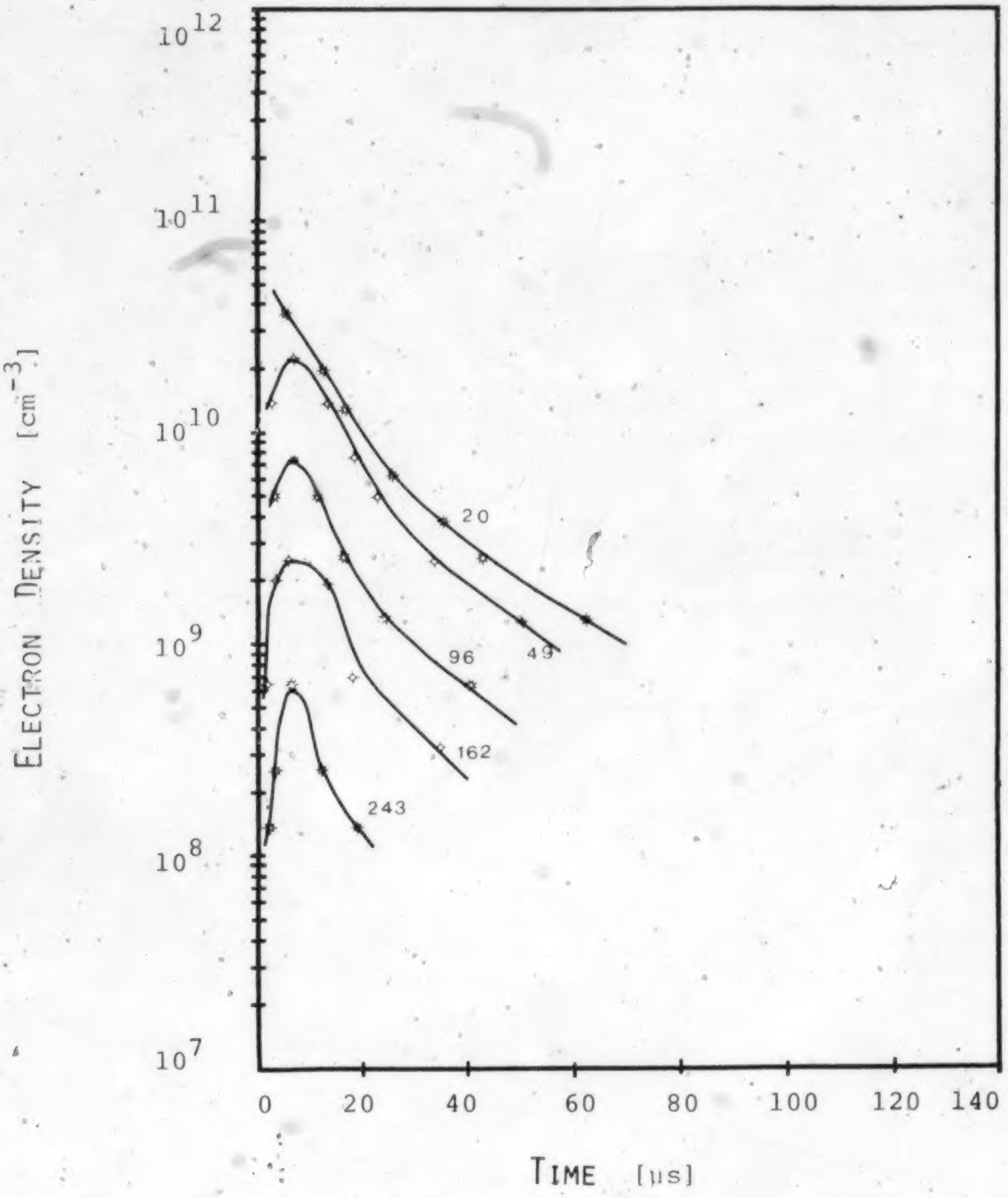

FIGURE 5-34 ELECTRON DECAY IN BENZENE Benzene vapor was added to a CO_2:N_2:He = 1:1:3 flow ratio by passing a portion of the flow through a bubble chamber. The number on each curve denotes the total pressure in torr.

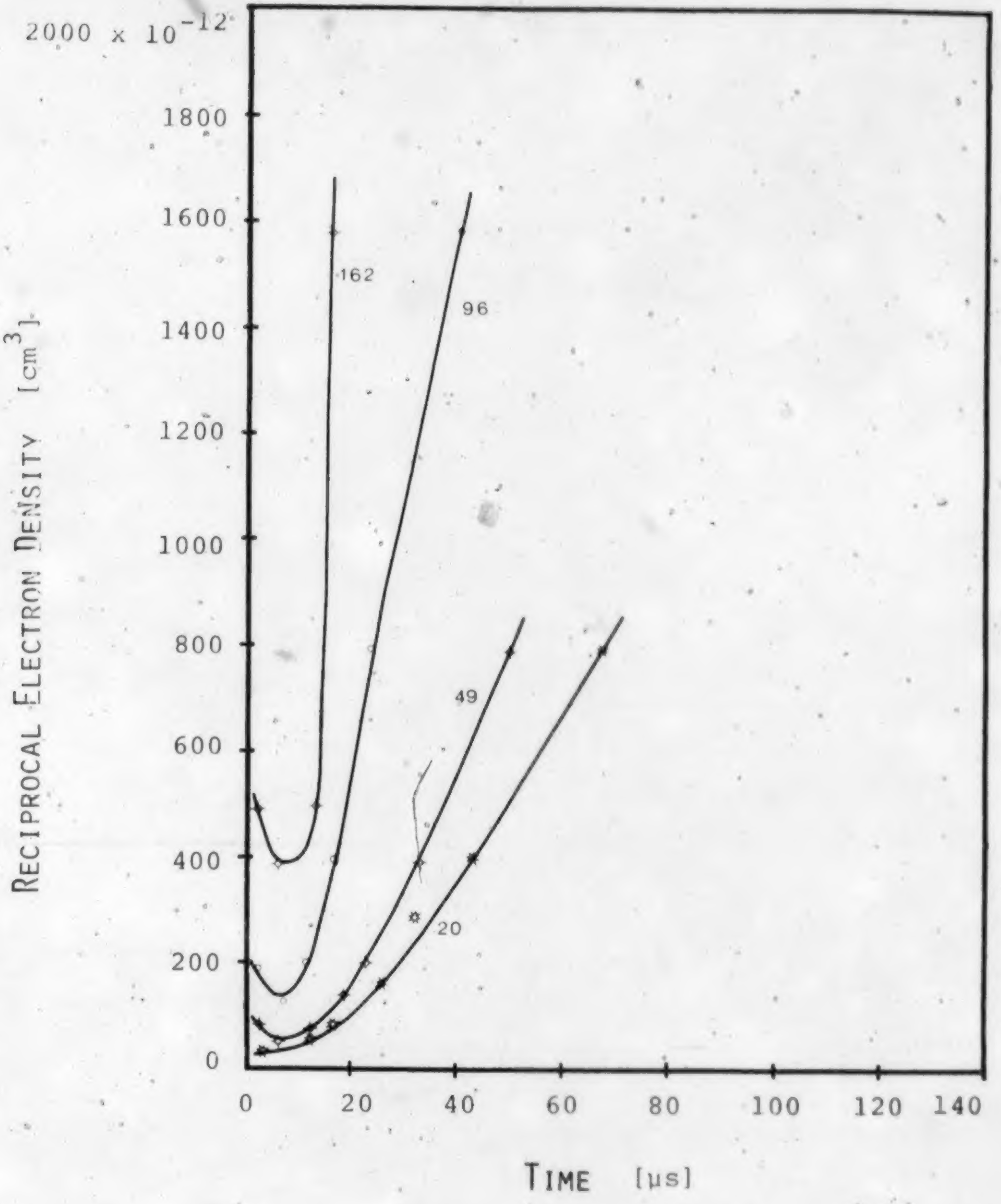

Figure 5-35 Reciprocal Electron Density Versus Time for Benzene Benzene vapor was added to a CO_2:N_2:He = 1:1:3 flow ratio by passing a portion of the flow through a bubble chamber. The numbers on the curves indicate total pressure in torr.

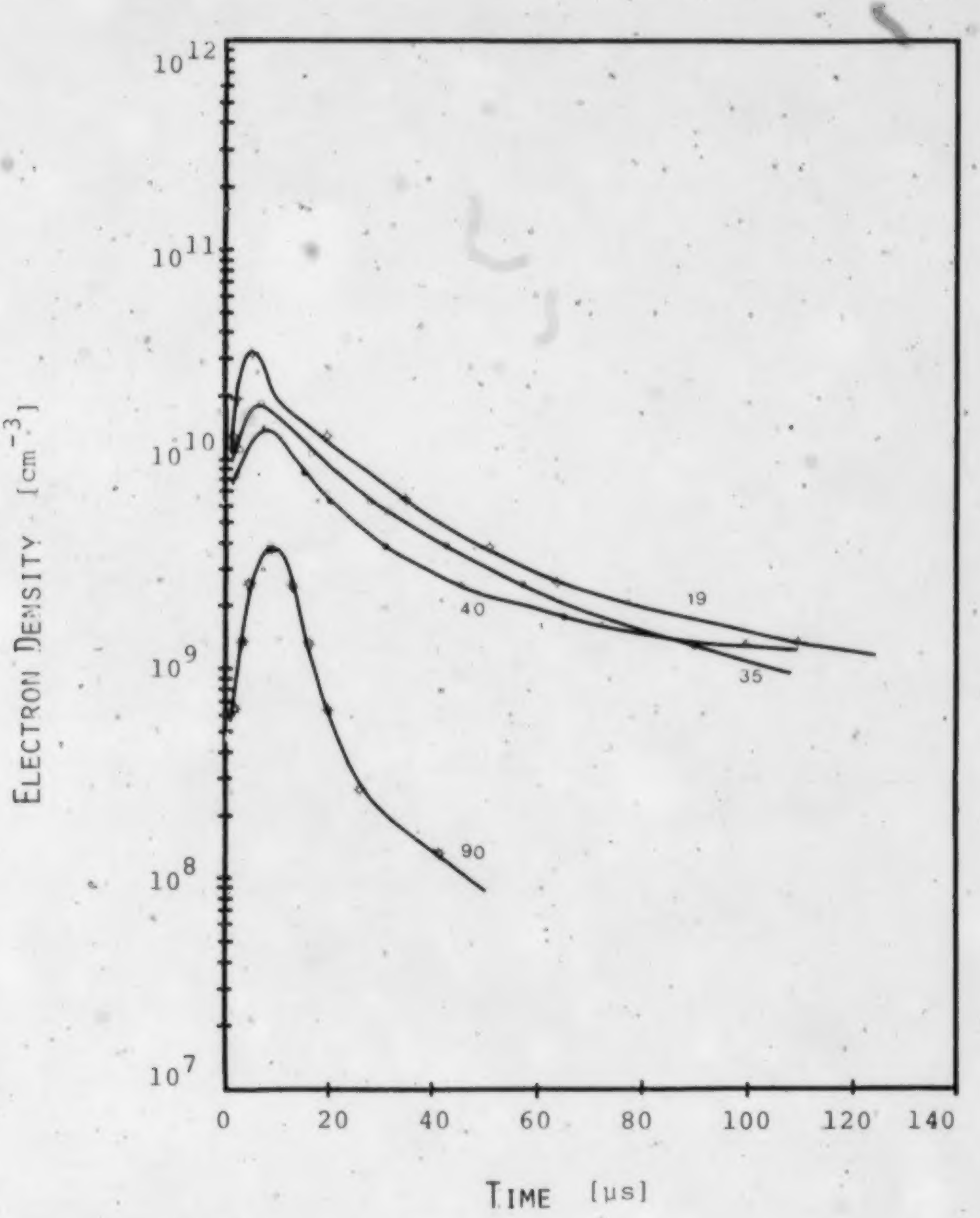

FIGURE 5-36 ELECTRON DECAY IN METHYL ETHYL KETONE
Methyl Ethyl Ketone vapor was added to a CO_2:N_2:He = 1:1:3 flow ratio by passing a portion of the flow through a bubble chamber. The numbers on the curves indicate total pressure in torr.

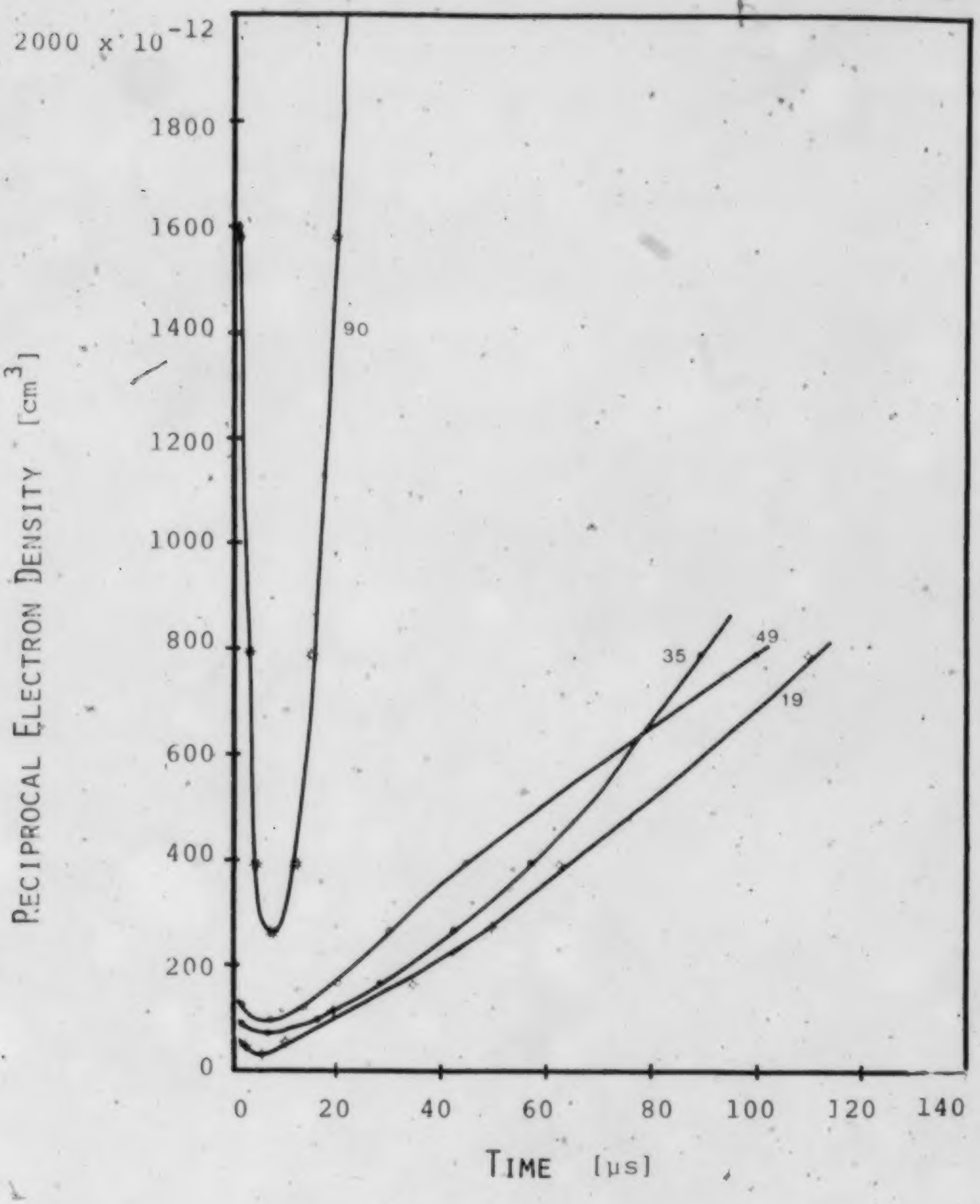

FIGURE 5-37 RECIPROCAL ELECTRON DENSITY VERSUS TIME FOR METHYL ETHYL KETONE Methyl Ethyl Ketone was added to a $CO_2:N_2:He = 1:1:3$ flow ratio by passing a portion of the flow through a bubble chamber. The numbers on the curves indicate total pressure in torr.

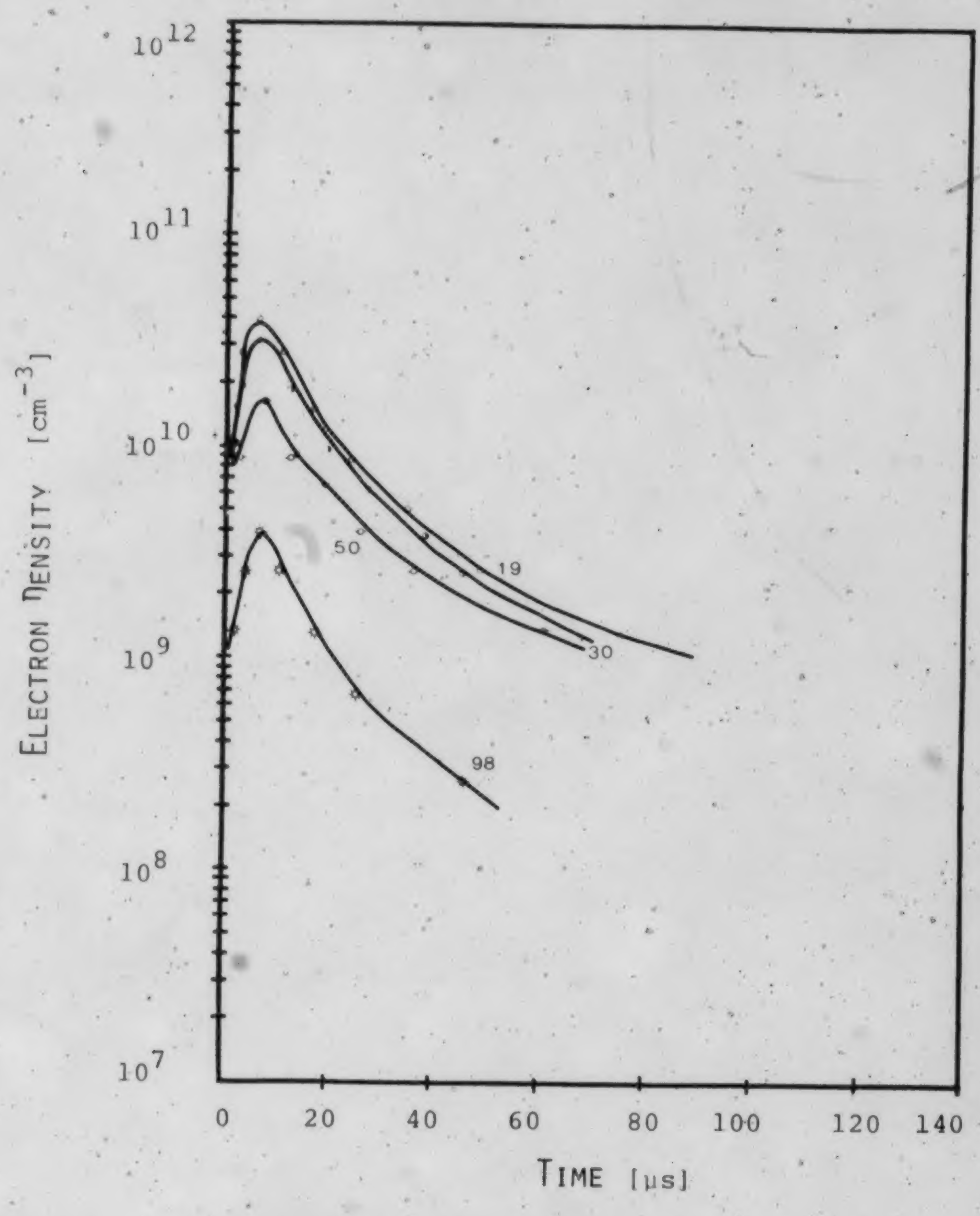

FIGURE 5-38 ELECTRON DECAY IN TRI-ETHYL AMINE Tri-ethyl Amine vapor was added to a CO_2:N_2:He = 1:1:3 flow ratio by passing a portion of the flow through a bubble chamber. The numbers on the curves indicate total pressure in torr.

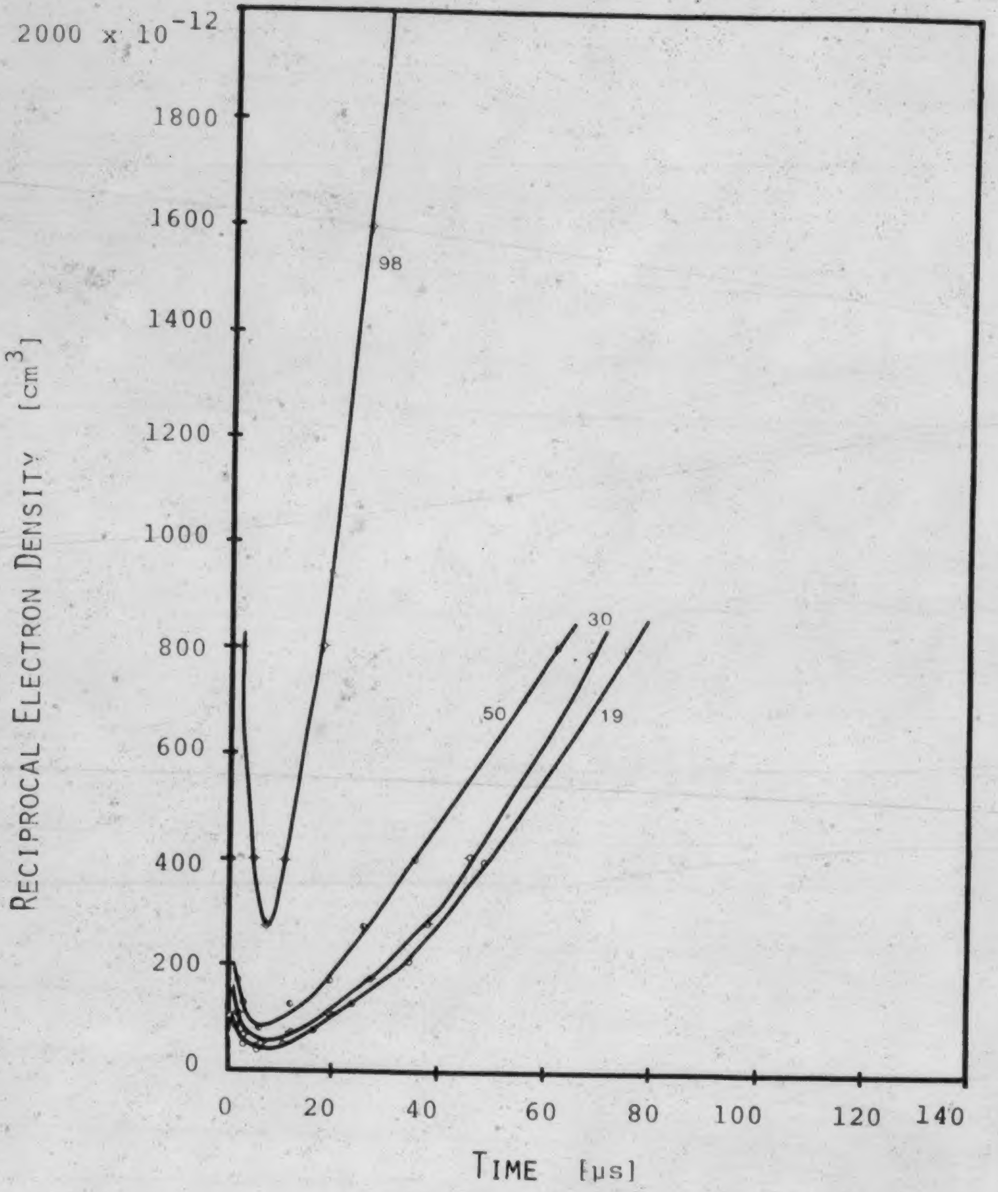

Figure 5-39 Reciprocal Electron Density Versus Time for Tri-ethyl Amine Tri-ethyl amine was added to a CO_2:N_2:He = 1:1:3 flow ratio by passing a portion of the total flow through a bubble chamber. The numbers on the curves indicate total pressure in torr.

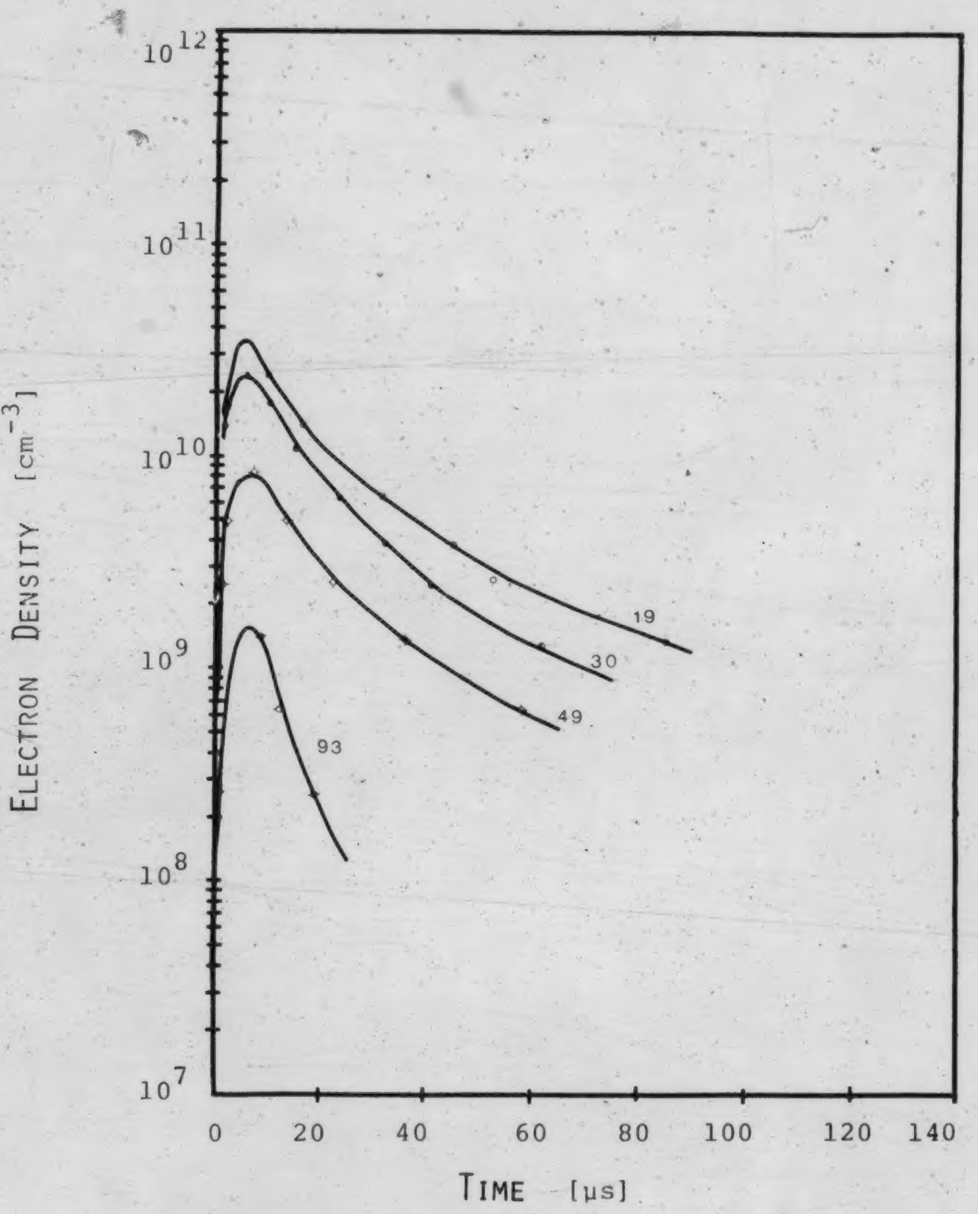

FIGURE 5-40 ELECTRON DECAY IN TRI-N-PROPYL AMINE . Tri-n-propyl amine was added to a CO_2:N_2:He = 1:1:3 flow ratio by passing a portion of the flow through a bubble chamber. The numbers on the curves indicate total pressure in torr.

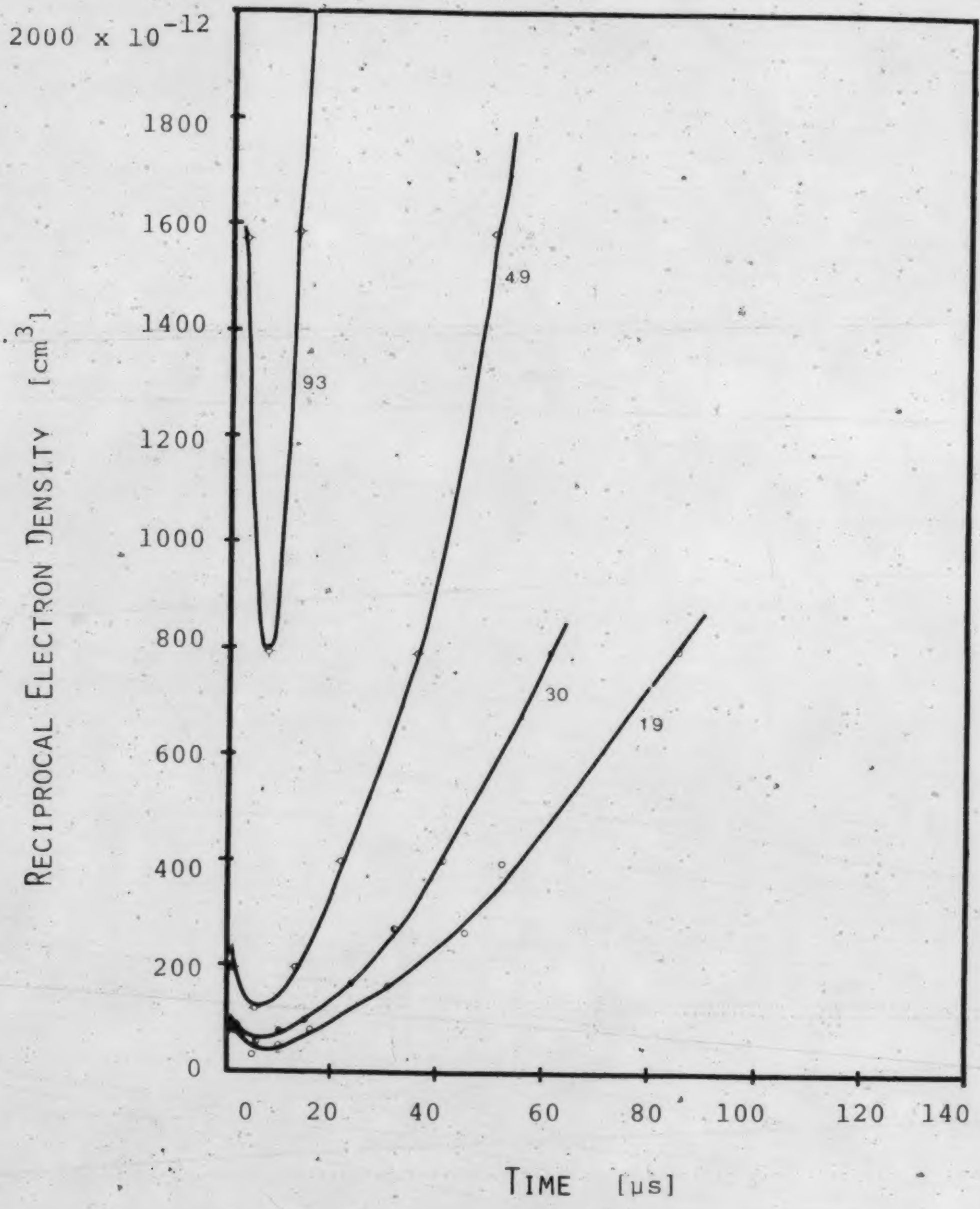

Figure 5-41 Reciprocal Electron Density Versus Time for Tri-n-propyl Amine Tri-n-propyl amine was added to a $CO_2:N_2:He$ = 1:1:3 flow ratio by passing a portion of the flow through a bubble chamber. The numbers on the curves indicate total pressure in torr.

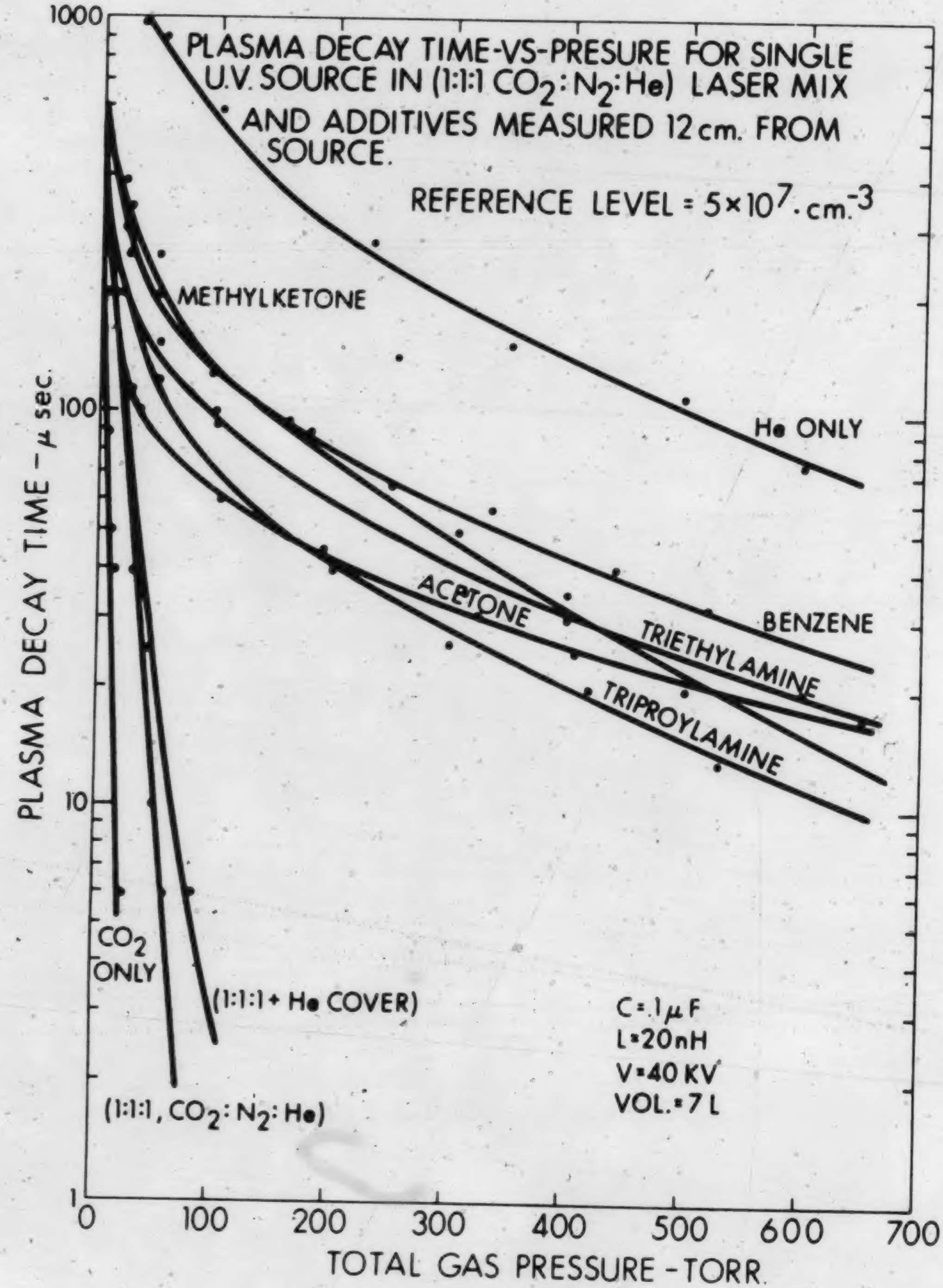

Figure 5-42 Plasma Decay Time Versus Gas Pressure

5-5-6. Effect of a Leak

It is important to determine the effect, if any, existing air leaks may have had on the foregoing data.

The leak rate of the ionization chamber and associated vacuum apparatus was monitored at regular intervals during the course of performing the tests. This was done by pumping the apparatus down to the limit of the rotary pump (approximately 1-2 microns) and then isolating the system with appropriate valves. The ensuing pressure increase was monitored with an ionization gauge calibrated for air. Whenever the leak rate exceeded 10-20 microns per hour, the leak was located and repaired. Such leaks occasionally resulted when changes were made on the apparatus to prepare it for specific tests. These changes were usually limited to such things as pressure gauges, tubing, and spark plugs. In addition, the spark plugs developed leaks after prolonged usage (typically many hours).

Any tests that had been performed, previous to discovering that a leak had developed were repeated, if there was reason to believe that they had been affected by the leak. Since no tests required more than 30 minutes to complete, and since the vacuum apparatus was evaucated between tests, no more than a few microns of air are expected to have been present during any test. The pump down time served as a convenient check on the vacuum integrity as well.

Only the oxygen component of the leak will be considered here since it is particularly notorious in terms of photoabsorption and electronegative behaviour. By comparison N_2 is relatively inert and its presence in small quantities is not expected to alter the results significantly. A contamination of 10 microns of O_2 will be taken as a worst case situation.

The photoabsorption suffered by light passing through the contaminant, may reduce the photon intensity at all points along the path. This would result in a reduced initial electron density. This effect can be described by Equations 3-75 and 3-77 resulting in

$$\frac{I}{I_o} = \exp\left[-\sigma_t \, n_o \, \chi\right] \qquad 5\text{-}32$$

n_o = Loschmidt's number [2.7×10^{19} cm^{-3}]

χ = $L\frac{P273}{760T}$[cm] (reduced length)

L = distance from the source to the position of measurement [cm]

σ_t is never larger than 20×10^{-18} cm^2 for O_2, except for narrow band resonance as illustrated in Figure 5-43. For L = 20 cm (distance from source to the center of the microwave horns) the decrease in photon intensity is about 12%. The decrease for the entire length of the ionization chamber is about 23%. These values are not large and can be ignored in the foregoing tests.

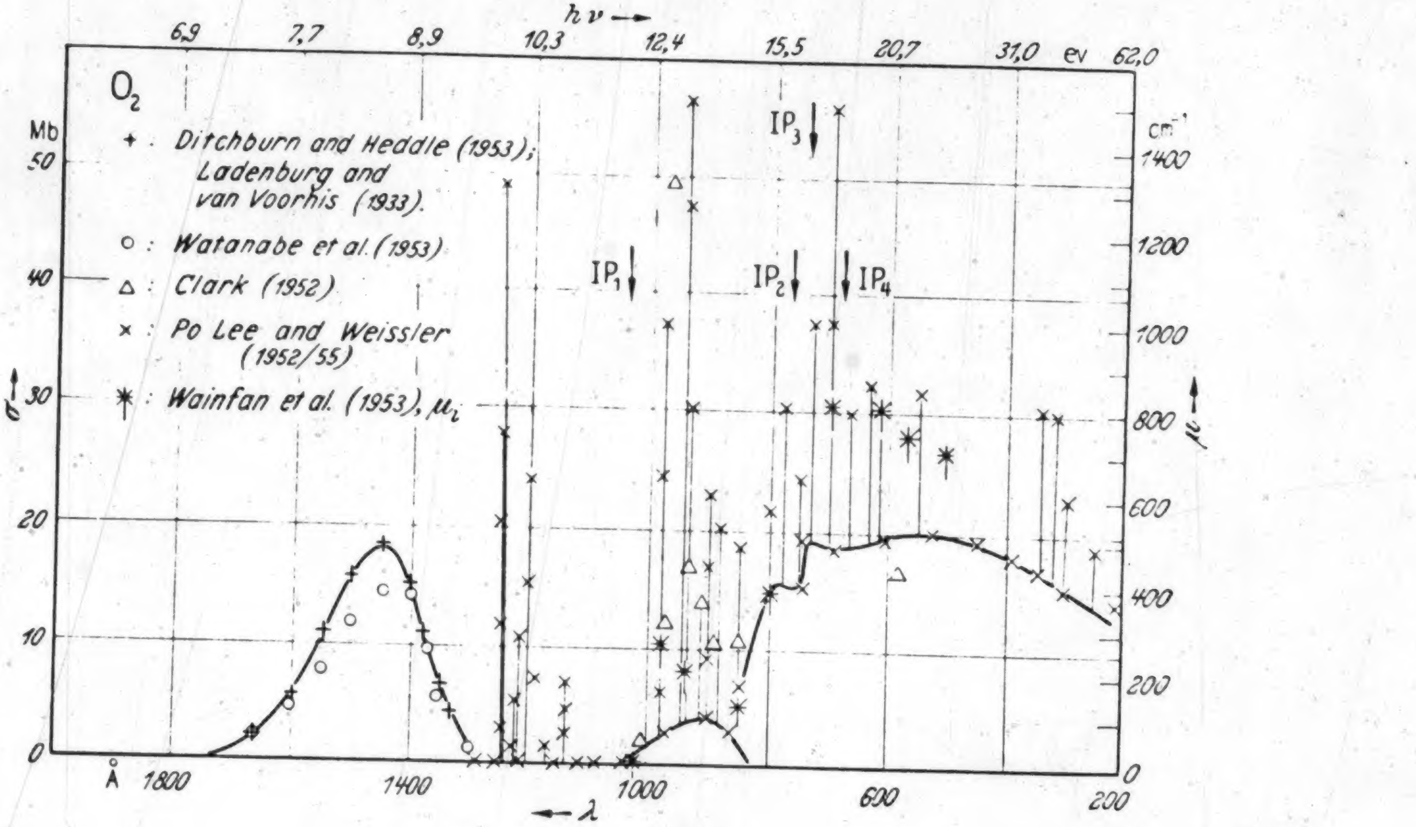

FIGURE 5-43 PHOTOABSORPTION CHARACTERISTICS OF O_2 [42]

O_2 is an electronegative gas and can form the negative molecular ion in a three body process for ambient temperature electrons. This may not only affect the electron decay rate but may have considerable effect on the coefficient of ambipolar diffusion [47]. If the electron decay was dominated by attachment to the O_2 contaminant, then Equation 5-14 applies with $\nu_a = K_a N(O_2) N(th)$

$$\frac{dn_e}{dt} = -K_a N(O_2) N(th) n_e \qquad 5\text{-}33$$

K_a = three body rate coefficient [$cm^6 sec^{-1}$]
$N(O_2)$ = number density of O_2 molecules [cm^{-3}]
$N(th)$ = number density of third bodies [cm^{-3}]

The solution to Equation 5-33 is:

$$n_e = n_{eo} \exp(-t/\tau) \qquad 5\text{-}34$$

with a time constant

$$\tau = [K_a N(O_2) N(th)]^{-1} \qquad 5\text{-}35$$

From Figure 5-30, $K_a = 2 \times 10^{-31}\ cm^6 sec^{-1}$ when N_2 molecules act as the stabilizing third bodies. This results in an attachment time constant of $\tau = \frac{0.4 \text{ sec torr}}{P}$ where P is the N_2 pressure in torr. This time constant is considerably longer than any of those observed, and it will not have a significant effect on the data. However, the late decay at high pressures may be controlled by attachment to the O_2 contaminant. If tests were performed in these regions the O_2 concentration would have to be further reduced.

Even at low pressures O_2 may affect the later decay by altering the diffusion time constant for all modes of diffusion. A proper analysis requires that attachment and diffusion be considered together. This can be described by the following rate equation:

$$\frac{dn_e}{dt} = \mathcal{D}\nabla^2 n_e - K_a N(O_2) N(th) n_e \qquad 5\text{-}36$$

The solution to this equation can be obtained in the same manner as for the independent diffusion equation presented earlier. The solution can be arrived at by simply replacing $1/\mathcal{D}\tau$ in Equation 5-13 by $(\frac{1}{\tau} - K_a)1/\mathcal{D}$.The resulting time constants are given by:

$$\tau_{ij} = \left\{ \mathcal{D}\left(\left(\frac{s_i}{r_o}\right)^2 + \left[\frac{(2j-1)}{H}\pi\right]^2\right) + K_a N(O_2) N(th) \right\}^{-1} \qquad 5\text{-}37$$

$i = 1,2,3,4...$

$j = 1,2,3,4...$

Again for the case of N_2

$$K_a N(O_2) N(th) = 2.5 P_{N_2}\ [\sec^{-1}]$$

As before, even the longest observed time constants were only a few milliseconds. Consequently, the first term in Equation 5-37 would have to be considerably larger than the second term, to account for the rapid decay. As before, the attachment is too slow to be a significant factor. However, if the electron decay is followed sufficiently long to ensure that the fundamental mode has developed, then the independent diffusion equation is correct for only the lowest pressures. For a total pressure of a few torr to a few tens of torr, attachment to the O_2 contaminant, would have to be considered along with diffusion. At pressures above 100 torr the attachment process would dominate the decay, and diffusion would become insignificant. Equation 5-36 would reduce to Equation 5-33.

In spite of the fact that electron attachment considered here is relatively slow, an accumulation of negative ions can increase the coefficient of ambipolar diffusion [47]. If a significant number of negative ions accumulate, they effectively shield the electrons from the positive ions and the ambipolar diffusion coefficient is increased by the factor, 1 + B where B is the ratio of negative ion density [n_i^-] to electron density.

$$B = n_i^-/n_e \qquad 5\text{-}38$$

Again taking N_2 at low pressures as an example where these effects will be most significant one can write for the negative ion production:

$$\frac{dn_i^-}{dt} = \nu_a n_e \qquad 5\text{-}39$$

where $\nu_a = K_a N(O_2) N(th)$ as before. From Figure 5-10, it can be assumed that the initial decay may be described in terms of a recombination coefficient of $\alpha = 1 \times 10^{-8}\ cm^3 sec^{-1}$.

Assuming that the increased decay of electrons as a result of attachment is small, then the electron density and positive ion density will still be approximately equal, and the electron density can be described by Equation 5-18. Substitution of this into Equation 5-39 results in:

$$\frac{dn_i^-}{dt} = \frac{\nu_a}{1/n_{eo} + \alpha t} \qquad 5\text{-}40$$

The solution is given by

$$n_i^- = \frac{\nu_a}{\alpha}\left[\ln(1/n_{eo} + \alpha t) + \ln n_{eo}\right] \qquad 5\text{-}41$$

In the case of N_2 at low pressures electron densities above cut-off ($10^{12}\ cm^{-3}$) were obtained for up to 1 ms. Extrapolation of the data in Figure 5-8 back to a few microseconds indicates initial densities that may be as high as $10^{15}\ cm^{-3}$. From Figures 5-10 and 5-11 diffusion appears to set in around 6 ms. Equation 5-41 is valid from t = 0 to t = 6 ms. The negative ion density accumulated during this period is:

$$n_i^- = 2 \times 10^9 P\ cm^{-3} torr^{-1}$$ where

P is the N_2 pressure.

The greatest effect will be in the later decay for low pressures as in Figure 5-11. The experimentally observed ambipolar diffusion coefficient for N_2 at 1 torr may be affected by 3% at 6 ms by this process.

In order to determine the shielding effect of negative ions for $t > 6$ ms the observed diffusion distribution must be used in Equation 5-39. The appropriate exponential (diffusion) distribution is given by:

$$n_e = 4 \times 10^{10} \exp(-t/4.1 \times 10^{-3}) \qquad 5\text{-}42$$

with the 6 ms onset time redefined as zero. The time constant was obtained from Table 5-1. Equation 5-39 becomes:

$$\frac{dn_i^-}{dt} = \nu_a \, 4 \times 10^{10} \exp(-t/4.1 \times 10^{-3}) \qquad 5\text{-}43$$

The solution is:

$$n_i^- = \nu_a \times 4 \times 10^{10} \times 4.1 \times 10^{-3}[1 - \exp(-t/4.1 \times 10^{-3})]$$

5-44

Using Equation 5-44 one finds that only 4×10^8 additional negative ions will have accumulated during the remaining 8 ms (total of 14 ms). This results in a possible total of about 2.4×10^9 negative ions at 14 ms for the 1 torr curve in N_2 in Figure 5-11. The coefficient of ambipolar diffusion may be as much as 40% higher than originally assumed. This would tend to reduce the requirement for higher order diffusion modes originally proposed to explain the rapid diffusion decay.

As the term B increases, the diffusion curve should exhibit a curvature in favour of increasing decay rate with time [47]. Curves of this nature were observed in the later decay of electrons in H_2 at low pressures. These are illustrated in Figure 5-44. Unfortunately, the effectiveness of H_2 molecules in acting as third bodies in three body attachment to O_2 is unknown, and a detailed analysis cannot be performed. However, this phenomenon can be expected to show up more easily in H_2 than in any of the heavier gases. The coefficient of ambipolar diffusion for a given ion would be relatively high in the light weight H_2 gas [41]. Consequently the diffusion would reduce to the fundamental mode correspondingly faster where the negative ion effect on *Da* can be more readily observed. If the diffusion has not fully developed to the fundamental mode the negative ion effect on *Da* can be masked by the decaying out of the higher order terms, hence the observation in H_2.

Although the mechanism is relatively insignificant for the data obtained, it may be highly significant under conditions of fundamental mode diffusion controlled decay at higher pressures. However, as the effect becomes greater the validity of the simple analysis diminishes. As successively more electrons are removed

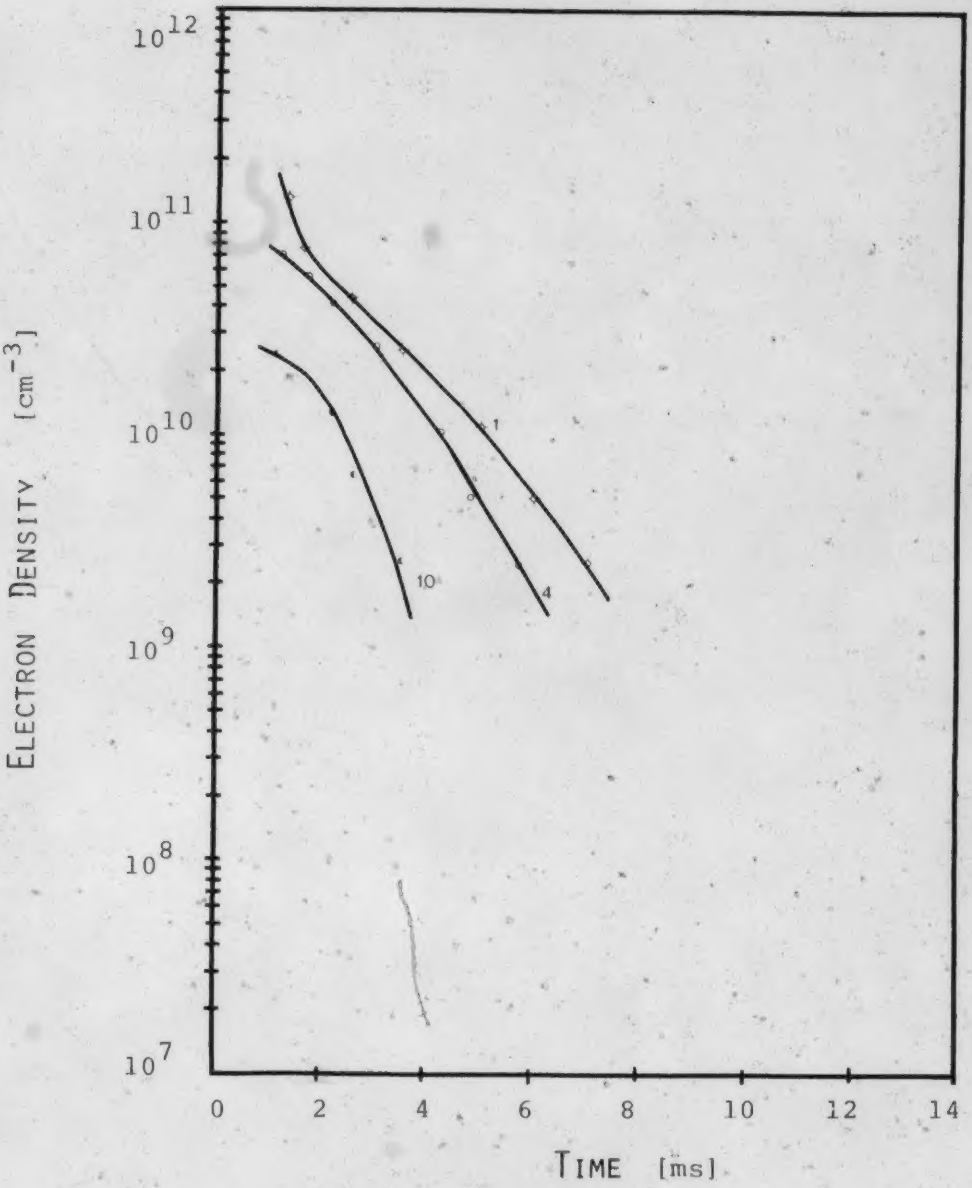

FIGURE 5-44 ELECTRON DECAY IN H_2 AT LOW PRESSURES
The numbers on the curves indicate pressure in torr.

by the attachment process, equality between the electron and the positive ion densities can no longer be assumed. Consequently, the recombination distribution for electrons used in Equation 5-39 would no longer hold.

The foregoing analysis has been done for N_2 since negative ion formation occurs more readily here. The analysis is equally appropriate to He. Since the three body attachment coefficient is about an order of magnitude less in He, all of the above mentioned effects will be correspondingly less for this gas.

Since the stabilizing effect of CO_2 and CO in three body attachment to O_2 is unknown, little can be said about the effect of the above mentioned anomalies in these gases. However, if one assumes that three body electron attachment to the O_2 contaminant is responsible for the observed decay one can obtain values of the coefficient with the following relation:

$$K_a = \frac{\ln n_{e1}/n_{e2}}{(t_2-t_1)\left(\frac{2.7 \times 10^{19}}{760}\right)^2 0.01\ P} \qquad 5\text{-}45$$

where $\frac{2.7 \times 10^{19}}{760} \times 0.01$ is the number density of the O_2 molecules and $\frac{2.7 \times 10^{19}}{760}\ P$ is the number density of the stabilizing particle. Here, it will be assumed that either CO_2 or CO are much more effective third bodies than even O_2. Consequently, P will be the pressure or the partial pressure of CO_2 or CO. The values of K_a

that appear in Table 5-6 are obtained from the curves in Figures 5-15 and 5-16 for CO_2. The values of K_a for CO_2 derived from the laser mixtures are a little higher than for the case of pure CO_2. These values are derived from Figures 5-20 and 5-23 and appear in Table 5-7. Values of K_a obtained for CO from Figure 5-18 are much the same as for CO_2. These values appear in Table 5-8.

Table 5-6

Three Body Attachment Rate Coefficient in CO_2

P[torr]	$K_a[cm^6 sec^{-1}]$
0.3	3.0×10^{-28}
1.2	1.4
2.3	3.4
8.1	0.6
4.9	1.1
15.5	0.6
20.	0.6

$$\bar{K}_a = 1.5 \times 10^{-28}$$

The electronegative species is assumed to be 10 microns of O_2. The values are obtained from Figures 5-15 and 5-16 along with Equation 5-45.

Table 5-7

Three Body Attachment Rate Coefficient in Laser Mixtures

(a)

P[torr]	$K_a[cm^6 sec^{-1}]$
7.4	4.8×10^{-28}
19	3.3
16	2.4
32	4.2
	$\bar{K}_a = 3.7 \times 10^{-28}$

(b)

P[torr]	$K_a[cm^6 sec^{-1}]$
7.1	2.0×10^{-28}
13	1.4
19	2.9
	$\bar{K}_a = 2.1 \times 10^{-28}$

(a) $CO_2 : N_2 : He = 1 : 1 : 8$ by volumetric flow.

(b) $CO_2 : N_2 : He = 1 : 1 : 3$ by volumetric flow.

The electronegative species is assumed to be 10 microns of O_2. The values are obtained from Figures 5-20 and 5-23 along with Equation 5-45.

Table 5-8

Three Body Attachment Coefficient in CO

P[torr]	K_a[$cm^6 sec^{-1}$]
15	0.73×10^{-28}
30	0.89
50	1.1
75	1.2
100	1.2
	$\bar{K}_a = 1.0 \times 10^{-28}$

The electronegative species is assumed to be 10 microns of O_2. The values are obtained from Figure 5-18 along with Equation 5-45.

5-6. Photoelectron Density Dependence on Pressure and Distance.

Initial photoelectron density measurements were performed at a distance of 12 cm from the source. 12 cm was chosen since it represents the required photon penetration depth for a typical CO_2 TEA laser. Various gases and mixtures of gases were tested at pressures ranging from a few parts of a torr to atmospheric pressure (about 700 torr in Edmonton). A standard mixture of gases ($CO_2 : N_2 : He = 1 : 1 : 1$ by volumetric flow) was used as a background to test additives. The results appear in Figures 5-46, 5-47 and 5-48. Some of the curves are duplicated in each figure to facilitate comparison.

The density of ionization observed in He and Ar was many orders greater than in the molecular gases, particularly CO_2 and O_2. The photoelectron density appears to be greatest for those gases that are most transparent to the hard ultra-violet. However, the relationship is not linear since N_2 is only transparent slightly farther into the ultra-violet than is Ar for example [37,38,41]. Figure 5-48 reveals that the electron density enhancement achieved with additives varies considerably from one additive to another, and approaches about 4 orders of magnitude in some cases. Figure 5-47 demonstrates that the photoionization density in the CO_2 laser mixture is dominated by the presence of CO_2. A large fraction of

CO_2 which is desirable from the laser standpoint results in reduction of the ionization density [57]. This accounts for at least part of the difficulty in obtaining a stable discharge in such lasers when the CO_2 fraction is increased. This is further illustrated in Figure 5-49 where the ionization density is plotted as a function of CO_2 partial pressure.

All curves of electron density against pressure appear to approach a straight line as the pressure increases, indicating that for the straight line portion of the curve, the radiation attenuation constant is proportional to gas density. An increase in pressure cannot be differentiated from an increase in distance for a photoabsorption process. Hence, for a constant pressure, a semilog plot of photoelectron density against distance from the source should yield similar results, if the radial fall-off of photon intensity is properly accounted for. Figure 5-50 reveals this relationship where the plasma density has been plotted against distance from the source for three selected cases.

Interpretation of the data is complicated by the fact that the ultra-violet spark was within the test chamber. Consequently, changing the test gas also changed the source parameters and constant intensity, and wavelength distribution was not maintained. An attempt to achieve control with windows resulted in failure. CaF_2 with a short wavelength cutoff of about 1250 Å severely reduced the peak ionization density in all gases tested. LiF with a short wavelength cutoff of about 1050 Å allowed only a little more ionization. In both cases, the resulting signals could be barely observed on the CRT. Also the window surfaces were rapidly damaged by the ultra-violet spark, and the transparencies were not expected to remain constant at the original values. In the case of LiF the first few spark discharges resulted in substantial bridge imbalance signals, but not as large as without a window. However, after a few spark discharges, the resulting signal diminished to a barely measureable value. The window deteriorated too rapidly to allow a differential phase measurement.

Limited source control was attempted by purging the tip of the spark source with He by way of a channel cut in the source mounting. The results are illustrated in Figure 5-49 for N_2 and a $CO_2 : N_2 : He = 1 : 1 : 3$ laser mixture. This resulted in a substantial increase in ionization density. However, the purge had to be larger than anticipated (15% to 20% of total flow) and therefore the ionization increase may have been a result of increased transparency. Conditions of a uniform mixture could no longer be assumed since the large independent flow of He could result in a concentration gradient. Consequently, the source purge method was also abandoned.

However, in the case of CO_2 or those mixtures of gases containing CO_2, the photoplasma was controlled by the CO_2 component. Provided the ionizing species is the same in all cases, then it can be assumed that the CO_2 controls the ionizing photons. Furthermore, it can be assumed that the source emission spectrum remains constant as viewed by the gas in the test region. This can be interpreted as, regardless of the source emission spectrum, the CO_2 controls what part of it penetrates to the test region.

CO_2 limited photoionization can be controlled by two bands of photons. With reference to Figure 5-45

(1) A window occurs in CO_2 centered on approximately a wavelength of $\lambda = 1200$ Å. It is about 75 Å wide with values of the absorption cross-section ranging from about 0.7×10^{-19} cm^2 to 3.0×10^{-19} cm^2 [41,42,58].

(2) CO_2 exhibits essentially zero absorption for all wavelengths above approximately $\lambda = 1800$ Å [41,42,58].

The latter case can be eliminated as a possibility because of the lack of absorption suffered by long wavelength photons. Figures 5-46, 5-47, 5-48 and 5-49 indicate that photoelectron density falls off rapidly with increasing pressure, implying a significant absorption. This argument applies equally well for multiple-step ionization as well as single-step ionization. The band of photons available through the CO_2 window around $\lambda = 1200$ Å can be shown to account for the observation in gases containing CO_2. Furthermore, 1200 Å photons are energetic enough to photoionize various types of substances that may be present as impurities in a single-step process. Under these conditions the rate of photoionization in terms of producing electrons is given by [16]:

$$\frac{dn_e}{dt} = \frac{\bar{I}}{h\bar{\nu}} \bar{\sigma}_i n \qquad 5\text{-}46$$

$\bar{I}$ = average photon intensity of those photons responsible for photoionization [ergs $sec^{-1} cm^{-2}$]

h = Planck's constant [6.6×10^{-21} erg sec]

$\bar{\nu}$ = average frequency of those photons responsible for photoionization [sec^{-1}].

$\bar{\sigma}_i$ = average photoionization cross-section [cm^2].

n = number density of the photoionizing species [cm^{-3}].

The solution to Equation 5-46 is:

$$\bar{n}_e = \frac{\bar{I}}{h\bar{\nu}} \bar{\sigma}_i nt \qquad 5\text{-}47$$

Equation 3-75 can be used to calculate the average intensity of a band of photons with an average attenuation coefficient $\bar{\mu}$. The point source characteristic can be incorporated by a L^{-2} multiplicative factor. The resulting equation is:

$$\bar{I} = \frac{\bar{I}_o}{L^2} \exp(-\bar{\mu}\chi) \qquad 5\text{-}48$$

$$\chi = L \frac{P}{760} \frac{273}{T} \qquad 5\text{-}49$$

$$\bar{\mu} = \bar{\sigma}_a n_o \qquad 5\text{-}50$$

$\bar{I}_o$ = average photon intensity at the source for those photons responsible for photoionization [ergs $\sec^{-1}$].

L = distance from the source to the midpoint of the measurement position [cm].

$\bar{\mu}$ = average attenuation constant for those photons responsible for photoionization [cm^{-1}].

χ = distance from the source reduced to conditions of STP.

P = pressure of absorbing species [torr].

T = gas temperature [°K]

$\bar{\sigma}_a$ = average attenuation cross-section of ionizing photons [cm^2].

n_o = Loschmidt's number [2.7×10^{19} cm^{-3}].

Equation 5-47 becomes

$$\bar{n}_e = \frac{\bar{I}_o}{L^2 h\bar{\nu}} \bar{\sigma}_i nt \exp(-\bar{\sigma}_a n_o L \frac{P273}{760T}) \qquad 5\text{-}51$$

Before proceeding, the pressure dependence of n must be determined. There are two possible sources of the ionizing species. One source is the inherent impurities in the gas supply cylinders. Typically, the impurity concentration is a few parts per million [59]. However, only at total pressures above 100 torr, can the cylinder impurities begin to compare to the background impurity pressure in the ionization chamber of at least 1 micron.

In an attempt to locate the source of the ionizing species He was tested after being passed through a cold trap at liquid N_2 temperature. Only a marginal decrease in electron density was observed and no definite conclusion could be drawn based on the test. Hence a constant value for n appears to be a reasonable approximation. Since the pressure of the ionizing species will only be a few microns, absorption due to the impurity will be negligible assuming a conventional absorption cross-section of a few Mb. Also He and N_2 will have negligible absorption in the λ = 1200 Å region under consideration. Therefore, Equation 5-51 applies with P equal to the pressure or partial pressure of CO_2. Since the coefficient of the exponential is constant, then a ratio method can be used to determine $\bar{\sigma}_a$.

$$\bar{\sigma}_a = \frac{760\ T\ \ln n_{e1}/n_{e2}}{n_o\ L\ 273\ (P_2 - P_1)} \qquad \text{5-52a}$$

Any two points on the straight line asymptotes to the curves involving CO_2 can be used in conjunction with Equation 5-52a. The resulting values appear in Table 5-9, and are seen to agree very well with those available in the literature [41,42,58] and Figure 5-45.

The rapid fall-off for low pressures may be due to an expanded window that rapidly diminishes. Shorter wavelength photons are able to penetrate

Table 5-9

Photoabsorption Cross-Section in CO_2

Source	$\bar{\sigma}_a$ [cm^2]
CO_2	2.2×10^{-19}
$CO_2 : N_2 : He = 1 : 1 : 1$	2.9
$CO_2 : N_2 : He = 1 : 1 : 3$	2.9
$CO_2 : N_2 : He = 1 : 1 : 8$	2.5

$\bar{\bar{\sigma}}_a = 2.6 \times 10^{-19}$

Photoabsorption cross-section for photons in the $\lambda = 1200$ Å CO_2 window. These values are derived from Figure 5-47 with Equation 5-52a.

to the required depth at low pressures, but suffer more serious attenuation with increasing pressure. Alternate arguments are also valid, however. If the impurity concentration in the supply cylinder was larger than specified by the supplier, (such an incident occurred) then the ionizing species would increase with pressure, resulting in a slower decrease in ionization density with increasing pressure, than otherwise would have occurred. This phenomenon would manifest itself in the form of ever decreasing absorption coefficients with pressure. The same argument applied to He would predict an increase with the pressure. However, this was not observed. A second argument involves the emission spectrum of He. At high current densities two He continua may be excited. The Hopfield continuum (550 Å to 1000 Å) is found at pressures up to 100 torr, while the (1000 Å to 4000 Å) Huffman continuum dominates at higher pressures [57,60,61]. There may be some very narrow regions of reduced absorption in CO_2 for $\lambda < 1000$ Å [42]. Consequently, the short wavelength, Hopfield continuum may be responsible for ionization for $P < 100$ torr. At higher pressures only longer wavelength photons may be available for the Huffman continuum, and these may be passed through the 1200 Å window to account for the photoionization. This argument could account for an increase in electron density when the source was covered with He as in Figure 5-49. In fact, it was this reasoning that prompted the use of He as a cover gas. However, measurements performed later which now appear in Figure 6-1 do not reveal the expected continuum in spite of having exceeded the minimum required spark current density of 30,000 $\mathring{A}$ cm^{-2} [39,62].

Returning to the determination of photoabsorption cross-sections, a consideration of laser mixtures with additives is in order. Figure 5-48 reveals that all plasma density versus total pressure curves involving additives, can be approximated by two straight lines. The straight line approximation for pressures up to 300 torr yield an average photoabsorption cross-section of $\bar{\sigma}_a \simeq 1.9 \times 10^{-19}$ cm^2 for all additives except benzene. This value is consistent with a limited photoionization process, where photons in the CO_2 window at $\lambda = 1200$ $\mathring{A}$ are responsible for the ionization in a one-step process. The ionization potentials of the additives under consideration are given in Table 5-10. None of the ionization potentials violate the possibility of one-step photoionization with photon wavelengths in the neighbourhood of 1200 $\mathring{A}$.

The situation is somewhat different for pressures above 300 torr. In this region the curves can be approximated by a straight line which is characterized by a photoabsorption cross-section of $\bar{\sigma}_a = 4.5 \times 10^{-20}$ cm^2. This coefficient is too small to account for the absorption that would be suffered in the CO_2 window at

Table 5-10

Ionization Thresholds of Some Gases and Vapors [37]

Substance		Ionization Potential (eV)	Ionization Potential (Å)
Helium	He	24.58	504.3
Neon	Ne	21.56	574.9
Argon	Ar	15.76	786.7
Krypton	Kr	14.00	885.6
Methane	CH_4	12.98	955
Nitrous Oxide	N_2O	12.90	961
Xenon	Xe	12.13	1022.1
Chlorine	Cl_2	11.48	1080
Methyl chloride	CH_3Cl	11.28	1099
Ethyl chloride	C_2H_5Cl	10.98	1129
Isobutane	C_4H_{10}	10.57	1173
Hydrogen sulfide	H_2S	10.46	1185
Ethyl bromide	C_2H_5Br	10.29	1205
Boron trifluoride	BF_3	10.25	1210
Ethyl acetate	$CH_3COOC_2H_5$	10.11	1226
Carbon disulfide	CS_2	10.08	1230
Nitrogen dioxide	NO_2	9.78	1268
Acetone	$(CH_3)_2CO$	9.69	1279
Iodine	I_2	9.28	1336
Nitric oxide	NO	9.25	1340
Benzene	C_6H_6	9.25	1340
Methyl amine	CH_3NH_2	8.97	1382
Ethyl amine	$C_2H_5NH_2$	8.86	1400
t-Butyl amine	$(CH_3)_3CNH_2$	8.64	1435
Di-methyl amine	$(CH_3)_2NH$	8.24	1505
Di-ethyl amine	$(C_2H_5)_2NH$	8.01	1548
Tri-methyl amine	$(CH_3)_3N$	7.82	1585
Tri-ethyl amine	$(C_2H_5)_3N$	7.50	1653
Tri-*n*-propyl amine	$(C_3H_7)_3N$	7.23	1715

---

[a] The ionization potentials for all gases and vapors with the exception of BF_3 and the rare gases were obtained from K. Watanabe, T. Nakayama, and J. Mottl, *J. Quant. Spectrosc. Radiat.* Transfer **2**, 369 (1962); BF_3 from B. Kaufman, *Phys. Rev.* **78**, 332 (1950); Rare gases from C. E. Moore, Natl. Bur. Std. (U.S.), Circ. **476**, Vol. 1 (1949), Vol. 2 (1952), Vol. 3 (1958).

λ = 1200 Å. Such an absorption cross-section is obtained in CO_2 only for photons with wavelengths greater than 1700 Å or 1800 Å [41,42,58]. With the possible exception of tri-n-propyl amine all additives have shorter ionization wavelengths than these. Consequently, a two or multiple-step process appears to be responsible for photoionization of these additives at total pressures above approximately 300 torr.

In the preceding analysis the additive densities have been assumed to remain constant with pressure. Of course each independent additive will have its own optimum concentration. The optimum concentration will be dependent on the additive's relative photoionization and photoabsorption cross-sections. The foregoing analysis implicitly assumes that additive photoabsorption is negligible compared to the CO_2 photoabsorption. This condition will be satisfied for low additive concentrations.

As mentioned earlier, gas pressure and absorption pathlength are synonymous in terms of photoionization cross-sections. In fact, photoabsorption cross-sections derived from Figure 5-50 are in very good agreement with those obtained from Figure 5-48. The same implications about the photoionization mechanisms are also obtained. The same conditions of CO_2 limited absorption are assumed to apply for Figure 5-50. As in the case for additives in Figure 5-48, the photoionization appears to result from two absorption bands. A short range process accounts for ionization close to the source and a long range process dominates farther away from the source. Such a situation can be described by the summation of two terms, each like that in Equation 5-51. Only the absorption and ionization cross-sections will be different. Such a relationship can be written as follows:

$$\bar{n}_e = \frac{A_s\bar{\sigma}_{is}}{L^2} \exp\left(-\bar{\sigma}_{as} \frac{n_o L\ P273}{760T}\right) + \frac{A_\ell\bar{\sigma}_{i\ell}}{L^2} \exp\left(-\bar{\sigma}_{a\ell} \frac{n_o L\ P273}{760T}\right) \qquad 5\text{-}52$$

$$A_{s(\ell)} = \frac{\bar{I}_{os(\ell)}}{h\bar{\nu}_{s(\ell)}}\, nt \qquad 5\text{-}53$$

$\bar{\sigma}_{is}$ and $\bar{\sigma}_{as}$ are the photoionization and photoabsorption cross-sections for a band of short wavelength photons. $\bar{\sigma}_{i\ell}$ and $\bar{\sigma}_{a\ell}$ are the corresponding parameters for a band of long wavelength photons. At short distances the first term can be expected to dominate, because of the relatively large photoionization cross-section value assumed for high energy short wavelength photons. At the longer distances, the short wavelength photons will have suffered severe attenuation and the second term can be expected to dominate. Equation 5-52 is then expected to apply one term at a time in the limit of short and long values of L. The short and long range absorption coefficients can be obtained by a ratio method and any two points, (n_{e1}, L_1) and (n_{e2}, L_2) taken from the appropriate portion of the plasma density versus distance curves.

The appropriate ratio equations are:

$$\bar{\sigma}_{as} = \frac{760T}{n_o} \ln \frac{n_{e1} L^2 / n_{e2} L_2^2}{P_{273} (L_2 - L_1)} \qquad 5\text{-}54$$

$$\bar{\sigma}_{a\ell} = \frac{760T}{n_o} \frac{\ln n_{e1} L_1^2 / n_{e2} L_2^2}{P273 \ (L_2 - L_1)} \qquad 5\text{-}55$$

The photoabsorption cross-sections thus obtained appear in Table 5-11 (a). The values obtained for the short wavelength photoabsorption cross-sections correspond to values expected for a narrow window around $\lambda = 1200$ Å [58]. The value of the long range photoabsorption cross-section is too small to attribute to absorption in the $\lambda = 1200$ Å window. However, the value corresponds to absorption at $\lambda \simeq 1700$ Å. Since the ionization potential of tri-n-propyl amine is $\lambda = 1715$ Å [37] then the assumed one-step photoionization is a borderline case and in fact the photoionization may be due to a two or multiple-step process [23]. If one were to consider the absorption of long wavelength photons by tri-n-propyl amine as well as CO_2, the actual photoabsorption cross-section at $\lambda = 1700$ Å may be larger than the one calculated from the data. In such a case the long wavelength photon may have to have a wavelength much larger than 1715 Å, in order to achieve an absorption cross-section comparable to the experimental value. This would preclude one-step photoionization as the long range mechanism.

A simplified approach to obtaining the short and long range absorption cross-sections can be obtained by considering the plasma density dependence on distance for He in Figure 5-50. This curve does not follow a L^{-2} law appropriate to a point source, indicating that the source is somewhat directional. As an approximation the source can be considered to be entirely collimated. Equations 5-52, 5-54 and 5-55 would apply with the Ls removed. The curves for the laser mixtures and tri-n-propyl amine in Figure 5-50, could each be approximated by two straight line segments drawn asymptotic to the curves at the shortest and longest distances over which the data extends. The resulting values appear in Table 5-11(b). These values are a little higher than those in Table 5-11(a) but the difference is not so great as to disallow the previous argument.

Having developed a somewhat empirical understanding of photoionization, Equation 5-52 can be used in conjunction with Figures 5-48 and 5-50 as an aid in designing photopreionized doped CO_2 lasers. For similar ultra-violet spark sources, the coefficients can be obtained from Figure 5-48. The experimental range of PL values covered by Figures 5-48 and 5-50 is large enough to cover most situations encountered in a typical laser device. Presumably the curves can be extrapolated to atmospheric pressure as well. However, for different sources, the equation is of limited use since the photon

Table 5-11

Short and Long Range Photoabsorption Coefficients

(a)

Pressure [torr]	Environment	Range [cm]	$\bar{\sigma}_{as}$ [cm^2]	$\bar{\sigma}_{a\ell}$ [cm^2]
200	CO_2 : N_2 : He = 1 : 1 : 3	$\lesssim$ 17	1.7×10^{-19}	
	+ tri-n-propyl amine	$\gtrsim$ 17		4.0×10^{-20}
200	CO_2 : N_2 : He = 1 : 1 : 1	$\lesssim$ 13	0.83×10^{-19}	
	+ tri-n-propyl amine	$\gtrsim$ 13		4.8×10^{-20}

(b)

Pressure [torr]	Environment	Range [cm]	$\bar{\sigma}_{as}$ [cm^2]	$\bar{\sigma}_{a\ell}$ [cm^2]
200	CO_2 : N_2 : He = 1 : 1 : 3	$\lesssim$ 15	3.5×10^{-19}	
	+ tri-n-propyl amine	$\gtrsim$ 22		8.8×10^{-20}
200	CO_2 : N_2 : He = 1 : 1 : 1	$\lesssim$ 11	2.3×10^{-19}	
	+ tri-n-propyl amine	$\gtrsim$ 16		8.9×10^{-20}

Table continued on next page

Table 5-11 continued

Short ($\bar{\sigma}_{as}$) and long ($\bar{\sigma}_{a\ell}$) range absorption cross-sections are derived for tri-n-propyl amine in 2 laser mixtures.

(a) Assuming a point source with a L^{-2} dependence.

(b) Assuming a collimated source. The "Range" values indicate the range over which the tabulated photoabsorption coefficient dominates.

output would have to be measured as well as the appropriate photoionization cross-sections, in order to determine the value of the coefficients.

This leads to the most important application of Equation 5-52. It can be used to determine the average photoionization cross-sections in the CO_2 limited ionization bands. This would require a measurement of n and I_o to obtain the coefficient A, for Equation 5-53. n could be easily obtained in a non-flowing system, and I_o could be obtained with a photomultiplier sensitized to ultra-violet with a phosphor such as sodium salicylate. A knowledge of the photoionization cross-sections of these additives would facilitate the design of CO_2 lasers to a much greater extent than the semi-empirical application of Equation 5-52.

It should be pointed out, that for very intense ultra-violet sources, photogeneration of plasma will be rapid, and large initial densities would be predicted by Equation 5-52. In practice, these densities may never be reached because of the stabilizing effect of recombination and/or attachment for large electron densities (diffusion is too slow to be considered here). In these cases the loss mechanisms would have to be accounted for in Equation 5-46.

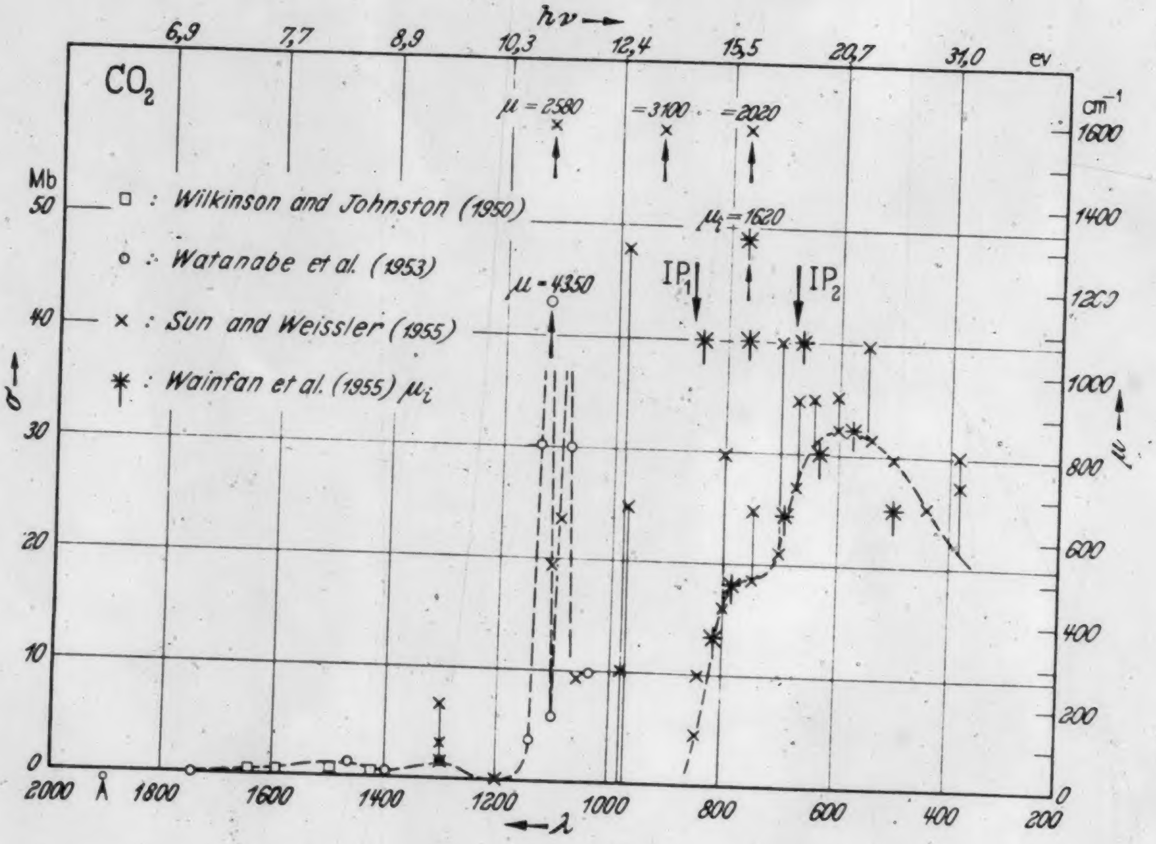

FIGURE 5-45 PHOTOABSORPTION CHARACTERISTICS OF CO$_2$ [42]

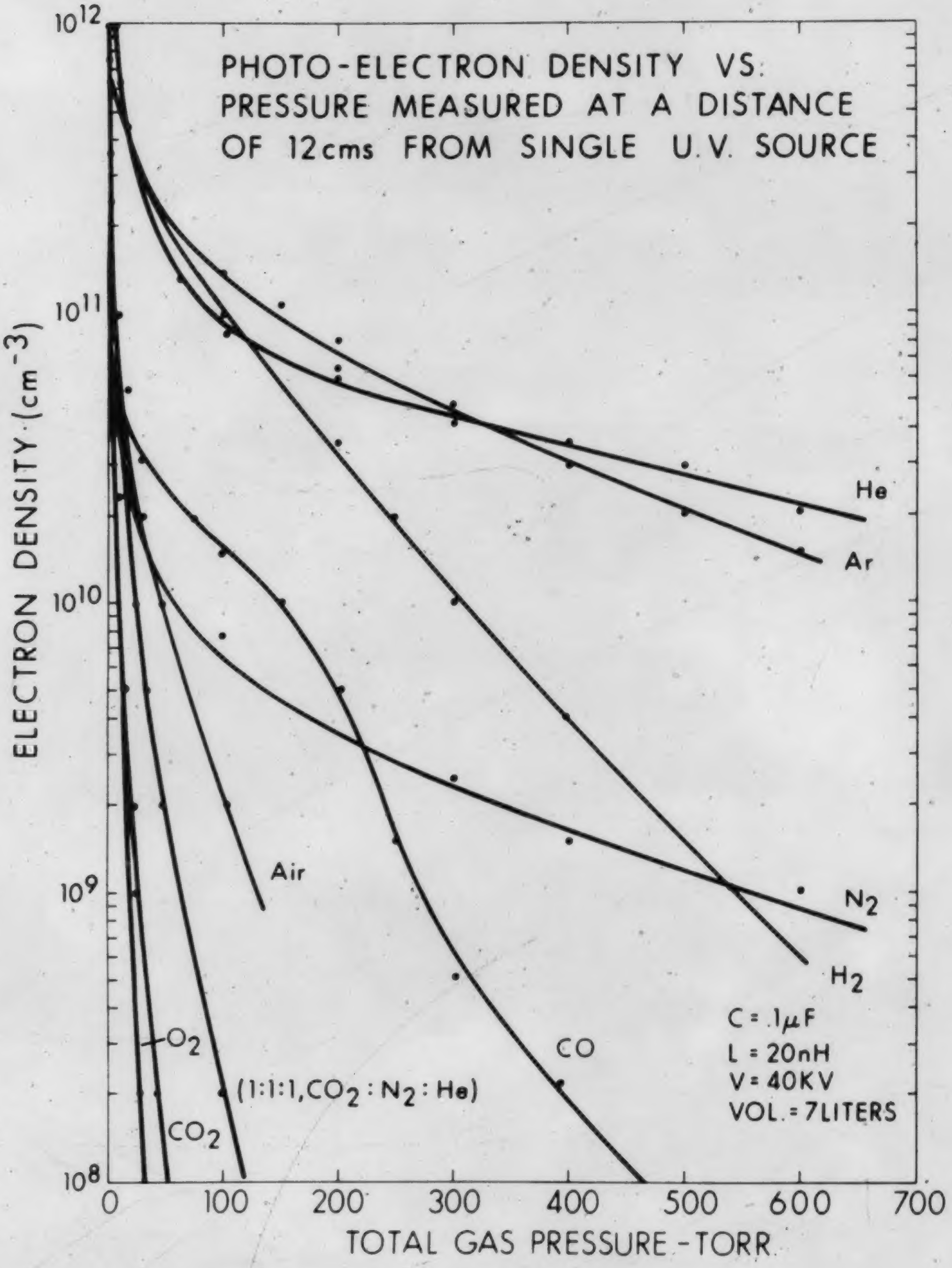

Figure 5-46 Photoelectron Density Versus Gas Pressure for Various Gases

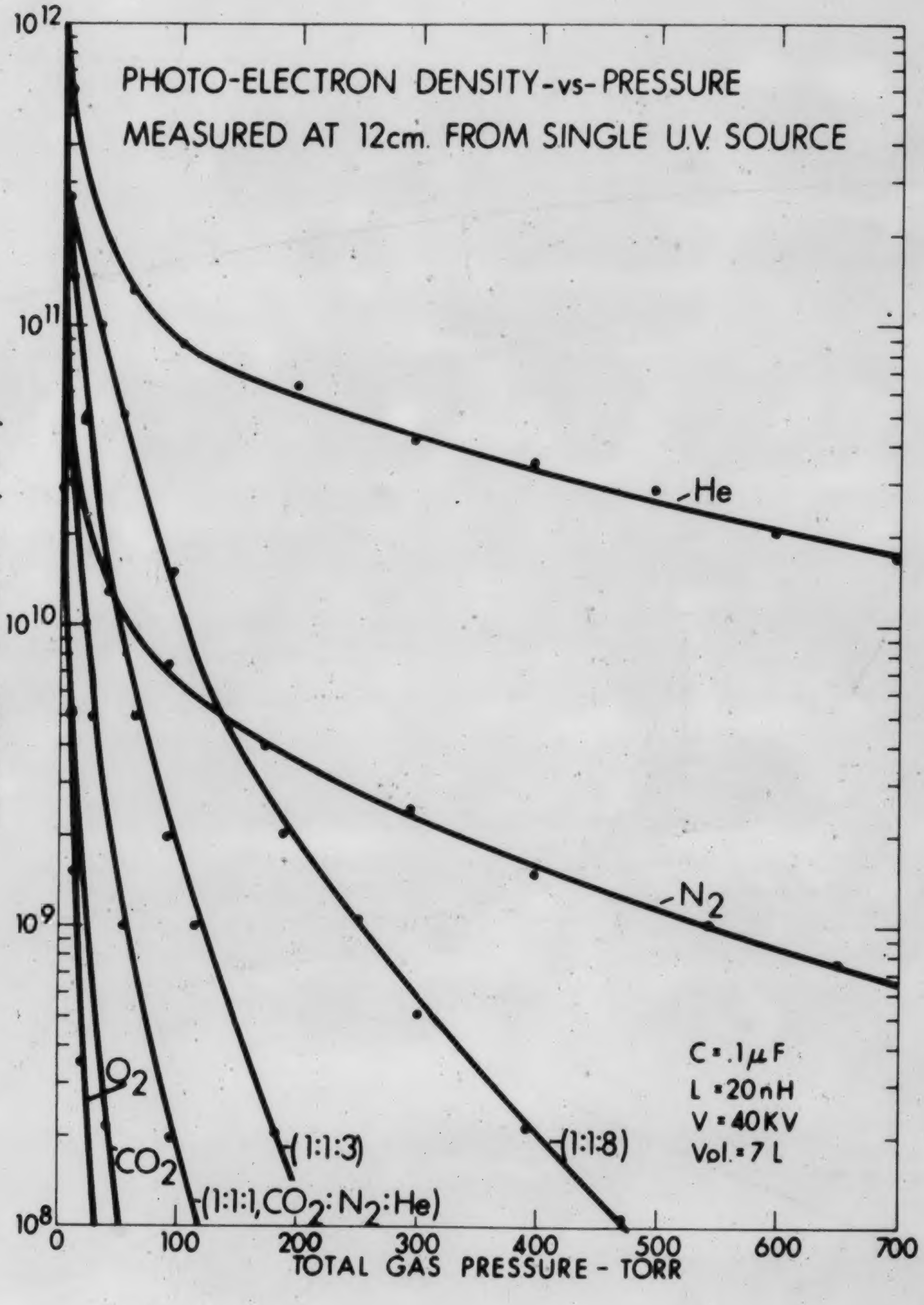

FIGURE 5-47 PHOTOELECTRON DENSITY VERSUS TOTAL PRESSURE FOR VARIOUS LASER MIXTURES

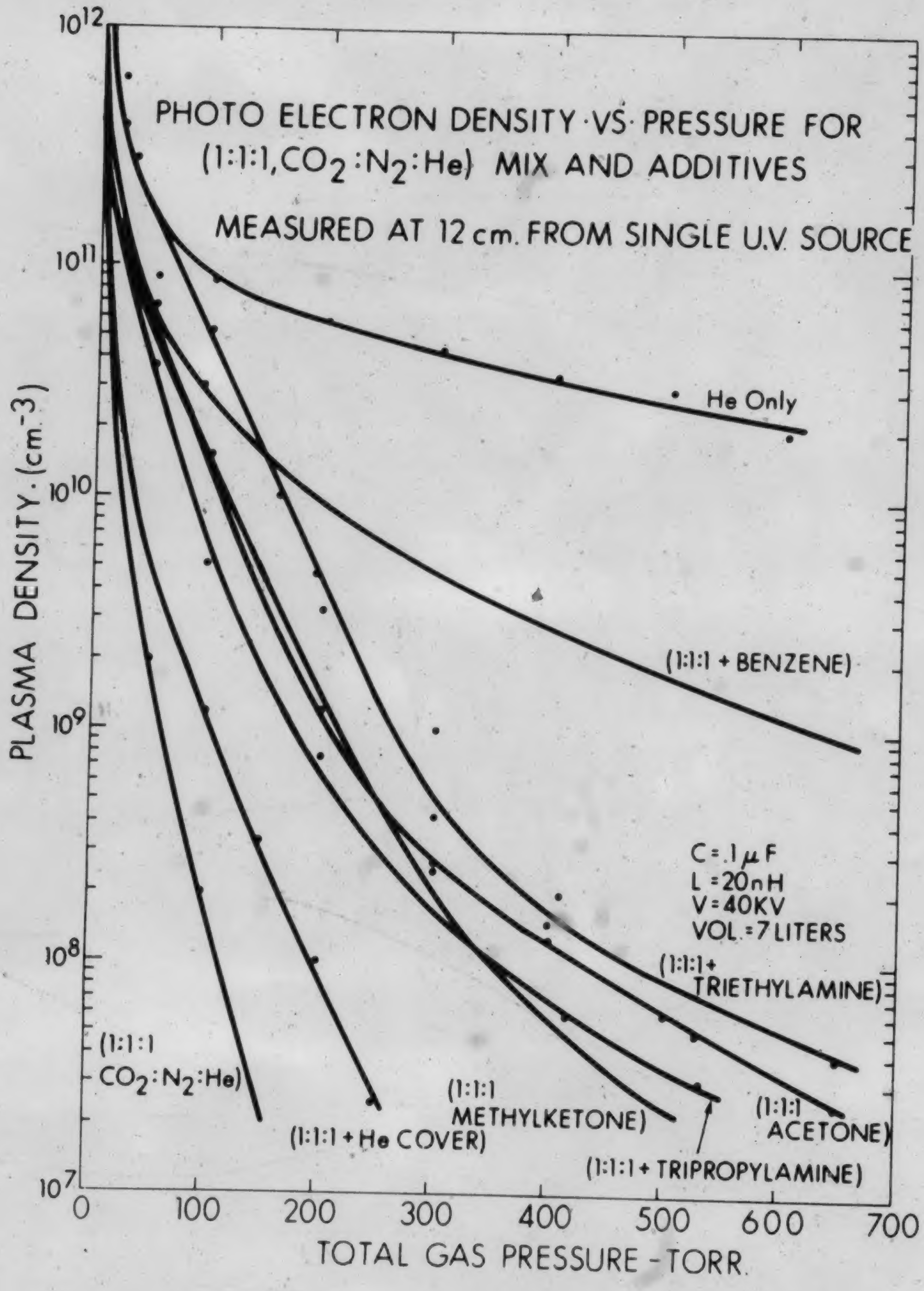

FIGURE 5-48 PHOTOELECTRON DENSITY VERSUS TOTAL PRESSURE FOR A $CO_2:N_2:He$ = 1:1:1 LASER MIXTURE WITH SELECTED ADDITIVES

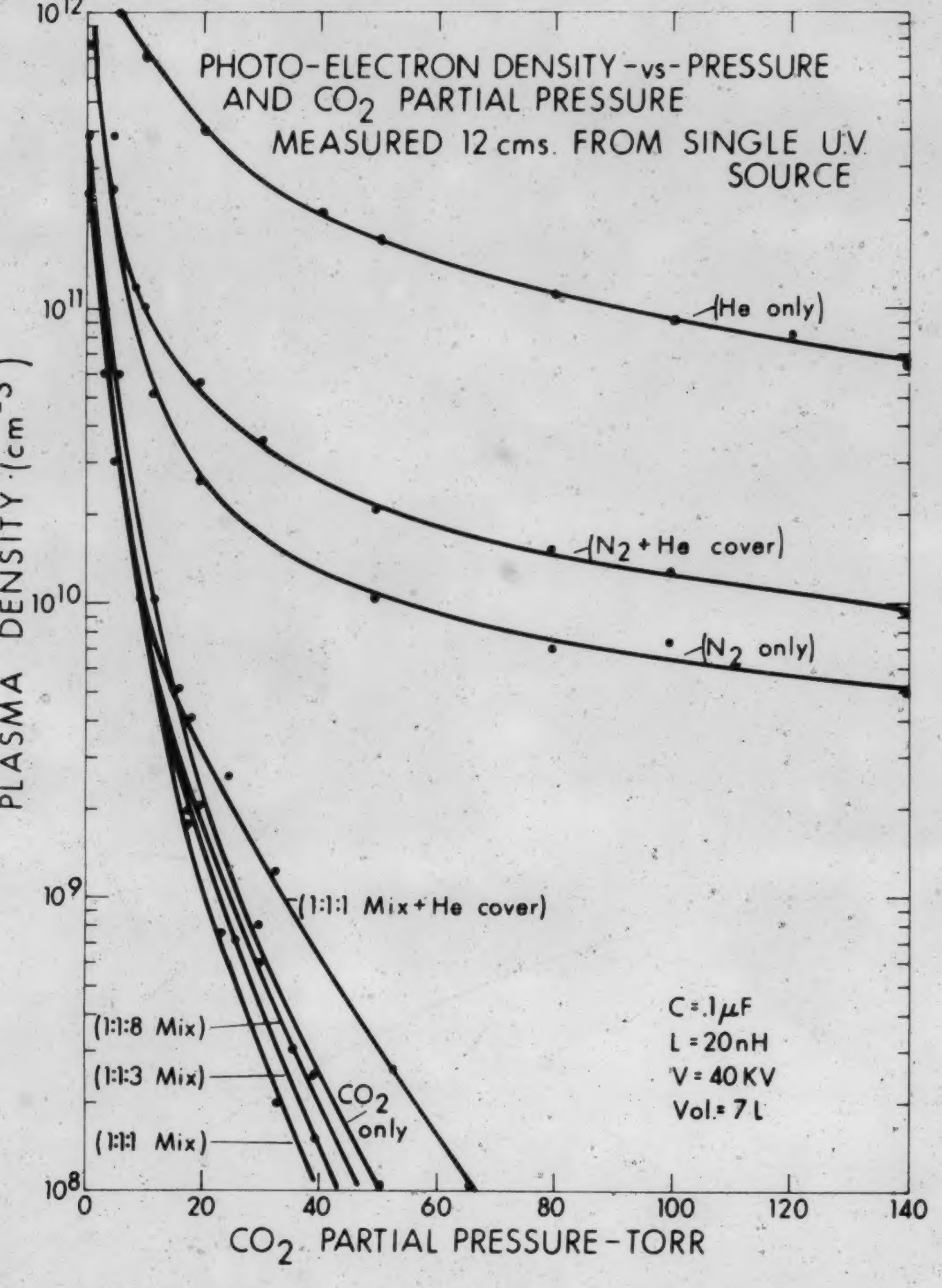

FIGURE 5-49 PHOTOELECTRON DENSITY VERSUS CO_2 PARTIAL PRESSURE FOR LASER MIXTURES This reveals the influence of He cover gas and dependence of photoelectron density on the CO_2 concentration.

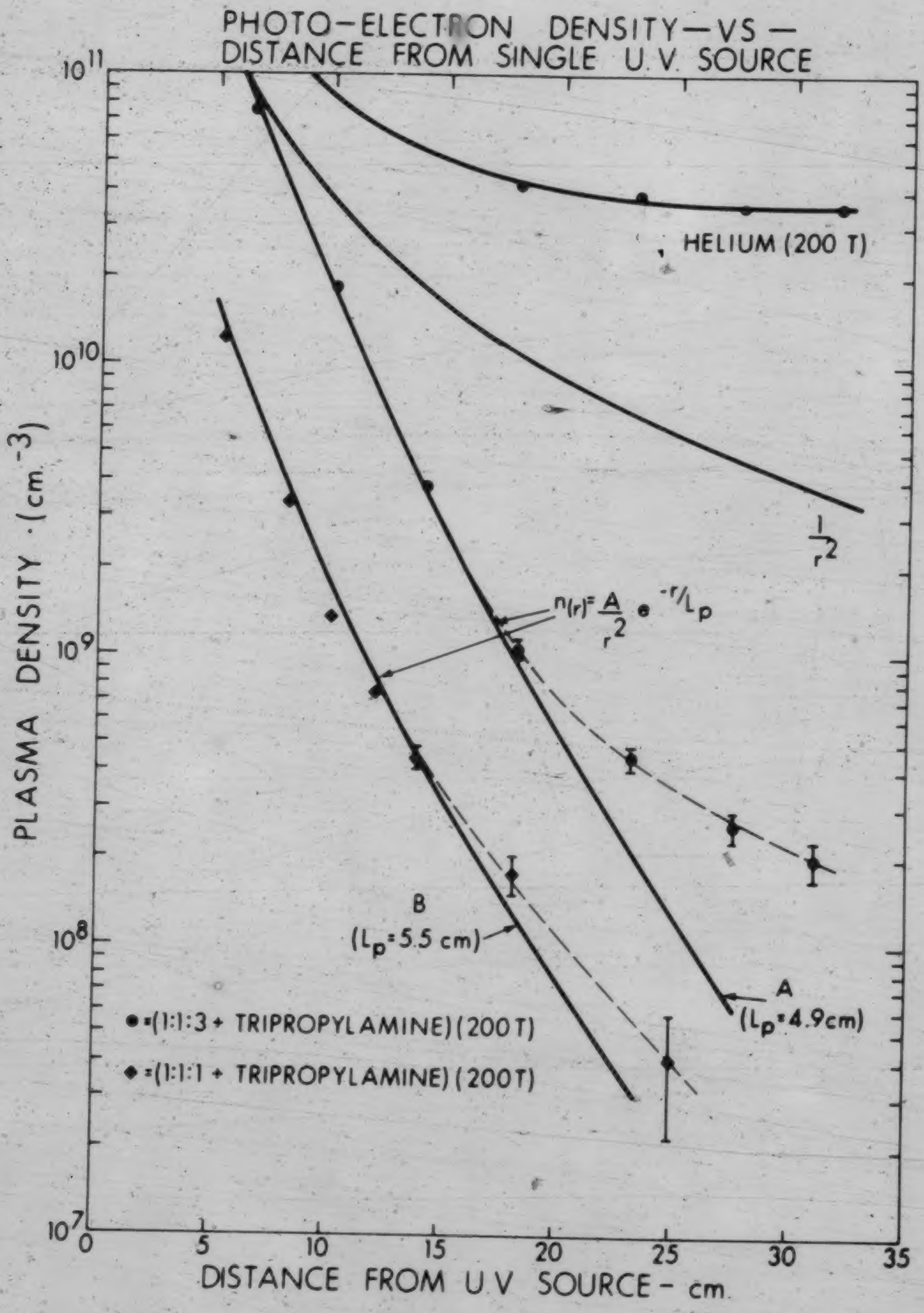

Figure 5-50 Variation in Photoelectron Density with Distance from a Single Ultra-Violet Source in Laser Mixtures plus Tri-n-propyl Amine

5-7. Investigation of Source Parameters.

Various source parameters were investigated in an attempt to develop an understanding of the ultra-violet photon production of the spark source employed. Attempts to isolate the source from the test gas in the ionization chamber with windows, or a source purge method, were unsuccessful as discussed in the previous section. Consequently, the conditions in the test chamber and therefore in the spark had to be standardized. Since He consistently yielded a high photoelectron density, differential phase measurements could be obtained with relative ease. In addition, at this stage of the project, it was still assumed that the Huffman continuum in He, was largely responsible for the production of ionizing photons in any mixture of gases containing over 100 torr of He (however, Figure 6-1 does not support this assumption). For these reasons He was chosen as the standard. A pressure of 400 torr was chosen as an approximation to the partial pressure of He in a typical laser device. Furthermore, a high pressure is required since the condensed spark discharge spectrum can be expected to be different at low pressure [37]. The measurement was performed at a distance of 12 cm from the source to simulate conditions in a typical laser device. The initial photoplasma density was measured for all tests, and is used as the "common denominator" by which the results of various tests can be compared.

The R.L.C. driving circuit is illustrated in

Figure 3-4. For the standard conditions of V = 40 kV and C = 0.1 μf, various spark source devices were tested. In addition to those illustrated in Figure 3-3 and discussed in that section, 1/8 inch diameter tungsten pins ground to a point were also tested. The pins were each 6 inches long and they lay in the same straight line with the separation distance adjustable. No change in photoplasma density was detected for all pin separations tested. (1 mm to 6 mm). The performance of the tungsten pins was improved by using the geometry illustrated in Figure 3-3(b) Here again the pin separation distance did not seem to play a significant role. The improvement was attributed to reduced circuit inductance. A coaxial source geometry in the form of a standard surface-gap automotive-type spark plug was found to yield an increase in photoplasma density approaching an order of magnitude [57]. The geometry of the device illustrated in Figure 3-3(c) is similar to that used in plasma focus devices, and the increased photoplasma density may be due in part to increased current density in the spark [63,64]. Reduced circuit inductance may also play a part. Further improvement by a factor of 2 or 3 was obtained with the device illustrated in Figure 3-3(a) The photoplasma density is increased as the adjustable center electrode (tungsten) is pulled back until it is about 1 cm from the face of the spark plug. Further separation does not have a significant effect on the performance. Devices with 1/8 inch and 1/16 inch center electrodes were tested and no measureable differences were observed. The improved performance observed here and in the case of the standard automotive surface-gap spark plug, may be partly due to the ceramic surface discharge inherent in these devices. Such discharges at high current are known to promote hard ultra-violet emissions [37,57].

In spite of the improved performance in the last instance, the standard surface-gap automotive spark plug was used as the source for the entire project. Commercial availability, low cost and extreme durability in addition to good performance were the features that dictated the choice. Capacitor values in excess of 0.1 μf charged to 50 kV could be discharged through these plugs many times without marked deterioration. With the spark source geometry established, photoplasma density was measured for various values of capacitance and charging voltage used to drive the spark source. The results appear in Figure 5-51. The energy for each voltage and capacitance point has been determined, and plasma density versus energy is plotted in Figure 5-52.

$$\varepsilon = \frac{1}{2} CV^2 \qquad 5\text{-}56$$

ε = energy [joules]

C = capacitance [farads]

V = voltage [volts]

Figure 5-51 reveals that the plasma density is directly proportional to the charging voltage for the values of capacitance and voltage considered. For a typical R.L.C. discharge circuit such as that used to drive the spark source, the maximum value of the discharge current is given by [74,82]:

$$I_{max} = V_o\left(\frac{C}{L}\right)^{1/2} \qquad 5\text{-}57$$

L = equivalent circuit inductance [henries]

which is an approximation of Equation 3-1.

It reveals that the maximum current is proportional to the charging voltage. Consequently, it can be assumed that the plasma density is proportional to the peak current. Furthermore, it can be assumed that photon production is proportional to peak current since, for a one-step photoionization process, plasma density is proportional to photon intensity.

It can be concluded that efficient operation of the spark source requires high discharge current. This can be accomplished by using high voltage, large capacitance and low inductance circuitry. Figure 5-52 shows that plasma density increases with input energy. It also reveals that for a given amount of energy, the most efficient way of delivering it is with small capacitor values, implying a need for high voltage. Figure 5-53 reveals the detrimental effect of high circuit inductance. The curve on the lower part of the plot is for a poor quality, high inductance capacitor. Other than for the last result the circuit inductance was assumed to remain constant, being controlled by the circuitry rather than by the parasitic inductance of the capacitors. Two 0.1 μf low inductance (20 nh) capacitors were available. These were placed in series and parallel to obtain the 0.05 μf and 0.2 μf values respectively. The inductance contributed by the capacitor was never more than 40 nh. The constant circuit inductance was assumed to be much larger than that. Later, analysis of discharge current waveforms obtained with a Ragowski probe proved the assumption to be valid. A photograph of a typical discharge current waveform appears in Figure 5-2.

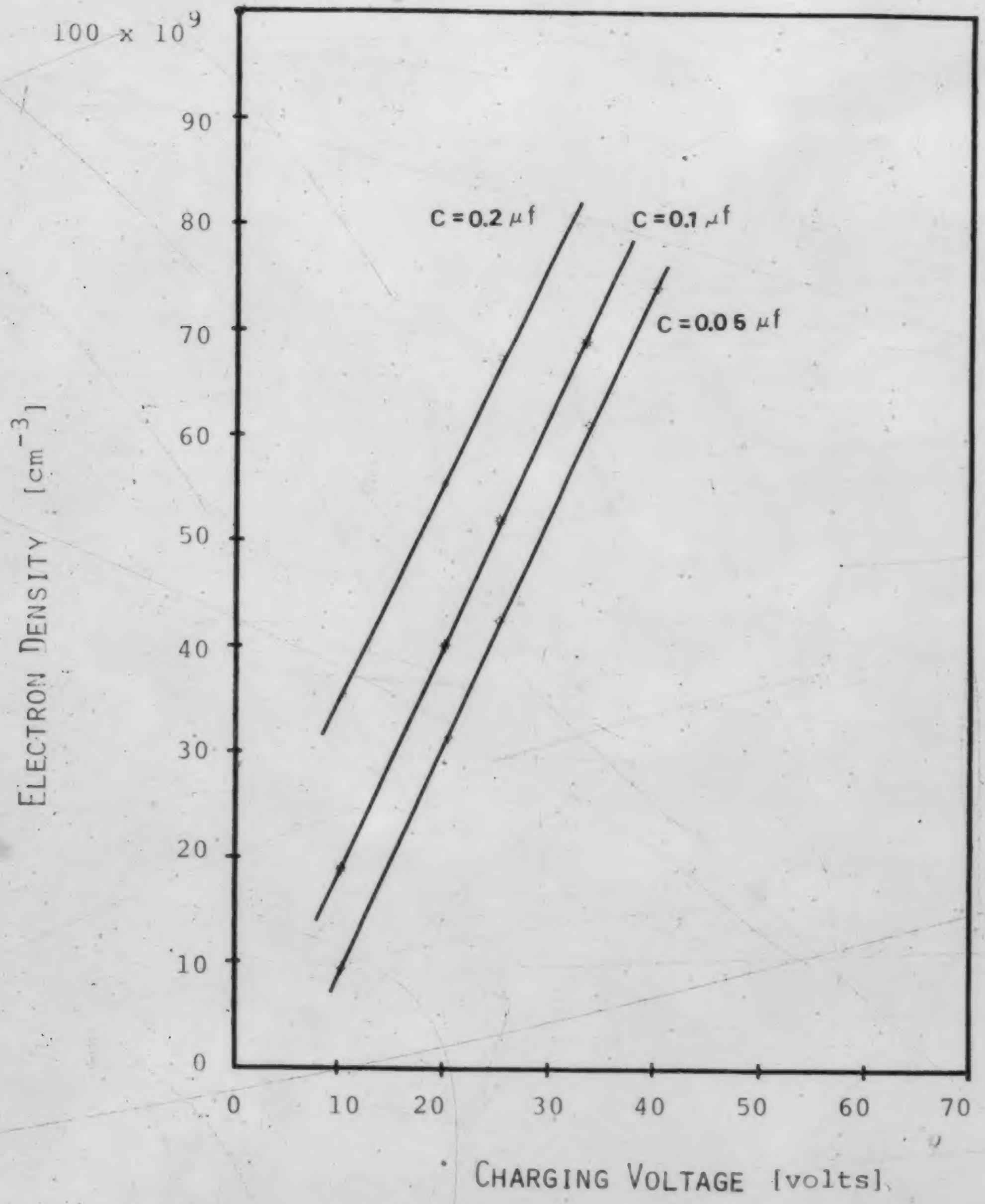

Figure 5-51 Electron Density Versus Charging Voltage for Various Capacitors

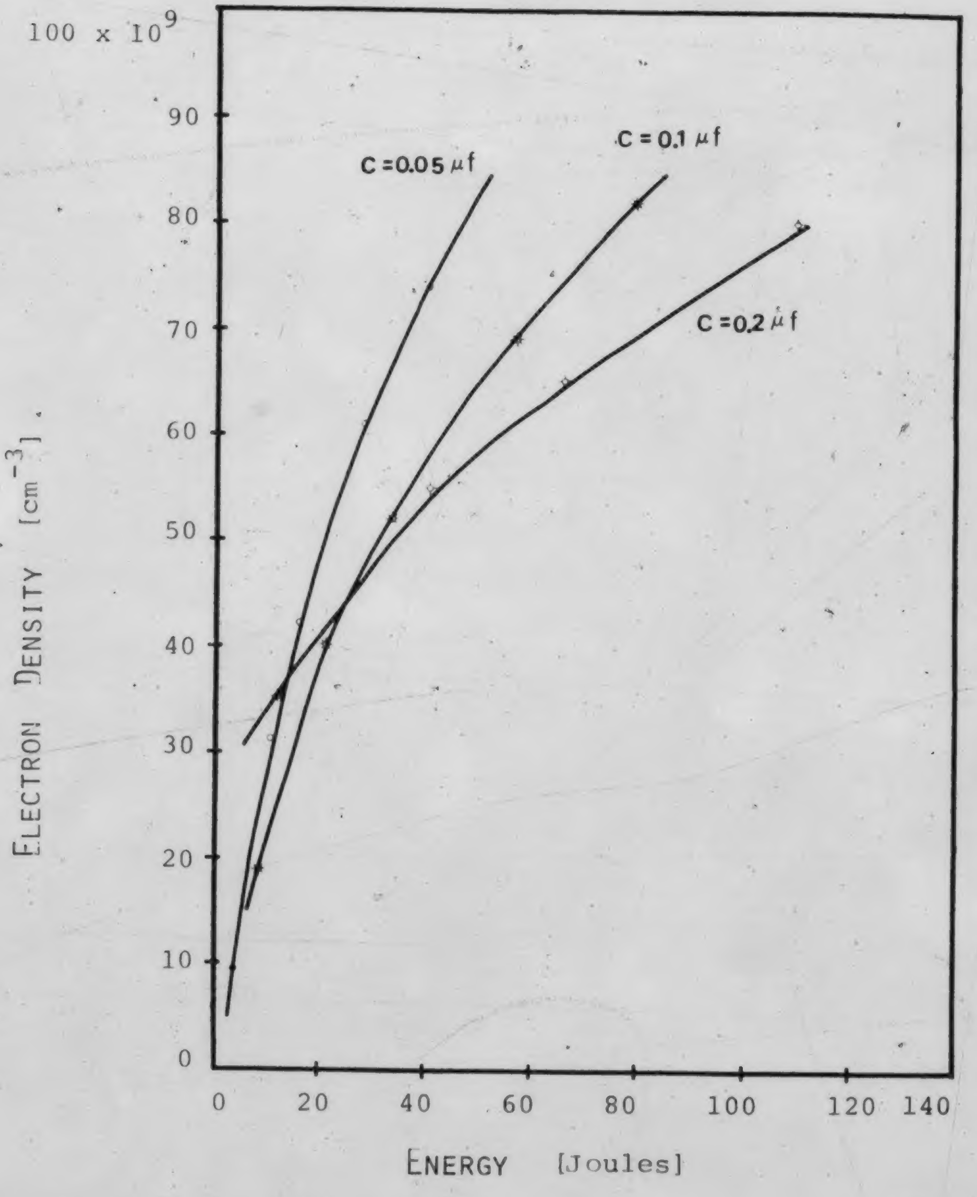

FIGURE 5-52 ELECTRON DENSITY VERSUS ENERGY STORED IN THE CAPACITOR

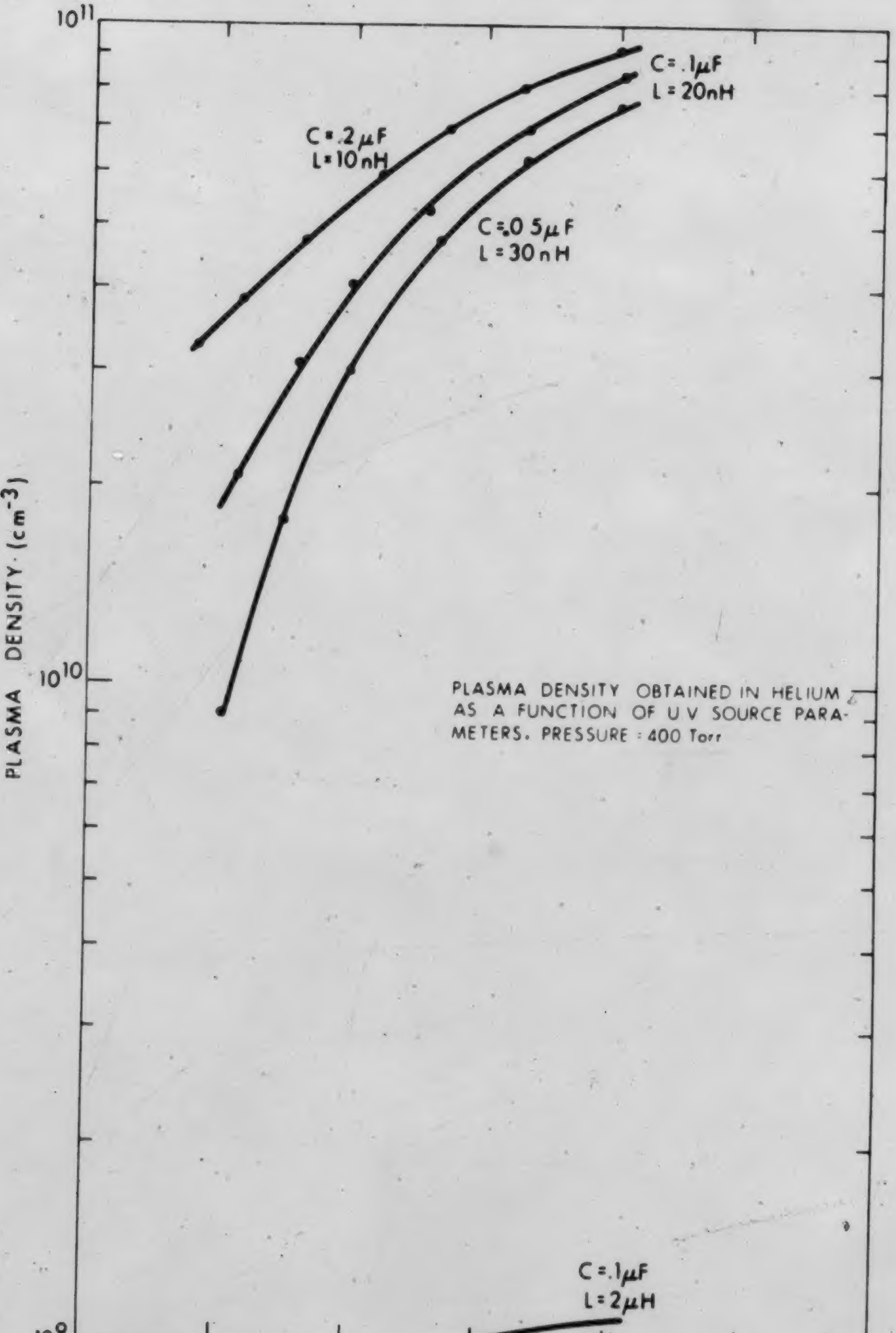

FIGURE 5-53 SEMI-LOG PLOT OF ELECTRON DENSITY VERSUS CHARGING VOLTAGE This reveals the detrimental effect of a high inductance spark driving circuit.

5-8. Validity of Method

Microwave plasma diagnostic techniques are attractive when working with low density plasma, as encountered in this project. These techniques typically offer good sensitivity and relative ease of analysis. However, complications develop when the plasma is located in a buffer gas at high pressure. Under these conditions the number of electron collisions with the neutral gas particles can be large. The electron collision frequency increases linearly with gas pressure and in so doing becomes more significant.

A number of conflicting factors had to be considered in the design of the test facility. In order to achieve good sensitivity for low plasma density diagnostics, a low test frequency was required. However, this conflicted with the requirement that the test frequency be higher than the electron collision frequency in order to simplify the analysis. In addition, as the test frequency is reduced, the dimension of the waveguide interferometer components become prohibitively large. Consequently, an X-band system frequency was selected as the best compromise among these considerations [60,71,72].

Although the electron collision frequency can be accounted for theoretically, it was very difficult to determine experimentally. Calculations show that for the majority of the data obtained, the electron collision frequency can be ignored without unacceptable error.

Equations 3-28 and 3-32 can be used in conjunction with Equation 3-34 in order to obtain the following relationship:

$$\Delta\phi = \frac{\omega}{c}\int_{o}^{L}\left[1 - \left\{\frac{1}{2}\left(1 - \frac{\omega_p^2}{\omega^2+\nu^2}\right) + \frac{1}{2}\left[\left(1 - \frac{\omega_p^2}{\omega^2+\nu^2}\right)^2 + \left(\frac{\omega^2}{\omega^2+\nu^2}\cdot\frac{\nu}{\omega}\right)^2\right]^{\frac{1}{2}}\right\}^{\frac{1}{2}}\right] dx \qquad 5\text{-}58$$

where ω_p is given by Equation 3-24. Equation 5-58 can be reduced to an algebraic equation by considering the electron density distribution to be a constant. However, the ensuing reduction of the equation to determine the electron density as a function of the other variables results in a multi-term equation. Such an equation would not be particularly suitable for the present purpose. Alternatively Equation 5-58 can be simplified for two limiting cases and solutions obtained more readily.

First Case

The significance of the electron collision frequency can be determined for those cases where it becomes approximately equal to the test frequency. Setting $\nu = \omega$ in Equation 5-58 and maintaining the above cut-off requirement of $\omega^2 >> \omega_p^2$ an approximate solution to Equation 5-58 is:

$$\bar{n}_e = \frac{4\varepsilon_o mc\omega\Delta\phi}{e^2 L} \qquad 5\text{-}59$$

By comparison to Equation 3-52 it can be concluded that if the electron collision frequency is approximatly equal to the test frequency then neglect of the electron collision frequency results in underestimating the plasma density by a factor of 2. For CO_2 the collision cross-section (q_m) (strictly the collision cross-section for momentum transfer) for room temperature electrons is about 8×10^{-15} cm^2. [41]. Use of Equation 3-12 results in

$$\nu = 3 \times 10^9 \, P_{CO_2} \quad \text{[rad/sec]} \qquad 5\text{-}60$$

P_{CO_2} = pressure or partial pressure of CO_2 [torr].

For a test frequency of 6×10^{10} rad/sec a CO_2 pressure of 20 torr is required before an error by a factor of 2 is encountered. Since the pressure of CO_2 never exceeded approximately 40 torr the error can be considered acceptable from this point of view for tests involving only CO_2 or mixtures without additives. By the same method the pressures at which a factor of 2 error may be introduced have been determined for the other independent gases and these appear in Table 5-12 [41,56].

Second Case

The error resulting in a situation for which the electron collision frequency is much greater than the test frequency can be determined by solving Equation 5-58 for such a condition. An approximate solution for $\omega_p^2 << \omega^2 << \nu^2$ is:

$$\bar{n} = \frac{2\varepsilon_o m c \nu \Delta\phi}{e^2 L \omega} \qquad 5\text{-}61$$

where all higher order terms have been neglected. By comparison to Equation 3-52 it can be concluded that, for electron collision frequencies exceeding the test frequency, neglecting the electron collision frequency results in underestimating the plasma density by a factor of ν^2/ω^2. This requires an electron collision frequency of about 2×10^{11} rad/sec to establish an error of one order of magnitude. For CO_2 Equation 5-60 predicts that such an error may occur when the pressure reaches about 70 torr. Values for the other gases have been found by the same method and appear in Table 5-12.

Just as CO_2 was found to set the limits for photoabsorption and hence photoionization in 5-7 it also appears to determine the range of validity of the formulation used to extract the plasma density from the phase shift data. Since the pressure or partial pressure of CO_2 never exceeded about 40 torr, the error may be as large as a factor of 2 but is well within an order of magnitude for CO_2 or mixtures containing no additives. This was considered to be quite acceptable. The allowed pressure range for all other independent gases is entirely acceptable with the exception of H_2. This may account for ap-

Table 5-12

Worst Case Error Involved in Neglecting the Electron Collision Frequency

Gas	Pressure [torr] (x 2 error)	Pressure [torr] (x 10 error)
CO_2	20	70
He	280	960
N_2	350	1200
H	180	530
CO	260	870
Ar	700	2400

Underestimation of the plasma density by factors of 2 and 10 will result for the tabulated gases and pressures if the electron collision frequency is neglected. The error decreases with decreasing pressure.

parent rapid plasma density fall-off with pressure for this gas, in Figure 5-46, as compared to He, Ar and N_2 which are essentially as transparent as H_2.

The validity of the data involving mixtures with additives at pressures over about 240 torr (partial pressure of CO_2 equal to 70 torr) may be in question by simply considering the values in Table 5-12. However, the analysis in the previous section concerning CO_2 controlled photoabsorption supports a much larger range of validity. For example a determination of photoabsorption cross-sections for the $CO_2 : N_2 : He = 1 : 1 : 3$ mixture containing tri-n-propyl amine in Figure 5-50 yields essentially the same results as an analysis for those cases in Figure 5-48. In the former the partial pressure of CO_2 is 40 torr and so even the worst case electron collision frequently considered in this section does not invalidate the data. Consequently, the latter case is also considered to be valid. In addition, the results presented in this chapter are in agreement with data obtained by charge collection measurements recently available in the literature [65].

For the results presented in Figures 5-46, 5-47, 5-48, 5-49 and 5-50 the valid pressure range may in fact be extended by considering the electron energy. In these cases the phase shift corresponding to the peak electron density was measured just as the spark was extinguished. Consequently, the electrons would not have had time to reach ambient temperature if they had received significant kinetic energy during the ionization process. As an example, if a particle with an ionization wavelength of about 1340 Å was ionized by a photon with a wavelength of 1210 Å, then the electron could acquire as much as 1 ev of energy. This would be particularly applicable to additives being ionized in a laser mixture with photons in the 1200 Å CO_2 window. The product of the electron collision cross-section and electron velocity decreases with increasing electron temperature for CO_2. Consequently, such a situation would tend to decrease the electron collision frequency in CO_2 and extend the range of validity. This is not a general relationship and is reversed in the case of N_2 and H_2 for example. Also, the electron temperature at the time of measurement will be different for all gases. H_2, for example can be expected to be effective in cooling down electrons because of its small mass.

In addition to the above mentioned uncertainties, the electron collision frequency in the mixtures of gases used, were not found in the literature. However, it has been assumed that, to a good approximation, the electron collision frequency can be assumed to be dominated by the CO_2. It was the forementioned uncertainties that prevented the correction of the data by use of electron collision cross-sections available in the literature.

A two frequency method was attempted in order to determine the electron collision frequency along with the electron density. Such a measurement was made in 100 torr of He, where Equation 3-67 applied for electron collision frequencies in the neighbourhood of the test frequency. The results indicated that the electron collision frequency was negligible in accordance with Table 5-12. However, the measurement was not considered accurate for a number of reasons. It was very difficult to tune the bridge since the difference frequency between the power oscillator and local oscillator had to be adjusted to within 2 MHz in order to remain within the amplifier bandwidth. The process required the use of frequency counters and was very tedious. In addition, the klystrons power output characteristics were very irregular with frequency. The highest power output occurred at 9.3 GHz and this supplied good signal-to-noise ratio. Another power peak occurred at 8.3 GHz but this one was much smaller and the signal-to-noise ratio was barely adequate. Such a small change in frequency did not supply good sensitivity. Where the possibility of large electron collision frequency existed, the phase shift was always small for a given plasma density at a given test frequency. This observation supported by Equation 5-61 made the two frequency method even more difficult to apply. Consequently, the actual influence of the electron collision frequency remains undetermined.

5-9. Role of Metastables

CO_2 TEA laser pulse stretching by Penning ionization of additives has recently been reported [66,67,68]. In these cases N_2 metastables were excited during an initial high voltage (above breakdown) fast discharge. Ensuing metastable ionization allowed the laser to be efficiently pumped with a below breakdown electric field for a number of microseconds. Although there are a number of metastable states in the laser gases, CO_2, He and N_2 as well as CO and O_2 [47], the action was attributed to the $a_1 \pi_g$ metastable state in N_2 primarily because of its large cross-section for excitation by electron impact [66]. The metastable has a lifetime of 115 μs and energy of 8.55 eV, large enough to ionize tri-n-propyl amine the additive employed.

Even though photo excitation of metastables and ensuing Penning ionization has not been accepted by Babcock et al [65] there is some merit in considering it in this thesis. For example, the initial increase in electron density observed in Figure 5-17 for CO_2 could be conceived to be due to Penning ionization.

Assuming that a number of metastables have been photo excited during the spark discharge and by further assuming that metastables are only lost by ionizing collisions relation 5-62 applies:

$$\frac{dn_m}{dt} = -k_m n_m n \qquad 5\text{-}62$$

n_m = metastable density [cm^{-3}]

k_m = two body rate constant [$\mathrm{cm}^{3}\mathrm{sec}^{-1}$]

n = density of ionizing species [cm^{-3}]

It has been implicitly assumed that the metastables are either CO, or N_2 from an air leak previously discussed. If it is further assumed that the metastables have sufficient energy to ionize some low concentration contaminant, then the rate equation describing the electron density is given by:

$$\frac{dn_e}{dt} = -\frac{dn_m}{dt} - \alpha n_e^2 - k_a n_e \qquad 5\text{-}63$$

where loss due to recombination and attachment has been incorporated. Substitution of the solution to Equation 5-62 into Equation 5-63 results in:

$$\frac{dn_e}{dt} = k_m n\, n_{om} \exp(-k_m nt) - \alpha n_e^2 - k_a n_e \qquad 5\text{-}64$$

n_{om} = metastable density just after the spark has been extinguished [cm^{-3}].

Elementary differential calculus theory [69,70] shows that a maximum value for n_e occurs at

$$t = -\frac{1}{k_m n}\ln\left(\frac{\alpha n_e^2 + k_a n_e}{k_m n\, n_{om}}\right) \qquad 5\text{-}65$$

For Penning ionization faster than electron loss, metastable action could account for the peaks observed in CO in Figure 5-17. Initial peaks in electron density for laser mixtures with additives may be due to Penning ionization. This would also account for the relatively long life-time of the plasma in laser mixtures containing additives evident in Figure 5-42. This was pointed out by Reitz and Oblertz [66]. For large initial metastable densities Equation 5-65 predicts that the peak occurs at progressively longer times. However, a limit is imposed by the life-time of the metastable and this mechanism may not be able to explain the occurance of peaks at the order of 1 ms in CO_2 and air, for example. These are illustrated in Figures 5-14 and 5-27 respectively.

This simple analysis has ignored the quenching effect that various buffer gases may have on the metastables. Since the quenching ability will vary with buffer gas species and pressure, observation of the Penning effect will depend on the rate of Penning ionization relative to the rate of collisional quenching of metastables by the buffer gas. This may account for the relatively better performance of benzene evident in Figure 5-48. Benzene is known to be a tightly bound molecule compared to the other additives used. Consequently, benzene may be more likely to ionize upon collision with a metastable than to absorb the energy in a molecular vibration. On the other hand, the other more loosely bound additive molecules may tend to absorb the energy in the molecular vibration. The excited molecule may then ionize by a process similar to autoionization or more likely, be collisionally relaxed by a collision of the second kind with a light particle such as He. These considerations are purely speculative at this stage. However, it is reasonable to expect that the significance of Penning ionization in contributing to the total electron density will depend on the gas mixture. A detailed treatment of this subject is precluded by a nonavailability of photoexcitation cross-sections and collisional relaxation cross-sections for the metastables of interest.

5-10. Discussion and Conclusion

The results provide several criteria on which to base the design of spark photopreionized CO_2 lasers.

(1) Inexpensive, commercially available automotive spark plugs provide a satisfactory spark source.

(2) The most efficient way of delivering energy to the spark source, is with high voltage, low inductance circuitry in order to provide high current.

(3) CO_2 limits the photoplasma density by photoabsorption

(4) Significant improvement in photoplasma density can be obtained with the addition of small amounts of various low ionization threshold vapors.

(5) For low $P_{CO_2}L$, photoionization of additives is available in a one-step process in the CO_2 window around 1200 Å.

(6) For high $P_{CO_2}L$, photoionization by additives may occur in a two or multi-step process for $\lambda \gtrsim 1800$ Å. This mechanism may be exploited for large aperture, high pressure lasers. Increased photon intensity with gas pressure evident in Figure 6-1 , indicates that photoionization may not be entirely constant with $P_{CO_2}L$, but may increase slowly as this parameter is increased.

(7) Addition of additives results in longer lived plasma possibly due to Penning ionization from metastables. This may be a significant criterion to consider in the design of quasi-continuous photoionized CO_2

lasers.

(8) Laser devices should be well sealed to prevent O_2 from contaminating the system. O_2 rapidly reduced the electron density by attachment.

"Experimental verification of the effectiveness of many of these photoionization parameters has been accomplished in working laser systems. For example, input and output energy densities in excess of 800 and 60 J/ℓ, respectively, have been obtained in a 5 cm aperture laser 50 cm long. This structure was operated at atmospheric pressure with a (1:1:3) (CO_2 : N_2 : He) mixture and a triethylamine plus tripropylamine additive. These results were achieved using the discharge and preionization configuration shown in Figure 12 (Figure 5-54 in this thesis). Two 15-source linear UV arrays were mounted on either side of the anode so as to provide relatively uniform irradiation of both the cathode and the discharge region. Surface-gap spark plugs individually fed from a low-impedance multiparallel strip transmission line conveniently performed as the preionization sources. In this discharge configuration the UV sources are seen to be in series with the main discharge and are, consequently operational during the entire current pulse. Best operation has been obtained using oriented nuclear-grade graphite electrodes machined to an approximate Rygowski profile." [57] In spite of the fact that benzene produced the largest electron density in a laser mixture under test

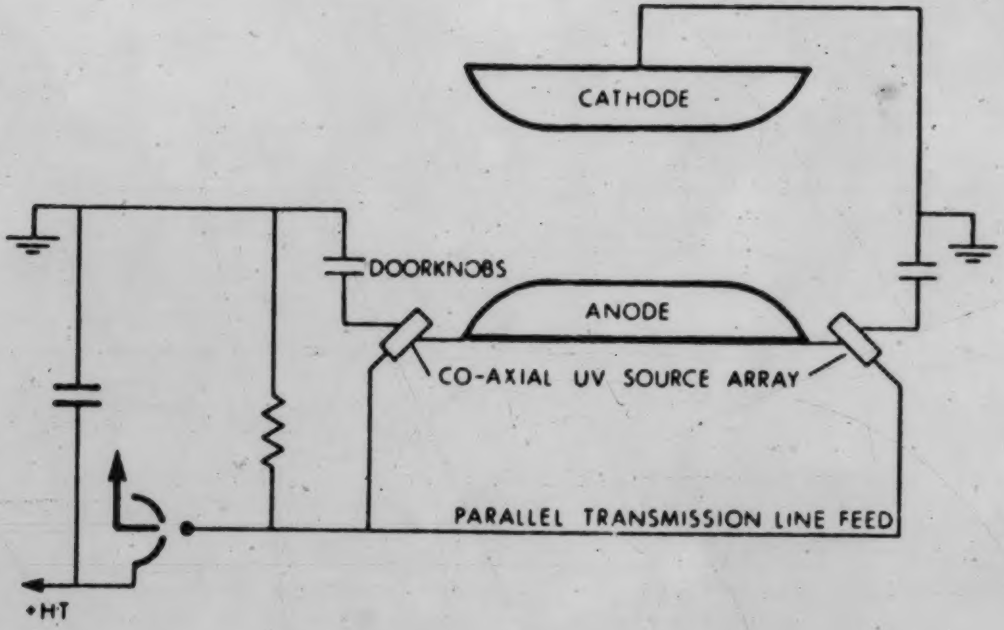
CATHODE
DOORKNOBS
ANODE
CO-AXIAL UV SOURCE ARRAY
PARALLEL TRANSMISSION LINE FEED
+HT

FIGURE 5-54 SCHEMATIC DIAGRAM OF A TEST DISCHARGE AND PREIONIZATION LASER SYSTEM

conditions, and that it provided good stabilization of the laser excitation discharge, its use did not provide good laser output. This was subsequently traced to a strong absorption in benzene close to the laser wavelength of 10.6 microns.

The data analysis presented in this Chapter reveals that the test facility could be used as the basic apparatus to determine a great deal more data. Much of this data would be of general interest and some would be suited primarily to photoionized CO_2 lasers. The X-band interferometer provides sufficient sensitivity to observe fundamental-mode diffusion controlled plasma decay. This would provide a means of determining the molecular weight of the positive ion. Two and three body attachment rate coefficients could be determined for various electronegative molecules. These tests would require an improvement in the vacuum integrity of the existing system, perhaps a bakeable system would have to be employed. Incorporation of a photomultiplier sensitized to the ultraviolet, would allow the determination of average photoionization cross-sections in CO_2 controlled ionization of additives. A second bridge operating at a high frequency (perhaps Q-band) could be constructed, and used along with the X-band bridge to determine the electron collision frequency when the plasma density was within the range of both bridges. This would probably occur in the case of additives.

Unfortunately, the test facility, designed to simulate conditions in a typical CO_2 laser has two major disadvantages. It does not provide for constant source environment, nor does it possess any wavelength resolution. Consequently, a vacuum ultra-violet monochromator equipped with electronic as well as photographic recording apparatus, has been employed to investigate the photoionization parameters more thoroughly. Tests performed with this equipment are seen to provide more information about the photoionization process and the nature of the photoionizing species. In addition, photoionization and photoabsorption cross-sections can be determined from the data with good wavelength resolution. This is the subject of the following chapter.

CHAPTER 6

Results of Photoionization Parameter

Investigation with a Vacuum Monchromator

Theoretical and design considerations have been dealt with in Chapter 3. In this Chapter only experimental results and appropriate analyses are presented. The test facility has been used to monitor photon intensity for various gases and gas pressures. Incorporation of the charge collector has allowed the determination of photoabsorption and photoionization cross-sections. Further support for CO_2 controlled photoabsorption and photoionization has been obtained. CO_2 has been observed to be opague for wavelengths shorter than approximately $\lambda = 1050$ Å. Consequently, LiF (with a short wavelength cutoff at $\lambda = 1050$ Å) could be used to isolate the test cell from the monochromator and spark source.

6-1. Photographic Record of Emission Spectra

Preliminary testing was done using a photographic technique to record the emission spectra from the spark sources in the three independent laser gases at three different pressures. The results of these tests appear in Figures 6-1 and 6-2. A key to these figures appears in Figure 6-3. The photographs were taken under identical conditions, except for the source geometry. A CaF_2 window was used at the entrance slit of the monochromator illustrated in Figure 3-2 . CaF_2 was used rather than LiF simply because the LiF that had been ordered had not arrived. It served primarily two purposes:

(1) It allowed a high source pressure to be maintained while keeping the absorption length short (10 cm). The monochromator was maintained at 1 to 2 microns with an oil rotary pump.

(2) It protected the grating from being damaged by the source.

Being located 10 cm from the spark source the window was not fouled so rapidly, as in the case of the microwave interferometer test facility. It was found that washing the window in alcohol after approximately every hour of operation maintained the transparency at a reasonably constant level. The source driving circuitry was the same as discussed in Section 5-2.

A number of features are immediately evident upon examining Figures 6-1 and 6-2 along with Figure 6-3.

(1) The wavelength content is remarkably independent of gas species and pressure. It seems to be a much stronger function of the electrode material and perhaps configuration. The tungsten pin spectra appear to be somewhat more characteristic of the gas species.

(2) The intensity of the emission spectra of the laser gases increases with increasing gas pressure. The only exception is CO_2 for wavelengths shorter than 1800 Å.

(3) The spectra appear to be primarily composed of lines with no strong evidence of a continuum. The continuous darkening in the high pressure cases may have been due to over exposure.

(4) The surface-gap spark plug yields higher intensity than the tungsten pins for all gases and pressures tested.

A closer examination reveals more subtle features. Each exposure corresponds to a grating angle adjustment that results in a 500 Å shift down in wavelength from each succeeding exposure. This value was chosen so as to allow some overlap of the spectrum as the film was racked up and the grating angle changed. Identification of duplicated lines allows the plate factor to be calculated. The plate factor is not constant with wavelength as revealed by Equation 3-68 and 3-71. This is particularly evident in Figure 6-4 where the film is exposed to a Hg vapor lamp with the grating angle set to a known line, and then exposed a second time (for the same film rack setting) with the grating angle shifted 200 Å. The plate factor can be calculated with ease from such data. The information can be applied to Figures 6-1 and 6-2, to calculate a window cut-off of $\lambda \approx 1230$ Å as expected. It also yields a high pressure CO_2 short wavelength cut-off of $\lambda \approx 1775$ Å which is in good agreement with the expected value [42]. At a pressure of 100 torr, a more realistic value for a CO_2 TEA laser, ultra-violet light down to $\lambda \approx 1630$ Å, is seen to penetrate 10 cm of CO_2.

In order to obtain data in the region of $\lambda < 1200$ Å the CaF_2 window was removed. Fortunately no noticable deterioration of the grating occured. Figure 6-5 can be compared to Figure 6-1 except that the window has been removed and the absorption path length has been extended to about 110 cm. Any increased intensity in Figure 6-5 is believed to be due to the removal of the clouded window. It is particularly evident that the gas species has not affected the wavelength distribution. Any disappearance of portions of the spectrum when CO_2 is present can therefore be attributed to CO_2 absorption and not to actual absence in the emission spectrum. Only for the case of the lowest pressure of CO_2 is there any appearance of photons in the 1200 Å window. Close examination of Figure 6-5 reveals transparency from $\lambda \approx 1200$ Å to $\lambda \approx 1280$ Å. Because of the long pathlength, the CO_2 pressure scaled to a typical CO_2 TEA laser would be about 20 torr. It is also apparent that the photon production in He and N_2 may extend below $\lambda = 1100$ Å. However, CO_2

can be expected to absorb this portion of the spectrum as evidenced in Figure 6-5, so it is of no interest in terms of CO_2 TEA laser photoionization. The absorption in N_2 around $\lambda \approx 1400$ Å was traced to an unusually high level of O_2 contamination in the N_2 cylinder used.

In summary, the photographic record presented here can be said to further substantiate CO_2 controlled photoionization by photoabsorption. In addition it has revealed that the emission spectrum is primarily a line spectrum independent of gas species but that the intensity varies with gas species and pressure. The emission spectrum of the adjustable spark plug, illustrated in Figure 3-3(a), could not be obtained with a window at the entrance. The spark was particularly notorious in obliterating the window with debris from the discharge. Testing without a window was decided against in order to ensure protection of the diffraction grating.

Numerous photomicrodensitometer scans were performed to facilitate relative comparison of the photographic records. However, the focussing across the width of the film was not found to be constant and this presented a severe limitation on the usefulness of the scans. One of the better focussed photographic records has been scanned and the result appears in Figure 6-2A. However, film darkening is non-linear with wavelength and exposure. Comparison of the scan to the photoelectrically obtained spectrum in Figure 6-7A shows that the film has saturated for intense exposure. Consequently no attempt was made to normalize the photographic data. At any rate the resulting information would only be duplicated by the more accurate photoelectric recording performed subsequently and presented in the following sections.

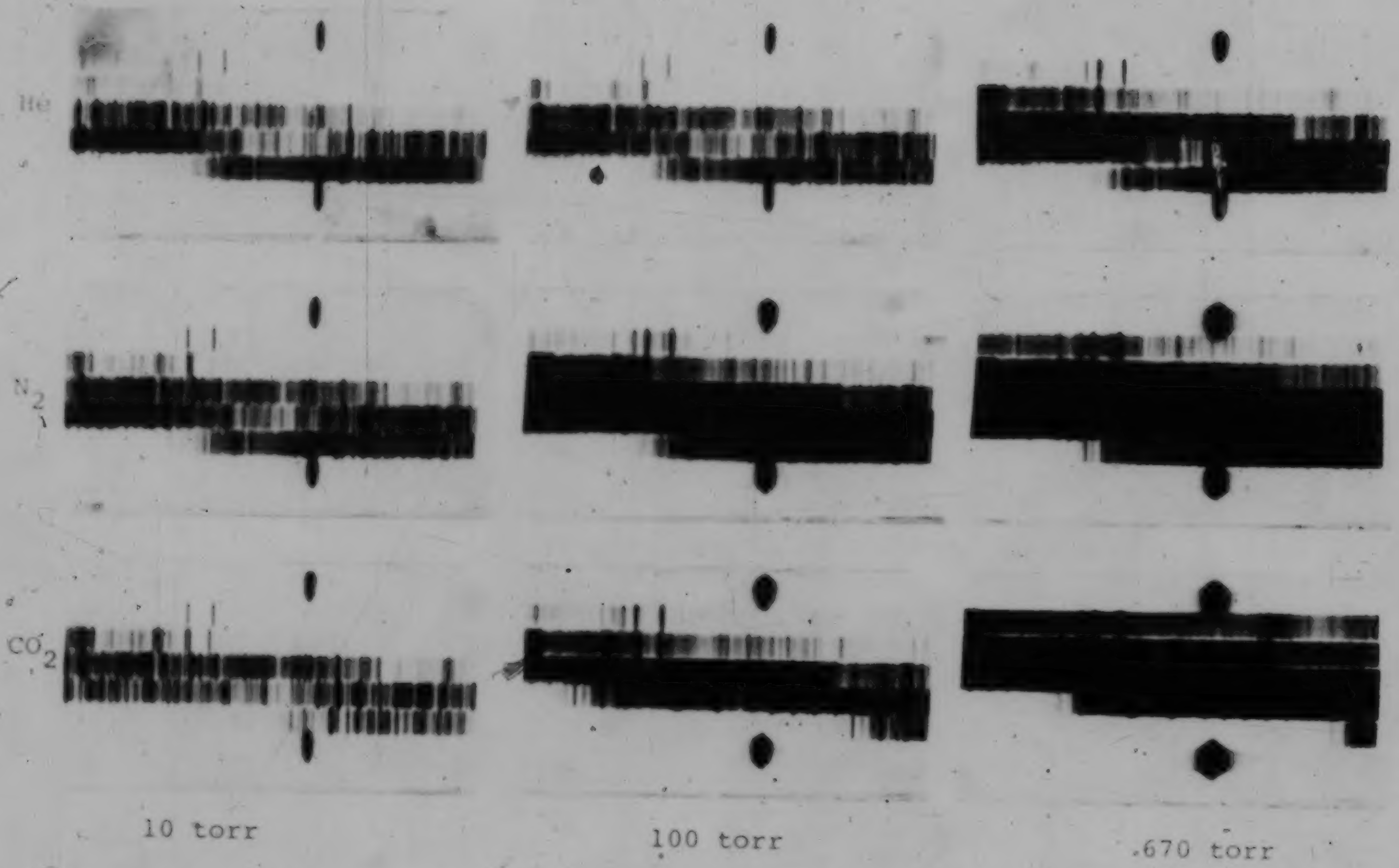
He
N2
CO2
10 torr
100 torr
670 torr

Figure 6-1. Emission spectra from an automotive surface gap spark plug. The spectra represent the integrated value of 10 shots. A key appears in Figure 6-3.

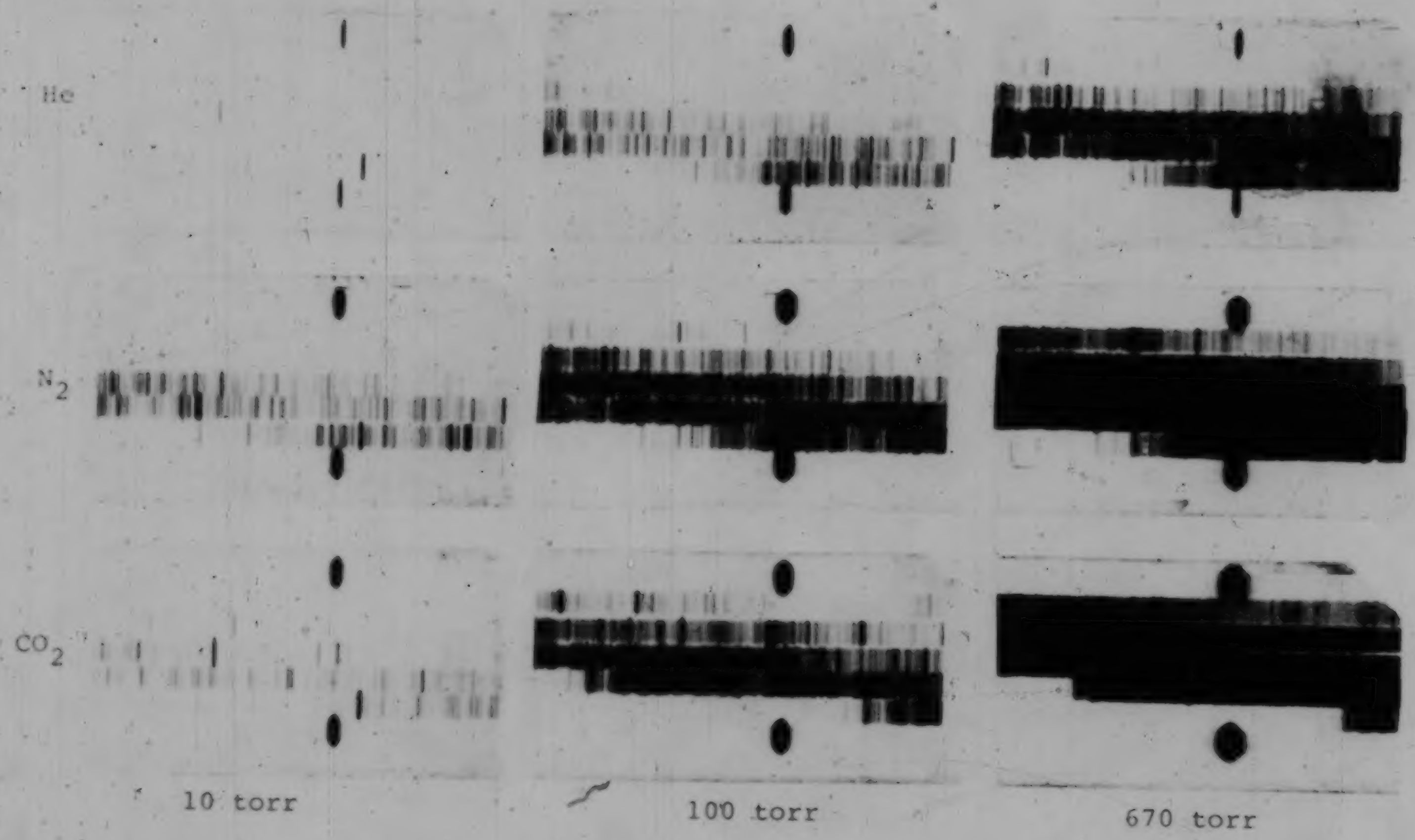

Figure 6-2. Emission spectra from colinear tungsten pins. The spectra represent the integrated value of 10 shots. A key appears in Figure 6-3.

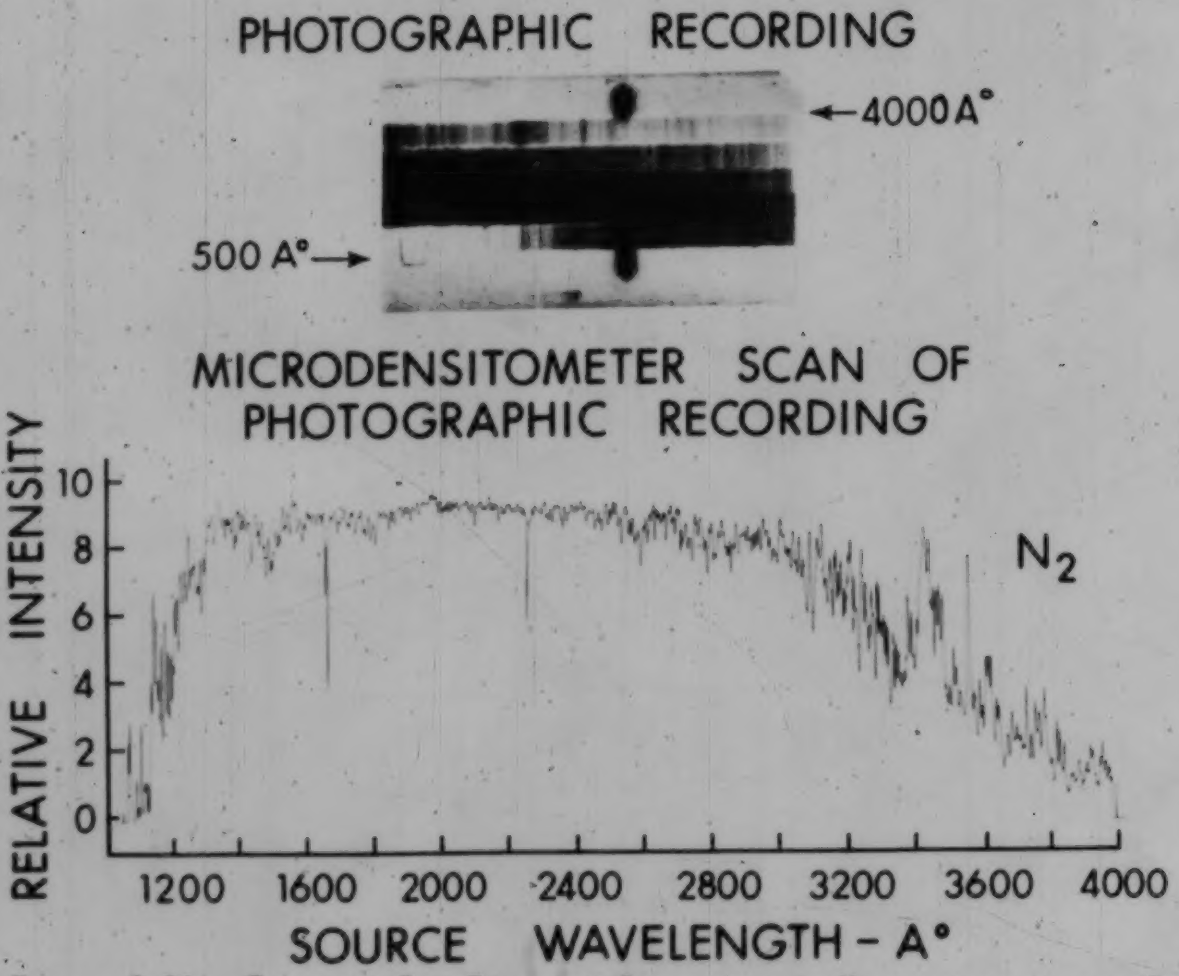

FIGURE 6-2A TUNGSTEN PIN EMISSION SPECTRUM AND MICRODENSITOMETER SCAN

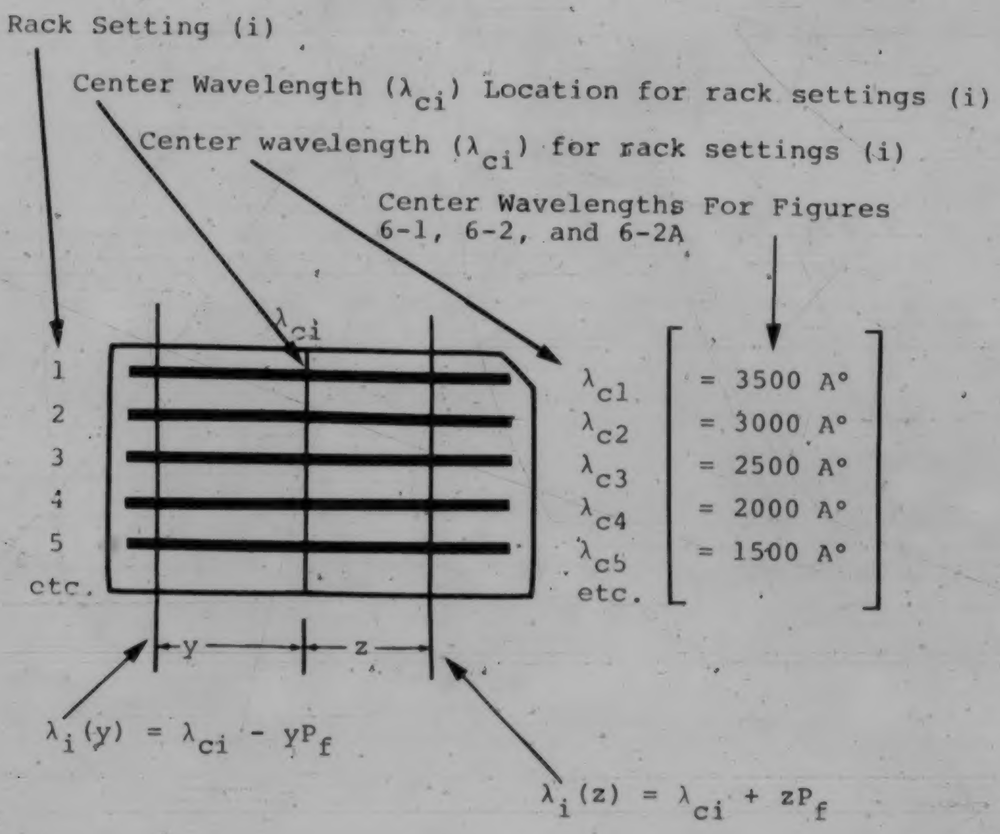
Rack Setting (i)
Center Wavelength (λ_{ci}) Location for rack settings (i)
Center wavelength (λ_{ci}) for rack settings (i)
Center Wavelengths For Figures 6-1, 6-2, and 6-2A
λ_{ci}
1
2
3
4
5
etc.
λ_{c1} = 3500 A°
λ_{c2} = 3000 A°
λ_{c3} = 2500 A°
λ_{c4} = 2000 A°
λ_{c5} = 1500 A°
etc.
y
z
$\lambda_i(y) = \lambda_{ci} - yP_f$
$\lambda_i(z) = \lambda_{ci} + zP_f$

FIGURE 6-3 KEY TO SPECTRA PHOTOGRAPHS This key provides the necessary information to read the spectra in Figures 6-1, 6-2, and 6-2A. The format for Figures 6-4 and 6-5 is similar; however, all rack settings are for the center wavelength indicated on these Figures.

P_f [Å/mm]	[Å]
10.58	4358.35
10.10	4046.56
10.47	3650.15
10.81	3341.48
10.99	3125.66
11.24	3021.50
11.11	2967.28
11.17	2893.60
11.27	2652
11.49	2537
11.76	1942
12.12	1850

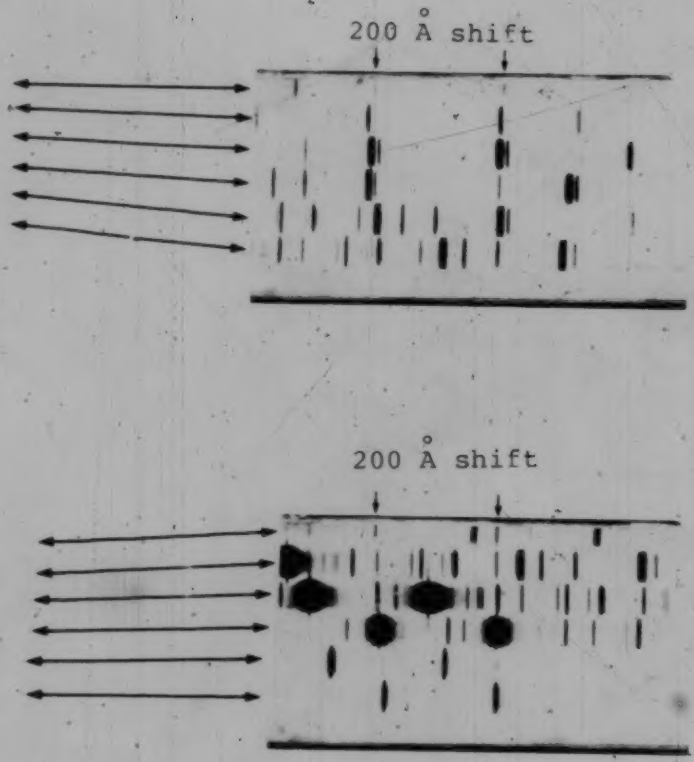

Figure 6-4. Spectra of a Hg - vapor lamp. A 200 Å shift has been incorporated to facilitate calculation of the plate factor, P_f.

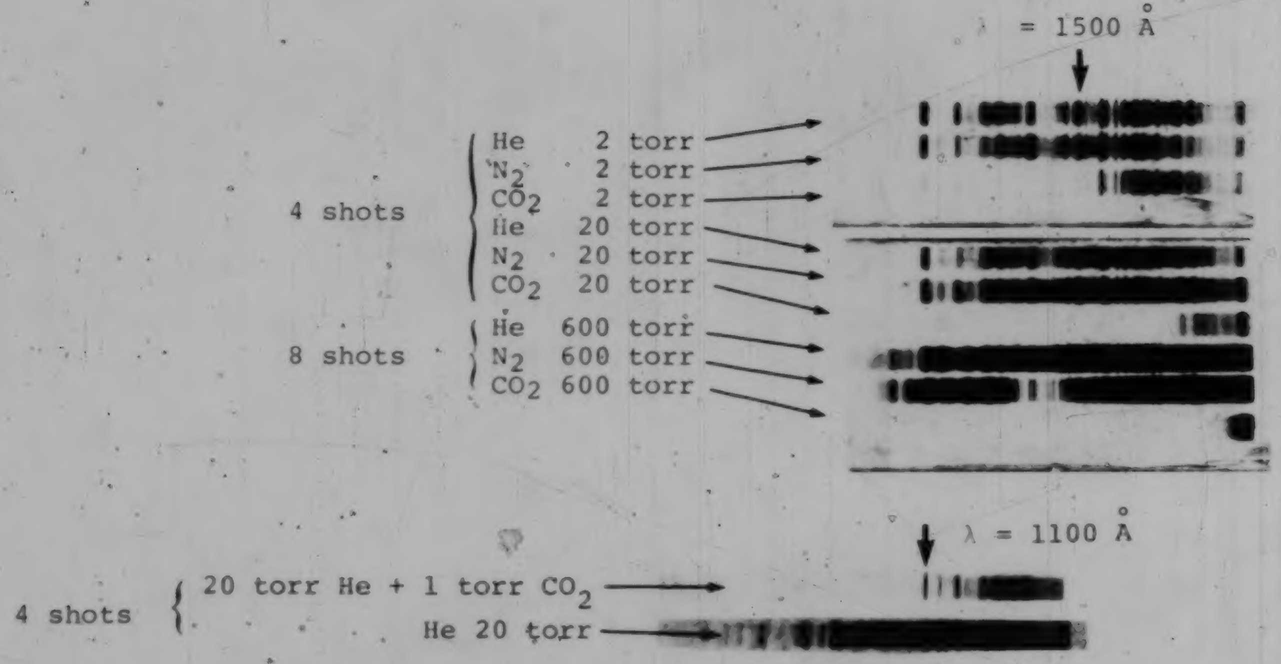
λ = 1500 Å
4 shots
He 2 torr
N2 2 torr
CO2 2 torr
He 20 torr
N2 20 torr
CO2 20 torr
8 shots
He 600 torr
N2 600 torr
CO2 600 torr
λ = 1100 Å
4 shots
20 torr He + 1 torr CO2
He 20 torr

Figure 6-5. Emission and absorption spectra from an automotive surface gap spark plug. No window has been employed. A key appears in Figure 6-3.

6-2. Electronic Recording of Emission Spectra, Absorption Spectra, and Photoplasma

Presentation and analysis of results obtained with the electronic recording equipped vacuum monochromator constitutes the remainder of the thesis. The design and operation of this test facility has been dealt with in Chapters 3 and 4.

Even though the tungsten pin spark plug, illustrated in Figure 3-3(b), did not yield the highest electron density when used in the microwave interferometer test facility, it was found to be the best choice of source geometry for the monochromator test facility. The pin geometry provided a constant spark location. The pins were locked about 2 mm apart and the spark could be accurately aligned with the entrance slit to provide optimum light intensity. The surface-gap spark plug also illustrated in Figure 3-3(c), did not provide the necessary shot-to-shot spatial reliability required.For this geometry the spark could be located on any radius of the coaxial structure. This parameter was observed to be entirely random from shot-to-shot even after a file mark was placed on the spark plug in an attempt to stabilize the spark location by disturbing the circular symmetry. Consequently, the spark did not always line up with the entrance slit and the photon counter output randomly varied from almost zero to an optimum value. Although this effect could be tolerated with photographic recording where the film integrates a number of shots and determines an average, it could not be tolerated here. The remaining source geometry illustrated in Figure 3-3(a) was not used because of its particularly disruptive nature.

Further information supporting CO_2 controlled photoionization in a CO_2 TEA laser is presented in the following section. Consequently, ultra-violet wavelengths shorter than $\lambda \approx 1100$ Å are of no interest for CO_2 TEA laser photoionization. This allows for test cell isolation from the monochromator by a LiF window (cut-off $\lambda \approx 1050$ Å). Also N_2 at atmospheric pressure has been found to provide the strongest spectrum in the region of interest. These features have eventually been incorporated into the test facility as standard.

6-2-1 Photoelectric Record of Emission Spectra

Further investigation into the emission spectra of the laser gases has been performed using the photon counter system discussed in Chapter 3. The results are presented here in a purely relative manner. Absolute values can be obtained by multiplying by the calibration constant derived in Section 6-2-6. However, such an exercise would be of no value to the subject matter presented in this Chapter.

The source was driven with a capacitor value of 0.014 μf at a voltage of 50 kV. This resulted in less energy dissipation per spark than for the previous condition of C = 0.1 μf and V = 40 kV. This was done in order to reduce the hazard of damaging the grating. The capacitor value was obtained with a bank of 16 barium titanate capacitors placed in series and parallel to obtain proper voltage rating and total capacitance. These capacitors continually failed by shorting after approximately every 50 hours of operation. However, they failed suddenly with no marked gradual deterioration. Observation of the current discharge waveform revealed a total series equivalent inductance of approximately 0.63 μh. This was due primarily to the circuitry, as in the case of the microwave interferometer. This source driving circuit was found to provide sufficient light intensity to perform the scheduled tests. The photon intensity was sufficient to allow the narrowing of the slits to obtain a bandwidth of approximately 5 Å.

All testing has been done under atmospheric pressure source conditions. Flow meters were used to regulate the flow of gas into the monochromator body and out through the entrance slit and source. No window was used at the entrance slit. The gas was exhausted to the atmosphere through a 50 foot length of 1/4 inch O.D. polyflow tubing. A lengthy piece of tubing was required in order to prevent back migration of air into the source and monochromator. An O-ring flap valve on the exhaust allowed the monochromator and source to be evacuated before being filled with the required gas.

Figure 6-6 reveals dramatically that N_2 is by far the best of the three laser gases to be used in the spark source. The performance of He as a source gas was poor in proper agreement with the photographic records in Figures 6-1 and 6-2. A cylinder of He approximately an order of magnitude higher in purity than the industrial grade of gases employed was also tested. No improvement in the emission spectrum was observed. Hence the poor performance could not be attributed to absorption by an impurity in the He. The increased electron density reported in Chapter 5 when the source was purged with He must have been due to reduced absorption rather than increased emission. An atmosphere of CO_2 with a path length of 122 cm absorbed all photons at $\lambda \lesssim 1800$ Å as expected.

No window was used at the exit slit so the path length was the sum of the test cell length and the monochromator and source length. With the X30 increase in gain used for $\lambda \lesssim 1800$ Å in CO_2, the amplifier noise was recorded and was sufficiently high to reset the integrator.

Figure 6-7 provides final evidence that the source emission spectrum is controlled by N_2 and that the absorption is controlled by the CO_2 with He being rather passive. The laser mixture by volumetric flow was in the ratio $CO_2 : N_2 : He = 0.1 : 1 : 1$. The CO_2 content was reduced so as to provide for a shorter effective pathlength, more typical of a CO_2 TEA laser. The reduced emission for $\lambda \gtrsim 1800$ Å compared to Figure 6-6, is believed to be a result of reduced N_2 pressure. Increased gain of X10 is required to obtain a good reading for $\lambda \lesssim 1800$ Å. The reduced intensity in this region is again believed to be, in part, a result of reduced N_2 partial pressure, but CO_2 absorption accounts for most of the loss. The second trace in Figure 6-7 reveals the importance of low circuit inductance. Here a 300 μh coil was placed in series with the source driving capacitor. Photon intensity for $\lambda \lesssim 1700$ Å was markedly reduced.

Identification of N_2 as the gas primarily responsible for the entire ultra-violet spectrum of interest simplified the choice of source selection for the remainder of the tests. Consequently, flowing N_2 at atmospheric pressure has been used to fill the monochromator and source for most of the remaining tests.

Figure 6-7A reveals the spectral distribution in N_2 over a broader bandwidth. Although a significant amount of energy is deposited in the short wavelength region, improvement in this area would markedly improve the efficiency. The second trace reveals the detrimental effect an inductive circuit has on the emission spectra. Here again, 300 μh was placed in series with the driving capacitor.

Figure 6-8 reveals that the use of an LiF window at the exit slit results in a reduction of intensity for $\lambda \lesssim 1750$ Å. However, the system still has plenty of gain available and an increase of X10 reveals that there are sufficient photons available in all parts of the spectrum to allow employment of the window.

Figure 6-9 reveals the importance of purity of gases in a laser system. The relative intensity was observed to increase with gas purity. The second trace in Figure 6-9 shows marked photoabsorption. The absorption corresponds to the absorption spectrum in O_2 and this was eventually traced to an unusually high O_2 concentration in the industrial grade N_2 cylinder [42,73].

No detailed effort has been made to test all possible combinations of spark electrode material and gas environment in search of a better emission spectrum. However, it is known that a small concentration of H_2 in

CO_2 TEA lasers improves the performance. Subsequent testing of H_2 as a source gas revealed the $\lambda = 1215$ Å line characteristic of H but it was not as intense as lines observed with N_2 in the same portion of the spectrum.

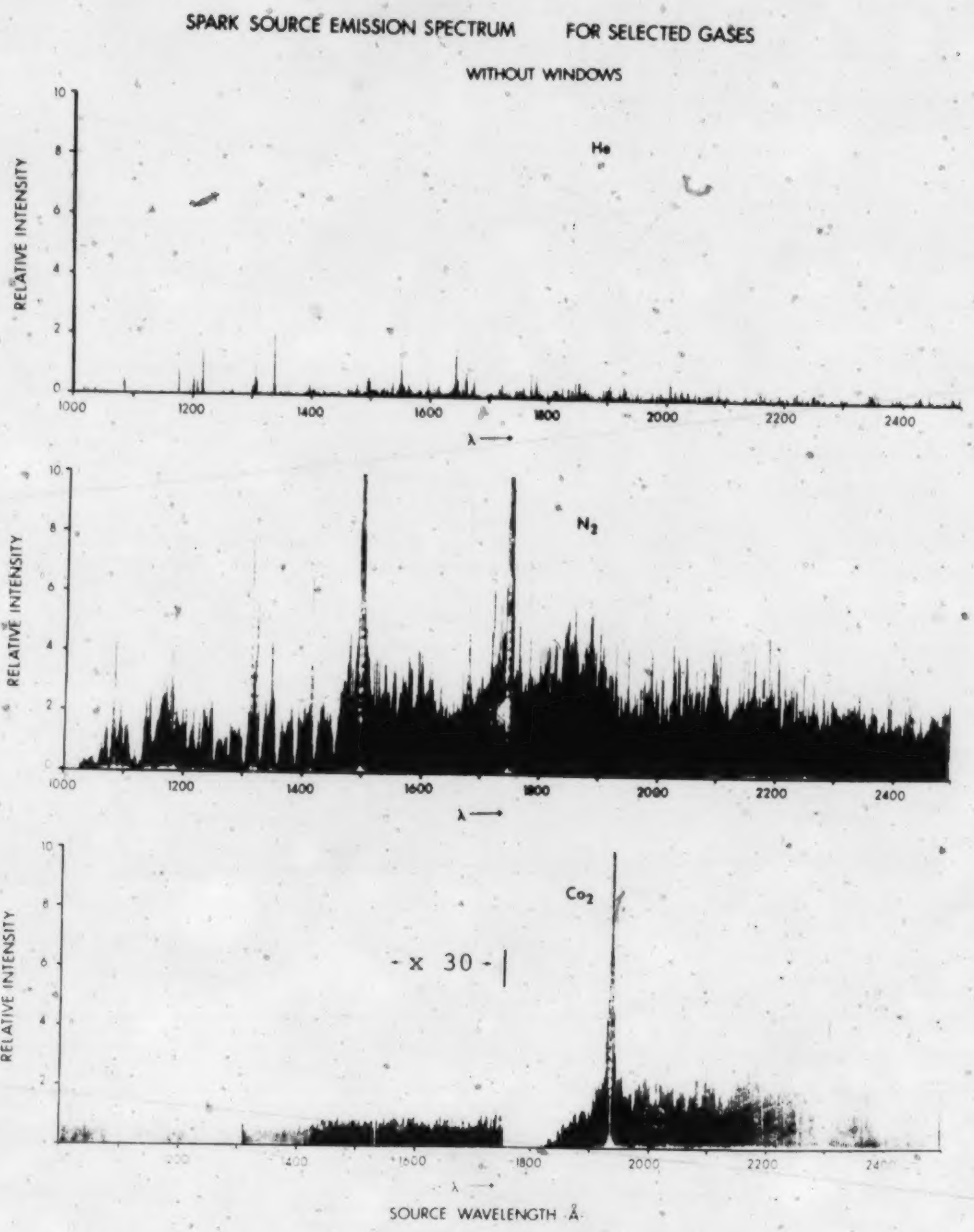

FIGURE 6-6 SPARK SOURCE EMISSION SPECTRUM FOR INDIVIDUAL LASER GASES Gas flow at one atmosphere has been employed. The optical pathlength was 122 cm.

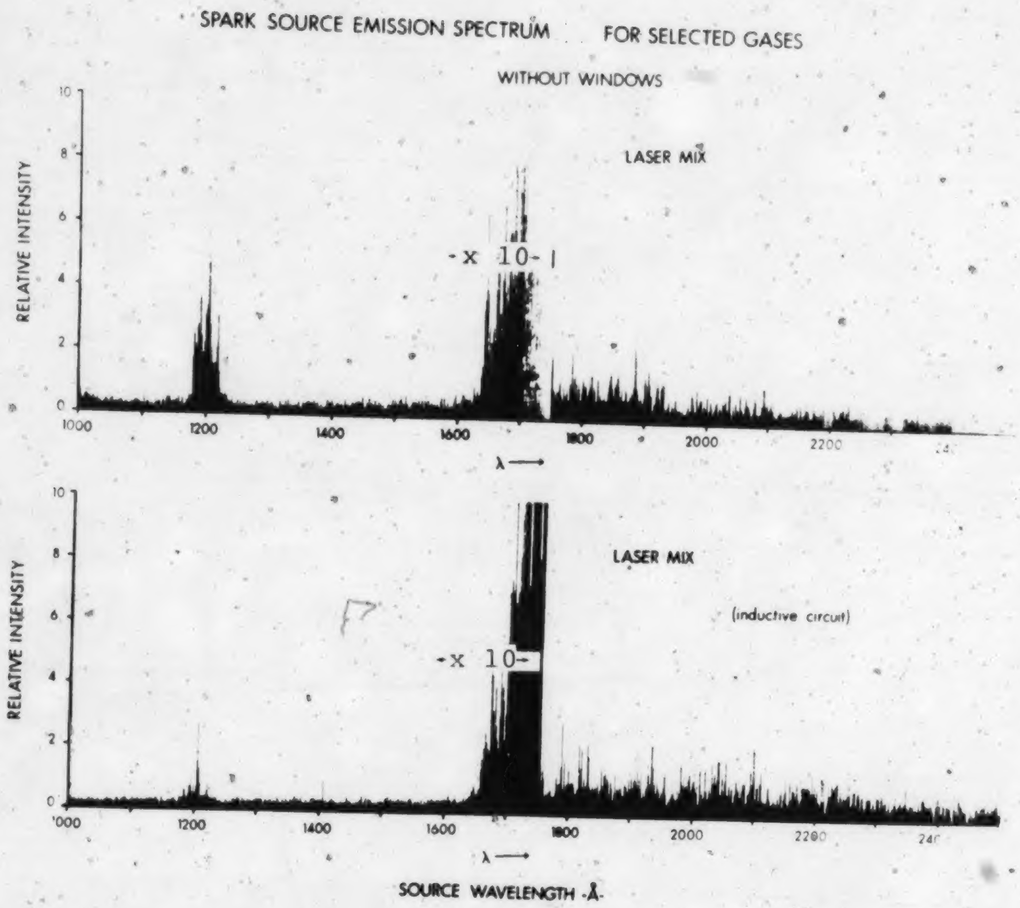

FIGURE 6-7 SPARK SOURCE EMISSION SPECTRUM FOR A LASER MIXTURE A $CO_2:N_2:He = 0.1:1:1$ (by volumetric flow) ratio at one atmosphere total pressure has been employed. The optical pathlength was 122 cm.

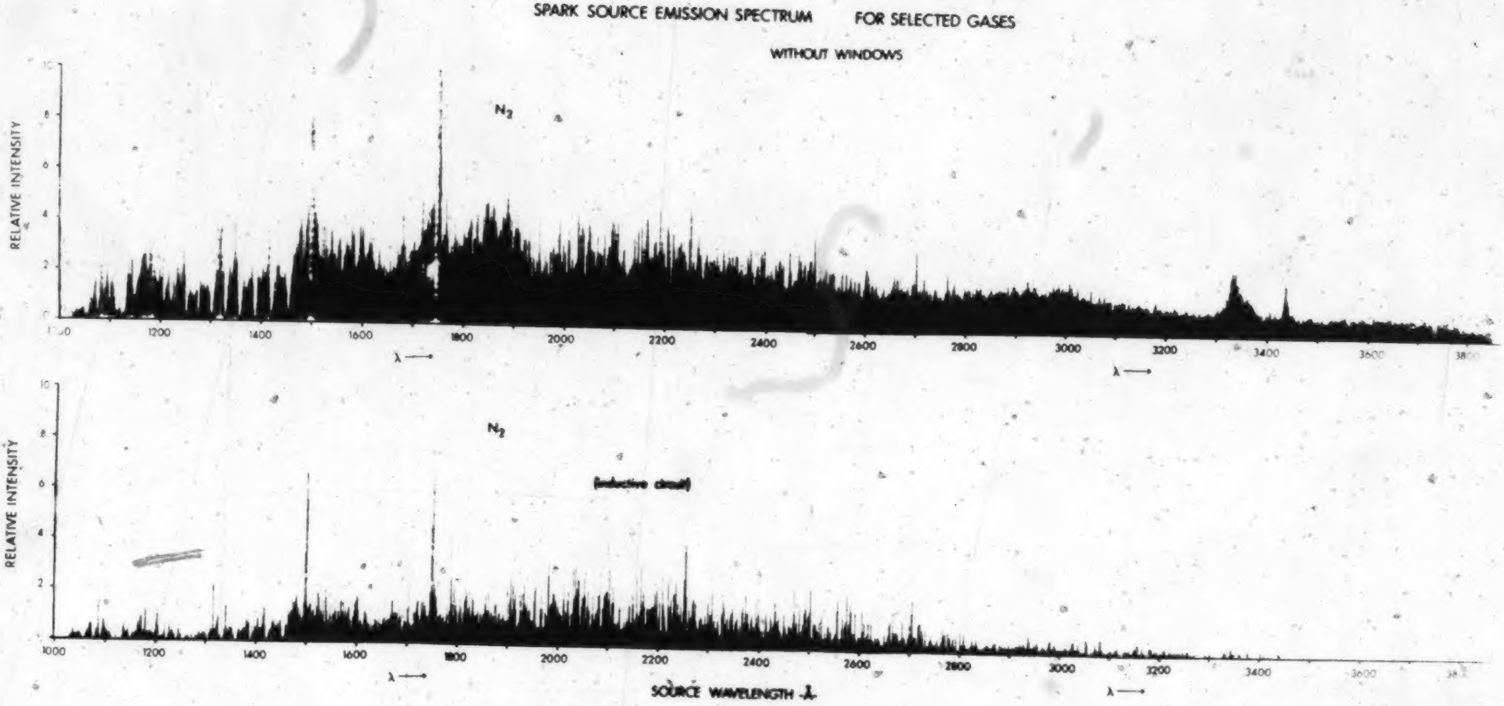

FIGURE 6-7A BROADBAND SPARK SOURCE EMISSION SPECTRUM FOR N_2 The lower spectrum reveals the detrimental effect of an inductive source driving circuit. Flowing gas at atmospheric pressure was employed. The optical pathlength was 122 cm.

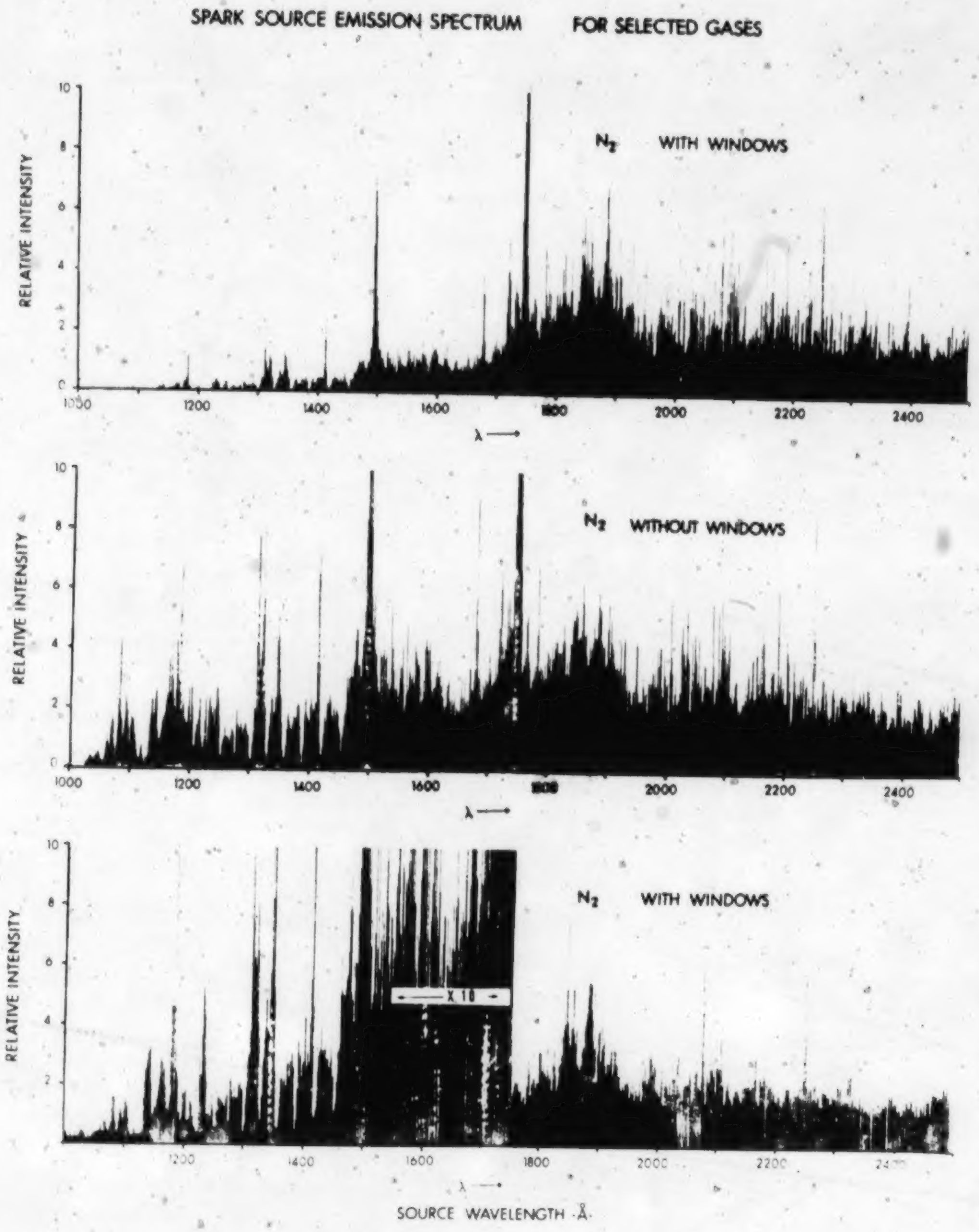

FIGURE 6-8 EFFECT OF A LIF WINDOW ON THE SPARK SOURCE EMISSION SPECTRUM. An atmosphere of flowing gas was employed. The optical pathlength was 122 cm.

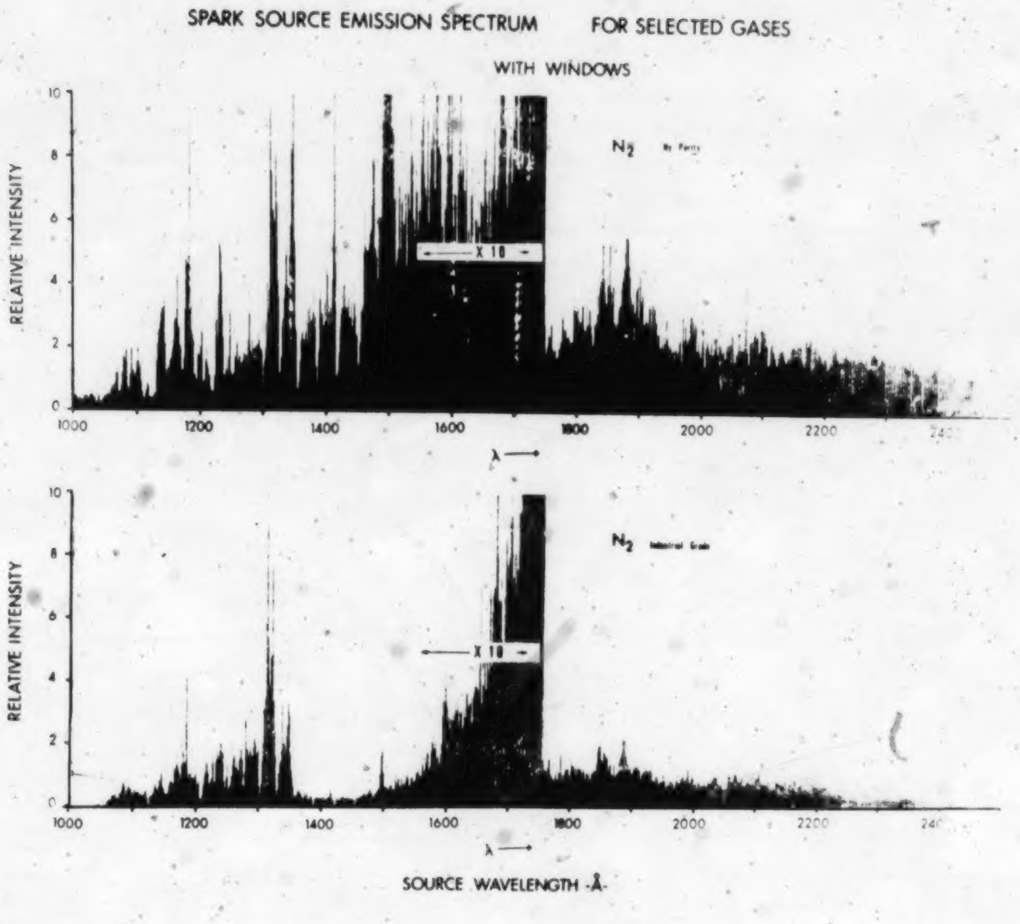

FIGURE 6-9 SPARK SOURCE EMISSION SPECTRA FOR HY-PURITY N_2 AND FOR CONTAMINATED N_2 An atmosphere of flowing gas was employed. The optical pathlength was 110 cm.

6-2-2. Charge Collection Mechanism

A sound knowledge of the voltage-current characteristics of any charge collector device is necessary in order to interpret the results. Although sufficient information about the collection mechanism allows results taken on any portion of the curve to be interpreted, tremendous simplification is obtained if the charge collector can be saturated. Figure 6-10 has been prepared to illustrate the type of V-IC (voltage-integrated current) curve expected. Here, the total amount of charge collected is plotted against the charge collector bias voltage. Space charge effects as well as loss mechanisms have been assumed to be negligible for the low density ensemble of charges expected.

Part A of the curve in Figure 6-10 corresponds to a situation where the field strength would not be sufficiently high to sweep all of the charge out of the volume, in the time allowed by the electronics. A further increase in the bias voltage results in saturation. Regardless of the bias voltage, all charge would be swept out of the volume in the allotted time for portion B of the curve. Further increase in voltage would result in operation in portion C. Here, the field is sufficiently high so as to accelerate electrons between collisions, to energies capable of ionization of a gaseous particle upon collision. The phenomenon is known as Townsend ionization

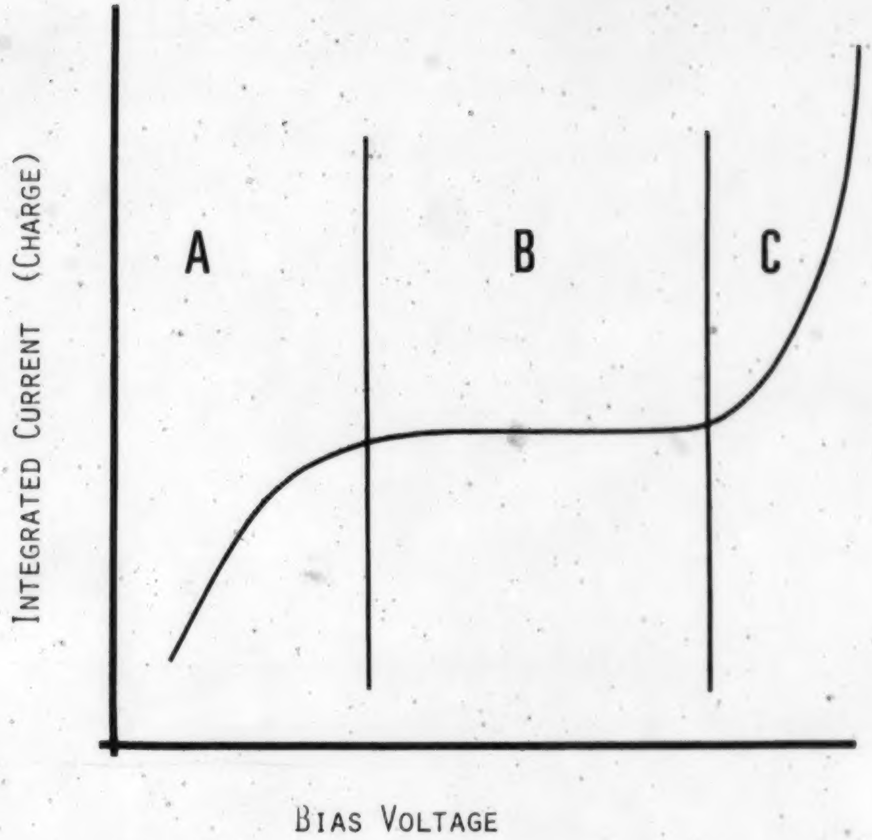

FIGURE 6-10 HYPOTHETICAL CHARGE COLLECTOR CHARACTERISTICS
In region "A" the bias voltage is not sufficiently high to collect all charge in the allotted time. All charge has been collected in region "B". This is the saturation region. In region "C" the bias voltage is high enough to cause Townsend avalanche multiplication of electrons.

[41,47,51,52]. The increase in ionization is exponential with bias voltage and gaseous breakdown eventually occurs.

If the V-IC curves were accurately established for all gases and pressure ranges of interest, then operation on any portion of the curve would allow for interpretation of the results. Of course if the curves could be obtained experimentally, then there would be no need to operate in any region other than the saturation region.

Total charge measurement in the laser gases with a 5 Å resolution, resulted in saturation signals barely larger than the amplifier noise. Increased bias voltage resulted in operation in part C of the curve. The signal was strengthened considerably and was easily measured. However, it was difficult to relate this to the true charge density.

Theoretical determination of the V-IC curve is precluded since the first Townsend ionization coefficient is unknown. The coefficient is available in the literature for uncontaminated gases, however, impurities significantly alter the coefficients [51,52]. The problem has been further complicated by the nature of the initial electron distribution between the collector plates. Nevertheless, an effort to gain a better understanding of Townsend avalanche multiplication has been made, and the results have been presented in Section 6-2-5.

Fortunately, the use of additives resulted in such a large electron density, that collector operation in the saturation region was easily obtained and the data could be interpreted with little trouble. In addition, the signals obtained under such conditions were much larger than the amplifier noise and the noise resulting from mechanical vibrations. This allowed the electronic noise suppressing filters to be removed. The increased bandwidth allowed the collector gate to be opened for longer periods of time. The longest time required to collect all the charge was approximately 80 μs. This was obtained for charge collection in a laser mixture containing approximately 100 torr of CO_2 with tri-n-propyl amine. A 10 volt collector bias has been employed. For higher E/P the required collection time was much shorter. In all cases involving laser gases at a few torr pressure and bias voltage above 40 or 50 volts, the required collection time was less than approximately 7 μs, the minimum electronic gate time. These observations were made with a bandwidth of about 50 Å in order to obtain a strong signal. These results correlated well with electron drift velocities, and considerations of ion mobility revealed that the ions would have been effectively motionless over such short intervals of time [41]. It was subsequently concluded that the charge collected, was due primarily to electron collection and that any amount due to ion collection was insignificant. Furthermore, the short collection intervals required, revealed that space charge development did not play a significant role. Collection of charge from a volume protected from electric fields by a space charge, depends on the diffusion of the charges to the space charge boundaries. Existence of a space charge implies that ambipolar diffusion applies and such a process would be much too slow to account for the short collection intervals observed.

One final point should be mentioned. The charge collector was too sensitive at maximum gain to allow even a small flow of gas through the test cell. Flowing gas resulted in vibration of the collector plates. The subsequent change in capacitance required redistribution of charge. This required current flow and large random noise signals resulted. Consequently, all tests requiring maximum gain have been performed in an entirely sealed off test cell.

Having determined the mode of charge collector operation the results applicable to CO_2 TEA laser photoionization can be presented.

6-2-3. Photoionization Dependence on Wavelength

Chart recorder scans have been obtained revealing photoionization in the laser gases as a function of wavelength. The source employed was the standard tungsten pin spark source in a N_2 environment described in Section 6-2. A LiF window has been used at the exit slit to isolate the test cell from the monochromator. A 5 Å bandwidth was used to provide good resolution. Unfortunately, the resulting photoelectron density was insufficient to yield a strong signal in a saturation mode of operation, with the exception of the use of an additive in Figure 6-12. A collector bias voltage of 200 volts resulted in Townsend multiplication of the original ensemble of photoelectrons. Although this removed the relative amplitude significance, the method provided the first information regarding the spectral distribution of the photoionization.

The first trace in Figure 6-11 shows the source spectrum with the test cell evacuated. The test chamber was opened to the diffusion pump, and the pressure could be maintained at about 10^{-6} torr as measured by an ionization gauge. Under these conditions, the ionization level in the test cell was within the amplifier noise. The second trace in Figure 6-11 shows the relative number of photons that were able to penetrate the test cell (12 cm) filled with 45 torr of $CO_2 : N_2 : He = 1 : 1 : 1$

laser mixture. The absorption in the 1200 Å window was approximately 90%, yielding an absorption cross-section of about 10^{-19} cm^2 in proper agreement with the expected value of about 0.7×10^{-19} cm^2 [58]. The last trace in Figure 6-11 reveals that photoionization occurs for short wavelengths in the 1200 Å window, and also for a portion of the spectrum at longer wavelengths between 1650 Å and 1900 Å.

Figure 6-12 reveals that a trace amount of (probably about 0.01 torr) tri-n-propyl amine significantly increases the ionization in both bands. It also broadens the bands. Further reduction of photon intensity in the 1200 Å window also occurred. The apparent ionization around λ = 2400 Å was due to the 1200 Å window in the second grating order. This was confirmed when a quartz window used (short wavelength cut-off of $\lambda \simeq 2000$ Å) in place of the LiF prevented ionization in all parts of the spectrum. Note the dispersion increase by a factor of 2 in accordance with Equation 3-71.

Figure 6-13 shows the wavelength distribution of photoionization in the independent laser gases. A 200 volt collector bias was used for all three cases. The N_2 and He pressures were 15 torr and the CO_2 pressure was reduced to about 2 torr in an attempt to reduce the total absorption. This made the CO_2 result more comparable to the other gases in terms of photoionization wavelength distribution. The distribution is seen to be the same in all the gases indicating that the ionizing species is common. The N_2 and CO_2 photoionization spectra show much the same intensity as well as wavelength distribution. These spectra are comparable to the ionization spectrum obtained when the test cell is being maintained at low pressure by the diffusion pump. However, under vacuum conditions the photoionization spectrum is only about 1/3 as intense as for the case of N_2 or CO_2. The increased intensity with the introduction of CO_2 or N_2 has been attributed to increased contamination from impurities inherent in the supply gases and possibly, to a Townsend multiplication factor. Collector operation in the saturation region was easily obtained when the test cell was kept at low pressure (less than 1 torr).

He resulted in a much stronger photoionization spectrum. This has been attributed primarily to an increased Townsend multiplication factor in the gas. Subsequent testing of a purer grade of He resulted in a loss of intensity across the entire spectrum by a factor of 2. This was attributed to reduced Townsend ionization due to increased gas purity. This implies that the impurities in the industrial grade of He first tested, were comparable in concentration to the residual impurities in the test cell. Consequently, the photoionization density was not expected to be as high for the case of purer He.

The apparent ionization for λ > 2000 Å was a result of short wavelength light in the second grating order as discussed in the previous section.

This investigation has revealed that the ionization spectrum, and perhaps the ionizing species, is independent of gas type. The photoionization cross-section increases with decreasing wavelength. In spite of the fact that there are fewer photons at the short wavelength end of the spectrum, the ionization was consistently greatest there, indicating that the photoionization cross-section increases with decreasing wavelength.

The ionizing species could be some material that ionizes in either a one or two-step process depending on the relative efficiency of these processes and the ionization threshold of the particle. It has been assumed throughout this thesis that if the photon energy is sufficient to ionize in a one-step process then, if ionization occurs, it has been a result of a one-step rather than a multi-step process. In addition, the ionizing species could be a mixture of many species at different concentrations, with ionization thresholds distributed randomly through the region of observed ionization. The possibilities are indeed numerous. However, some further insight regarding ionization thresholds can be gained by determining whether a one or two-step process is involved at a particular wavelength. This is the subject of the next section.

Furthermore, the results presented here, clearly indicate that a more thorough investigation of the charge collection process is necessary. This has been done and the results have been presented in Section 6-2-5.

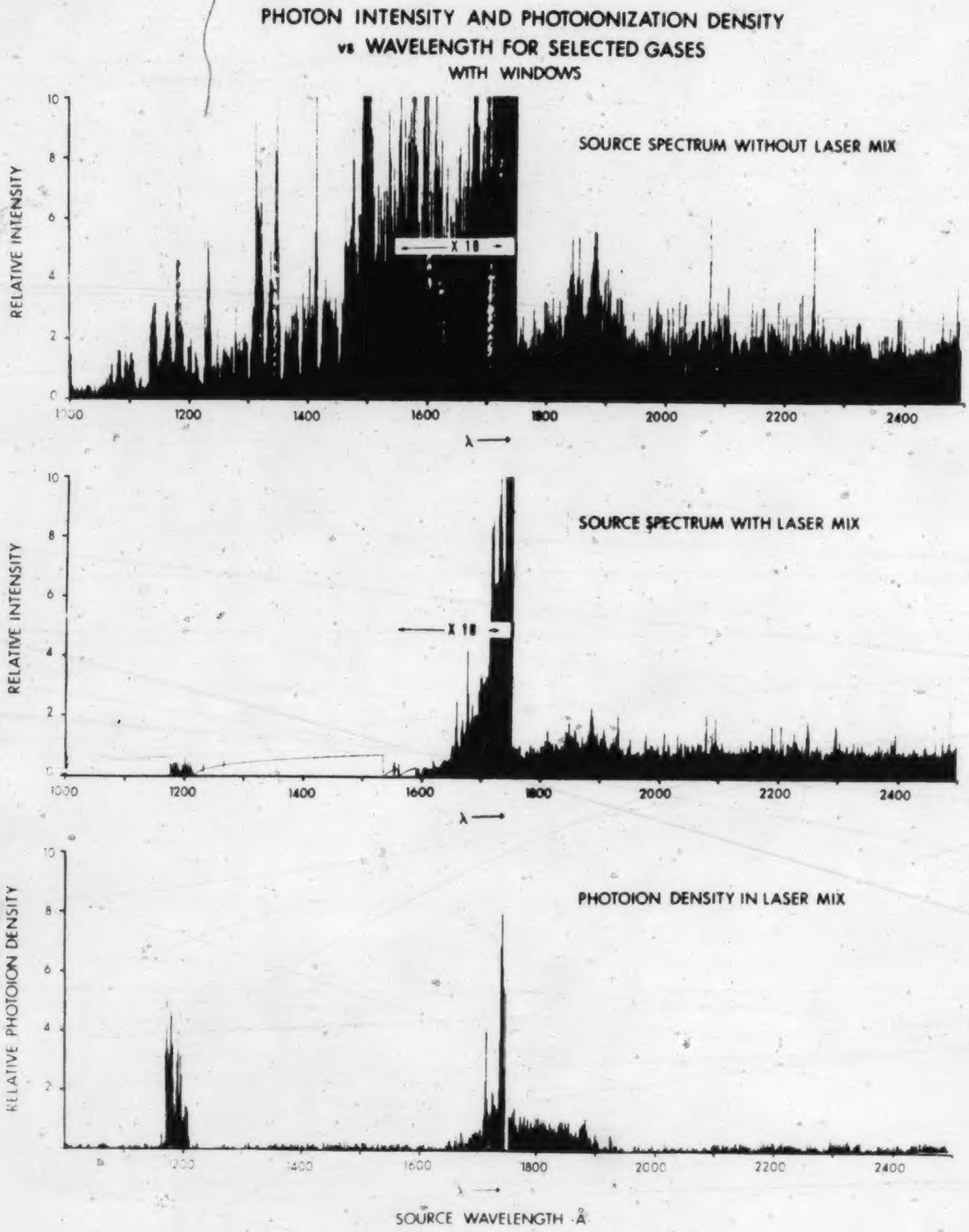

FIGURE 6-11 PHOTON INTENSITY AND PHOTOIONIZATION DENSITY IN A LASER MIXTURE The first trace is the emission spectrum of N_2. The second trace reveals absorption in the test cell (12 cm) filled with 45 torr of CO_2:N_2:He = 1:1:3 laser mixture. The lower trace reveals the photoionization spectrum in this mixture.

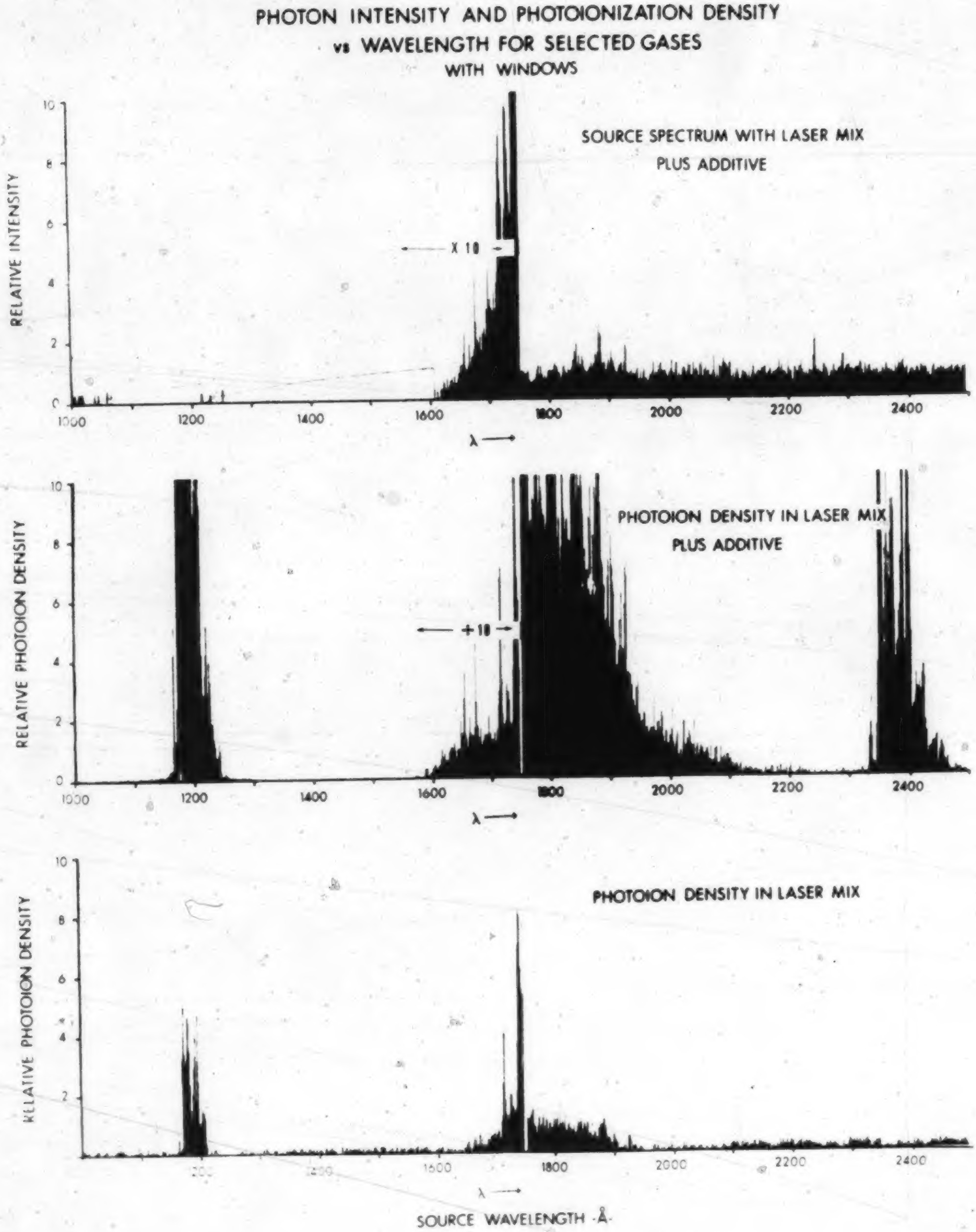

FIGURE 6-12 PHOTON INTENSITY AND PHOTOIONIZATION DENSITY IN A LASER MIXTURE PLUS TRI-N-PROPYL AMINE
The laser mixture is the same as for Figure 6-11. Approximately 0.01 torr of tri-n-propyl amine has been added.

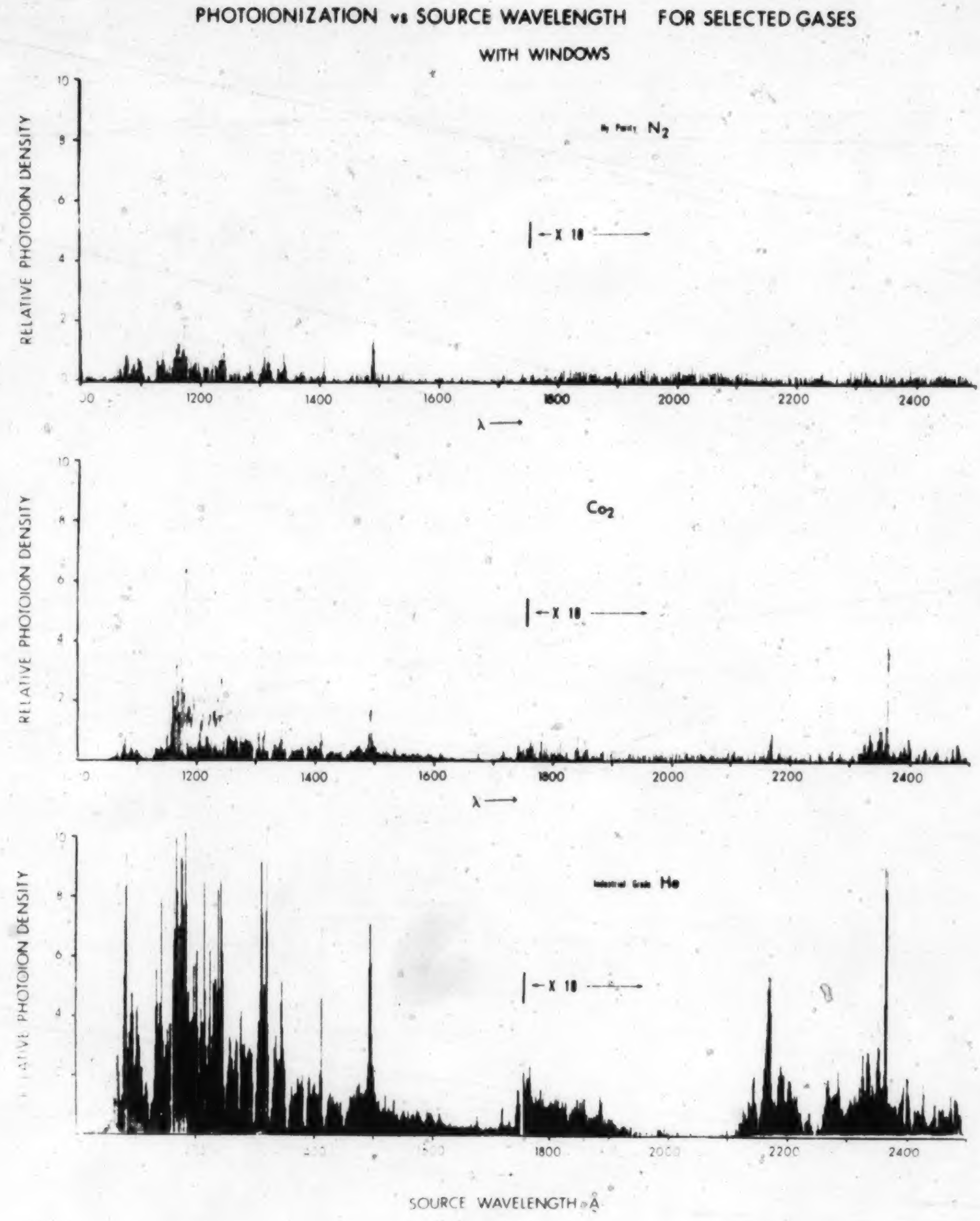

FIGURE 6-13 PHOTOIONIZATION SPECTRA OF THE INDIVIDUAL LASER GASES The N_2 and He were present at a pressure of 15 torr, while the CO_2 pressure was about 2 torr.

6-2-4. Photon Production and Photoionization Mechanism

The assumption that hard ultra-violet production was a linear function of the discharge current was made on the basis of data presented in Section 5-7. The electron density was observed to increase with capacitor charging voltage for constant L and C. Since the peak discharge current was linearly dependent on the charging voltage, then the photon production was assumed to be linearly dependent on the peak discharge current for a one-step process. Subsequently it came to the attention of the author that the photon production may be dependent on the peak rate of current discharge, rather than the peak current discharge. The peak rate of discharge has been shown to also be linearly dependent on the charging voltage for constant C and L.

Such a dependence would provide a major design criteria for the spark driving circuitry. Under such conditions, the reduction of circuit inductance to provide a fast discharge would be even more important that dictated by peak discharge current requirements alone. Hence, an experiment has been performed to determine the actual dependence. Simultaneously, the electron density in He was measured allowing the confirmation of a one-step photoionization process. This has been discussed later in this section.

For a typical R-C-L series circuit, the current wave form for the underdamped case (low R) is: [74,75]

$$i = V_o \left(\frac{C}{L}\right)^{1/2} \exp(-Rt/2L) \sin \frac{t}{(LC)^{1/2}} \qquad 6\text{-}1$$

and the rate of change of current is given by:

$$\frac{di}{dt} = V_o \left(\frac{C}{L}\right)^{1/2} \exp\left(\frac{-Rt}{2L}\right) \left[\frac{1}{(LC)^{1/2}} \cos \frac{t}{(LC)^{1/2}} - \frac{R}{2L} \sin \frac{t}{(LC)^{1/2}}\right]$$

6-2

The maximum value of the current occurs approximately when

$$t = (LC)^{1/2} \frac{\pi}{2}$$

$$i_{max} = V_o \left(\frac{C}{L}\right)^{1/2} \exp\left[- \frac{\pi R}{4} \left(\frac{C}{L}\right)^{1/2}\right] \qquad 6\text{-}3$$

For large L and small R Equation 6-3 reduces to

$$i_{max} \cong V_o \left(\frac{C}{L}\right)^{1/2} \qquad 6\text{-}4$$

The maximum value of the rate of change of current is

$$\left.\frac{di}{dt}\right|_{max} = \frac{V_o}{L} \qquad 6\text{-}5$$

The nature of the L dependence can be best revealed by a logarithmic plot. Taking the logarithms of Equations 6-4 and 6-5 results in:

$$\ln i_{max} = \ln V_o C^{1/2} - \frac{1}{2} \ln L \qquad 6\text{-}6$$

$$\ln \left.\frac{di}{dt}\right|_{max} = \ln V_o - \ln L \qquad 6\text{-}7$$

If the photon output is proportional to i_{max} then a plot of ln N_p against ln L would yield a curve with a slope $-\frac{1}{2}$. However, if it were proportional to $\left.\frac{di}{dt}\right|_{max}$ then a plot of ln N_p against ln L would yield a slope of -1. N_p is the total number of photons produced.

A number of air core inductors were made and the value of inductance measured. These were inserted one at a time in series with the discharge capacitor and spark source. The resulting photon output was measured at two different wavelengths ($\lambda = 1180$ Å and $\lambda = 1750$ Å). Because photon output diminished dramatically with increased L, a bandwidth of 50 Å had to be used in order to obtain good signal strength. The tungsten pin spark plug in a N_2 enviroment was used for the source.

The results of the test are contained in Figure 6-14. A slope of $-\frac{1}{2}$ has been obtained for both wavelengths indicating that the photon production was proportional to peak current as asserted in Section 5-7. The departure from the straight line of slope $-\frac{1}{2}$ for small values of L was a result of the breakdown of the assumption made to obtain Equation 6-4 from 6-3. The exponential term became significant for the smallest values of L used,

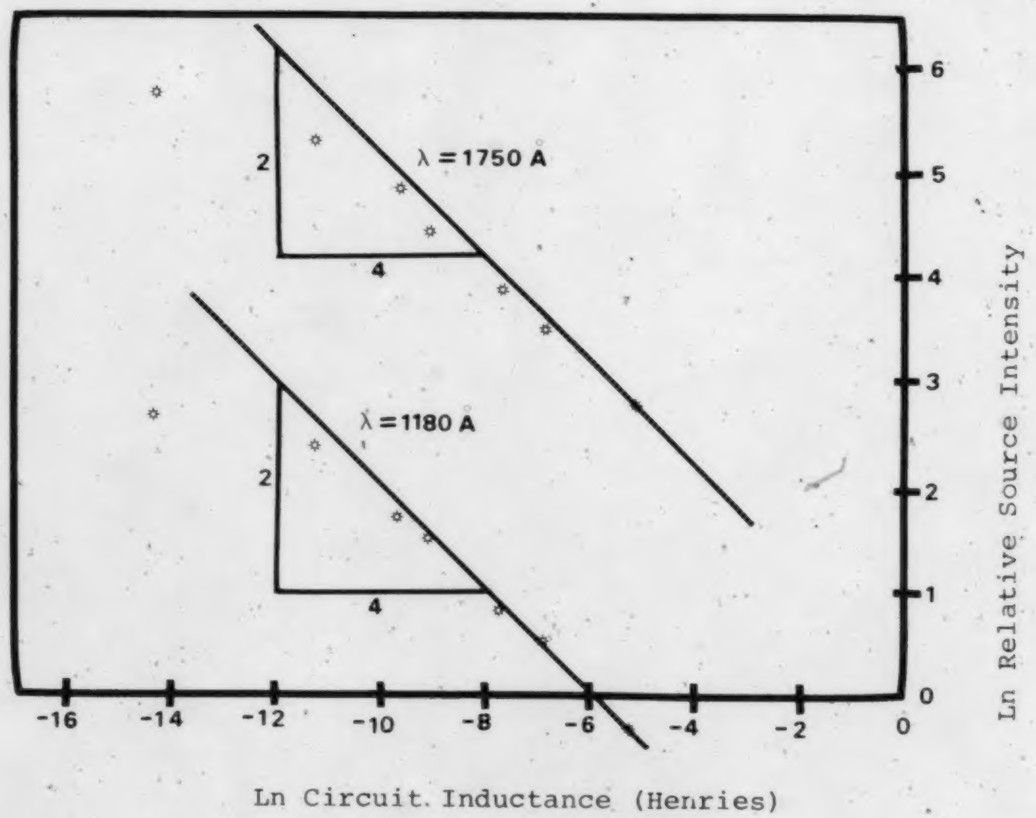

FIGURE 6-14 LOGARITHM OF PHOTON INTENSITY VERSUS LOGARITHM OF CIRCUIT INDUCTANCE

and it served to reduce the maximum current faster than $L^{-1/2}$ dependence. The measured values of the inductors employed agreed within a few percent of the values calculated from the current waveform. The conclusion reached here is in agreement with the information in Figure 6-15. The integrated photon signal and spark discharge current waveforms have been displayed simultaneously with a dual beam oscilloscope. The photon output peaks correspond to the discharge current peaks. The photon output minimums correspond to the zero values of the current where the rate of change of current is maximum. This type of photon signal was typical of all wavelengths. The weaker photon signals were somewhat smoothed out and the peaked structure was not so visible.

The same experiment lent itself to determining the dependence of photoelectron density on photon strength. Filling the test cell with 15 torr of He did not result in any measurable absorption. Consequently, the photoelectron density as a function of photon intensity was determined simultaneously. Introduction of L in the circuit served to vary the photon intensity. A collector bias voltage of 200 volts was employed and Townsend multiplication was assumed to occur. The multiplication factor was constant and so relative values were unaffected. Even though a 50 Å bandwidth was used, the signal was not sufficiently strong in all cases to allow the electronic filter to be bypassed.

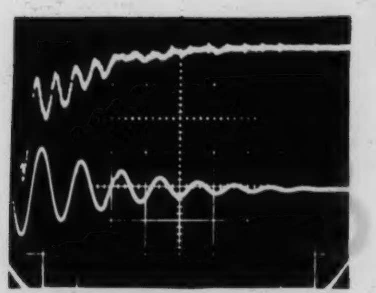

Photons 0.05 μ/div

λ = 1080 A°   0.5 μs/div

Current 50μ/div

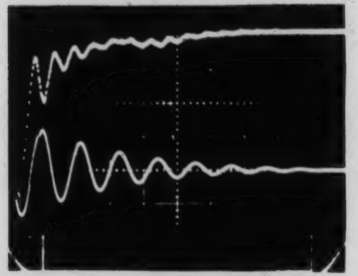

Photons 0.1 μ/div

λ = 1180 A°   0.5μs/div

Current 50 μ/div

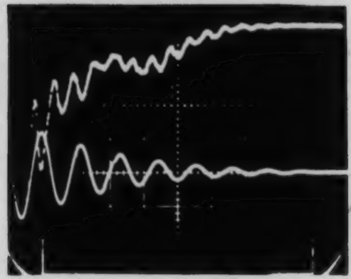

Photons 0.1 μ/div

λ = 1300 A°   0.5 μs/div

Current 50 μ/div

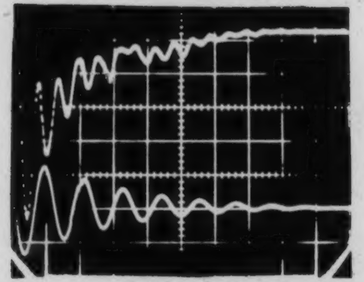

Photons 0.1 μ/div

λ = 1480 A°   0.5 μs/div

Current 50 μ/div

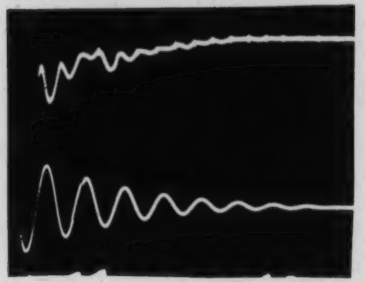

Photons 0.5 μ/div

λ = 1750 A°   0.5 μs/div

Current 50 μ/div

FIGURE 6-15   SPARK DISCHARGE CURRENT AND PHOTON WAVEFORMS

However, the collector could be gated open for 80 μs. This was sufficient time to collect all electrons, even for the longest spark discharge intervals, where larger values of inductance were used. Knowledge of the relationship between photon density and photoelectron density can be shown to reveal the nature of the photoionization process [16,17,23].

Electron loss has been assumed to be negligible for the low density of charged particles under consideration here. The photoelectron generation rate for a one-step process is given by Equation 5-46 rewritten here for convenience

$$\frac{dn_e}{dt} = \frac{I}{h\nu} \sigma_i n \qquad 6\text{-}8$$

There is no need to consider only average values in this case because of the improved wavelength resolution (50 Å). In addition, the photon intensity has been electronically integrated. The solution to Equation 6-8 is:

$$n_e = \sigma_i n N_p \qquad 6\text{-}9$$

where $\int \frac{Idt}{h\nu} = N_p\,[\text{cm}^{-2}]$ 6-10

N_p is the total number of photons collected within a given bandwidth per shot. Since σ_i and n are constants the total number of photoelectrons produced per spark must be proportional to the total number of photons incident on the test gas. Since the test gas has been observed to be optically thin, photoabsorption need not be considered.

The situation is somewhat different for a two-step process. An intermediate bound state in the ionizing species may be excited by a photon in the line width of the transition. A second photon of any frequency of sufficient energy may then ionize the excited particle. At the gas pressure under consideration (15 torr of He) the line width is determined primarily by collision effects. 50 MH/torr is a reasonable value for collision broadening [16,76]. At 15 torr the linewidth is only 750 MHz. The amount of light in so narrow a band was very little and so a two or multi-step process was not expected to have been operating. The two-step process can be most readily analysed, if the photon intensity over the duration of the spark is considered to be approximately constant. The rate equation describing the population of the excited intermediate state is:

$$\frac{dn^*}{dt} = \frac{I}{h\nu} n\sigma^* \frac{\Delta\nu}{\Delta f} - \frac{n^*}{\tau_\ell} - \frac{dn_e}{dt} \qquad 6\text{-}11$$

τ_ℓ = lifetime of intermediate state [sec]

n^* = density of excited intermediate state [cm^{-3}]

I = average photon flux over the available bandwidth, Δf. I has been assumed to be constant [erg $\mathrm{cm}^{-2}\mathrm{sec}^{-1}$].

The rate of appearance of electrons can be described by:

$$\frac{dn_e}{dt} = \frac{I}{n\nu} n^* \sigma_i{}^* \qquad 6\text{-}12$$

$\sigma_i{}^*$ = the photoionization cross-section for the excited intermediate state [cm^2].

Equations 6-11 and 6-12 can be combined and algebraically manipulated to read:

$$\frac{dn^*}{\frac{I}{h\nu}\, n\sigma^* \frac{\Delta\nu}{\Delta f} - \left(\frac{1}{\tau_\ell} + \frac{I}{h\nu}\sigma_i^*\right) n^*} = dt \qquad 6\text{-}13$$

The variables have been separated and a solution can be obtained from standard integration tables [70]:

$$n^*(t) = \frac{\frac{I}{h\nu}\, n\sigma^* \frac{\Delta\nu}{\Delta f}}{\frac{1}{\tau_\ell} + \frac{I}{h\nu}\sigma_i^*} \left[1 - \exp-\left(\frac{1}{\tau_\ell} + \frac{I}{h\nu}\sigma_i^*\right) t\right] \qquad 6\text{-}14$$

Substitution of Equation 6-14 into Equation 6-12 yields:

$$dn_e = \frac{\left(\frac{I}{h\nu}\right)^2 n\sigma_i^*\, \sigma^* \frac{\Delta\nu}{\Delta f}}{\frac{1}{\tau_\ell} + \frac{I}{h\nu}\sigma_i^*} \left[1 - \exp-\left(\frac{1}{\tau_\ell} + \frac{I}{h\nu}\sigma_i^*\right) t\right] dt \qquad 6\text{-}15$$

The solution readily follows:

$$n_e(t) = \frac{\left(\frac{I}{h\nu}\right)^2 n\sigma_i^*\sigma^* \frac{\Delta\nu}{\Delta f}}{\frac{1}{\tau_\ell} + \frac{I}{h\nu}\sigma_i^*} \left[t + \frac{\exp-\left(\frac{1}{\tau_\ell} + \frac{I}{h\nu}\sigma_i^*\right)}{\frac{1}{\tau_\ell} + \frac{I}{h\nu}\sigma_i^*} t - 1\right] \qquad 6\text{-}16$$

The constants of integration for Equations 6-14 and 6-16 have been obtained by applying the initial conditions. i.e. $n^*(0) = n_e(0) = 0$. Furthermore, Equations 6-14 and 6-16 apply only for the duration of the spark.

Two limiting cases can be considered:

(1) The radiative lifetime of ordinary bound states is very short ($\approx 10^{-8}$ sec) and so $\frac{1}{\tau_\ell} >> \sigma_i{}^* \frac{I}{h\nu}$

Consequently Equation 6-16 reduces to

$$n_e(t_d) = \left(\frac{I}{h\nu}\right)^2 n\sigma_i{}^*\sigma^* \frac{\Delta\nu}{\Delta f} \tau_\ell t_d \qquad 6\text{-}17$$

t_d = spark duration time [sec].

$n_e(t_d)$ is the total number of electrons produced during the spark discharge duration, t_d. The charge collector output is proportional to $n_e(t_d)$. Also the photon counter output, N_p, is equal to $t_d(\frac{I}{h\nu})$. The important feature here is that the electron production is proportional to the square of the photon intensity.

(2) For a metastable intermediate state where τ_ℓ is considerably larger than in case (1) or for a very intense source then one may obtain

$$\frac{1}{\tau_\ell} << \sigma_i{}^* \frac{I}{h\nu}$$

Equation 6-16 then reduces to

$$n_e(t_d) = \frac{It_d}{h\nu} n\sigma^* \frac{\Delta\nu}{\Delta f} + n \frac{\sigma^*}{\sigma_i{}^*} \frac{\Delta\nu}{\Delta f} \left[\exp\left(\frac{-I}{h\nu} t_d\sigma_i{}^*\right) -1\right] \qquad 6\text{-}18$$

For very large values of photon intensity the term containing the exponential goes to zero and the electron density depends only on the first power of the photon intensity. For intermediate values of intensity the electron density exhibits an exponential dependence on photon intensity. For the low values of photon intensity employed in the test Equation 6-18 can be reduced to:

$$n_e(t_d) = n\sigma^* \frac{\Delta\nu}{\Delta f}\left(\frac{I}{h\nu}\, t_d - \frac{1}{\sigma_i^*}\right) \qquad 6\text{-}19$$

For typical values of $n_e(t_d) \doteq 10^4$ and $\frac{I}{h\nu}\, t_d \approx 10^8$, σ_i^* would have to be unrealistically large. Consequently, a two-step process via a metastable intermediate excited state can not be considered as a candidate here. Furthermore it would be unreasonable to expect that long lived, easily excited, metastable states would be readily available across the entire spectrum ($1150\ \text{Å} \lesssim \lambda < 1700\ \text{Å}$).

Figure 6-16 reveals electron density versus photon intensity characteristics for center wavelengths at 1180 Å and 1750 Å respectively. The plots are both linear revealing that the photoionization follows a one-step process in accordance with Equation 6-9. The steeper slope in Figure 6-15(b) reveals that the process was more efficient for the shorter wavelength light. The test bandwidth was only 50 Å so it is possible that a two or multi-step process dominates in another portion of the spectrum. However, comparison of the other regions of the spectrum to the two regions presented, has revealed no differences worthy of implying anything other than a one-step process for the entire spectrum.

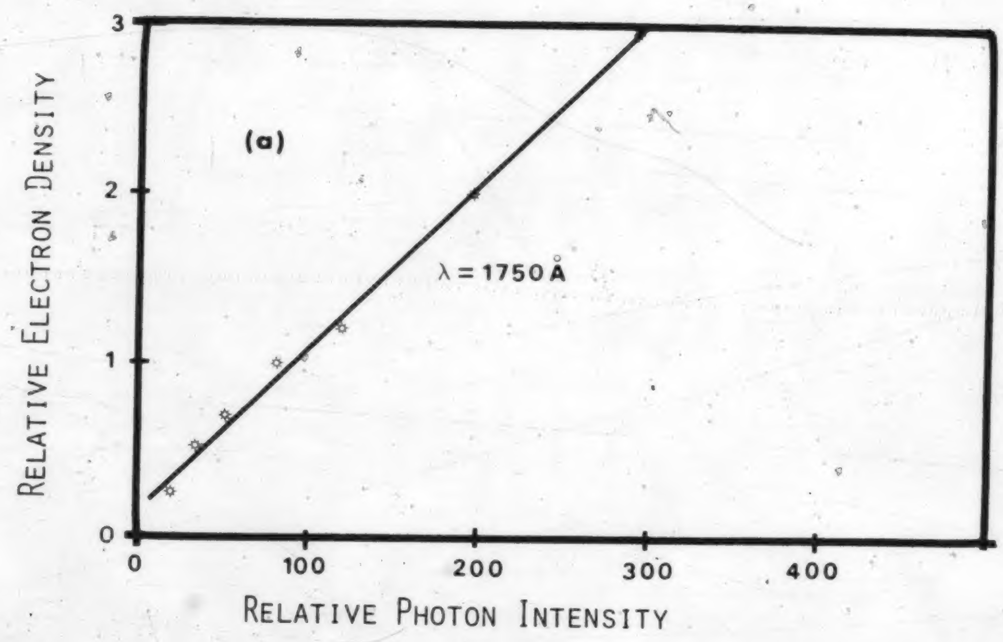

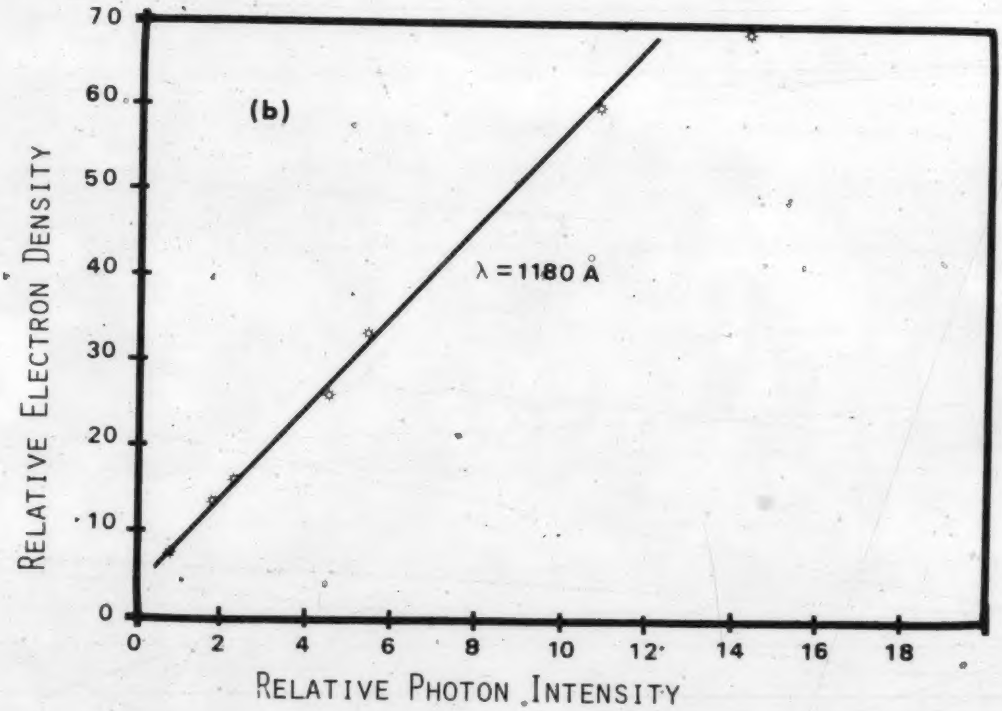

Figure 6-16 Relative Electron Density Versus Relative Photon Intensity

6-2-5. Charge Collection Characteristics

Increased charge collected with increased collector bias voltage prompted an investigation of the voltage-integrated current characteristics of the charge collector. The results appear in Figures 6-17, 6-18 and 6-19 for the three independent laser gases. The collector plate separation of 2.54 cm has been used to convert the bias voltage to electric field E. The tests were performed using a N_2 source with a LiF window. The grating was centered on $\lambda = 1800$ Å with a bandwidth of 50 Å. The test cell was evacuated and refilled with fresh gas for each test in an attempt to prevent degassing impurities from accumulating. Overnight pumping with the diffusion pump reduced the impurity level so that a relative ionization reading of approximately 2 was obtained.

If the test cell was then isolated from the pump, the ionization increased to a reading of approximately 6 in about 2 hours. Over a period of 48 hours the isolated test cell leaked up 0.1 torr. An ionization test resulted in a reading of 60. The gas was subsequently pumped out and replaced with 0.1 torr of air. The resulting ionization then dropped to 4. Consequently, it was assumed that the gas was largely a result of a virtual leak associated with absorbed gases. Unfortunately, a significant quantity of material that readily absorbs and releases gas had to be used within the test cell. Teflon was used to

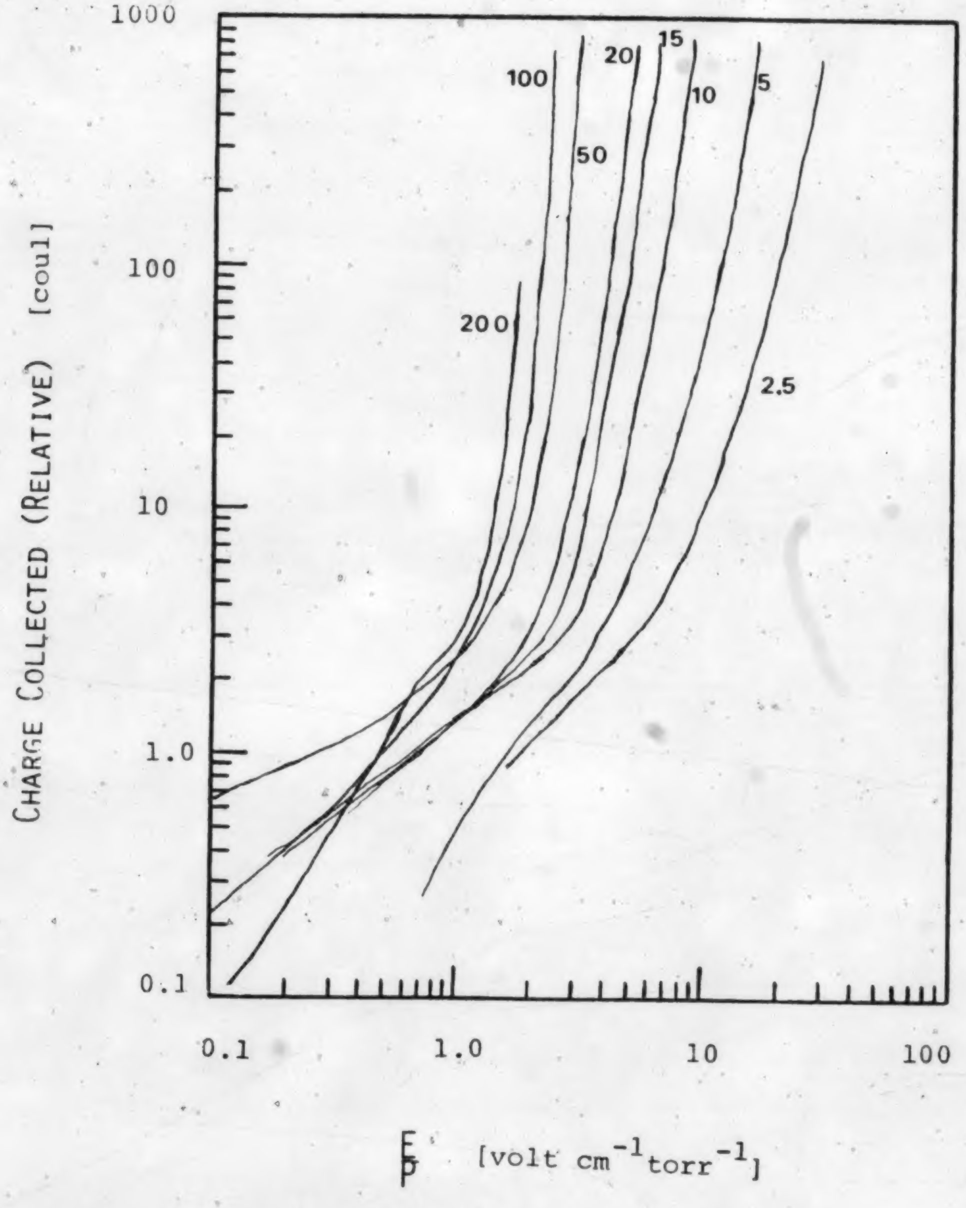

Figure 6-17 Charge Collector Characteristics in He
The numbers on the curves denote pressure in torr. The vertical scale is the output voltage (÷0.2) referred to maximum charge collector gain.

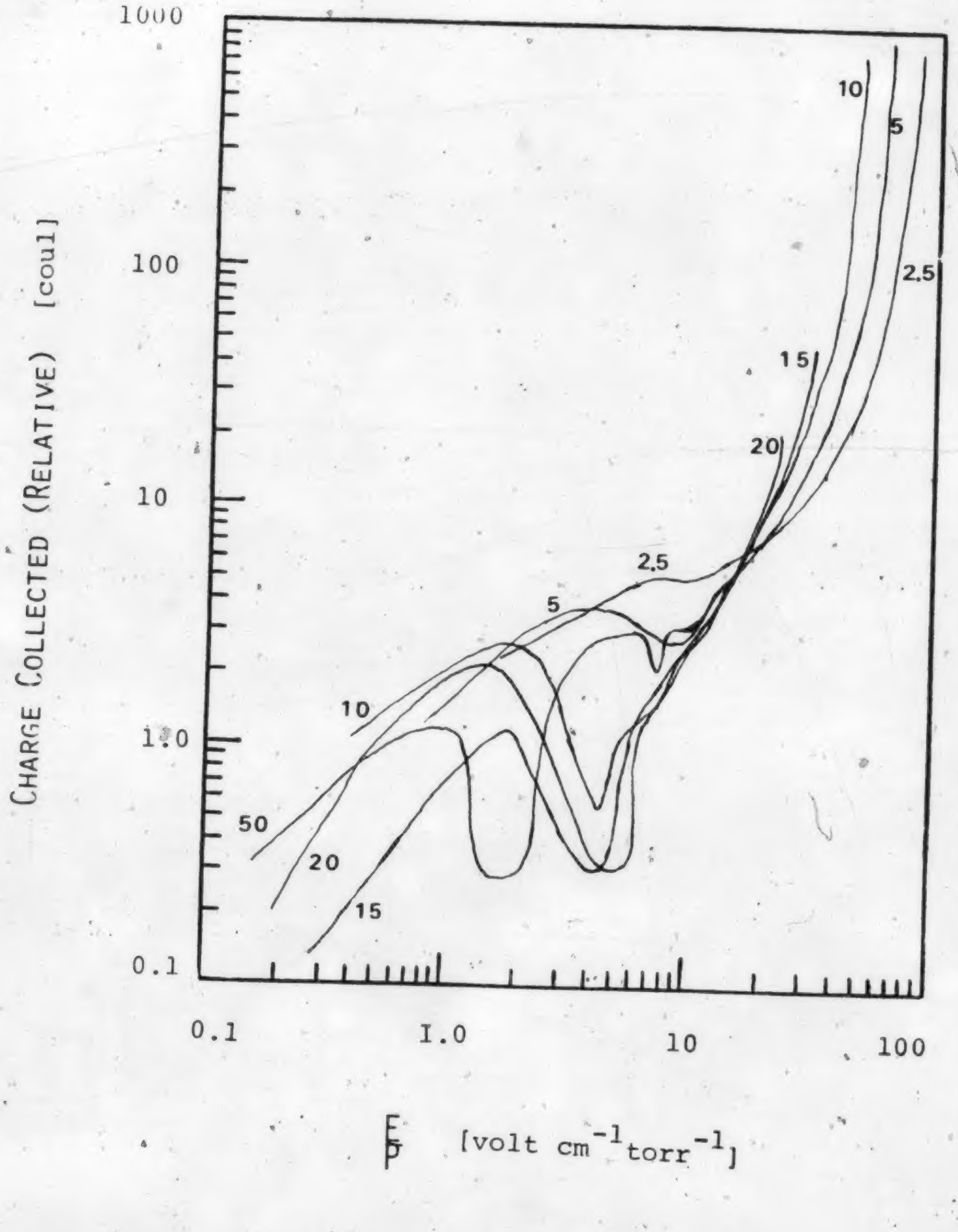

FIGURE 6-18 CHARGE COLLECTOR CHARACTERISTICS IN CO_2
The numbers on the curves denote pressure in torr. The vertical scale is the output voltage (÷0.2) referred to maximum charge collector gain.

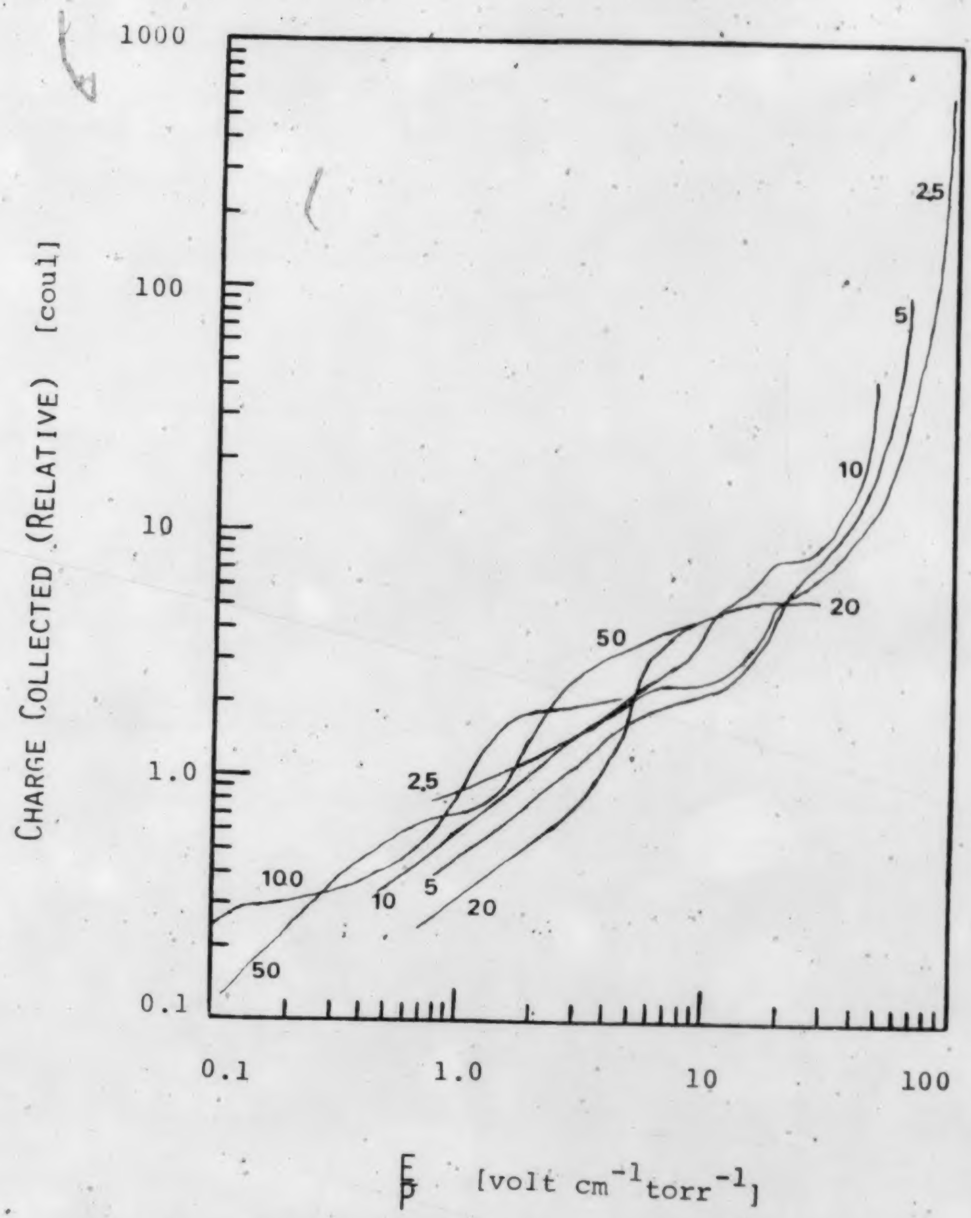

Figure 6-19 Charge Collector Characteristics in N_2
The numbers on the curves denote pressure in torr. The vertical scale is the output voltage (÷0.2) referred to maximum charge collector gain.

support the collector electrodes and to insulate the leads. The preamplifier had to be placed inside the test cell to reduce noise pickup and input capacitance. This was constructed on a print circuit board backed with fiberglass. Hence, a large degassing rate was expected. Since each test required 1/2 an hour to perform, then about one micron of impurity could be expected to have accumulated. The supply gas had an impurity rating of about 20 ppm [59] and so the impurity concentration in the test cell would be approximately constant at low test pressure, where it would be dominated by the background impurities. However, at high pressures, it may vary with the test gas pressure. With this as a starting point an analysis of the collector characteristics can be attempted.

For each of the gases, the collected charge eventually increased exponentially with the bias voltage until gaseous breakdown resulted. This region of operation was clearly the Townsend avalanche region. For lower values of E/P, the curves were expected to become horizontal, indicating operation in a saturation mode - the desired condition. Furthermore, for low pressures at least, the saturation level was expected to be approximately constant with pressure as a result of domination by background impurities. Only in the case of N_2 in Figure 6-19 is this evident and then only marginally. The curves exhibit a flat portion around E/P = 10 and a relative charge density of 4. For the lesser values of E/P, the collected charge continued to drop off, although not so rapidly as for the large E/P. An electron loss mechanism has been assumed to be responsible for this. As the E/P value increased, so did the electron drift velocity and electrons were collected in a shorter interval. Therefore, the electron loss mechanism operates for less time and less electrons are lost with a correspondingly greater amount collected. In order to nullify the loss mechanism a large E/P appears to be required. However, before the E/P has been increased sufficiently to obtain saturation, it has become sufficiently large to result in multiplication by the Townsend avalanche mechanism. Only in the case of N_2 has there been an indication of a saturation region.

As mentioned in an earlier section the amount of charge collected did not increase with collection time beyond a critical value. For most of the data obtained, the required collection time was less than the minimum time that could be resolved with the electronic gating device (7 μs). Only for CO_2 at the lowest values of E/P was a collection time of 30 to 40 μs required. These values correlate with electron drift velocity data in the literature [41,56]. A consideration of the electron drift velocities [41,56] and the plate separation (2.54 cm) reveals that the collection time would have ranged from approximately 2 μs to 40 μs depending on the gas species and E/P. A gate time of 80 μs was used throughout to assure that sufficient time was allowed to collect all electrons. Charge due to positive ion collection was insignificant for the lower values of E/P. For the higher values, the positive ion may be collected in 80 μs depending on their mass. However, this would result in no more than a factor of 2 increase at most.

The candidates for electron loss processes are the same as the ones discussed in Chapter 5. These are diffusion, attachment and recombination. The recombination coefficient decreases with electron density [41] and for the low densities and short collection intervals considered here, recombination would be much too slow to be a significant factor. Attachment will depend on the concentration of an electronegative species and the electron energy. This is particularly evident in Figure 6-18 where the number of electrons collected actually drops for particular values of E/P. The electron energy corresponding to the E/P values at the valleys can be obtained from values of the Townsend energy factor available in the literature [41]. The valleys obtained here do not line up with the peaks in the electron attachment cross-section versus electron energy curves for CO_2 [56]. This may be due to the complex electron collection mechanism and to Townsend multiplication. However, besides the valleys in the CO_2 curves, the problem of increasing signal strength with increasing E/P was evident. The only other electronegative gas that may have been present was O_2. However, no more than a few microns of O_2 are likely to have been present resulting from gas supply contamination and residual O_2 in the test cell. Even considering the largest collision attachment cross-section for O_2 occurring at an electron energy of 7 eV, one obtains negligible loss in 80 μs.

The only remaining candidate is diffusion. The volume between the collector electrodes is essentially a parallelepiped being 12 cm x 2.54 cm x 10 cm in dimension. The diffusion equation can be found in Section 5-4 and a solution can be obtained in a manner similar to that outlined in Section 5-4. Rectangular rather than cylindrical coordinates are more appropriate for this application, however. The solution is given by: [41]

$$n_e(x,y,z,t) = \sum_{i=1}^{\infty} \sum_{j=1}^{\infty} \sum_{k=1}^{\infty} G^*_{ijk}(x,y,z)\exp(-t/\tau_{ijk}) \qquad 6\text{-}20$$

where

$$G^*_{ijk}(x,y,z) = G_{ijk} \cos\left(\frac{2i-1}{a}\right)\pi x \cos\left(\frac{2j-1}{b}\right)\pi y \cos\left(\frac{2k-1}{c}\right)\pi z \qquad 6\text{-}21$$

and the time constants are given by:

$$\frac{1}{\tau_{ijk}} = D_e \pi^2 \left[\left(\frac{2i-1}{a}\right)^2 + \left(\frac{2j-1}{b}\right)^2 + \left(\frac{2k-1}{c}\right)^2\right] \qquad \text{6-22}$$

$a = 2.54$ cm

$b = 12$ cm

$c = 10$ cm

$i = 1,2,3,4...$

$j = 1,2,3,4...$

$k = 1,2,3,4...$

The measured collection intervals indicate that electrons can diffuse independent of the positive ions and can therefore be relatively fast. Also the mobility concept for electrons applies and one may write:

$$V_d = K_e E \qquad \text{6-23}$$

V_d = electron drift velocity [cm sec^{-1}]
K_e = electron mobility [cm^2 volt^{-1} sec^{-1}]
E = electric field [volt cm^{-1}]

and for electrons not in thermal equilibrium [41]:

$$\frac{K_e}{D_e} = \frac{e}{\eta k T} \qquad \text{6-24}$$

η = Townsend energy factor (the ratio of electron energy at an elevated temperature to the electron energy at ambient temperature T).

k = Boltzman constant [erg K^{-1}]

e = electronic charge [coul]

Combination of Equations 6-23 and 6-24 results in:

$$D_e = \frac{v_d}{(\frac{E}{P})P} \frac{\eta kT}{e} \qquad \text{6-25a}$$

values of v_d and η can be found in the literature [41, 56] and these are tabulated in Table 6-1 along with the resulting values of D_e for the ps and E/Ps of interest.

The electrons are photogenerated with sharp boundaries as a result of the wedge of photons effectively emitted by the monochromator slit. The nonuniform spatial distribution can be expected to exhibit high mode diffusion in all three dimensions. Consequently, the diffusion time constants have been calculated for $i = j = k = 2$. For E/P = 10, the first term in Equation 6-22 has been omitted. For large E - fields, back diffusion should not be significant. The time constants appear in Table 6-2. The electron clearance time, t_c, defined as the distance between the plates (2.54 cm) divided by the electron drift velocity has also been included in Table 6-2. The factor exp $(-t_c/\tau_{ijk})$ represents the loss due to diffusion during the clearance time. The factor has been calculated and tabulated in Table 6-2. Having completed the table in this manner it becomes quite obvious that diffusion losses can be extreme. The table

Table 6-1

Electron Diffusion Coefficients

Gas	E/P [volt cm^{-1} $torr^{-1}$]	P [torr]	v_d [cm sec^{-1}]	$\eta kT/e$ [ev]	D_e [cm^2 sec^{-1}]
He	0.1	2.5	5×10^5	0.2	4×10^5
	0.1	20	5×10^5	0.2	5×10^5
	0.1	200	5×10^5	0.2	5×10^3
	1.0	2.5	1×10^6	2.0	8×10^5
	1.0	20	1×10^6	2.0	1×10^5
	1.0	200	1×10^6	2.0	1×10^4
N_2	0.1	2.5	4×10^5	0.2	3.2×10^5
	0.1	50	4×10^5	0.2	1.6×10^4
	0.1	100	4×10^5	0.2	8×10^3
	1.0	2.5	8×10^5	1.0	3.2×10^5
	1.0	50	8×10^5	1.0	1.6×10^4
	1.0	100	8×10^5	1.0	8×10^3

Table continued on next page

Table 6-1 continued

Gas	E/P [volt cm^{-1} $torr^{-1}$]	P [torr]	V_d [cm sec^{-1}]	ηkT/e [ev]	D_e [cm^2 sec^{-1}]
N_2 continued	10	2.5	5×10^6	2.0	4×10^5
	10	50	5×10^6	2.0	2×10^4
	10	100	5×10^6	2.0	1×10^4
CO_2	0.1	2.5	5×10^4	0.005	1×10^4
	0.1	50	5×10^4	0.005	5×10^2
	0.1	100	5×10^4	0.05	2.5×10^2
	1.0	2.5	1×10^5	0.1	2×10^4
	1.0	50	1×10^5	0.1	1×10^3
	1.0	100	1×10^5	0.1	5×10^2
	10	2.5	1×10^7	1.7	6.8×10^5
	10	50	1×10^7	1.7	3.4×10^4
	10	100	1×10^7	1.7	1.7×10^4

also reveals that the way to combat the diffusion losses is by operating the charge collector at high P (to reduce $\mathcal{D}_e$) and high E/P (to reduce t_c). The values of E/P and P required by Table 6-2 for $\exp(-t_c/\tau_{ijk}) \simeq 1$ (no losses) can be seen to be in the vicinity of the onset of Townsend multiplication evident in Figures 5-17, 5-18 and 5-19.

A more accurate account of diffusion losses could be made if one considered the kinetic equations governing the photoelectron production along with electron collection and electron loss. Such an equation can be written as follows:

$$\frac{dn_e}{dt} = \left.\frac{dn_e}{dt}\right|_{\text{prod}} - \left.\frac{dn_e}{dt}\right|_{\text{coll}} + \mathcal{D}_e \nabla^2 n_e \qquad [6\text{-}25]$$

where

$$\left.\frac{dn_e}{dt}\right|_{\text{prod}} = \frac{I(x,y,z,t)}{h\nu} \sigma_i n \qquad [6\text{-}26]$$

$$\left.\frac{dn_e}{dt}\right|_{\text{coll}} = \frac{n_e}{V} V_d A \qquad [6\text{-}27]$$

V = volume containing the electrons [cm^3]

A = charge collector area [cm^2]

n_e = total number of electrons within V.

n = total number of particles capable of being ionized in the volume swept out by the photon beam.

Table 6-2

Electron Diffusion Losses

Gas	E/P [volt cm^{-1} $torr^{-1}$]	P [torr]	t_c [μs]	τ_{i22} [μs]	$\exp(-t_c/\tau_{i22})$
He	0.1	2.5	5	0.16	2.7×10^{-14}
	0.1	20	5	1.3	2.2×10^{-2}
	0.1	200	5	13	0.68
	1.0	2.5	2.5	0.08	5.4×10^{-14}
	1.0	20	2.5	0.66	2.2×10^{-22}
	1.0	200	2.5	6.6	0.68
N_2	0.1	2.5	6.4	0.2	2.6×10^{-14}
	0.1	50	6.4	4.1	0.2
	0.1	100	6.4	8.2	0.5
	1.0	2.5	3.2	0.2	1.6×10^{-7}
	1.0	50	3.2	4.1	0.5
	1.0	100	3.2	8.2	0.7

Table continued on next page

Table 6-2 continued

Gas	E/P [volt cm^{-1} $torr^{-1}$]	P [torr]	t_c [μs]	τ_{i22} [μs]	$\exp(-t_c/\tau_{i22})$
N_2 continued	10	2.5	0.5	1.7 i=0	0.7
	10	50	0.5	33.0 i=0	1.0
	10	100	0.5	66.0 i=0	1.0
CO_2	0.1	2.5	51	6.6	4.1×10^{-4}
	0.1	50	51	131	0.7
	0.1	100	51	262	0.8
	1.0	2.5	5	3.3	0.2
	1.0	50	5	66	0.9
	1.0	100	5	131	1.0
	10	2.5	0.25	1.0 i=0	0.8
	10	50	0.25	20 i=0	1.0
	10	100	0.25	40 i=0	1.0

Equation 6-25 becomes:

$$\frac{dn_e}{dt} = I\frac{(x,y,z,t)}{h\nu}\,\sigma_i\, n - \frac{n_e v_d A}{V} + D_e\,\nabla^2 . n_e \qquad 6\text{-}28$$

Equation 6-28 can be simplified by assuming that I(x,y,z,t) is very short in time and has gone to zero before significant collection or diffusion has taken place. An exponential time dependence can be assumed and a solution similar to Equation 6-20 follows, except that $\frac{1}{\tau_{ijk}}$ is replaced by $\frac{1}{\tau_{ijk}} + \frac{v_d A}{V}$ in Equation 6-22.

The method has not been pursued however, since the previous analysis served well in identifying the significance of diffusion and more rigorous mathematics is not warranted. Furthermore, the simplifying assumption of a fast light pulse may be justified mathematically but not physically. The collection of electrons as they are formed, and the dispersion of the ions to fill a larger volume keep the density lower than it may otherwise be. This tends to prevent the development of space charge limited collection.

Consideration of the first Townsend ionization coefficient leads to initial electron densities and saturation points in agreement with those predicted by the diffusion analysis. However, the correct form of the avalanche equation must be determined by taking the initial spatial distribution of the electrons into account. The volume density will be in the shape of a wedge symmetrically uniform about the mid plane between the collector electrodes. This is illustrated in Figure 6-20. For avalanche multiplication of the electrons in the volumes designated dn_{e1} and dn_{e2}, one may write the total number of electrons reaching the collector plate at $y = f$ as:

$$dn_e = (dn_{e1} + dn_{e2}) \exp[\alpha_t (f-y)] \qquad 6\text{-}29$$

where

$$dn_{e1} = \frac{n_{e01}}{V} (l) \left(- \frac{by}{d} + b\right) dy \qquad 6\text{-}30$$

and

$$dn_{e2} = \frac{n_{e02}}{V} (l) \left(- \frac{by}{d} + b\right) dy \qquad 6\text{-}31$$

$$V = bd(l) \qquad 6\text{-}32$$

α_t = Townsend first ionization coefficient [cm^{-1}]

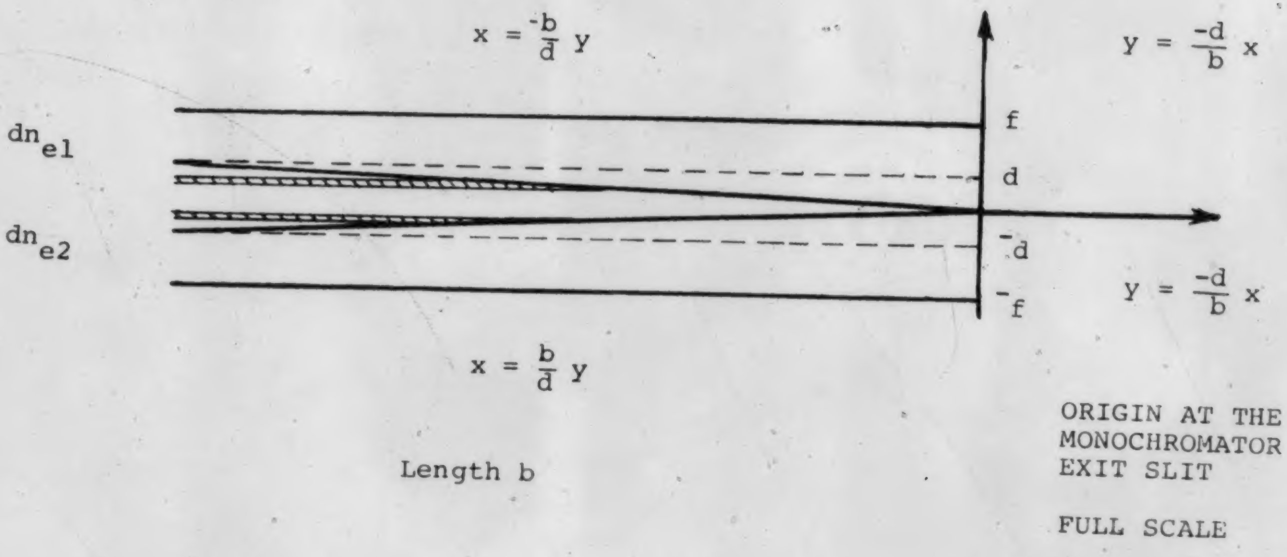
x = -b/d y
y = -d/b x
dn_e1
f
d
dn_e2
-d
-f
y = -d/b x
x = b/d y
ORIGIN AT THE MONOCHROMATOR EXIT SLIT
Length b
FULL SCALE

FIGURE 6-20 CHARGE COLLECTOR GEOMETRY The transit distance for all charged particles is not the same. This must be taken into account when calculating electron multiplication due to Townsend avalanching.

The wedge defined by the photon beam was about 1 cm in depth.

Equation 6-29 becomes

$$n_e = \frac{n_{eo}}{d} \exp(\alpha f)\left[\int_o^d \left(1 - \frac{y}{d}\right) \exp(-\alpha_t y)\,dy + \int_{-d}^{o} \left(1 + \frac{y}{d}\right) \exp(-\alpha_t y)\,dy\right] \qquad 6\text{-}33$$

The solution is given by:

$$n_e = n_{eo} \exp(\alpha_t f) \left[\frac{\exp(-\alpha_t d) + \exp(\alpha_t d) - 2}{\alpha_t^2 d^2}\right] \qquad 6\text{-}34$$

n_{eo} = initial total number of photo electrons

Also $\lim_{d \to o} n_e = n_{eo} \exp(\alpha_t f)$ as required.

This can be seen to be true if $\exp(\alpha_t d)$ and $\exp(-\alpha_t d)$ are approximated by the first two terms of the Taylor series expansion about zero for these functions.

Since n_{eo} can be expected to be proportional to the density of the ionizing species, n, then a knowledge of n would permit the determination of α_t. However, the only information available about n is that it is approximately constant for pressures up to approximately 50 torr. For the larger pressures under consideration it can also be assumed to be constant since the error would be no more than a factor of 2 or 3. The functional dependence of α_t can be found in the literature [51,52]. The important feature is that α_t/P is constant for constant E/P. Consequently, one may write for constant E/P:

$$\alpha_t = k_i P \qquad 6\text{-}35a$$

where k_i = constant [cm^{-1} $torr^{-1}$]. The factor k_i can be determined for any two points on the curves in Figures 6-17, 6-18 and 6-19. The two points must have a common value of E/P thus requiring the pressures to be different. Of course the points must be located on the avalanche portion of the curves. The values of k_i can then be determined from a ratio of Equation 6-34 at point (P_1, n_{e1}) to Equation 6-34 at point (P_2, n_{e2}). The two points are for constant E/P. The resulting equation is:

$$\frac{n_{e1}}{n_{e2}} = \frac{n_{e01}}{n_{e02}} \frac{P_2^2}{P_2^2} \exp[(P_1 - P_2) k_i f \left[\frac{\exp(-k_i P_1 d) + \exp(k_i P_1 d) - 2}{\exp(-k_1 P_2 d) + \exp(k_i P_2 d) - 2}\right] \qquad 6\text{-}35$$

For constant ionizing species density with gas pressure $n_{e01} = n_{e02}$ and Equation 6-35 can be solved for k_i by trial and error. This has been done for a number of gas pressures and values of E/P and the results have been tabulated in Table 6-3. Equation 6-34 has been employed to find n_{eo} having determined k_i for the point (p_1, n_{e2}) or (P_2, n_{e2}) on the curve. These have also been tabulated in Table 6-3. The k_i values are about a factor of 3 to 5 larger than the values available in the literature for N_2 and He [51,52]. Such an increase can be expected for the contaminated gases used here.

The small variation in n_{eo} obtained, provides further evidence that ionizing species density was approximately constant. This can be seen to be particularly true for N_2 and CO_2. Good correlation between the diffusion loss and Townsend multiplication analysis has been obtained. Table 6-2 indicates that for the conditions of P and E/P for N_2 and CO_2 in Table 6-3, no diffusion loss should occur. The values of n_{eo} obtained for N_2 and CO_2 can be assumed to be the result of collecting all of the photoelectrons produced. The equality of the values for CO_2 and N_2 further substantiates that all electrons have been collected. The assumption of constant ionizing species density requires equality to hold for all gases and pressures. (The photoabsorption of CO_2 in the $\lambda = 1200$ Å window can be considered to be negligible for the low pressures under consideration.) Correlation within a factor of 2 or 3 has been obtained between the n_{eo} values in Table 6-3 and the section of flat curves in Figures 6-18 and 6-19 for CO_2 and N_2 respectively. He however,

Table 6-3

Electron Avalanche Data

Gas	P [torr]	E/P [volts cm^{-1} sec^{-1}]	k_i [cm^{-1} $torr^{-1}$]	α_t [cm^{-1}]	n_{eo}
He	2.5	15	0.77	1.9	2.7
	5	15	0.77	3.9	2.8
	10	5	0.22	2.2	1.5
	15	5	0.22	3.2	1.3
	20	5	0.22	4.3	1.4
	50	1.7	0.012	.6	3.2
	100	1.7	0.012	1.2	2.7
	200	1.7	0.012	2.4	3.0
N_2	2.5	60	0.28	0.7	9.0
	5	60	0.28	1.4	9.0
	2.5	50	0.13	0.33	9.0
	5	50	0.13	0.65	9.5
	10	50	0.13	1.3	9.3

Table 6-3 continued

Gas	P [torr]	E/P [volts $cm^{-1} sec^{-1}$]	k_i [cm^{-1} $torr^{-1}$]	α_t [cm^{-1}]	n_{eo}
	2.5	46	0.29	0.73	10.0
	5	46	0.29	1.5	9.5
	10	46	0.29	2.9	11.0
CO_2	2.5	30	0.074	0.19	9.5
	5	30	0.074	0.37	10.0
	10	30	0.074	0.74	10.0
	15	30	0.074	1.1	9.5

does not follow the pattern. The nonconformity can be attributed to the large first Townsend ionization coefficient characteristic of this gas. Table 6-2 indicates that for the range of P and E/P considered for He in Table 6-3 diffusion loss may still be significant. Consequently, as E/P is increased Townsend multiplication becomes significant even before all the initial photoelectrons can be collected. This is further evidenced by the lack of even short, horizontal intervals in the curves in Figure 6-17 for He.

In spite of the fact that uncertainty of collector saturation precludes accurate calibration for the independent laser gases, useful information has been obtained. The photoemission and photoionization spectra have been identified. CO_2 controlled photoionization by photoabsorption has been substantiated. Furthermore, background impurities have been found to dominate the ionization even in the case of the test cell that could be maintained at 10^{-6} torr with a diffusion pump. This can be assumed to apply to lasers as well, since most CO_2 TEA laser devices are contaminated and do not generally have good vacuum integrity. The contaminant species may vary from laser to laser depending on the construction materials used. Detailed information about one device may not necessarily apply to another. However, for very clean laser systems the impurity inherent in the industrial grade of He may dominate the ionization. The ionizing species can be enriched in a flowing system where the He is exhausted through a small orifice. The effect was observed after He had been passed slowly through the test cell for a number of hours. Furthermore a strong photoelectron signal was obtained which dropped off around $\lambda = 1600$ Å indicating that this may have been the ionization potential of the enriched species. The measurement was made at $P = 15$ torr and $E/P = 1$ volt $cm^{-1}torr^{-1}$. The effect was not observed when a purer grade of He was employed, nor was it observed in CO_2 or N_2. However CO_2 and N_2 are known to have a much higher viscosity than He and the impurity enrichment would be much more difficult [77].

The study of photoionization in laser mixtures containing known concentrations of additives represents a more practical situation in view of the poor performance by the independent laser gases in supporting photoionization. The resulting photoelectron signals were relatively large and easy to monitor being well removed from the amplifier noise. Furthermore, collection operation in the saturation region was found to be the rule rather than the exception, thus allowing calibration of the ionization spectrum. The results of the tests have been presented and analysed in the following sections.

6-2-6. Calibration of the Electronic Recording Devices.

Low concentrations of certain additives in the test cell resulted in a dramatic increase in the amount of charge collected. Furthermore, charge collector operation in the saturation region was obtained with ease. For the calibrated charge collector operating in the saturation region, the absolute number of photoelectrons produced can be determined. In addition, calibration of the photon counter to determine the number of photons incident on the sodium salicyalate scintillator, allows the photoionization efficiency to be determined. This in turn allows for the calculation of photoionization cross-sections.

Charge Collector

The calibration of the charge collector requires that the transfer function of the device be determined. The transfer function can be obtained relatively easily by considering each component in Figure 4-3. It should be pointed out that the following calibration procedure allows one to determine the amount of charge that has been collected. Only for collection operation in the saturation region is this quantity equal to the amount of charge produced by photoionization. The final calibration formula can be best appreciated by considering the following sequence of events with reference to Figures 4-3, 4-4, and 4-5.

(1) During any given spark discharge a certain number of charged particles are produced in the test cell. In a completely general situation these charged particles may be either positive or negative or a mixture of particles of opposite polarity. Furthermore, the charge of the particles may be any integral number of the basic electronic charge. The charged particles will immediately respond to the applied electric field. When all of the charge has been swept to the collector plate, the front end capacitance, will have charged to a voltage, V_i.

$$V_i = \frac{|Q|}{C_1} \qquad 6\text{-}36$$

$|Q|$ is the summation of the absolute value of the charge on the charged particles. [Coul].

(2) The acquired voltage was then amplified with a preamp of gain G_{q1}

$$V_1 = G_{q1} V_i = \frac{Q}{C_1} G_{q1} \qquad 6\text{-}37$$

(3) Bandpass filtering to suppress noise was optional. At any rate the filter stage had a gain of 0 db (X 1) so consideration here is immaterial. High gain amplification followed. Three values of gain, G_{q2}, could be selected as desired. These were 21 db (X 11), 30 db(X 32),and 40 db (X 100). In addition the am-

plifier section could be bypassed yielding an effective value of $G_{q2} = 0$ db (X 1). The resulting voltage signal can be written as follows:

$$V_2 = G_{q2}V_1 = \frac{Q}{C_1} G_{q1}G_{q2} \qquad 6\text{-}38$$

(4) Voltage V_2 was then coupled to the x-y recorder by an optical transmitter-receiver device. The gain of this section can be represented by G_{tr}. Finally, the relationship between the output voltage monitored on an x-y recorder and the total charge produced can be written:

$$V_o = G_{tr}V_2 = \frac{|Q|}{C_1} G_{q1}G_{q2}G_{tr} \qquad 6\text{-}39$$

This can be rearranged to read:

$$|Q| = \frac{V_oC_1}{G_{q1}G_{q2}G_{tr}} \qquad 6\text{-}40$$

Equation 6-40 is completely general for any type of charge configuration. However, for all cases under consideration in this thesis, the positive charged species are singly charged positive ions and the negatively charged species are electrons. Furthermore, the total number of each species must be the same. The quantity of interest is the total number of electrons produced. If the total charge collected has resulted from collecting all electrons and all ions, then the total number of electrons can be determined by dividing Equation 6-40 by 2e:

$$n_{eo} = \frac{V_o C_1}{2e\ G_{q1} G_{q2} G_{tr}} \qquad 6\text{-}41$$

However, the observed collection time has precluded significant ion collection in most cases. The total number of electrons would then be given by:

$$n_{eo} = \frac{V_o C_1}{e\ G_{q1} G_{q2} G_{tr}} \qquad 6\text{-}42$$

$e = 1.6 \times 10^{-19}$ coul (electronic charge)

In addition, for all tests performed, $G_{q1} = 40$ db (x 100) and G_{tr} was experimentally measured to be -12 db (x 0.25). The front end capacitance consists of a 10 cm length of coaxial cable and the parasitic input capacitance of the operational amplifier employed. Measurement on a capacitance bridge yielded a value of 13 pf for C_1, as do independent calcualtions. Under these conditions, Equations 6-41 and 6-42 become respectively:

$$n_{eo} = 1.63 \times 10^6 \frac{V_o}{G_{q2}} \qquad 6\text{-}43$$

$$n_{eo} = 3.25 \times 10^6 \frac{V_o}{G_{q2}} \qquad 6\text{-}44$$

where G_{q2} is the desired gain setting, and V_o is the output voltage monitored on an x-y recorder.

Photon Counter

As for the case of the charge collector, calibration of the photon counter requires a determination of the transfer function. With reference to Figures 4-1 and 4-2 one may proceed by treating each component separately.

(1) Consider a beam of photons of frequency ν and intensity $I(t)$ incident on the scintillator surface. The beam of photons diverge to an area of 1 cm^2 on the scintillator surface, which has a diameter of 1.5 cm. Consequently, all photons fall on the surface of the scintillator. The incident power is $I(t)$ watts.

(2) Division of the photon energy in Joules yields $I(t)/h\nu$ photons per second incident on the scintillator.

(3) Multiplication by the scintillator "quantum efficiency" ξ, yields $\frac{I(t)}{h\nu}\xi$ photons per second incident on the photomultiplier cathode. All flourescent photons do not strike the photomultiplier cathode, but the loss has been incorporated into the "quantum efficiency" ξ. The perspex substrate and quartz window on the photomultiplier tube are totally transparent at the fluorescent frequency.

(4) Multiplication by the energy of the fluorescent photonsin joules yields $\frac{I(t)\xi h\nu_s}{h\nu}$ watts incident on

the photomultiplier cathode.

ν_s is the frequency of the fluorescent photons.

(5) Current generated at the input of the photomultiplier tube, i_i, is given by:

$$i_i = \frac{I(t)\xi\, h\nu_s\, S_s}{h_\nu} \qquad 6\text{-}45$$

where S_s is the photomultiplier cathode sensitivity at the fluorescent frequency.

(6) The photomultiplier output current, i_o, can be obtained by multiplying the photomultiplier current gain, G_{pl}.

$$i_o = \frac{I(t)\xi\, h\nu_s\, S_s\, G_{pl}}{h\nu} \qquad 6\text{-}46$$

(7) The output current is transformed to a voltage V_{pi}, by resistor R_{76} in Figure 4-2.

$$V_{pi} = \frac{I(t)\xi\, h\nu_s\, S_s\, G_{pl}\, R_{76}}{h\nu} \qquad 6\text{-}47$$

(8) The resulting voltage signal is then amplified by an amplifier of gain G_{p2}.

$$V_{pl} = \frac{I(t)\xi\, h\nu_s\, S_s\, G_{pl}\, R_{76}\, G_{p2}}{h\nu} \qquad 6\text{-}48$$

Two values of G_{p2} can be selected. These are 23 db (x 14.2) and 42 db (x 131).

(9) V_{p1} is then integrated with an operational amplifier with capacitive feedback and resistor input [78]. These components are C_{46} and R_{88} in Figure 4-2.

$$V_o = \frac{1}{R_{88}C_{46}} \int_o^\infty V_{p1}dt \qquad 6\text{-}49$$

$$V_o = \int_o^\infty \frac{I(t)\xi\, h\nu_s\, S_s\, G_{p1}\, R_{76}\, G_{p2}\, dt}{R_{88}C_{46}h\nu} \qquad 6\text{-}50$$

Only the photon intensity is a function of time. The sampling time is long (100 μs) compared to the spark duration (5 μs) and so the integration effectively goes to infinity.

(10) Finally, the total amount of energy incident on the scintillator surface can be related to the output voltage, V_o, recorded by an x-y recorder.

$$\int_o^\infty I(t)dt = \frac{V_o\, R_{88}\, C_{46}\nu}{\xi\, \nu_s\, S_s\, G_{p1}\, R_{76}\, G_{p2}} \qquad 6\text{-}51$$

(11) Division by the energy of the photon incident on the scintillator yields the total number of photons incident on the scintillator, N_{P0}.

$$N_p = \frac{V_o\, R_{88}\, C_{46}}{\xi\, \nu_s\, S_s\, G_{p1}\, R_{76}\, G_{p2}\, h} \qquad 6\text{-}52$$

For this work, wavelength rather than frequency has been used to characterize the photons. The relationship is as follows:

$$\nu_s = \frac{C}{\lambda_s}$$

$C = 3 \times 10^8$ m $\sec^{-1}$ (velocity of light)

$\lambda_s = 4200 \times 10^{-10}$ m (average wavelength of the fluorescent photons [37]

Equation 6-52 becomes:

$$N_p = \frac{V_o R_{88} C_{46} \lambda_s}{\xi C S_s G_{p1} R_{76} G_{p2} h} \qquad 6\text{-}53$$

Equations 6-52 and 6-53 are independent of λ. This is a direct consequence of the "quantum efficiency" of the scintillator being independent of λ. Most of the terms in Equation 6-53 are known. These are listed below.

R_{88} = 2.2 Kohms [from Table 4-1]

R_{76} = 910 ohms [from Table 4-1]

C_{46} = 1000 pf [from Table 4-1]

λ_s = 4200×10^{-10} m [37]

C = 3×10^8 m $\sec^{-1}$ [79]

S_s = 0.064 watts A^{-1} manufacturer's specification [98]

G_{p2} = x 14.2 or x 131

h = 6.6×10^{-34} J $\sec^{-1}$ Planck's constant [79].

All terms have been assigned values with the exception of G_{p1} and ξ. The photomultiplier tube current gain has been specified by the manufacturer to be $G_{p1} = 8.0 \times 10^4$ for a -1500 volt bias. The gain at other photomultiplier tube bias voltages have been experimentally determined relative to the value at -1500 volts. These values appear in Table 6-4. The only remaining term to be assigned a value is ξ, the scintillator "quantum efficiency". Calibration of the scintillator under experimental conditions would be a difficult task requiring the use of a fast absolute energy meter. However, the particularly amiable properties of the scintillator employed have allowed a calibration by a relatively simple technique using a Hg-vapor lamp.

Sodium salicylate has been used as the scintillator throughout the project. A layer thickness of 1 mg cm^{-2} has been shown to be the optimum thickness for the highest quantum efficiency [37,46]. However, the maximum is quite broad [37,46]. The sodium salicylate was deposited on a perspex substrate 1/4 inch thick, by spraying methol alcohol saturated with sodium salicylate onto the substrate. A heat gun was employed to facilitate evaporation of the alcohol. The method has been described in the literature [37,46]. Three separate coatings were prepared each about 1 mg cm^{-2} in thickness. Little difference was observed between the samples. In all cases the efficiency dropped by about 25% after exposure to the test environment for 48 hours [37]. However, after this,

Table 6-4

Photomultiplier Current Gains

$G_{pl} = 2.4 \times 10^5$ at -1800 volts

$G_{pl} = 8.0 \times 10^4$ at -1500 volts

$G_{pl} = 2.9 \times 10^4$ at -1300 volts

$G_{pl} = 2.1 \times 10^3$ at -1000 volts

$G_{pl} = 3.5 \times 10^2$ at -800 volts

G_{pl} is the photomultiplier current gain. The value at -1500 volt bias has been supplied by the manufacturer. All other values at different bias voltages have been measured relative to this one.

the efficiency remained constant. Consequently, all tests have been performed using sodium salicylate coatings older than 48 hours. The decay time for sodium salicylate is less than 12 ns [37], sufficiently fast to follow the temporal characteristics of the spark. Furthermore, the quantum efficiency and fluorescent spectrum of sodium salicylate can be expected to remain constant for λ = 600 Å to at least λ = 3600 Å [37,40,46,80]. The fluorescent emission from the sodium salicylate peaks at about 4200 Å [37,40].

This last characteristic allows for the calibration of sodium salicylate at a wavelength for which the photomultiplier tube cathode sensitivity is known. The calibration can be assumed to apply for the shorter wavelengths as well. A Hg-vapor lamp has been used as the source. The photomultiplier tube and scintillator were maintained in the same position as for all tests. The current output of the photomultiplier was converted to a voltage by a resistor of value 1.2 megaohms. The photomultiplier tube was operated at a -1800 volt bias and the output voltage was monitored with an oscilloscope. The resulting output voltage with the scintillator removed, V_o, and the output voltage with the scintillator in place, V_o , have been tabulated in Table 6-5 for various values of wavelengths. The photomultiplier cathode sensitivities have also been tabulated for the various values of $\lambda(S_\lambda)$ and for the fluorescent wavelength $(S_{\lambda s})$. From these values the "quantum efficiency" has been calculated. The procedure can be best appreciated by considering the following steps:

With Scintillator Removed

(1) The current at the output is given by the measured output voltage divided by the resistor value:

$$I_o = \frac{V_o}{R} \qquad 6\text{-}54$$

(2) The current generated by the cathode can be determined by division by the photomultiplier tube current gain.

$$I_i = \frac{V_o}{RG_{pl}} \qquad 6\text{-}55$$

(3) Further division by the appropriate cathode sensitivity yields the power incident on the cathode (Intensity)

$$I = \frac{V_o}{RG_{pl}\,S_\lambda} \qquad 6\text{-}56$$

(4) Division by the photon energy yields the number of photons incident on the cathode per second.

$$N_p = \frac{V_o\lambda}{RG_{pl}\,S_\lambda\,hc} \qquad 6\text{-}57$$

With Scintillator

With the scintillator in place the same formula applies, however,

$$\lambda \rightarrow \lambda_s, V_o \rightarrow V_{os}, \text{ and } S_\lambda \rightarrow S_{\lambda s}.$$

$$N_{ps} = \frac{V_{os}\lambda_s}{RG_{pl}S_{\lambda s}hc} \qquad 6\text{-}58a$$

N_{ps} is the number of photons per second which have been transformed by the scintillator and which are incident on the cathode. With the scintillator in place, the number of photons per second incident on the scintillator must be given by Equation 6-57. The "quantum effiqiency" is simply the ratio of these two values.

$$\xi = \frac{N_{ps}}{N_p} \qquad 6\text{-}58$$

or

$$\xi = \frac{V_{os}}{V_o}\,\frac{S_\lambda}{S_{\lambda s}}\,\frac{\lambda_s}{\lambda} \qquad 6\text{-}59$$

These values appear in Table 6-5 and can be seen to be an order of magnitude larger for the longer wavelengths relative to the shorter wavelengths. This can be explained by the transparency of the perspex substrate. The transparancy of a 1/16 inch thick piece of perspex was tested at all the wavelengths tabulated. The resulting output voltage V_p can be compared to V_o when no filter has been used. For the first two wavelengths (low ξ) the perspex was observed to be relatively opaque. For the long wavelengths (high ξ) the perspex was totally transparent. Consequently, a large percentage of the long wavelength photons may have passed directly through the scintillator without suffering absorption. The high cathode sensitivity at these wavelengths would result in a large signal (V_{os}). This would have the effect of increasing the apparent value of ξ. The large value of ξ has been discarded in favor of the smaller value, where direct excitation of the cathode is precluded by the reduced perspex transparency and reduced cathode sensitivity. The value of the "quantum efficiency" found here is much smaller than the value of 0.5 reported in the literature [37]. The fluorescent photons can be expected to be emitted in all directions. Consequently, only a small fraction are incident on the photomultiplier cathode.

With $\xi = 0.0026$ Equation 6-53 becomes:

$$N_p = 3.1 \times 10^{13} \frac{V_o}{G_{p1} G_{p2}} \qquad 6\text{-}60$$

The accuracy of this method of calibration is limited by the absorption characteristics of sodium salicylate (assumed to be constant for $\lambda = 1000$ Å to $\lambda = 3150$ Å) [40] and by the accuracy of the photomultiplier tube specifications, but is considered to be well within an order of magnitude.

The value of S_λ for $\lambda = 2537$ Å was not available on the manufacturers specification sheet. However, the relative intensity of the Hg vapor lamp lines were specified. The photomultiplier output at $\lambda = 2537$ Å and $\lambda = 3125$ Å were monitored with the scintillator removed.

Table 6-5

Calibration of the "Quantum Efficiency"

λ [Å]	V_p [volts]	V_o [volts]	V_{os} [volts]	S_λ [A Watt^{-1}]	$S_{\lambda s}$ [A Watt^{-1}]	ξ.
2537	0.3	1.5	6.3	2.3 $\times 10^{-5}$	0.064	0.0025
3125	0	25	0.25	0.013	0.064	0.0027
3650	23	26	0.34	0.05	0.064	0.012
4047	27	28	0.48	0.064	0.064	0.018
4358	57	58	1.3	0.064	0.064	0.022

A simple ratio method was used to obtain the sensitivity at $\lambda = 2537$ Å relative to the value by the manufacturer at $\lambda = 3125$ Å. The efficiency of the diffraction grating was assumed to be approximately the same at these two wavelengths [38].

The calibration equations can be used to determine the sensitivity of the system having determined the maximum output noise. In the case of the charge collector, amplifier noise limits the sensitivity. For maximum gains ($G_{q2} = 100$), the amplifier noise at the output and recorded by the x-y recorder was observed to be 0.2 volts. The corresponding sensitivity for electron and ion collection is given by Equation 6-43 with $V_o = 0.2$ volts and $G_{q2} = 100$. This translates to a minimum observable signal of

$$n_{eo\ min} = 3.3 \times 10^3 \text{ electron-ion pairs} \qquad 6\text{-}61$$

For only electron collection, Equation 6-44 applies and the minimum number of electrons that can result in a measurable signal is:

$$n_{eo\ min} = 6.6 \times 10^3 \text{ electrons} \qquad 6\text{-}62$$

In the case ofthe photon counter operating at maximum gains of $G_{p1} = 2.4 \times 10^5$ and $G_{p2} = 131$, the noise signal at the output was 0.2 volts. This signal was observed when CO_2 was used to absorb all of the short wavelength photons. Equation 6-60 can be used to determine the minimum number of photons that may be detected. This is the number of photons that will give rise to a signal equivalent to the noise

$$N_{p\ min} = 2 \times 10^5 \text{ photons} \qquad 6\text{-}63$$

The largest fraction of noise was found to be optical noise. That is, long wavelength light was scattered in the monochromator and some was incident on the photmultiplier. The long wavelength scattered light did not suffer absorption by the CO_2. This conclusion was reached when it was observed that closure of the exit slit significantly reduced the noise. Previously, the noise was about a factor of 3 higher. Subsequent covering of shiny surfaces in the monochromator (such as screw heads) resulted in a reduction of noise to the present value. The remaining noise has been attributed to amplifier noise and pick-up of external electrical noise. The device is not sensitive to photomultiplier dark current. The dark current drains away through R_{76} in Figure 4-2 and the resulting D.C. voltage is blocked by capacitor C_{39} also shown in Figure 4-2.

6-2-7. Photoionization and Photoabsorption Spectra of Selected Additives.

The results of tests performed on tri-n-propyl amine, nitric oxide, and benzene are presented in this section. N_2 flows into the monochromator and has been vented to the atmosphere through the tungsten pin spark source. The resulting photoemission spectrum with a 50 Å bandwidth appears in Figure 6-21. The lower trace is a result of bubbling about 1% of the N_2, through tri-n-propyl amine and then into the source chamber. N_2 flows from the monochromator into the source chamber through the exit slit preventing the tri-n-propyl amine from entering the monochromator. The only effect that the tri-n-propyl amine had on the source, was to reduce the intensity slightly, presumably by absorption. It can be concluded that any effect tri-n-propyl amine may have on the photoionization spectrum is a consequence of photoabsorption and photoionization and is totally unrelated to the source emission spectrum. These traces, as for all remaining photoionization spectra were taken with a -1300 volt photomultiplier tube bias, a chart recorder sensitivity of 0.2 volts per division, and a gain $G_{p2} = 14.2$. Selection of the appropriate value from Table 6-4 and use of Equation 6-60 results in a calibration factor of:

$$N_p = R_p \, 1.5 \times 10^7 \text{ photons} \qquad 6\text{-}65$$

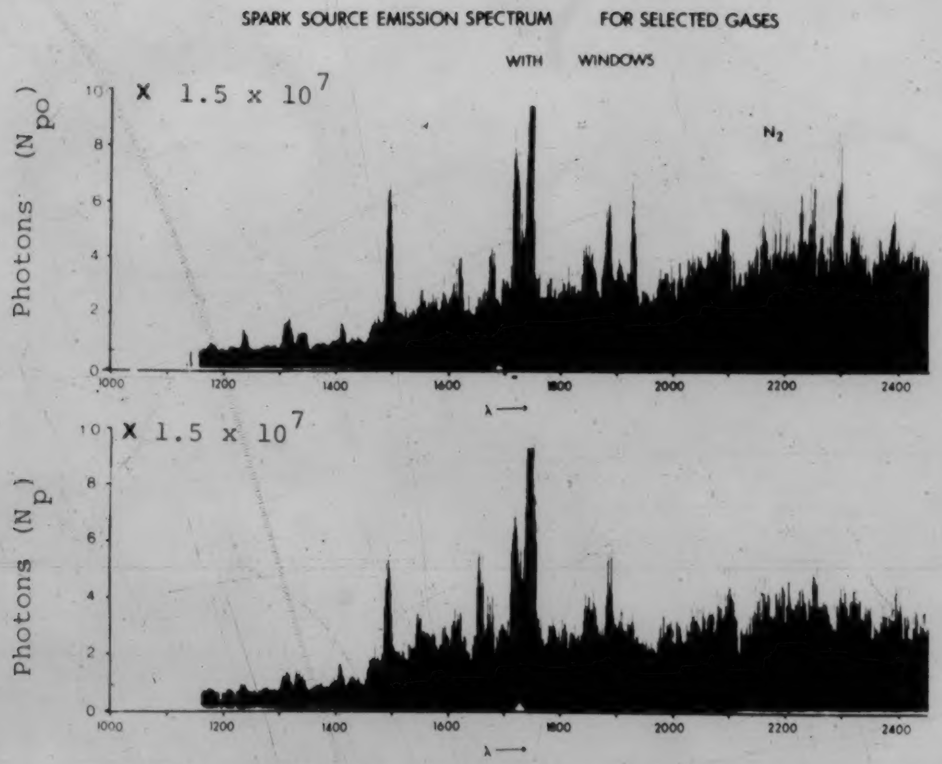

FIGURE 6-21 EFFECT OF TRI-N-PROPYL AMINE ON THE SPARK SOURCE EMISSION SPECTRUM The upper trace is the result of a N_2 flow at atmospheric pressure. For the second trace, about 1% of the N_2 has been bubbled through Tri-n-propyl amine and then into the source chamber (optical pathlength of 10 cm).

where R_p is the number of divisions. The upper trace in Figure 6-21 represents the emission spectrum incident on the test cell for most remaining tests.

At this stage of the project the bank of titanium capacitors (0.014 uf) in the spark driving circuit was replaced with two 0.01 uf low inductance (20 nh) capacitors in series (0.05 uf). The barium titanate capacitors failed periodically as discussed previously. The stock of titanium capacitors was exhausted and the change to the more reliable but larger capacitors was forced. The charging voltage was reduced to 26 kV from 50 kV to maintain the same total energy of 17 joules. The inductance was dominated by the circuitry external to the capacitor, and so the total inductance remained constant upon changing the capacitors and charging voltage. Constant L maintained constant peak current and the photon output remained essentially unchanged in accordance with previous tests regarding these parameters.

Collector operation in the saturation region was obtained for relatively small values of E/P. Here, P denotes the total pressure. Typically $E/P > 0.2$ volts cm^{-1} $torr^{-1}$ was sufficient. In addition large values of E/P did not result in Townsend avalanching. The observed collection time decreased with E/P and the value precluded significant positive ion collection. Consequently, Equation 6-44 applies for the charge collector calibration.

Gain changes (G_{q2}) in the following figures can be easily recognized. These have been reflected in the vertical scale multiplying factor. Since the x-y chart recorder sensitivity was adjusted to 0.2 volts per division throughout, then Equation 6-44 reduces to:

$$n_{eo} = R_q \frac{6.5 \times 10^5}{G_{q2}} \text{ electrons} \qquad 6\text{-}66$$

All of the gas mixtures tested and discussed from this point on were prepared by evacuating the test cell to the limit of the diffusion pump, and then back filling to the desired pressure. Upon isolating the evacuated test cell from the diffusion pump the seed vapors were introduced first, and then the laser gases individually. The partial pressures were monitored with absolute pressure meters. Upon completing a series of tests with one additive, the test cell was pumped with the diffusion pump for at least 24 hours to ensure that concentration of the additive previously tested was reduced to an insignificant level.

Absolute intensity photoabsorption and photoemmission spectra have been prepared for various concentrations of tri-n-propyl amine in a $CO_2 : N_2 : He = 1 : 1 : 1$ (by pressure) laser mixture at three different total pressures. These appear in Figures 6-22 through 6-30. The optimum pressure of tri-n-propyl amine was ob-

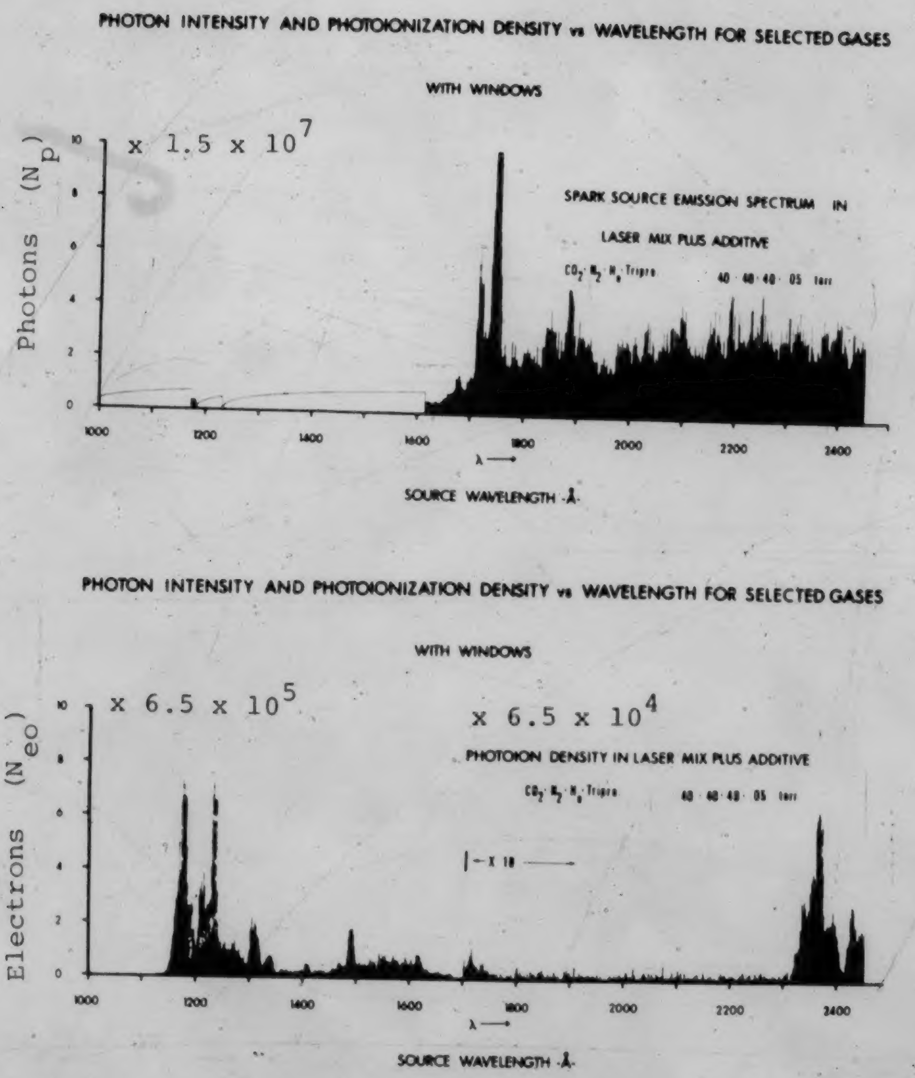

FIGURE 6-22 PHOTOABSORPTION AND PHOTOIONIZATION IN 40 TORR OF LASER MIXTURE PLUS 0.05 TORR TRI-N-PROPYL AMINE The photon spectrum incident on the test cell is shown in Figure 6-21. The calibration factors have been included. $CO_2:N_2:He = 1:1:1$.

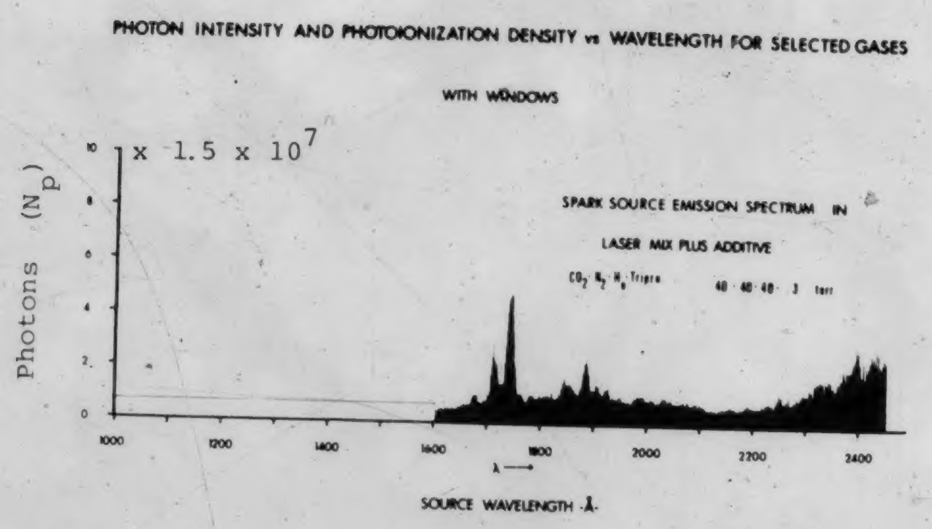

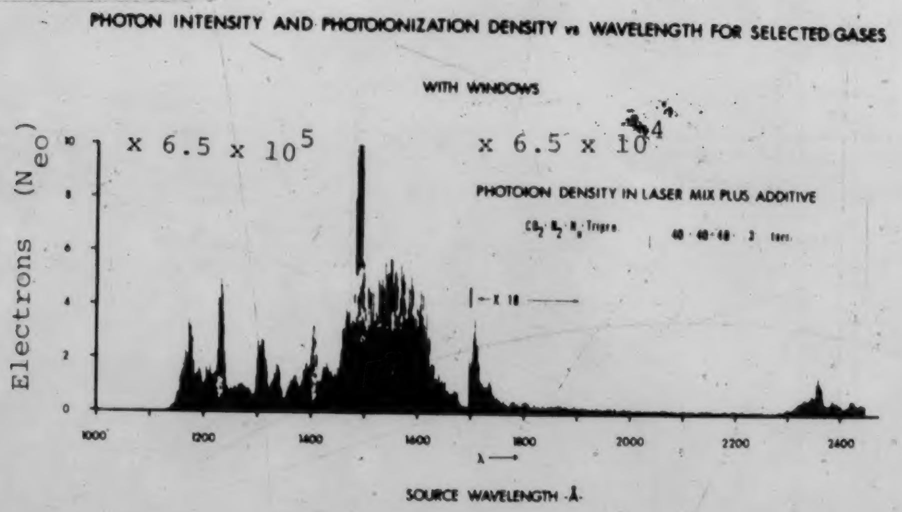

FIGURE 6-23 PHOTOABSORPTION IN 40 TORR OF LASER MIXTURE PLUS 0.3 TORR OF TRI-N-PROPYL AMINE The photon spectrum incident on the test cell is shown in Figure 6-21. The calibration factors have been included. $CO_2:N_2:He = 1:1:1$.

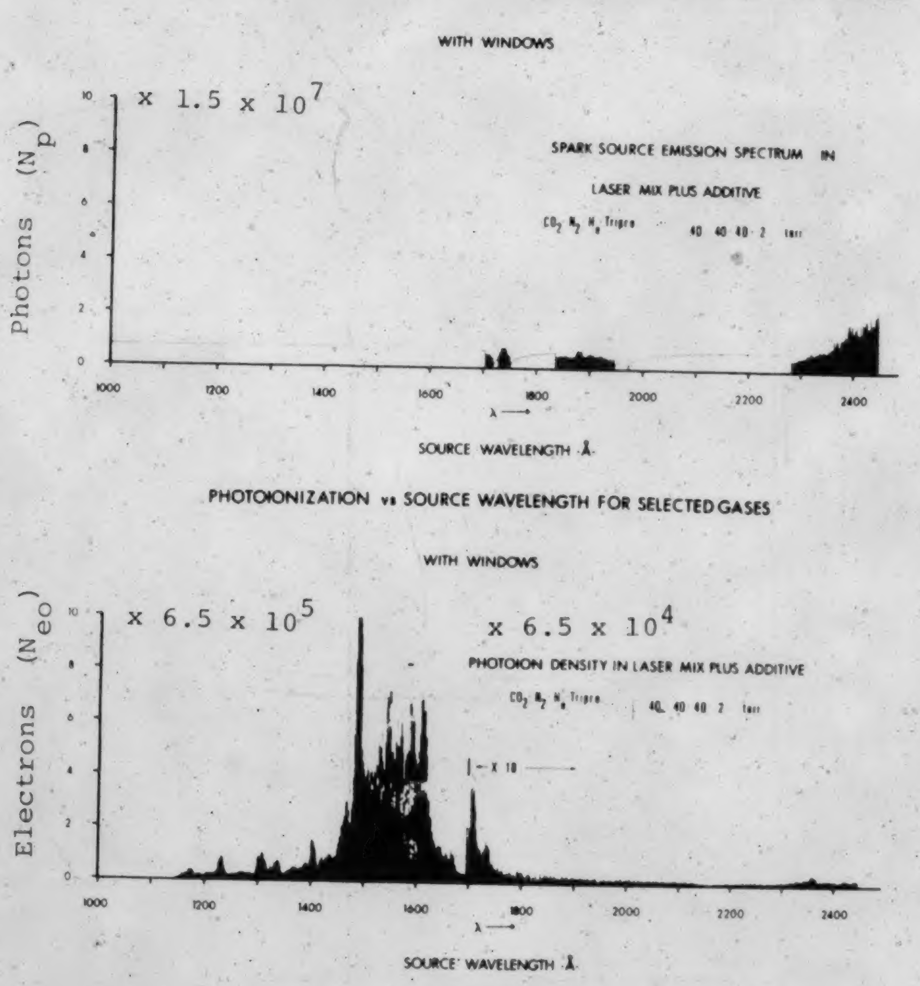

FIGURE 6-24 PHOTOABSORPTION AND PHOTOIONIZATION IN 40 TORR OF LASER MIXTURE PLUS 2 TORR TRI-N-PROPYL AMINE The photon spectrum incident on the test cell is shown in Figure 6-21. The calibration factors have been included. CO_2:N_2:He = 1:1:1:.

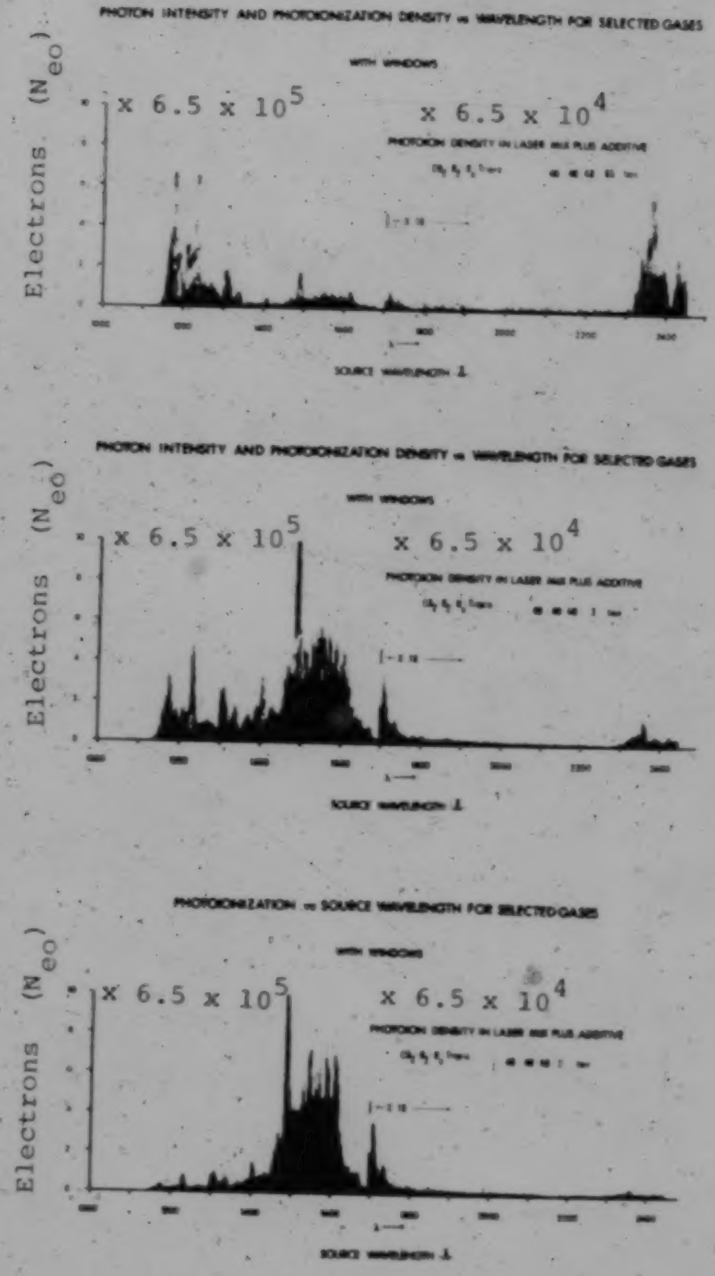

FIGURE 6-25 PHOTOIONIZATION IN 40 TORR OF LASER MIXTURE PLUS TRI-N-PROPYL AMINE The photon spectrum incident on the test cell has been shown in Figure 6-21. The calibration factors have been included. $CO_2:N_2:He = 1:1:1$.

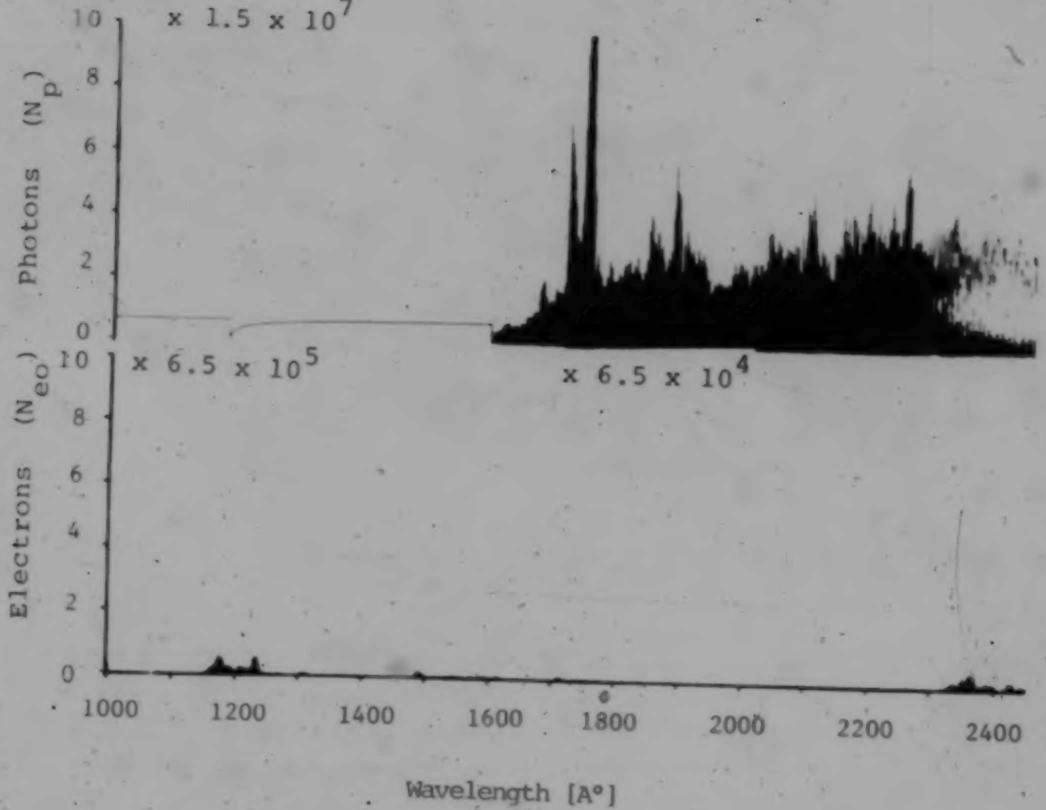

FIGURE 6-26 PHOTOABSORPTION AND PHOTOIONIZATION IN 60 TORR OF LASER MIXTURE PLUS 0.05 TORR OF TRI-N-PROPYL AMINE The photon spectrum incident on the test cell has been shown in Figure 6-21. The calibration factors have been included. $CO_2:N_2:He = 1:1:1$.

/

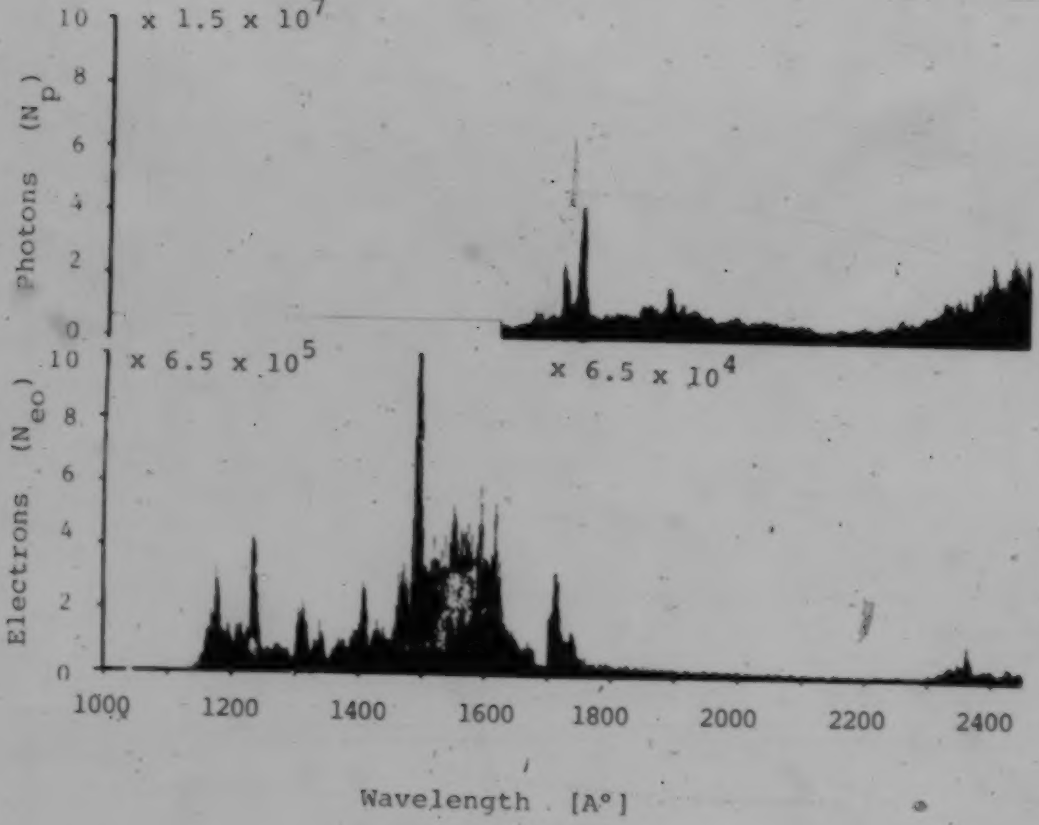

FIGURE 6-27 PHOTOABSORPTION AND PHOTOIONIZATION IN 60 TORR OF LASER MIXTURE PLUS 0.25 TORR OF TRI-N-PROPYL AMINE The photon spectrum incident on the test cell has been shown in Figure 6-21. The calibration factors have been included. CO_2:N_2:He = 1:1:1.

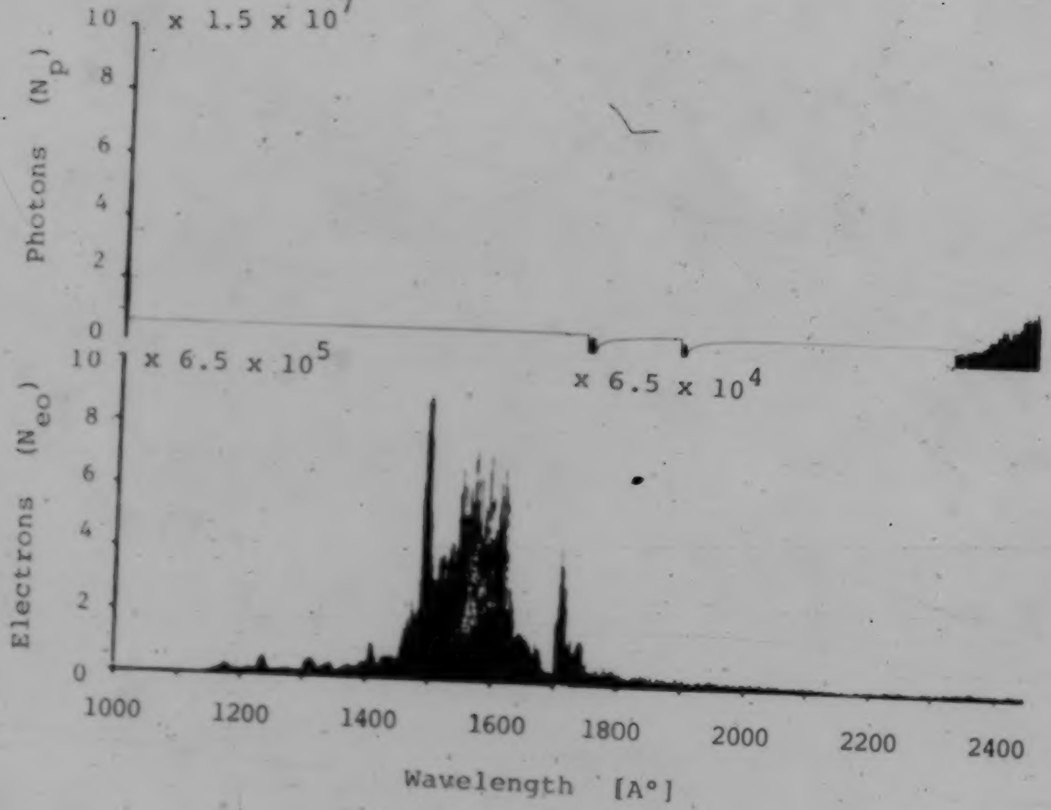

FIGURE 6-28 PHOTOABSORPTION AND PHOTOIONIZATION IN 60 TORR OF LASER MIXTURE PLUS 2 TORR OF TRI-N-PROPYL AMINE
The photon spectrum incident on the test cell has been shown in Figure 6-21. The calibration factors have been included. $CO_2:N_2:He = 1:1:1$.

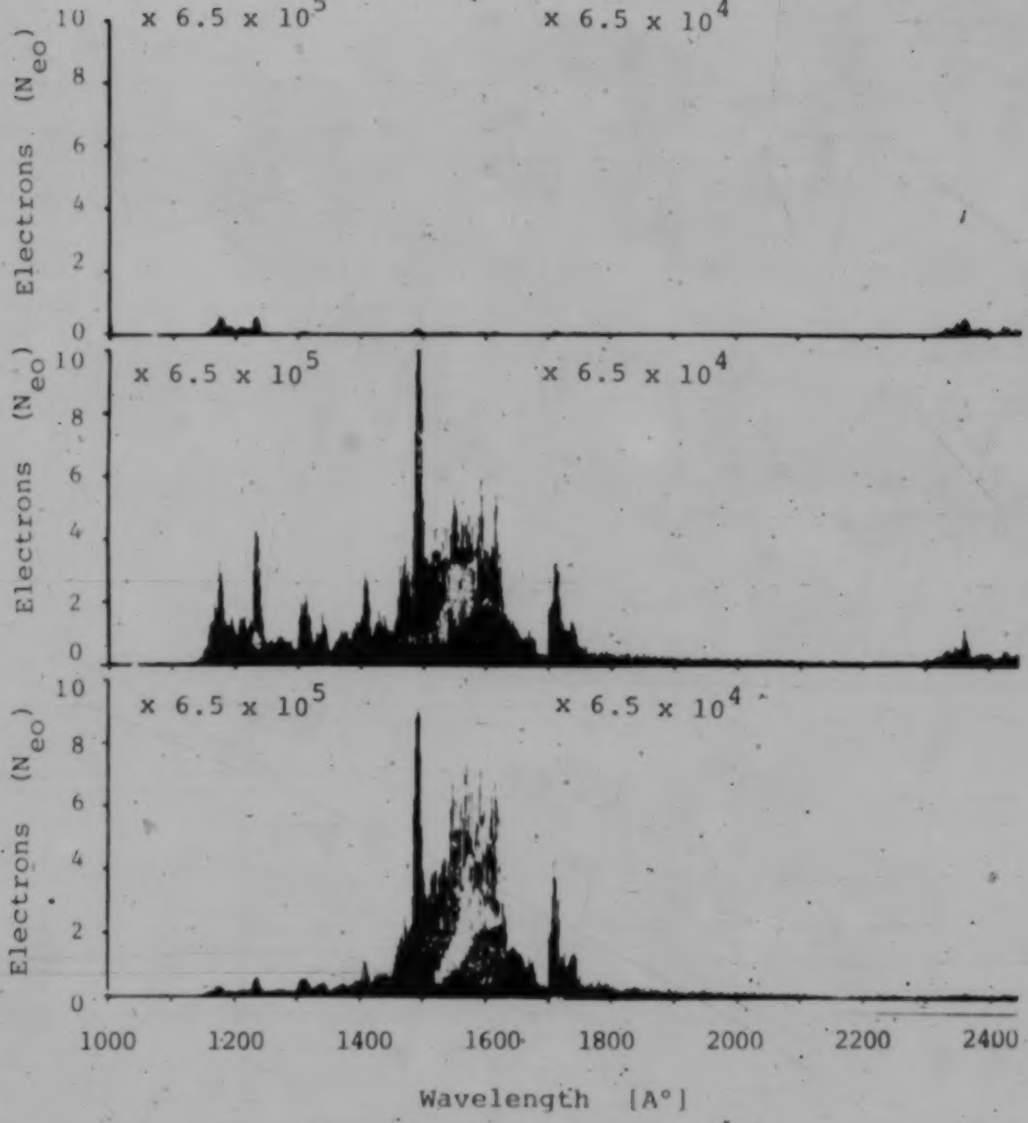

FIGURE 6-29 PHOTOIONIZATION IN 60 TORR OF LASER MIXTURE PLUS TRI-N-PROPYL AMINE The photon spectrum incident on the test cell has been shown in Figure 6-21. The calibration factors have been included. $CO_2:N_2:He = 1:1:1$. Tri-n-propyl amine pressures of the first, second, and third traces were 0.05 torr, 0.25 torr, and 2 torr respectively.

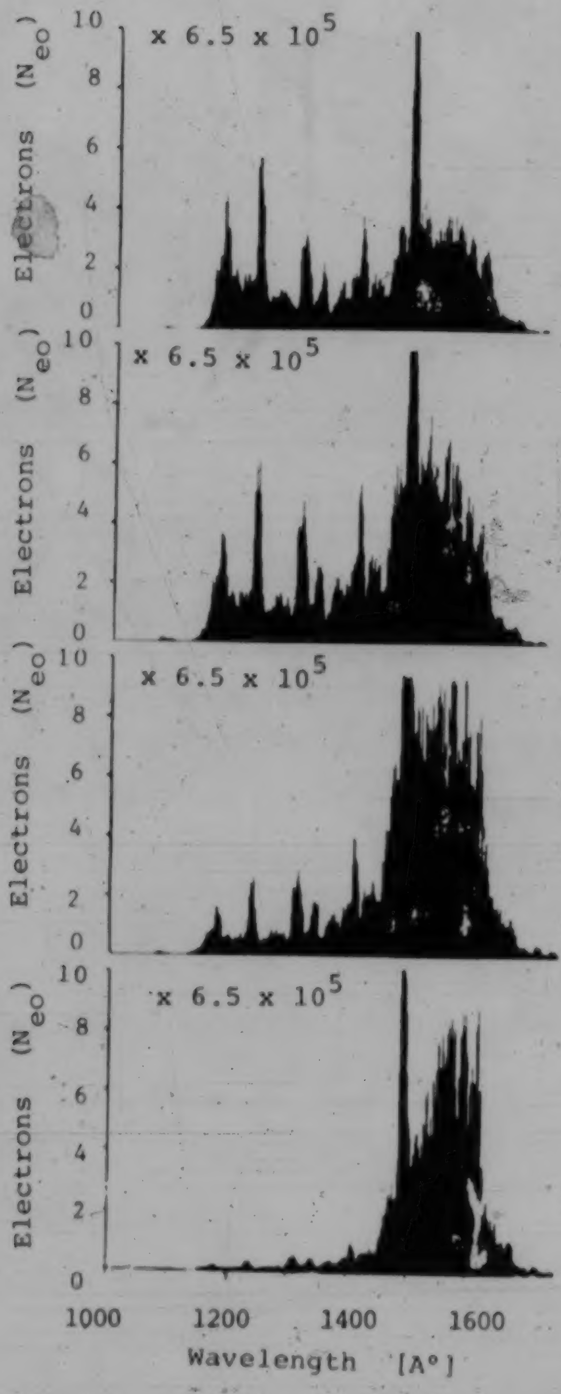

FIGURE 6-30 · PHOTOIONIZATION IN 20 TORR OF LASER MIXTURE PLUS TRI-N-PROPYL AMINE. The photon spectrum incident on the test cell has been shown in Figure 6-33 (upper trace). The calibration factors have been included. CO_2:N_2:He = 1:1:1. Tri-n-propyl amine pressures from top to bottom were 0.05 torr, 0.2 torr, 1 torr, and 2.5 torr.

served to be wavelength dependent. The optimum value was quite broad and was unaffected by the background pressure of the laser mixture. A concentration of about 0.05 to 0.1 torr at λ = 1180 Å and 1 to 2 torr for the range λ = 1490 Å to λ = 1700 Å appeared to yield maximum ionization. Figures 6-22, 6-23, 6-24, 6-26, 6-27, and 6-28 reveal that tri-n-propyl amine is a heavy absorber extending to longer wavelengths than in CO_2. This can be concluded from the observations of decreased photon intensity with increased tri-n-propyl amine concentration for the longer wavelengths. For the shorter wavelengths the photon intensity was insufficient to register on the counter. However, heavy absorption can be inferred from the reduction of photoelectrons with increased tri-n-propyl amine concentration for $\lambda < 1600$ Å. Also, in this portion of the spectrum Figure 6-25, 6-29 and 6-30 reveal that for a constant tri-n-propyl amine concentration, the number of photoelectrons decreases, as the total laser mixture pressure increases. This can only be attributed to CO_2 absorption in this region. Furthermore, in this region, the largest photoelectron signal appears in the vicinity of 1200 Å consistent with the window in the CO_2 absorption spectrum. For the longer wavelengths and specifically for those greater than 1650 Å the number of photoelectrons has been relatively unaffected by the buffer gas pressure. This, too, is consistent with the lack of absorption in the laser gas in this portion of the spectrum. These figures also indicate that two processes are responsible for the ionization. An efficient short range one-step mechanism could be used to explain the ionization for the short wavelengths ($\lambda \leq 1450$ Å). Conversely, a less efficient long range one-step mechanism could explain the observation in the range 1450 Å $< \lambda <$ 1715 Å. 1715 Å is the ionization wavelength of tri-n-propyl amine. It appears in Table 5-10. For the smallest tri-n-propyl amine concentrations in Figures 6-25, 6-29 and 6-30 an efficient short wavelength process apparently dominates. It results in relatively more photoelectrons than the long wavelength process, in spite of the fact that less photons are available. This implies a relatively larger photoionization cross-section for the short wavelength process compared to the long wavelength process. As the concentration of tri-n-propyl amine increases, the photoelectrons due to the long wavelength process also increases. However, the number of photoelectrons collected decreases with increasing tri-n-propyl amine concentration. This has been attributed to the apparent high photoionization cross-section for the short wavelength process. For a large tri-n-propyl amine concentration, essentially total absorption and photoionization can be expected to occur in a thin layer in front of the window. The created charge can be expected to be lost by recombination and eventually diffusion to the wall (window). Hence, less charge will be collected in this portion of the spectrum as the tri-n-propyl amine pressure goes up, even if charge has been created. In contrast, the less efficient long wavelength process apparently suffers less photoabsorption by photoionization or otherwise. Photoelectron creation was relatively uniform down the length of the test cell allowing essentially all of them to be collected. Hence, the term "short range" and "long range" were contrived to describe these processes.

Increased charge collector gain has revealed that significant ionization occurs for wavelengths longer than the ionization wavelength of tri-n-propyl amine (λ = 1715 Å). This effect has been observed immediately upon placing the tri-n-propyl amine in the test cell as well as after many minutes of operation. (The spectra are traced at 50 Å per 60 sec with a spark rate of 1 Hz.) Furthermore, the photoionization spectrum for tri-n-propyl amine does not change significantly over the time it takes to trace the spectrum from 1000 Å to 2500 Å (30 min). This would seem to preclude that the phenomenon for $\lambda > 1715$ Å is due to ionization of photodissociated products of tri-n-propyl amine with longer ionization wavelengths. Consequently, a two-step process has been assigned to account for this phenomenon.

The large photoelectron signal for $\lambda > 2300$ Å is due to photons with $\lambda > 1100$ Å in the second grating order as before. This signal also decreases with increasing tri-n-propyl amine and CO_2 concentrations as expected.

NO and benzene behave somewhat differently than tri-n-propyl amine. The photoabsorption and photoionization characteristics for these additives appear in Figures 6-31 and 6-32 respectively. Although both additives give rise to large photoelectron densities at short wavelengths, the photoionization drops off sharply for $\lambda > 1340$ Å. Table 5-10 shows that the ionization wavelength for both of these substances is 1340 Å. Even maximum gain on the charge collector does not reveal substantial photoionization for $\lambda > 1355$ Å in benzene. Figures 6-31 and 6-32 only go to 1750 Å, however, no ionization was observed for wavelengths up to 2500 Å. This is, in spite of the observation of significant photoabsorption by benzene in this region.

In the case of NO and benzene the photoelectron signal dropped exponentially from a strong signal at the ionization wavelength of $\lambda = 1340$ Å to essentially zero at $\lambda \approx 1350$ Å. This occurred in spite of relatively constant photon intensity in this region evident in Figure 6-21 and Figure 6-33. The phenomenon appears to be consistent with a Boltzmann distribution of energy in the ionizing species.

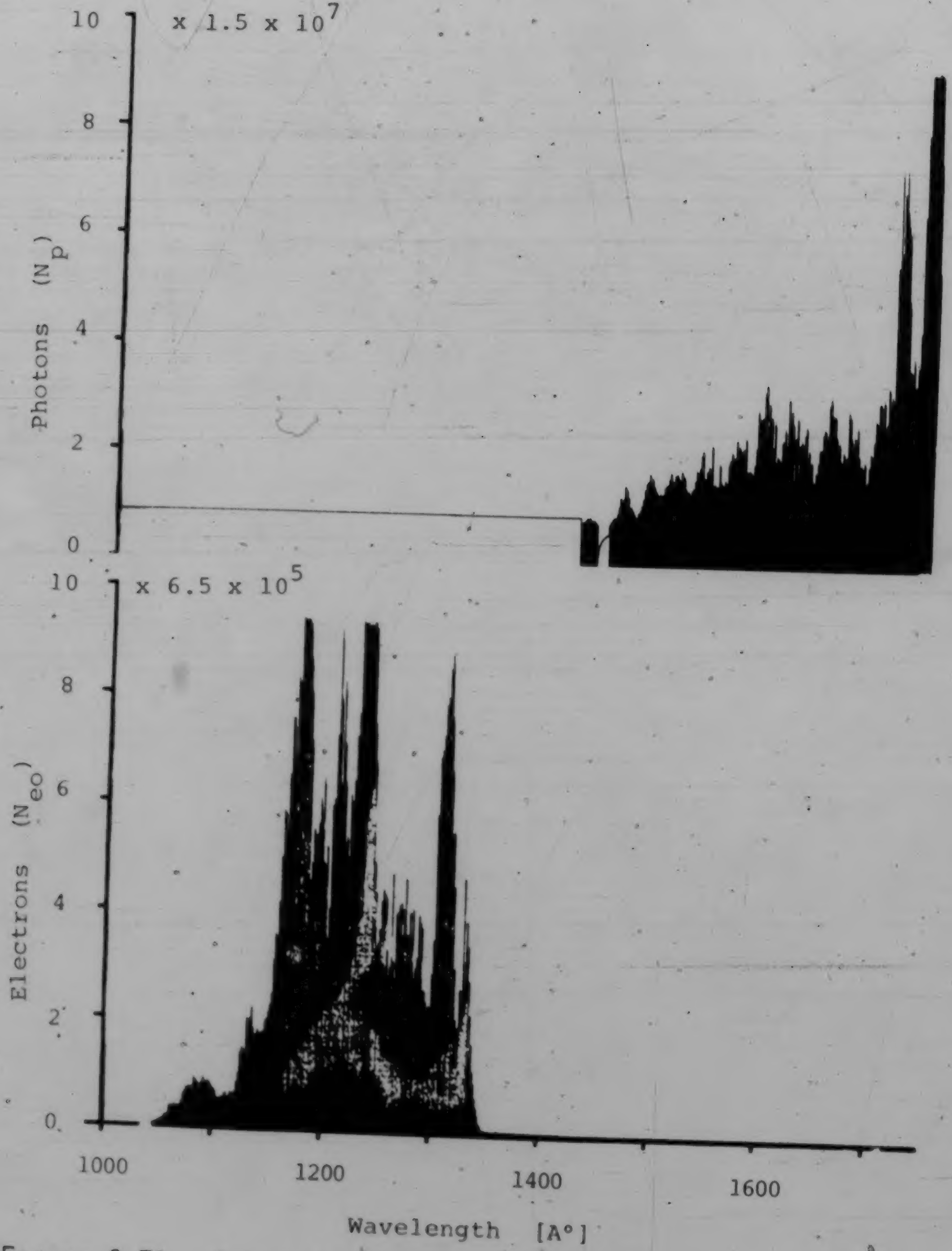

FIGURE 6-31 PHOTOABSORPTION AND PHOTOIONIZATION IN 4 TORR OF NO No buffer gas was present for this test. The photon spectrum incident on the test cell has been shown in Figure 6-33. The calibration factors have been included.

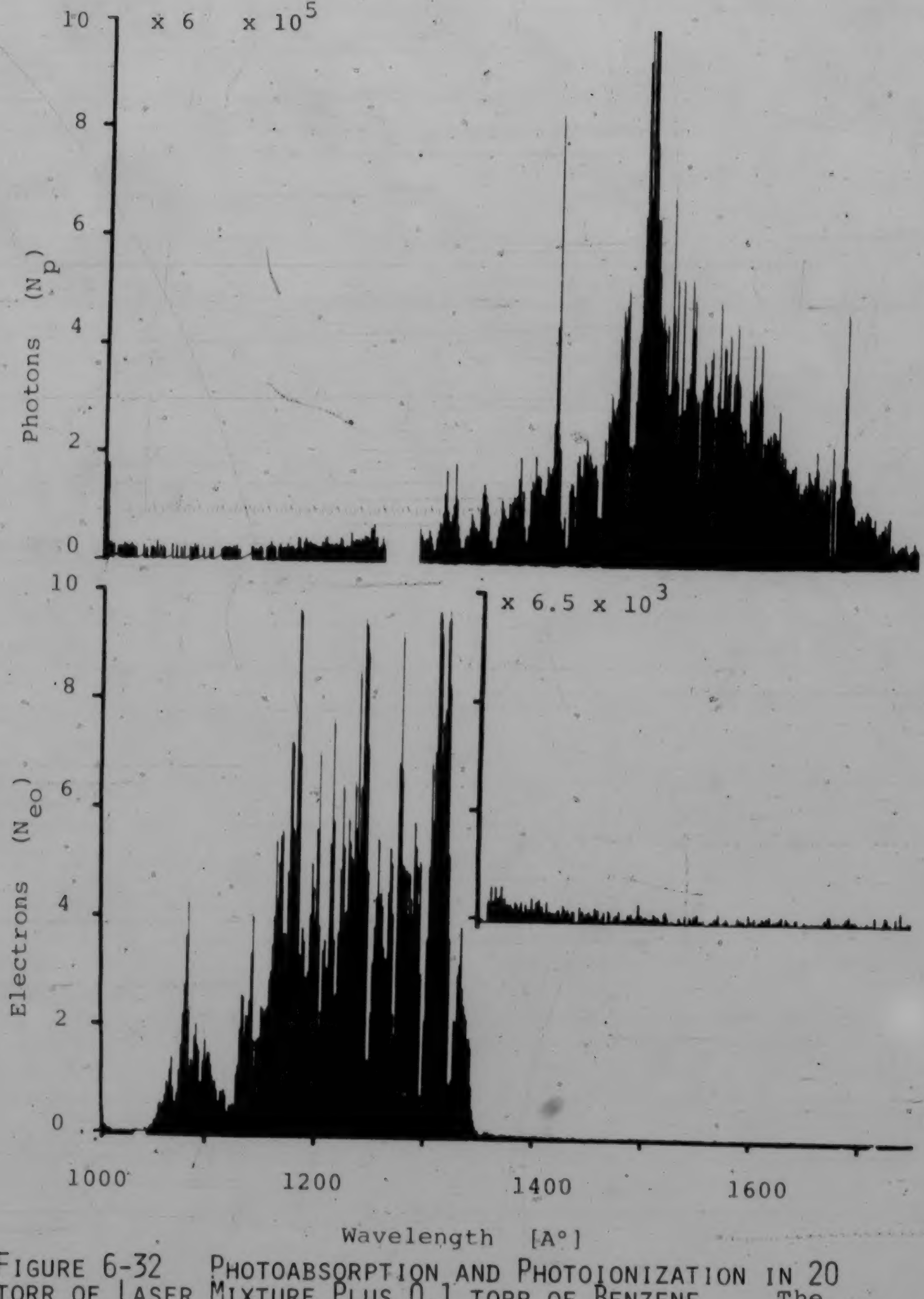

FIGURE 6-32 PHOTOABSORPTION AND PHOTOIONIZATION IN 20 TORR OF LASER MIXTURE PLUS 0.1 TORR OF BENZENE The photon spectrum incident on the test cell has been shown in Figure 6-33. The calibration factors have been included. $CO_2:N_2:He = 1:1:1$.

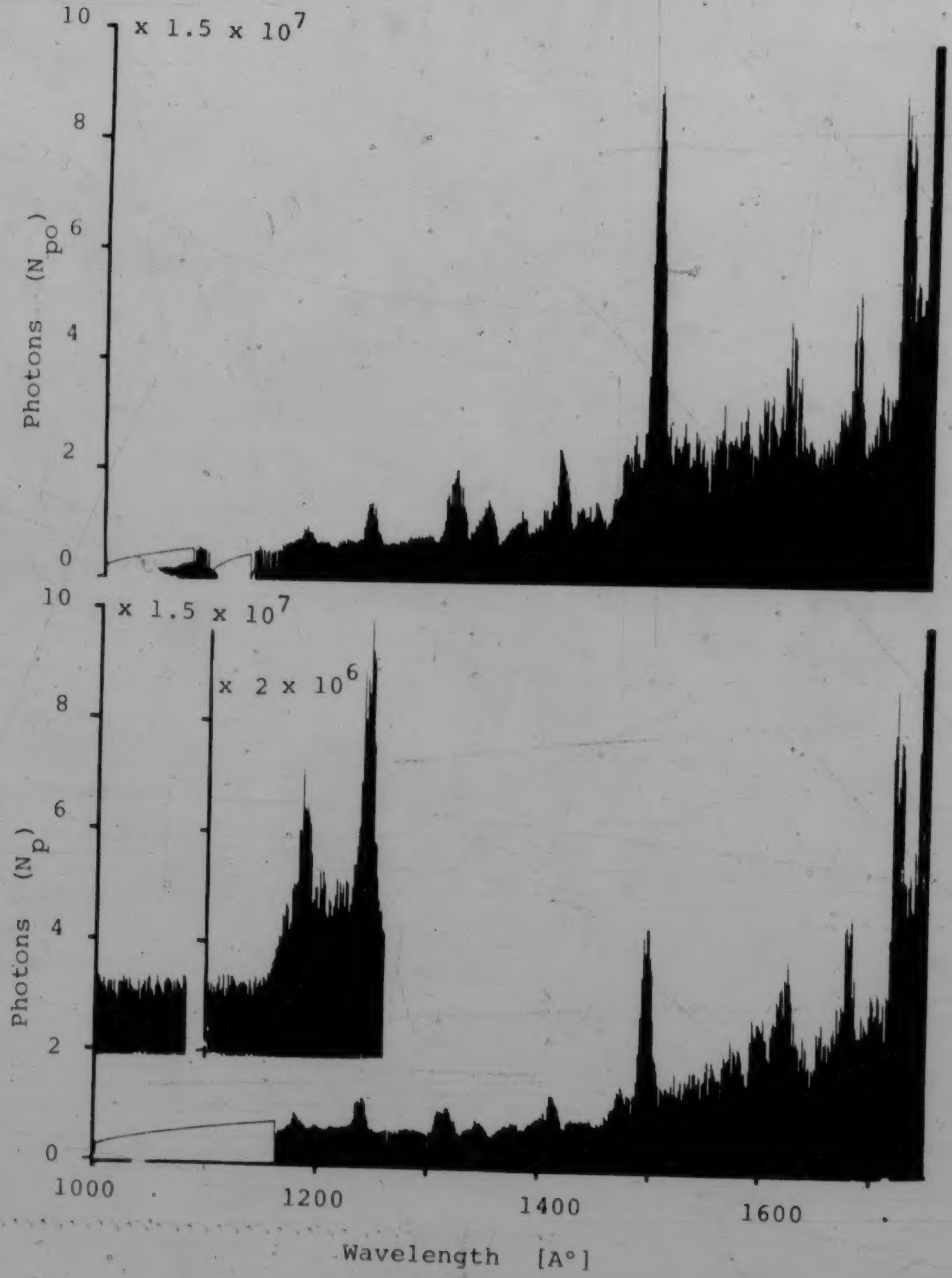

FIGURE 6-33 PHOTOABSORPTION SPECTRA OF CO_2 The upper trace is for an evacuated test cell, whereas the lower trace resulted from filling the test cell with 2.5 torr of CO_2. The calibration constants have been included.

For a large number of molecules n_o, in thermal equilibrium, at absolute temperature T the distribution of energy among the different states will follow Boltzmann's law [83,84,85,86].

$$n_j = \frac{n_o \exp(-E_j/kT)}{\sum_i \exp(-E_i/kT)} \qquad 6\text{-}67$$

n_o = total number of additive molecules

n_j = number of additive molecules in state j

E_j = energy of state j [ergs]

k = 1.38×10^{-16} erg K^{-1} (Boltzmann's constant)

T = absolute temperature of the gas [K]

$\sum_i$ = summation over all possible states.

Furthermore, the number of molecules in energy level n (m) will be given by the number of molecules in a given state with energy E_n (E_m) multiplied by the total number of states with the same energy, g_n (g_m). g_i is commonly called the degeneracy of state i. Finally, the ratio of the number of moelcules in level n to the number in level m is given by

$$\frac{n_n}{n_m} = \frac{g_n}{g_m} \exp \frac{E_m - E_n}{kT} \qquad 6\text{-}68$$

For NO and benzene, photoionization in a one-step process for λ > 1340 Å requires that the molecules be initially in an excited state. The additional energy required to satisfy photoionization for those wavelengths above 1340 Å ranges up to 1.1 x 10^{-13} ergs. This figure is the difference in energy at λ = 1340 Å and the energy at the longest wavelength where photoionization was observed ($\lambda \approx$ 1350 Å). The energy difference can be calculated with the following formula:

$$\Delta E = hc\left(\frac{1}{\lambda_i} - \frac{1}{\lambda_{ob}}\right) \qquad 6\text{-}69$$

λ_i = ionization wavelength [cm]

λ_{ob} = wavelength greater than λ_i where photoionization has been observed [cm].

c = 3 x 10^{10} cm sec^{-1} (velocity of light)

h = 6.6 x 10^{-27} erg sec (Planck's constant)

For m = 0, E_m = 0, and $E_n = \Delta E$. Equation 6-68 reveals that the number of molecules n_n with the additional energy ΔE drops off exponentially with increasing ΔE. This is consistent with the decrease in photoionization observed in Figures 6-31 and 6-32. The photoionization cross-section has been assumed to be approximately constant in the region under consideration.

Equation 6-67 and 6-69 can be used to determine the number of molecules with sufficient energy to be ionized in a one-step process by photons with wavelengths greater than the ionization wavelength. For example at

λ = 1345 Å, the ratio of sufficiently excited molecules to those in the ground state is 0.27. This is high enough to give rise to a large photoionization signal. The ratio drops to 0.07 at λ = 1350 Å. The effective density is more than an order of magnitude less than the total concentration and this has been reflected in the observed photoionization. At λ = 1400 Å, the effective reduction is seven orders of magnitude and no photoionization has been observed. Actually, the total number of molecules available for ionization at $\lambda > 1340$ Å would be somewhat larger than calculated here since all excited states with energies above the threshhold ΔE would be effective. Exclusion of these does not affect the general principle that has been illustrated. Furthermore, the foregoing argument may seem to imply that all energies are possible - this is not true since the energy of bound states is quantized. 50 Å and 5 Å bandwidths were used for NO and benzene respectively. In neither case was the wavelength resolution sufficiently high to reveal the quantized nature.

This argument applies equally well to tri-n-propyl amine for photoionization at wavelengths perhaps 5 or 10 Å longer than the ionization wavelength of λ = 1715 Å. However, photoionization at wavelengths longer than approximately 1725 Å can only be attributed to a two-step photoionization process.

The degeneracy ratio has been ignored in this discussion. However, the value is unlikely to be much different from 1 and its exclusion will not have affected the validity of the discussion as it has been presented.

Reports in the literature of Penning ionization sustained CO_2TEA laser discharges [66,67,68] prompted a limited investigation. Photoionization was observed in 0.1 torr of tri-n-propyl amine with no other gases present. The results appear in Figure 6-34. Addition of 10 torr of N_2 did not result in a significant change in the photoionization spectrum of tri-n-propyl amine. The same result was obtained with 4 torr of Kr in 4 torr of NO. Kr has a metastable state with energy of about 10 ev (λ = 1230 Å) [47].

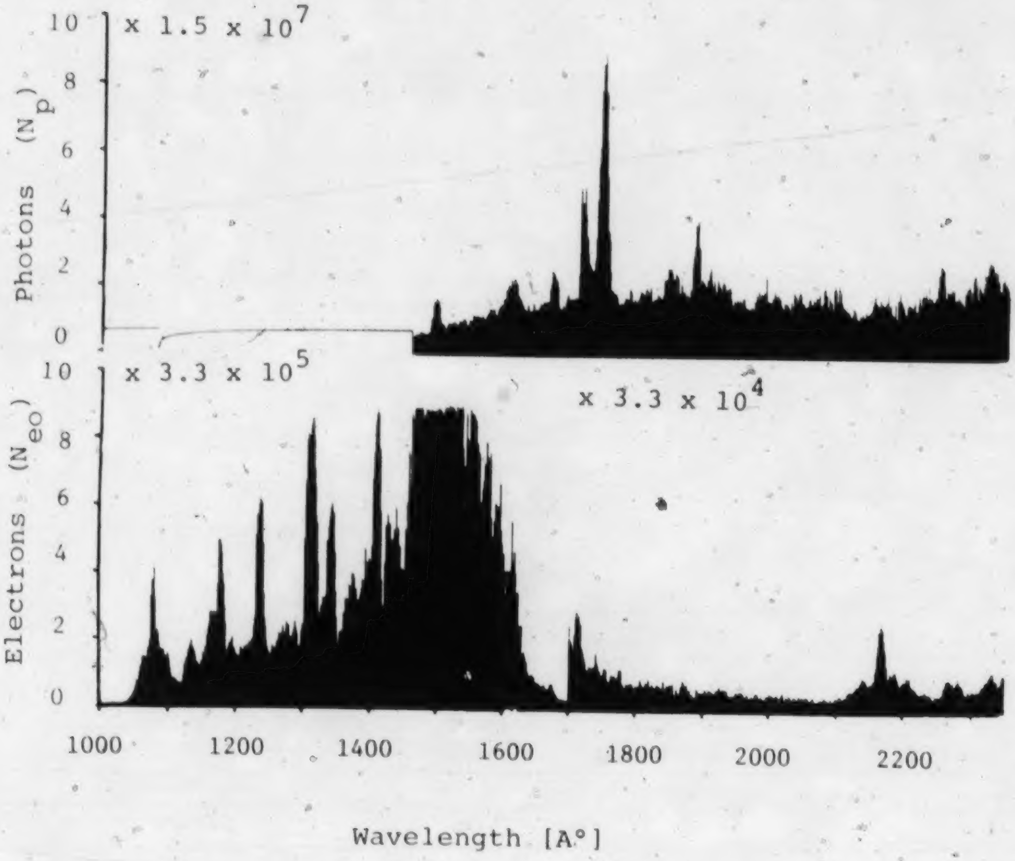

FIGURE 6-34 PHOTOABSORPTION AND PHOTOIONIZATION IN 0.1 TORR OF TRI-N-PROPYL AMINE No buffer gas was present. The photon spectrum incident on the test cell has been shown in Figure 6-33 (upper trace). The calibration factors have been included. Collection of positive ions has been accounted for. (E/P was very high here).

6-2-8 Determination of Photoabsorption and Photoionization Cross-Sections

The theory relevant to calculating photoabsorption and photoionization cross-sections from the experimental data has been developed in Chapter 3. The final relationships are given in Equations 3-81 and 3-84. These have been repeated here to facilitate reference.

$$\sigma_t = \frac{760T}{LP273n_o} \ln N_{po}/N_p \qquad 6\text{-}70$$

$$\sigma_i = \frac{760T}{LP273\, n_o} \frac{n_{eo}}{N_{po} - N_p} \ln N_{po}/N_p \qquad 6\text{-}71$$

σ_t = total photoabsorption cross-section [cm^2]

σ_i = photoionization cross-section [cm^2]

N_{po} = number of photons incident on the gas in the test cell. This quantity is equal to the number of photons measured with the test cell evacuated.

N_p = number of photons monitored by the charge collector under test conditions. i.e., the test cell must have been filled with the gas to be tested.

T = ambient temperature [300°K]

L = the length of the test cell [12 cm].

P = the pressure of the gas in the test cell [torr].

n_o = Loschmidt's number [2.7 x 10^{19} cm^{-3}]

Figure 6-33 reveals the absorption characteristics for CO_2 from about $\lambda = 1075$ Å to $\lambda = 1750$ Å. The upper trace is the number of photons incident on the test cell or the number of photons measured with the test cell evacuated. The lower trace shows the number of photons that have successfully traversed the test cell filled with 2.5 torr of CO_2. The resulting ionization was very small and it could not be determined with accuracy because of charge collector saturation problems discussed in Section 6-2-5. Since photoionization was very low level, all photoabsorption can be attributed to nonionizing absorption by CO_2. Consequently, Equation 6-70 applies to calculate the photoabsorption cross-section of CO_2. Values of N_{po} and N_p for various wavelengths have been taken from Figure 6-33. These appear in Table 6-6 along with the calculated value of σ_t. The photoabsorption cross-sections obtained can be seen to agree very well with the curve in Figure 5-45.

Calculation of the photoabsorption and photoionization cross-sections for tri-n-propyl amine with data presented in the previous section is complicated by the presence of the buffer laser mixture. Consequently, the photoabsorption and photoionization spectra for 0.1 torr of tri-n-propyl amine has been obtained without the presence of a buffer gas. This data appears in Figure 6-34. Charge collector saturation required a 29 volt bias ($E/P = 114$ volts cm^{-1} $torr^{-1}$) with a 80 μs collection

Table 6-6

CO_2 Photoabsorptions Cross-Sections

[Å]	N_{po}	N_p	σ_t [cm^2]
1085	$0.6 \times 1.5 \times 10^7$	?	high
1100	?	?	?
1150	$0.5 \times 1.5 \times 10^7$	?	high
1167	0.7	$0.5 \times 1.5 \times 10^7$	3.5×10^{-19}
1180	0.95	0.9	0.56
1200	0.7	0.69	0.15
1225	0.72	0.68	0.59
1242	1.4	1.2	1.6
1275	0.8	0.6	3.0
1300	0.72	0.54	3.0
1313	1.8	0.95	6.6
1317	2.0	1.0	7.1
1350	1.3	0.7	6.4
1375	1.1	0.7	4.7
1400	1.25	0.85	4.0
1412	2.4	1.3	6.3
1425	0.92	0.65	3.6
1450	1.2	0.75	4.8
1475	2.3	1.4	5.1
1495	9.0	4.3	7.6
1525	2.8	1.5	6.4

Table continued

Table 6-6 continued

λ [Å]	N_{po}	N_p	σ_t [cm^2]
1550	2.4	1.6	4.2
1575	2.6	2.2	1.7
1600	3.2	2.6	2.1
1625	4.5	3.8	1.7
1650	2.4	1.8	3.0
1680	5.0	4.5	1.1
1700	3.3	3.2	0.32
1725	7.6	7.0	0.85
1740	5.0	5.0	low

Data relevant to the calculation of photoabsorption cross-sections for CO_2 has been obtained from Figure 6-33 where absorption in 2.5 torr of CO_2 was measured. σ_t has been obtained with Equation 6-70.

time. Since electrons could be expected to be collected much faster than this it has been concluded that the increased time and E/P necessary to obtain saturation, was probably due to collection of positive ions as well as electrons. Therefore, Equation 6-43 applies to calibrate the charge collector. The chart recorder sensitivity was 0.2 volts per division. A change in gain is indicated in Figure 6-34. The calibration relationship for the photons is given by Equation 6-65. For wavelengths up to $\lambda = 1715$ Å the concentration of the ionizing species is accurately known. The incident photons can be obtained from Figure 6-33. Values of N_{po}, N_p and n_{eo} for various wavelengths are obtained from Figures 6-33 and 6-34 and these are tabulated in Table 6-7. Equations 6-70 and 6-71 apply for the calcualtion of the total photoabsorption cross-sections and photoionization cross-sections respectively. These have been determined and tabulated in Table 6-7 as well.

The resulting photoionization cross-sections are large for the short wavelengths and diminish for the longer wavelengths. This is constant with the short and long range processes that were discussed in the previous section. Furthermore, the total absorption cross-sections are seen to be considerably larger than that for CO_2. Hence, photoabsorption for the data in Figure 6-22 throughout to Figure 6-30 can be assumed to be dominated by the tri-n-propyl amine when the concentration is sufficiently high. This would allow the determination of the photoabsorption and photoionization cross-sections for tri-n-propyl amine for the data involving the laser gas mixture. This is desirable since these cross-sections may change with the pressence of a buffer gas [16].

A criterion must be established to specify the CO_2 and tri-n-propyl amine pressure range for which photoabsorption will be dominated by tri-n-propyl amine.

Equations 3-75 and 3-77 reveal that the intensity of a monochromatic beam of light is reduced by the factor $\exp(-\sigma_t\ n_o\ \chi)$ upon passing through an absorbing medium, characterized by these parameters. The criterion will be defined as follows: The reduction due to tri-n-propyl amine must be at least 10 times more than the reduction due to CO_2. This can be represented mathematically by:

$$\frac{\exp - n_o(\sigma_t\chi)_{\text{tri-n-p}}}{\exp - n_o(\sigma_t\chi)_{CO_2}} < 0.1 \qquad 6\text{-}72$$

where $\chi = \frac{L273P}{760T}$

and P is the pressure of tri-n-propyl amine or CO_2.

Equation 6-72 can be manipulated to yield the required range of the tri-n-propyl amine pressure for a given CO_2 pressure.

Table 6-7

Photoabsorption and Photoionization Cross-Sections for Tri-n-propyl Amine

λ[Å]	N_{po}	N_p	n_{eo}	σ_t[cm^2]	σ_i[cm^2]
1080	$0.6 \times 1.5 \times 10^7$	$0.1 \times 1.5 \times 10^7$	$3.7 \times 3.3 \times 10^5$	4.6×10^{-17}	1.5×10^{-18}
1080-1460	?	?		?	?
1460	1.4	0.2	6.5	5.0	6.0
1470	2.3	0.6	8.9	3.5	4.0
1508	2.7	0.8	8.7	3.1	3.1
1540	2.5	0.9	6.0	2.6	2.2
1575	2.5	1.3	7.5	1.7	2.3
1600	3.0	1.5	4.5	1.8	1.2
1625	3.0	1.5	2.0	1.8	0.50
1650	2.5	1.4	0.8	1.5	0.24
1675	4.5	2.3	0.7	1.7	0.12
1700	3.3	1.7	0.2	1.7	0.047
1715	8.0	4.5	0.25	1.5	0.023

Table continued on next page

Table 6-7 continued

Data have been obtained from Figures 6-33 and 6-34 for 0.1 torr of tri-n-propyl amine. Equations 6-70 and 6-71 have been used to calculate σ_t and σ_i respectively.

$$P_{tri-n-p} > \frac{(\sigma_t P)_{CO_2} - \frac{760T}{L273\ n_o} \ln 0.1}{\sigma_{t\ tri-n-p}} \qquad 6-73$$

Observation of Figures 6-22 throughout to Figure 6-30 and Figure 6-35 reveals that photoabsorption has been measured over the largest portion of the spectrum for $CO_2 : N_2 : He$ = 20 torr : 20 torr : 20 torr laser mixture. Hence, this will be used to calculate the photoabsorption and photoionization cross-sections. Furthermore, the measureable photoabsorption extends only to $\lambda = 1500$ Å. Since the CO_2 photoabsorption cross-section peaks at this point (Table 6-6) and the tri-n-propyl amine photoabsorption cross-section is relatively constant, (Table 6-7) this point can be taken to establish the range of tri-n-propyl amine pressure for a worst case condition. Equation 6-73 requires that $P_{tri-n-p} > 0.68$ torr. Only the last two traces in Figure 6-30 have sufficient tri-n-propyl amine concentrations.

Figure 6-35 reveals that the photoabsorption for the highest concentration has so attenuated the photon signal, that it has not been able to be monitored. This leaves only the third trace in Figures 6-30 and 6-35 as useful to calculate the photoabsorption and photoionization cross-sections for tri-n-propyl amine in the laser mixture. The upper trace in Figure 6-33 yields the photon spectrum incident on the test cell. Values of N_{po}, N_p and n_{eo} are

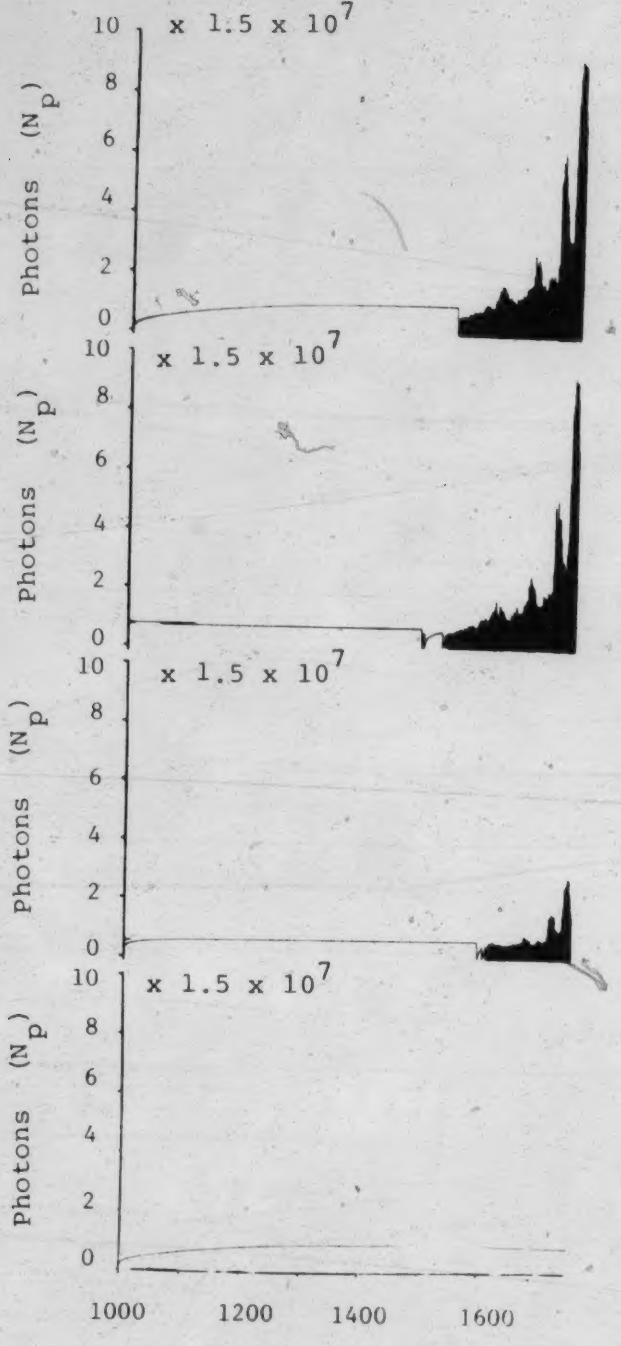

FIGURE 6-35 PHOTOABSORPTION IN 20 TORR OF LASER MIXTURE PLUS TRI-N-PROPYL AMINE The photon spectrum incident on the test cell has been shown in Figure 6-33 (upper trace). The calibration factor has been included. $CO_2:N_2:He = 1:1:1$. The pressure of tri-n-propyl amine is (from top to bottom) 0.05 torr, 0.2 torr, 1.0 torr, and 2.5 torr.

obtained from Figures 6-33, 6-35 and 6-30 respectively. These are tabulated in Table 6-8. Equations 6-70 and 6-71 with P = 1.0 torr of tri-n-propyl amine have been used to determine σ_t and σ_i. These also appear in Table 6-8. The resulting values of σ_i agree very well with those in Table 6-7 for pure tri-n-propyl amine. The photoionization cross-sections are only slightly smaller when the tri-n-propyl amine is placed in the laser mixture [16]. The photoabsorption cross-sections are a factor of 2 or 3 smaller when the tri-n-propyl amine is placed in the laser mixture.

The photoionization cross-sections calculated thus far are particularly relevant to a CO_2 TEA laser. However, for multi-atmosphere CO_2 lasers, strong photoabsorption by CO_2 for $\lambda \leq 1750$ Å may limit tri-n-propyl amine photoionization in this portion of the spectrum. Tri-n-propyl amine exhibits significant two-step photoionization for wavelengths greater than $\lambda \simeq 1715$ Å and this feature may be taken advantage of for high pressure CO_2 lasers.

Equation 6-16 is appropriate for the analysis of the two-step photoionization data. The equation can be simplified considerably if it is assumed that

$$\frac{1}{\tau_\ell} >> \frac{I}{h\nu} \sigma_i^* \qquad 6\text{-}74$$

and

$$\tau_\ell << t_d \qquad 6\text{-}75$$

Table 6-8

Photoabsorption and Photoionization Cross-Sections for tri-n-propyl Amine in a Laser Mixture

λ [illegible]	N_{po}	N_p	n_{eo}	σ_t [cm^2]	σ_i [cm^2]
1600	$3.0 \times 1.5 \times 10^7$	$0.1 \times 1.5 \times 10^7$	$7.5 \times 6.5 \times 10^5$	0.88×10^{-17}	1.0×10^{-18}
1625	4.5	0.5	3.3	0.57	0.20
1650	2.3	0.5	1.5	0.39	0.14
1675	4.0	0.8	1.0	0.41	0.055
1700	3.3	0.65	0.3	0.42	0.021
1715	8.0	1.4	0.4	0.45	0.012

N_{po}, N_p, and n_{eo} have been obtained from Figures 6-33, 6-35 and 6-30 respectively. Equations 6-70 and 6-71 have been used to determine σ_t and σ_i with P = 1.0 torr of tri-n-propyl amine.

These relationships will be true if the intermediate state is an ordinary state with a radiative lifetime of about 10^{-8} seconds. Figures 6-22 throughout to Figure 6-29, and Figure 6-34 indicate that the rate of the two-step photoionization process is relatively constant. If a metastable intermediate state was responsible at some wavelength, one would expect a significant increase in the measured value of n_{eo} for the excitation wavelength of the metastable. However, this has not been observed and ordinary bound states have been assumed to act as the intermediate levels in the two-step photoionization process. Relation~~s~~ 6-74 and 6-75 having been established, Equation 6-16 can be reduced to

$$n_{eo} = \left(\frac{I}{h\nu}\right)^2 n\sigma^* \sigma_i^* \frac{\Delta\nu}{\Delta f} \tau_\ell t_d \qquad 6\text{-}76$$

Equation 6-76 applies only to an optically thin system since I was assumed to remain constant in the defining relations. 50% absorption ~~has~~ occurred in Figure 6-34 and this data will be used as an approximation for the optically thin requirement. The term I/hν is the average number of photons per second per cm^2 that passes through the test cell [23]. In terms of the measured quantities, this factor is:

$$\left(\frac{I}{h\nu}\right) = \frac{N_{po} + N_p}{2t_d} \qquad 6\text{-}77$$

Equation 6-76 reduces to:

$$n_{eo} = \left(\frac{N_{po} + N_p}{2}\right)^2 \frac{\chi_p}{t_d} \qquad 6\text{-}78$$

where

$$\chi_p = n\sigma^* \sigma_i^* \frac{\Delta\nu}{\Delta f} \tau_\ell \qquad 6\text{-}79$$

χ_p has units of [sec cm] (the photon beam covers an area of 1 cm^2)

Values of N_{po}, N_p and n_{eo} have been taken from Figures 6-21 and 6-34. These appear in Table 6-9 along with the calculated values of χ_p with $t_d = 5$ μs and $n = \frac{0.1}{760} \times 2.7 \times 10^{19}\ cm^{-3}$

The resulting values of χ_p are very large. Equation 6-79 yields an average value for $\sigma^* \sigma_i^* \frac{\Delta\nu}{\Delta f}$ of $2.7 \times 10^{-27}\ cm^4$ with $\tau_\ell = 10^{-8}$ seconds.

This large value has been attributed to the nature of the tri-n-propyl amine molecule. It is an extremely large molecule presumably with many energy states lying so close together so as to effectively form a continuum. This would result in the factor $\Delta\nu/\Delta f$ being close to unity. Furthermore a large number of energy states would serve to increase the photoexcitation cross-section of the intermediate state, σ^*. NO and benzene are relatively simple molecules compared to tri-n-propyl amine and they do not exhibit significant two-step photoionization. Figures 6-25

Table 6-9

Two-Step Photoionization Coefficients for Tri-n-propyl amine

λ[Å]	N_{po}	N_p	n_{eo}	χ_p [sec cm^{-3}]
1725	$5.0\times1.5\times10^{7}$	$2.2\times1.5\times10^{7}$	$0.9\times3.3\times10^{4}$	8×10^{-20}
1760	3.0	1.8	0.7	14
1800	3.0	1.9	0.7	14
1850	3.8	2.3	0.7	8.8
1900	3.6	2.0	0.5	7.2
1950	2.8	1.6	0.5	12
2000	3.0	1.8	0.5	10
2050	3.8	1.5	0.4	6.8
2100	3.5	1.5	0.35	6.4

Values of N_{po}, N_p and n_{eo} have been obtained from Figures 6-21 and 6-34 for 0.1 torr of tri-n-propyl amine. Equation 6-78 has been used to calculate the values of χ_p.

and 6-29 reveal that the two-step photoionization diminishes slightly for increased buffer gas pressure. This has been attributed to collisional de-excitation of the intermediate state by the buffer gas molecules. This effect can probably be compensated for by increased photon flux.

Unfortunately, failure of the photon counter amplifier supplying gain of X 131 (G_{p2}) prevented the measurement of photoabsorption and photoionization cross-sections for tri-n-propyl amine at wavelengths shorter than approximately 1460 Å. However, a measurement was obtained at 1080 Å. Reduced photoabsorption by CO_2 at this wavelength is evident in Figure 5-45. This measurement was obtained at the limit of the photon counter sensitivity. Hence, it may not be accurate. But taking this into consideration, the regions of photoionization controlled by CO_2 photoabsorption have been dealt with.

6-3 Discussion and Conclusion

The results of the tests performed with the ultra-violet vacuum monochromator and presented in this chapter correlate well, with the results of the tests performed on the microwave interferometer. Qualitative agreement with published material on the same subject has also been obtained [16,22,23,65,87,88,89]. In effect, results obtained with the monochromator test facility have either confirmed conclusions drawn on the basis of information gathered with the microwave interferometer, or have served to answer questions raised by it.

(1) Photographs of the spark source emission spectrum reveal that it is primarily a line spectrum and that the Hopfield and Huffman continuum do not play a significant role.

(2) Photographic and electronic records of emission spectra reveal that the spectral content is largely independent of gas type for the automotive surface gap spark plug. The tungsten pin emission spectrum is somewhat more characteristic of the gas species.

(3) The intensity of the spectrum increases with source gas pressure.

(4) N_2 has been identified as the laser gas that promotes the most intense emission spectrum. This is in contradiction to the implicit assumption made in the earlier work with the microwave interferometer where

He was credited for the majority of the hard ultra-violet emission.

(5) CO_2 photoionization control by photoabsorption has been well documented. CO_2 appears to be totally opaque for wavelengths shorter than 1150 Å. It also, is a relatively heavy photoabsorber for 1230 Å < λ < 1700 Å.

(6) Importance of high spark discharge current for efficient hard ultra-violet production has been further documented.

(7) Photoionization in the laser gases has been shown to be the result of a one-step process for wavelengths up to 1750 Å.

(8) Difficulty in obtaining charge collector saturation for the low level photoionization obtained in the laser gases precluded a detailed analysis. However, the photoionization spectrum was identified and only hard ultra-violet photons were found to be effective. Furthermore, impurities inherent in the gas supply cylinder were found to contribute significantly to the photoionization. However, this was easily masked by the residual impurities in the test cell depending on the relative cleanliness. This would apply to a typical laser device as well.

(9) Significant electron loss by attachment to CO_2 was observed when the value of E/P resulted in the correct energy

for this process.

(10) Low ionization threshold vapors resulted in increased photoionization by at least three orders of magnitude whether tested independently or in a buffer laser mixture.

(11) Subtle differences in the photoionization properties of the vapors were observed. In addition to yielding different levels of photoionization, tri-n-propyl amine photoionized at wavelengths longer than its photoionization wavelength. This was unlike NO and benzene that did not exhibit measureable photoionization at wavelengths appreciably longer than their photoionization wavelengths.

(12) The photoionization spectrum of tri-n-propyl amine exhibits a dependence on concentration. For low concentrations efficient photoionization at short wavelengths dominates. For increased concentrations, the dominant photoionization signal shifts to the longer wavelengths. This phenomenon was also shaped by CO_2 absorption. Furthermore, tri-n-propyl amine has been observed to photoionize, presumably by a two-step process, at wavelengths extending to at least 2200 Å. This part of the photoionization spectrum was relatively unaffected by the presence of a laser mixture buffer. This characteristic may be able to be exploited for discharge stabilization in large aperture

multi-atmospheric pressure CO_2 TE lasers.

(13) Photoabsorption and photoionization cross-sections have been obtained for tri-n-propyl amine for wavelengths greater than $\lambda = 1460$ Å. The value obtained at $\lambda = 1080$ Å may be questionable.

(14) Measured photoabsorption cross-sections for CO_2 correlate well with published values [42,58].

Collector saturation problems for low photoionization density in the laser gases when no seedant vapors are used have been shown to be caused primarily by diffusion. Such a significant diffusion effect was not anticipated when the charge collector was in the design and fabrication stages. Only after detailed testing was the diffusion effect identified. Prevention of photoemission, reduction of charge transit distance,and simplicity were the criteria given primary consideration in the geometrical design of the charge collector. Flat, parallel collector plates or electrodes were certainly the simplest configuration. Close spacing was required to reduce charge transit time; conversely, prevention of photoemission demanded wide separation. A separation of 2.54 cm was chosen as the best compromise. The rectangular wedge of light expanded from a narrow line (depending on the bandwidth adjustment) at the exit slit of the monochromator to 1 cm at the scintillator.

No evidence of photo emission has been obtained.

Before the test cell was contaminated with seedant vapors, continued pumping with a diffusion pump resulted in reduction of any photoionization signal to below the charge collector sensitivity (6.6 x 10^3 elementary charges). As a result, this design criteria may be relaxed in favor of reduction of the transit length. This would serve to reduce the effect of diffusion because transit time would also be reduced. Furthermore, it may be desirable to contour the collector electrodes to the same shape as the wedge of photons. In addition to maximally reducing the transit time for any charged particle, this would serve to linearly increase the applied E/P value toward regions of higher photoionization density. The light is more concentrated near the exit slit and so the photoionization density would be highest there (but not the total number of photons per unit distance along the collector plate for an optically thin gas).

Electrodes shaped in such a fashion would tend to automatically and rapidly reduce the high density photoionization in the vicinity of the exit slit by virtue of the increased E-field. This could be sufficiently rapid so as to remove charge as it is produced,thus preventing accumulation of charge to densities high enough to result in significant space charge effects. Alternatively, since only electron collection has been observed in most cases with the present system, electron diffusion to the end walls could be markedly reduced by maintaining these at a negative potential. Such E-field shaping may be able to be applied to prevent diffusion loss to the side walls as well.

No space charge effects were observed for either the low photoionization density obtained with the laser gases (maximum value of $\approx 8 \times 10^3$ electrons) or for the relatively high level obtained when seedant vapors were used (maximum observed values were about 10^6 electrons). Determination of the Debye length yields information regarding the ability of an ensemble of charges to establish a space charge to cancel an applied electric field [41].

$$\lambda_{Di} = \left(\frac{\varepsilon k T_i}{4\pi e^2 n_{io}}\right)^{1/2}$$

λ_{Di} = Debye shielding length for electrons by ions [cm]

ε = permittivity of free space [8.8×10^{-21} cm^3 g sec^{-1} Å^{-1}].

k = Boltzmann constant [1.38×10^{-16} erg K^{-1}]

T_i = ion temperature [300°K]

e = electron charge [1.6×10^{-19} coul]

n_{io} = ion density [cm^{-3}]

The density of ions will have been equal to the density of electrons. However, the above numbers refer to the total number of electrons and hence ions rather than the density. Since the ions will immediately respond to the applied electric field, they will tend to occupy a volume larger than that volume in which they were formed. Diffusion effects will also tend to increase the value, particularly high mode diffusion at the boundaries defined by the wedge of light. It has been estimated that the expanded volume may be as high as 50 cm^3. Taking this into account, equation 6-80 yields Debye shielding lengths of 2.7 cm for the worst case in the laser gases and 0.24 cm for the worst case when seedant vapors were employed. The ensemble of charges cannot form protective space charges within these distances. Consequently, space charge effects are precluded for the laser gases. However, when seedants are employed space charge may have a limited effect on the charge collection. This may in fact be the reason collector saturation can be so easily obtained when seedants are employed. The relatively high positive ion density may result in reducing the diffusion coefficient for electrons from fast free electron diffusion towards slower ambipolar diffusion. Ambipolar diffusion cannot be expected to be fully developed for the photoionization densities under consideration, however [47]. The test facility has performed well and has supplied information pertinent to further understanding of photoionization in CO_2 lasers. In addition, it has shown how substantial photoionization can be obtained in CO_2 lasers of various dimensions operating over a broad pressure range. Tri-n-propyl amine has been tested more thoroughly since its use in lasers has yielded more promising results than any other tried to date [20,23,24,25]. Benzene and NO have actually been observed to reduce laser output in spite of their relatively high electron yield by photoionization [60,88]. However, a small but critical concentration of NO has been shown to improve laser output [87].

The test facility lends itself to the determination of other physical data as well. It has been shown that the Townsend first ionization coefficient can be determined for various gases. Electron drift velocities and possibly ion mobilities can be determined. Electron attachment as a function of electron energy to traces of additives in a buffer gas may be observed. The accuracy may leave something to be desired, but order of magnitude values at least establish the range of these parameters and provide criteria on which to base the design of a more accurate experiment. Furthermore, order of magnitude values can be of great value to facilitate the design of CO_2 lasers. At present,design is often based on parameter values much less accurate than an order of magnitude.

Recently, the photon counter has undergone a major redesign. The integrator has been discarded in favor of the type used in the charge collector. This device presently under construction, should provide better sensitivity and greater reliability. Its use should provide for the determination of photoabsorption and photoionization cross-sections over a larger region of the spectrum than has been done here. Calibration of the diffraction grating would allow for the absolute intensity measurement of the emission spectrum of various sources. This would be of extreme usefulness in designing spark sources whose emission spectrum matched the useful photoionization spectrum in a CO_2 laser. For instance, a source that concentrated its energy in the region $1750\ \text{Å} < \lambda < 2200\ \text{Å}$ would be most efficient for use in a multi-atmosphere pressure CO_2 laser seeded with tri-n-propyl amine.

The test facility has provided useful data and should continue in a similar fashion for some time.

Chapter 7

Concluding Remarks

Two test facilities appropriate to the procuring of data relevant to photoionization in a CO_2 laser device have been designed, constructed, and operated. The first test facility is a microwave interferometer. It is capable of providing average plasma density measurements in a gas photoionized by sparks of the type used in CO_2 lasers. The response time of the interferometer provides adequate time resolution to follow the plasma decay to a lower limit of about 10^7 cm^{-3}. This value was experimentally determined to be the maximum sensitivity of the device. With a plasma cut-off density of 10^{12} cm^{-3}, the interferometer technique can be seen to provide a large dynamic range. In addition to providing time resolution, the interferometer also allowed for limited spatial resolution. Average plasma density measurements could be obtained as a function of distance from the ultra-violet source. Gas pressure could also be varied allowing for plasma density as a function of pressure to be obtained. This test facility could also be modified to measure photoionization or discharge plasma density orthogonal to the discharge and optical axes of a CO_2 laser, providing adequate external noise suppression could be supplied. However, no resolution would be provided for densities greater than 10^{12} cm^{-3}. Provision of adequately directional horns to act as transmitter and receiver would allow for the determination of the average density down the bore of the laser.

Bare sparks were used in the microwave interferometer facility, primarily because window materials would not stand up to the disruptive environment provided by the high voltage, high current spark. Consequently, the source emission spectrum could not be expected to remain constant with changes of gas pressure and species. Also, the interferometer did not provide for resolution of the source emission spectrum. These two factors were the primary motivation resulting in the design and construction of a test facility involving a vacuum ultraviolet monochromator.

A Jarrell-Ash vacuum monochromator with a concave reflecting grating ruled to 30,000 lines per inch provided more than adequate spectral resolution. The monochromator was equipped with a camera assembly, and this provided a convenient means of identifying the spark emission spectrum as a line spectrum. It also provided a means of determining the extent of the spectrum. However, the photographic technique was not as sensitive as desired, and a number of spark discharges had to be used to obtain a noticeable film darkening for the weaker portions of the spectrum. Furthermore, the film is linear only over a small region. Alternatively, a photomultiplier tube can be accurately calibrated over a broad dynamic range. Conveniently, a photomultiplier tube was available with a cathode bearing an S-11 surface. Such a surface exhibits a peak sensitivity at $\lambda = 4200$ Å. This matches the peak of the fluorescent spectrum of sodium salicylate which was used to sensitize the photomultiplier to the hard ultra-violet light. The dynamic range of the photomultiplier was increased by providing additional gain in the form of an electronic amplifier. This also provided a matching network to prevent loading of the photomultiplier output by the oscilloscope. The output signal was subsequently integrated electronically. This provided an output related to the total number of photons incident on the scintillator per spark discharge. Hence, the device was termed a photon counter. The resulting dynamic range extended from a maximum sensitivity of 2×10^5 photons to a saturation of 1×10^{10} photons. The calibration was performed by considering electronic amplifier gains, photomultiplier specifications provided by the manufacturer, and by experimentally determining the quantum efficiency of the scintillator.

An x-y recorder was used to monitor the photon counter output and with the horizontal drive synchronized to the monochromator drive, a bar-graph type of display was obtained. The height of each bar represented the number of photons per spark discharge in a bandwidth determined by the slit adjustment of the monochromator. The photon counter was placed 12 cm back from the exit slit of the monochromator. A charge collector was placed in this region and was housed in a vacuum tight ferromagnetic shield which served the dual purpose of a test cell. The charge created by photoionization was collected by an electric field. The resulting current was electronically integrated, amplified, and displayed by an x-y recorder. The same type of bar-graph display as for the photon counter was generated. The horizontal drive of the x-y recorders were mechanically linked and the photoabsorption and photoionization spectra of a gas under test could be generated simultaneously. The charge counter was calibrated simply by considering the gain of the electronic components constituting the charge collector. The dynamic range of this device depends on the value of the front end capacitance. The lowest value of capacitance determined the maximum sensitivity of the device. Parasitic capacitance was 13 pf. 6.6×10^3 elementary charges resulted in a front end capacitor voltage sufficiently high to overcome amplifier noise. As the device was set up, saturation was obtained for an increase in total charge of about 4 orders of magnitude. This value could be extended by increasing the front end capacitance if desired.

The photon counter (as well as the photographic technique) revealed that the useful part of the spectrum was limited to wavelengths greater than approximately 1100 Å because of heavy CO_2 absorption. Therefore a LiF window was used at the exit slit to isolate the source from the test cell.

Source photoemission spectra as well as photoabsorption and photoionization spectra of various gases and vapors have been obtained with this test facility. From these recordings, photoabsorption and photoionization cross-sections have been obtained. Numerous characteristics of photopreionization in a CO_2 TEA laser have been inferred from the results of these tests. An important observation was the control of photoionization by CO_2 absorption. Addition of long ionization wavelength gases in small concentrations increased the photoionization by 3 to 4 orders of magnitude. A gas such as NO, and benzene vapor can be expected to promote photoionization in a CO_2 laser by photoionization in a CO_2 window at 1200 Å. This window may be closed to practical light sources for pressures exceeding 200 or 300 torr of CO_2. Alternatively, photoionization of tri-n-propyl amine is available in three bands. These can be divided approximately as follows: 1150 Å $< \lambda <$ 1230 Å; 1600 Å $< \lambda <$ 1715 Å; 1715 Å $< \lambda <$ 2200 Å or higher. The efficiency of these processes diminishes with increasing wavelengths.

The first band may be assumed to be effective for low pressure CO_2 lasers, (less than 100 torr of CO_2), the second for medium pressure devices (100 - 350 torr of CO_2); and the third, for higher pressure devices (greater than 350 torr of CO_2). The upper pressure limits have been obtained by calculating the pressure for which 90% absorption of photons by CO_2 can be expected for a 10 cm penetration depth. Requirements of a longer penetration depth would require a reduction in pressure, i.e., the product Pd must be kept constant. A two-step process has been assumed to be responsible for the third band of photoionization.

Future plans for the test facility include the search for a gas or vapor which exhibits photoionization characteristics that can be matched to the peak output of a photon source. Furthermore, laser gases must be transparent for the required band of photons. Hydrocarbons are of particular interest since relatively large vapor pressures can be obtained at room temperature. The list of hydrocarbons is large, and exhaustive testing may reveal one or more that may be even more desirable than tri-n-propyl amine. Among these, the author has suggested the hydrazines. Some members of this family have ionization wavelengths comparable to tri-n-propyl amine. Also, many hydrazil radicals have ionization potentials as low as 4.95 eV [90]. These apparently are bound to the parent molecule by approximately the same amount of energy as the ionization potential. The author has suggested that the radical bond may be broken with one photon and ionized with another, constituting a two-step process overall. Photons of wavelengths up to 2500 Å would be useful. CO_2 is totally transparent here. Window materials are readily available and the intensity of available light sources typically increases with wavelength. Alternatively, the efficiency may be increased if the radicals could be more easily produced, perhaps by a chemical reaction. In addition, some of the boron trihalides may operate in a similar manner to that proposed for the hydrazines [91]. Some of the amino acids possess very low ionization potentials (≈ 2 ev), at least in aqueous solution [81]. Perhaps this may be exploited.

Many of the metal vapors possess low ionization energies but typically their vapor pressures are very low at room temperature. Cs, however, with an ionization potential of 3.9 ev ($\lambda \approx 3183$ Å) has a vapor pressure of 10^{-9} atmospheres at room temperature, and may prove to be useful [17,79,81]. Russian work and a limited investigation performed by the author (previously discussed) tend to disfavor the use of metal vapors, however.

The list of possibilities is effectively endless and a systematic search should result in a number of candidates. Subsequent testing with the facilities made available as a result of this project should reveal how, and to what extent, the candidate can be exploited in a CO_2 laser.

REFERENCES

1. G.J. Dezenberg, Roy, McKnight, "Performance of High Voltage Axially Pulsed CO_2 Lasers", IEEE J. of Quantum Electronics QE-8, No. 2, 58 (Feb. 1972).
2. A.E. Hill, "Multijoule Pulses from CO_2 Lasers", Appl. Phys. Lett., 12, No. 9, 324 (May 1968).
3. A.J. Beaulieu, "Transversely Excited Atmospheric Pressure CO_2 Lasers", Appl. Phys. Lett., 16, No. 12, 504 (June 1970).
4. D.C. Smith and A.J. DeMaria, "Parametric Behaviour of the Atmospheric Pressure Pulsed CO_2 Laser", J. of Applied Phys., 41, No. 13, 5212 (August 1970).
5. J.A. Beaulieu, "High Peak Power Gas Lasers", Proc. of the IEEE, 59, No. 4, 667 (April 1971)
6. A.K. LaFlamme, "Double Discharge Excitation for Atmospheric Pressure CO_2 Lasers", Rev. Sc. Inst., 41, No. 11, 1578 (November 1970).
7. Yu-Li Pon, Bernhardt and Simpson, "Construction and operation of a Double Discharge TEA CO_2 Laser", Rev. Sc. Inst., 43, No. 4, 662 (April 1971).
8. H.M. Lamberton and Pearson, "Improved Excitation Techniques for Atmospheric Pressure CO_2 Lasers", Electron. Lett. 7, 141 (January 1971).

9. D.B. Nichols and W.M. Brandenberg, "Radio Frequency Preionization in a Supersonic Transverse Electrical Discharge Laser", IEEE J. of Quantum Electronics, QE-8, No. 8, 718 (August 1972).

10. C.A. Fenstermacher, Nutter, Leland and Bayer, "Electron Beam Controlled Electrical Discharge as a Method of Pumping Large Volumes of CO_2 Laser Media at High Pressure", Appl. Phys. Lett., 20, No. 2, 56 (January 1972).

11. H.G. Ahlstrom, Pindroh, Holzrichter, Kan, Inglesakis, Kolb and Jansen, "Results of the Time-Dependent Gain with a High-current Electron-Beam Sustained Discharge in CO_2", IEEE J. of Quantum Electronics, QE-10, No. 1, 26 (January 1974).

12. R.K. Garnsworthy, L.E.S. Mathias and C.H.H. Carmichael, "Atmospheric-Pressure Pulsed CO_2 Laser Utilizing Preionization by High-Energy Electrons", Appl. Phys. Lett., 19, No. 12, 506 (December 1971).

13. M.C. Richardson, Alcock, Leopold and Burtyn, "A 300 J Multigigawatt CO_2 Laser", IEEE J. of Quantum Electronics, QE-9, No. 2, 236 (February 1973).

14. N.G. Basov, Belenov, Donilychev, and Sachkov, "High Pressure Pulsed CO_2 Laser", Soviet J. of Quantum Electronics, 1, No. 3, 306 (November-December 1971).

15. P.R. Pearson and H.M. Lamberton, "Atmospheric Pressure CO_2 Lasers Giving High Output Energy Per Unit Volume", IEEE J. of Quantum Electronics, QE-8, No. 2, 145 (February 1972).

16. A. Javan and J.S. Levine, "The Feasibility of Producing Laser Plasmas via Photoionization", IEEE J. of Quantum Electronics, QE-8, No. 11, 827 (November 1972).

17. K.J. Nygaard, "On the Effect of Cesium in Photoionization Laser Plasmas", IEEE J. of Quantum Electronics, QE-9, No. 10, 1020 (October 1973).

18. H. Seguin and J. Tulip, "Photoinitiated and Photosustained Laser", Appl. Phys. Lett., 21, No. 9, 414 (July 1972).

19. O.P. Judd, "An efficient electrical CO_2 laser using preionization by Ultra-violet Radiation", Appl. Phys. Lett., 22, 95 (October 1973).

20. J.S. Levine and A. Javan, "Observation of Laser Oscillation in a atom CO_2-N_2-He laser Pumped by an Electrically Heated Plasma Generated via Photoionization", Appl. Phys. Lett., 22, No. 5, 55 (January 1973).

21. M.C. Richardson, Leopold, Alcock, "Large Aperture CO_2 Laser Discharges", IEEE J. of Quantum Electronics, QE-9, No. 9, 934 (September 1973).

22. O.P. Judd and Wada, "Investigations of a U.V. Preionized Electrical Discharge and CO_2 Laser", IEEE J. of Quantum Electronics, QE-10, No. 1, 42 (January 1974).

23. J.S. Levine and A. Javan, "Spatial Distribution of Electrons in a High-Pressure Plasma Produced by Two-Step Photoionization", Appl. Phys. Lett., 24, No. 6, 258 (March 1974).

24. W.M. Clark and R.C. Lind, "Space and Time Resolved Gain Measurements of a UV-Sustained CO_2 Laser", Appl. Phys. Lett. 25, No. 5, 284 (September 1974).

25. R.C. Lind, J.Y. Wada, G.J. Dunning and W.M. Clark Jr., "A Long-Pulse High Energy CO_2 Laser Pumped by an Ultra-Violet-Sustained Electric Discharge", IEEE J. Quantum Electronics, 818 (October 1974).

26. C.K.N. Patel, W.L. Faust, and R.A. McFarlene, "CW Laser Action on Rotational Transition of the $\Sigma u+$ - $\Sigma g+$ Vibrational Band of CO_2", Bull, Amer. Phys. Soc., 9, 500 (April 1964).

27. C.K.N. Patel, "Interpretation of CO_2 Optical Maser Experiments", Phys. Rev. Lett., 12, 588 (May 1964).

28. C.K.N. Patel, "Continuous wave Laser Action on Vibrational-Rotational Transitions of CO_2", Phys. Rev., 136, A1187 (May 1964).

29. F. Legay and N. Legay-Sammaire, "Sur les possibilités de réalisation d'un maser optic utilisant l'énergie de vibration des gaz excités par l'azote active," R.A. Acad. Sci., 259, 99, (July 1964).

30. C.K.N. Patel, "Selective Excitation Through Vibrational Energy Transfer and Optical Maser Action in N_2-CO_2", Phys. Rev. Lett., 13, 617 (November 1964).

31. G. Moellar and J.O. Rigden, "High-power Laser Action in CO_2-He Mixtures", Appl. Phys. Lett., 7, 274 (November 1965).

32. C.K.N. Patel, P.K. Tien and J.H. McFee, "CW High-Power CO_2-N_2-He Laser", Appl. Phys. Lett., 7, 290 (December 1965).

33. O.R. Wood, "High-Pressure Pulsed Molecular Lasers", Proc. of the IEEE, 62, No. 3, 355 (March 1974).

34. M.A. Lutz, "The Glow to Arc Transition", Hughs Research Laboratories Research Report No. 430 (November 1970).

35. P.K. Cheo, "CO_2 Lasers", *Lasers*, edited by A.K. Levine and A.J. DeMaria, (Marcel Dekker, 1971).

36. A.J. DeMaria, "Review of CW High Power CO_2Lasers", Proc. of the IEEE, 61, 731 (June 1973).

37. J.A.R. Samson, "Techniques of Vacuum Ultra-Violet Spectroscopy", (John Wiley and Sons, Inc., New York, London, Sydney, 1967).

38. A.N. Zaidel and E.Y.A. Shreider, "Vacuum Ultra-Violet Spectroscopy",(Ann Arbor-Humphrey Science Publishers, Ann Arbor, London, 1970).

39. W.R.S. Garton, P. Sc., A.R.C.S., "Improved Lyman-Continuum Flash-Source of Large Aperture", J. of Sc. Inst., 36, 11 (January 1959).

40. N. Kristionpaller and R.A. Knapp, "Some Optical Properties of Sodium Salicylate Films", Appl. Optics, 3, No. 8, 915 (August 1964).

41. E.W. McDaniel, "Collision Phenomena in Ionized Gases", (John Wiley and Sons, Inc., New York, London, Sydney, 1964).

42. G.L. Weissler, "Photoionization in Gases and Photoelectric Emission from Solids", *Handbuch der Physik*, 21, 304, Berlin: Springer (1965).

43. E.G. Schneider, "A Note on the Photographic Measurement of the Transmission of Fluorite in the Extreme Ultra-Violet", Phys. Rev., 45, 152 (February 1934).

44. R.H. Huddlestone and S.L. Leonard, "Plasma Diagnostics Techniques",(Academic Press, New York, London, 1965).

45. M.A. Heald and C.B. Wharton, "Plasma Diagnostics with Microwaves", (John Wiley and Sons, Inc. New York, London, Sydney, 1965).

46. K.J. Nygaard, "The Variation of the Quantum efficiency of Sodium Salicylate with Thickness of Material", Brit. J. Appl. Phys., 15, 597 (1964).

47. J.B. Hasted, "Physics of Atomic Collisions", (Butterworths, London, Sydney, Toronto, Wellington, Auckland, Dunban, 2nd Edition, 1972).

48. A. Gilardini, "Low Energy Electron Collisions and Gases", (John Wiley and Sons, New York, London, Sydney, Toronto, 1972).

49. E.W. McDaniel and M.R.C. McDowell, "Case Studies in Atomic Collision Physics", 11, (North Holland Publishing Company, Amsterdam, 1972).

50. W.B. Kunkel and M.N. Rosenbluth, "Plasma Physics in Theory and Application", (McGraw-Hill Book Company, New York, 1966).

51. L.B. Loeb, "Basic Processes of Gaseous Electronics", (University of California Press, Berkeley, 1961).

52. J.D. Cobine, "Gaseous Conductors", (Dover Publications, New York, 1958).

53. R.K. Asundi, J.D. Craggs, M.V. Kurepa, Proc. Phys. Soc. (London), 82, 967 (1963); Third International Conference on the Physics of Electronic and Atomic Collision, London (1963).

54. M.S. Bhalla, J.D. Craggs, Proc. Phys. Soc., London, 76, 369 (1960).

55. M.S. Bhalla, J.D. Craggs, Proc. Phys. Soc., London, 78, 438 (1961).

56. S.C. Brown, "Basic Data of Plasma Physics", (M.I.T. Press, Cambridge, Massachusetts, London, 2nd Ed., 1966).

57. H.J. Seguin, J. Tulip and D. McKen, "Ultraviolet Photoionization in TEA Lasers", IEEE J. of Quantum Electronics, QE-10, No. 3, 311 (1974).

58. E.C.Y. Inn, K. Watan Abe and M. Zelikoff, "Absorption Coefficients of Gases in the Vacuum Ultraviolet. Part III. CO_2", The J. of Chem. Phys., 21, No. 10, 1648 (1953).

59. Linde Speciality Gas Catalogue, Union Carbide Canada Limited, (1971).

60. J.J. Hopfield, "Continuous Spectrum in the Region 500-1100A°", Phys. Rev., 36, 784-788 (1930).

61. R.E. Huffman, Y. Tanaka and J.C. Larabee, "New Vacuum Ultraviolet Emission Continua of Helium Produced in High Pressure Discharges", Amer. J. Opt. Soc., 52, 851-867 (August 1962).

62. W.R.S. Garton, I.W. Celnick, H. Hessburg and J.E.G. Wheaton, "Optical and Electrical Characteristics of a High Brightness Flash Discharge of Short Duration", in Proc. 4th Int. Conf. Ionization Phenomena in Gases (Amsterdam, The Netherlands), 518-523 (1960).

63. W.H. Bostick, V. Nardi, W. Prior, "X-ray Fine Structure of Dense Plasma in a Co-axial Accelerator", J. Plasma Phys., 8, 7-20 (March 1972).

64. V.V. Kremnev, Y.A. Kurbatov, "X-rays from a Gas Discharge in a Strong Electric Field", Sov. Phys.-Tech. Phys., 8, 626-629 (October 1972).

65. R.V. Babcock, I. Liberman, W.D. Partlow, "Volume Ultraviolet Preionization from Bare Sparks", IEEE J. of Quantum Electronics, QE-12, No. 1, 29-34 (January 1976).

66. B.J. Reits, A.H.M. Olbertz, "Low Ionization Seed Gases in CO_2 TEA Lasers", Physics Dept., Twente University of Technology, Enschede, The Netherlands. (Private Communication).

67. B.J. Reits, A.H.M. Olbertz, "Doped CO_2 TEA Laser", Appl. Phys. Lett., 27, No. 1, 24-25 (July 1975).

68. A.H.M. Olbertz, B.J. Reits, "CO_2 TEA Lasers Sustained by Metastable N_2", Appl. Phys. Lett., 28, No. 4, 199-201 (February 1976).

69. T.S. Peterson, "Calculus with Analytic Geometry", (Harper & Row, Publishers, New York, Evanston, London, 1960).

70. S.M. Selby, "Standard Mathematical Tables", (CRC Press, Cleveland, 23rd Edition, 1975).

71. H.J.J. Seguin, J. Tulip, D. McKen, "UV Photoionization Density Measurements in TEA Lasers", Appl. Phys. Lett., 23, No. 6, 344-346 (September 1973).

72. H.J.J. Seguin, J. Tulip, D. McKen, "Enhancement of Photoelectron Density in TEA Lasers Using Additives", Appl. Phys. Lett., 23, No. 9, 527-529 (November 1973).

73. R.D. Hudson, "Critical Review of Ultraviolet Photoabsorption Cross Sections for Molecules of Astrophysical and Aeronomic Interest", Rev. of Geophys. and Space Phys., 9, No. 2, 306-397 (May 1971).

74. M.E. Van Valkenberg, "Network Analysis", (Prentice-Hall, London, Sydney, Toronto, New Delhi, Tokyo, 2nd Edition, 1965).

75. S.B. Hammond, "Electrical Engineering", (McGraw-Hill Book Company, New York, 1961).

76. A.E. Seigman, "An Introduction to Lasers and Masers", McGraw-Hill Series, New York, 1971).

77. C.M. Van Atta, "Vacuum Science and Engineering", (McGraw Hill Book Company, New York, San Francisco, Toronto, London, Sydney, 1965).

78. K. Ogata, "Modern Control Engineering", (Prentice-Hall, Inc., New Jersey, 1970).

79. "American Institute of Physics Handbook", (McGraw-Hill Book Company, New York, 3rd Edition, 1972).

80. J. Watanabe, E.C.Y. Inn, "Intensity Measurements in the Vacuum Ultraviolet", J. Optical Soc. 43, No. 1, 32-35 (January 1953).

81. "Handbook of Chemistry and Physics", The Chemical Rubber Company, Cleveland, 47th Edition, 1962).

82. "Standard Handbook for Electrical Engineers", (McGraw-Hill Book Company, New York, 10th Edition, 1969).

83. A. Beiser, "Perspectives of Modern Physics", (McGraw-Hill Series, New York, 1969).

84. B.A. Lengyel, "Introduction to Laser Physics", (John Wiley and Sons, Inc., New York, London, Sydney, 1966).

85. W.V. Smith, P.P. Sorokin, "The Laser", (McGraw-Hill Book Company, New York, 1966).

86. E.L. Steele, "Optical Lasers in Electronics", (John Wiley and Sons, New York, London, Sydney, 1968).

87. A.L.S. Smith, T.H. Bett, P.G. Brown, "The Effects of Gas Additives on TEA CO_2 Lasers", IEEE J. of Quantum Electronics, QE-11, No. 7, 335-340 (July 1975).

88. P. Bletzinger, D.A. LaBorde, W.F. Bailey, W.H. Long, P.D. Tannen, A. Garscadden, "Influence of Contaminants on the CO_2 Electric-Discharge Laser", IEEE J. of Quantum Electronics, QE-11, No. 7, 317-321 (July 1975).

89. N.M. Ceglio, J.D. Lawrence, E.V. George, "Spark Photoionization of CO_2 Laser Gases", M.I.T. Cambridge, Massachusetts, (Private Communication).

90. V.H. Dibeler, J.L. Franklin, R.M. Reese, "Electron Impact Studies of Hydrazine and the Methyl-Substituted Hydrazines", (Publication by Mass Spectrometry Laboratory, National Bureau of Standards, Washington D.C., U.S.A.)

91. W.S. Koski, J.J. Kaufman, C.D. Pachucki, "A Mass Spectroscopic Appearance Potential Study of Some Boron Trihalides", (Publication by Dept. of Chem., The John Hopkins University and The Knolls Atomic Power Laboratory, General Electric Company, March 1959).

92. A.J. Palmer, "A Physical Model on the Initiation of Atmospheric-Pressure Glow Discharges", Appl. Phys. Lett., 25, No. 3, 138-140 (August 1974).

93. E.A. Crawford, A.V. Phelps, "Formative Time Lags in CO_2 Laser Discharges", Appl. Phys. Lett., 25, No. 1, 59-61 (July 1974).

94. Varian and Associates Reflex Klystron, Type X-13c, Varian Associates, California.
Operating and Service Manual, (HP Pat. No. 00716-99001) Model 716B, Klystron Power Supply, Hewlett Pack and Company, Colorado (1963).

95. "The Microwave Engineers' Handbook and Buyers' Guide", (Horizon House Publication, Massachusetts, 1965).

96. S.F. Adam. H. Packard, "Microwave Theory and Applications", (Prentice-Hall, Inc., New Jersey (1969).

97. Operating and Service Manual, K10-8551B Spectrum Analyser Converter Section, Hewlett-Packard Company, California (1966).

98. RCA Brochure of Photomultiplier Tubes for Laser Beam Detector Applications in the 3000 to 11,000A° Range.

99. "Instrument Instruction Manual", (Jarrel Ash Company, Massachusetts, February 1963).

100. "The Radio Amateur's Handbook", (The American Radio Relay League, Newington, Conn. 53rd Edition, 1976).

101. R. Morrison, "DC Amplifiers in Instrumentation", (Wiley-Interscience, New York, 1970).

102. C.A. Desoer, E.S. Kuh, "Basic Circuit Theory", (McGraw-Hill Book Company, New York, 1969).

103. L. Strauss, "Wave Generation and Shaping", (McGraw-Hill Inc., New York, 2nd Edition, 1970).

104. F.K. Manasse, J.A. Ekiss, C.R. Gray, "Modern Transistor Electronics and Design", (Prentice-Hall, New Jersey, 1967).

105. J. Millman, C.C. Halkias, "Electronic Devices and Circuits", (McGraw-Hill Book Company, New York, 1967).

106. Semiconductor Data Library, Series A, Motorola Inc., (1974).

107. Signetics Digital Linear Mos Data Book, Signetics Corporation, California (1974).

108. Semiconductor Data Handbook, General Electric Company, New York, 2nd Edition (1973).

109. Fairchild Linear Integrated Circuits Data Catalog, Fairchild Semiconductor, California (1973).

110. Signetics Digital Linear Mos Applications, Signetics Corp., California (1974).

111. Electronics Circuit Designers' Casebook, McGraw-Hill Publication, New York (1967).

112. Mos Integrated Circuits National, National Semiconductor Corp., California (1974).

113. RCA Linear Integrated Circuits and DMOS Devices, RCA Corporation (1975).

114. RCA COS/MOS Digital Integrated Circuits, RCA Corp. (1975).

115. Linear Integrated Circuits, National Semiconductor Corp., California (1975).

116. Nickel-Cadmium Battery Application Engineering Handbook, General Electric Company, Florida, 2nd Edition (1975).

117. Voltage Regulator Handbook, National Semiconductor Corp., California (1975).

118. G.A. Mesyats, Y.I. Bychkov, V.V. Kremnev, "Pulsed Nanosecond Electric Discharges in Gases", Sov. Phys. Uspekhi, 15, No. 3, 282-297 (November-December 1972).

119. (Russian work involving C_S) Private Communication.

VITA

NAME: Donald Charles David McKen

PLACE OF BIRTH: Yorkton, Saskatchewan

YEAR OF BIRTH: 1949

POST-SECONDARY EDUCATION AND DEGREES:

University of Alberta, Edmonton, Alberta

1967-1971

B.Sc. in Electrical Engineering with Distinction

University of Alberta

1971-1976

Ph.D. in Electrical Engineering

HONORS AND AWARDS

Grade 12 Graduating Class Valedictorian 1967

Reader's Digest Valedictorian 1967

High School Proficiency Pin 1966 and 1967

Yorkton Kiwanis Award 1967

Sunwapta Broadcasting Ltd., Scholarship 1970

National Research Council of Canada Postgraduate Scholarships 1971-1975

Research Assistanceship University of Alberta 1975-1976

RELATED WORK EXPERIENCE

Part-time teaching assistant, University of Alberta 1971-1975

PUBLICATIONS

1. H.J.J. Seguin, J. Tulip and D. McKen, "UV Photoionization Density Measurements in TEA Lasers", Appl. Phys. Lett., 23, No. 6, 344-346 (September 1973).
2. H.J.J. Seguin, J. Tulip and D. McKen, "Enhancement of Photoelectron Denisty in TEA Lasers Using Additives", Appl. Phys. Lett., 23, No. 9, 527-529 (November 1973).
3. H.J.J. Seguin, J. Tulip and D. McKen, "Ultra-Violet Photoionization in TEA Lasers", IEEE J. of Quantum Electronics, QE-10, No. 3, 311 (1974).
4. H.J.J. Seguin, D. McKen and J. Tulip, "Photon Emission and Photoionization Measurements in the CO_2 Laser Environment", to be published Appl. Phys. Lett., April, 1976.
5. D. McKen, H.J.J. Seguin and J. Tulip, "Photoionization Parameters in the Carbon Dioxide Laser Gases", to be published IEEE J. of Quantum Electronics, August, 1976.
6. H.J.J. Seguin, D. McKen and J. Tulip, "Source Emission and Photoelectron Production in a Seeded CO_2 Laser Mixture", to be published Can. J. of Physics.